UNIVERSITÉ DU LUXEMBOURG

PhD-FSTM-2024-060

The Faculty of Science, Technology and Medicine

DISSERTATION

Presented on 20/08/2024 in Esch-sur-Alzette

to obtain the degree of

DOCTEUR DE L'UNIVERSITÉ DU LUXEMBOURG EN PHYSIQUE

by

Aubin Jean-Claude Mireille PROT

Born on March 13th 1997 in Strasbourg, France

PHOTOLUMINESCENCE ASSESSMENT OF GRADED CHALCOPYRITE ABSORBERS

Dissertation defense committee

Prof. Dr. Susanne Siebentritt, dissertation supervisor

Professor, Université du Luxembourg

Dr. Thomas Dalibor

Director CTO, AVANCIS GmbH

Prof. Dr. Daniele Brida, Chairman

Professor, Université du Luxembourg

Dr. Romain Carron

Empa - Swiss Federal Laboratories for Materials Science and Technology

Prof. Dr. Thomas Kirchartz

Professor, Forschungszentrum Jülich

„The power of the sun, in the palm of my hand”

Dr. Otto Octavius

Table of contents

List of symbols

E_{g}	Band gap
E_{ph}	Photon energy
n_0	Equilibrium density of electrons
p_0	Equilibrium density of holes
n	Non-equilibrium density of electrons
p	Non-equilibrium density of holes
n_{i}	Intrinsic carrier concentration
n^*	Auxiliary density of electrons
p^*	Auxiliary density of holes
h	Planck's constant, $h = 4.135 \cdot 10^{-15}$ eV/K
c	Speed of light, $c = 299792458$ m/s
λ	Wavelength
α	Absorption coefficient
B	Radiative recombination coefficient
k_{B}	Boltzmann constant, $k_{\mathrm{B}} = 8.617$ eV/K
E_{C}	Conduction band energy
E_{V}	Valence band energy
E_{F}	Fermi energy
E_{Fn}	Electron quasi-Fermi level
E_{Fp}	Hole quasi-Fermi level
ΔE_{F}	Quasi-Fermi level splitting
E_{d}	Defect energy
σ_{d}	Defect capture cross section
τ_{e}	Carrier emission time by a defect
τ_{c}	Carrier capture time by a defect
N_{C}	Effective density of state in the conduction band
N_{V}	Effective density of state in the valence band
N_{A}	Acceptor density ~ doping level in a p-type absorber
N_{d}	Defect density
Δn	Excess electron density
q	Elementary charge, $q = 1.602 \cdot 10^{-19}$ C

v_{th}	Thermal velocity
$A(E)$	Absorptance
ϕ_{BB}	Black body emission flux
ϕ_{PL}	Photoluminescence emission flux density
Φ_{PL}	Total emitted photon flux
ϕ_{laser}	Incident photon flux density (from laser)
Φ_{laser}	Total incident photon flux (from laser)
G_{sun}	Total incident photon flux (from sun)
Y_{PL}	Photoluminescence quantum yield, PLQY
$\sigma_{E_{\mathrm{g}}}$	Standard deviation from the mean band gap
m_{e}^{*}	Electron effective mass
m_{h}^{*}	Hole effective mass
m_0	Free electron mass, $m_0 = 9.1 \cdot 10^{-31}$ kg.
τ_{n}	Electron lifetime
τ_{p}	Hole lifetime
j	Current density
j_0	Saturation current density
j_{ph}	Photogenerated current density
j_{SC}	Short-circuit current density
V	Voltage
V_{OC}	Open-circuit voltage
$V_{\mathrm{OC}}^{\mathrm{SQ}}$	Shockley-Queisser open-circuit voltage
FF	Fill factor
A_{el}	Electrical (ideality) diode factor
A_{opt}	Optical diode factor
f_{rep}	Pulsed laser repetition rate
$S_{\mathrm{f,b}}$	Front, back surface recombination
D	Diffusion coefficient

Abstract

It is an accepted fact, the Earth temperature is raising at an alarming rate, having devastating repercussions on the life on the planet. To mitigate this effect, it is paramount to reduce the emission of greenhouse gases, major responsible of the global warming. Among other technologies, solar cells are active players in reducing the emission of greenhouse gases. In particular, chalcopyrite-based solar cells, with a low carbon footprint and current record power conversation efficiency of 23.6%, participate to accelerate the energy transition. Despite the already good performance of $Cu(In,Ga)Se_2$ solar cells, higher theoretical efficiency could potentially be achieved (nearly 34% for a material of 1.34 eV band gap), indicating a margin for further improvement.

The aim of the current work is to characterize high quality industrial $Cu(In,Ga)(S,Se)_2$ (CIGSSe) absorbers in order to understand the underlying efficiency limitations and their physical origin. Specifically, the intentional band gap gradient formed towards the metallic back contact is investigated. Such an absorber architecture is traditionally used to reduce the back surface recombination, responsible for significant non-radiative losses. Furthermore, the impact of silver (Ag) alloying on the band gap gradient and the performance of the absorbers and corresponding submodules is examined.

Photoluminescence (PL) spectroscopy represents the primary investigation method used during this thesis at the Laboratory for Photovoltaics. On one hand, absolute PL measurements allow for quantitative analysis of the absorbers, yielding values for the quasi-Fermi level splitting, the non-radiative losses and the optical diode factor. Combined with a gradual etching of the absorbers, a depth-resolved investigation of the radiative recombination activity is achieved. On the other hand, time-resolved PL (TRPL) leads to an estimation of the charge carrier lifetime and doping density in various absorbers. Collaborations with several European research groups provided access to other investigation techniques such as cathodoluminescence (CL) spectroscopy or Raman spectroscopy, both contributing greatly to the findings of this work. From a combination of the diverse mentioned measurement techniques, a novel model for the band gap gradient is proposed. Instead of the gradual band gap variation suggested by compositional analysis (e.g. GDOES), it is found that mostly two

chalcopyrite phases of low (~ 1.04 eV) and high ($\sim 1.5 - 1.6$ eV) band gap form respectively towards the front and the back sides of the absorber and interlace in the bulk of the material, leading to an apparent gradient. Furthermore, alloying the CIGSSe absorbers with low amounts of Ag leads to a decreased number of band gap jumps as observed in the Ag-free samples. The resulting smoother band gap gradient is attributed to an enhancement of the Ga and In interdiffusion in the ACIGSSe absorbers. Moreover, PL decay measurements indicate that the minority carrier lifetime increases upon Ag-alloying. Additionally, a reduction of the non-radiative recombination losses by as much as 30 meV is measured for the best ACIGSSe absorber compared to the Ag-free reference. Furthermore, it is found that improved performance can be achieved in ACIGSSe absorbers grown at a lower process temperature, what could lead eventually to a reduction of the production costs. Nevertheless, a comparison between absorbers and corresponding finished submodules, which showed only a relative improvement of 1.6% in terms of efficiency in the best case, suggests that the cell-making process could be optimized further to fully benefit from the improved ACIGSSe absorbers.

All in all, this thesis provides new insights about the CIGSSe absorbers grown at AVANCIS. It challenges the current view of the band gap gradient in graded absorbers and demonstrates that improvement of both the absorbers and the resulting submodules is possible upon Ag-alloying. Finally, it is established how TRPL investigation may be utilized to determine reliable charge carrier lifetime and doping densities.

Chapter 1

Introduction

It's official, the year 2023 is the warmest year recorded until today. All the months of the second part of the year, i.e., June to December, reached their hottest record since 1850 [1]. According to the latest Intergovernmental Panel on Climate Change (IPPC) report [2], the global Earth surface temperature over the timespan 2011-2020 has reached a value 1.1°C above the one from 1850-1900. Global surface temperature encompasses both lands and oceans' surface temperatures, both raising [3]. Considering the very high ocean's heat capacity and that about 70% of the Earth is covered by water, it takes a tremendous amount of added heat energy to increase the global surface temperature by 1.1°C. Although 1.1°C may not seem much of an increase, it has catastrophic repercussions on the planet and the life on it. In summer 2023, wildfires ravaged Canada and widespread drought throughout the whole country [4]. More recently, massive rainfalls flooded several countries in East Africa, destroying infrastructures, livestock and causing hundreds of deaths [5]. Over the course of the previous years, the occurrence of such extreme weather events has considerably augmented, as a direct consequence of the global warming. But why is this happening? The reason is simple: human activity and the resulting greenhouse gas emissions, such as carbon dioxide (CO_2). Since the beginning of the industrialization (mid-19th century) a near-linear relationship between the cumulative CO_2 emissions and the increase in average Earth temperature is observed. In 2015, 196 countries signed the Paris Agreement [6], pledging to reduce the greenhouse gas emissions to mitigate the global warming and remain below the 1.5°C temperature increase. However, given the current trends, it is very likely that the threshold of 1.5°C will be exceeded during the 21st century, and even keeping global warming below 2°C might prove difficult [2]. Hence, the challenge that we are currently facing is to achieve the net zero carbon emission as fast as possible, i.e., moving away from the fossil fuels (oil, coal and natural gas) that still represented more than 80% of the global primary energy consumption in 2022 [7].

Fortunately, this energy transition from fossil fuels towards low CO_2 emitting energy sources is already happening. Since the beginning of the current century, an exponential increase of the share of renewable sources in the global energy mix is observed, reaching 14% on average in the world. In 2022, more than 8000 TWh of renewable energy was generated worldwide [7]. While more than half of it came from hydropower, wind and solar production participated respectively for 2300 TWh and 1600 TWh, and their share is foreseen to increase rapidly in the future. In 2023, the global cumulative installed photovoltaic (PV) capacity reached above 1.4 TWp vs. about 1.1 TWp in 2022 [8]. Among the PV technologies, Si-wafer based modules accounted for about 97% of the total production of the year 2023 and the remaining 3% represented the share of thin films. Thin films, such as CIGS, offer the possibility of being flexible and colorful, making them suitable for building integration. With their colorful CIGSSe-based SKALA modules, AVANCIS implements aesthetic solar facades on various industrial and residential buildings. Another European company, Midsummer, develops flexible CIGS modules for creating full solar roofs. Recently, they announced two new production factories in Sweden and Italy, of 200 MW and 50 MW capacity, respectively, participating to the global expansion of PV.

Beside increasing the production and installation capacity of PV, it is primordial to boost in parallel the power yield per square meter to accelerate the energy transition. This can be achieved either by improving the efficiency of current solar modules (reaching a record efficiency of 20.3% for CIGSSe submodules [9]) or by developing multi-junction structures, known as tandem cells, which can efficiently harvest a broader spectrum of light [10]. Both approaches require a deeper understanding of the physical mechanisms limiting the current cells' performance and the optimization of the growth and cell-making processes. This is where my PhD research project intervenes. The POLCA project is a collaboration between the funding industrial partner AVANCIS [11] and the Laboratory for Photovoltaics (LPV), as part of the University of Luxembourg. The former provided high quality CIGSSe absorbers, and the in-depth investigation of the material was performed at LPV. This thesis consists of seven chapters, including the current introduction, and is organized as follows.

Chapter 2 provides the background knowledge necessary for the good understanding of the results discussed in the core chapters (4-6). First, the CIGSSe material and corresponding cell structure is presented, followed by an introduction to the carriers' dynamics in a semiconductor

upon light absorption. Further, the solar cell parameters, defining the efficiency of a solar cell are discussed. Finally, a detailed overview is given of what can be measured via photoluminescence, using either a continuous wave or a pulsed laser.

Chapter 3 introduces the main investigation techniques used in this work. An extensive presentation of the PL and TRPL setups is provided, as well as the procedure for the spectral and intensity calibration of the absolute measurements. Due to numerous collaborations with other laboratories, most measurements other than PL were not performed by myself, in particular cathodoluminescence spectroscopy, glow discharge optical emission spectroscopy and Raman spectroscopy. Nevertheless, as these measurement techniques contributed greatly to the findings of this thesis, they are introduced in chapter 3 as well.

Chapter 4 is based on the 2023 published work "Composition variations in $Cu(In,Ga)(S,Se)_2$ solar cells: Not a gradient, but an interlaced network of two phases" [12]. The investigated absorbers are grown with an intentional band gap gradient towards the back contact. Despite the gradual change of band gap suggested by compositional analysis, it is demonstrated that instead, two chalcopyrite phases of high and low band gaps interlace in the bulk of the absorber. The former one being present in higher density towards the back side, whereas the latter one is mostly present towards the front, leading to an apparent band gap gradient. In addition, it is shown that the high band gap phase is of poorer quality than the low band gap one, due to the presence of deep defects.

Chapter 5 focuses on the effect of Ag-alloying in CIGSSe absorbers. Most of the discussed findings are reproduced from the 2024 published work entitled "Improved Sequentially Processed $Cu(In,Ga)(S,Se)_2$ by Ag Alloying" [13]. In general, it is found that with added Ag larger grains are obtained and that the interdiffusion of Ga and In is enhanced, leading to a smoother band gap gradient as compared to the model proposed in chapter 4. The ACIGSSe absorbers (and resulting submodules) were optically (and electrically) characterized. Compared to the Ag-free reference sample, a decrease of the non-radiative losses by as much as 30 meV is measured on the bare Ag-alloyed absorbers. While the improvement measured on the submodules is lower than on the bare absorbers, a relative improvement of 1.6% could be achieved for the best performing device.

Chapter 6 differs slightly from the previous two chapters as it does not result from a published work. It concentrates on the time-resolved photoluminescence investigation of a collection of various CIGSSe absorbers, including some discussed in the previous chapters. A lot of technical and understanding questions about TRPL transient decays could be answered in this chapter. In particular, it is proposed that the excitation dependence of the measured decay time is mainly due to the excitation dependence of the Shockley-Read-Hall lifetime that limits the recombination in chalcopyrite solar cells. Reasonable carriers' lifetime can be determined from the experimental data, and combined with absolute PL, an estimation of the doping density can be made, leading to values comparable to that from CV measurements. Furthermore, it is discussed that a temperature dependence of the decay time does not necessarily indicate the presence of trap states but could be explained by thermally activated multiphonon recombination. Finally, the effect of the buffer layer on the transient decays is addressed and it is speculated that the sputtered ZnOS buffer layer alone can lead to the formation of a small space charge region.

Last but not least, chapter 7 summarizes the main findings of the core chapters and suggests additional measurements that could be performed to complement the ones from this work.

Chapter 2

Background

The aim of this chapter is to introduce the relevant physical concepts necessary for the good understanding of this thesis. First, a general introduction to the CIGSSe material and associated solar cell is given in section 2.1. The basic principles of semiconductors, such as charge carrier densities, light absorption and carriers recombination are discussed in section 2.2. The solar cell parameters, paramount for the assessment of the efficiency of a cell, are described in section 2.3. Finally, sections 2.4 and 2.5 cover the working principle of steady state photoluminescence spectroscopy and time-resolved photoluminescence spectroscopy. The related measurable quantities of importance for this work are presented. The general information discussed in this chapter is principally adapted from various textbooks [14–18].

2.1. The CIGSSe material

While all investigated absorbers were provided by the external industry partner, AVANCIS [11] and not grown in the laboratory, it is essential to understand the nature of the material in order to improve it.

2.1.1. Crystal structure

The CIGSSe abbreviation is commonly used to refer to the chalcopyrite compound $Cu(In,Ga)(S,Se)_2$. This material crystalizes in a tetragonal structure and originally gets its name from the copper iron sulfide mineral ($CuFeS_2$) that crystallizes in this particular structure. CIGSSe is a I-III-VI_2 compound (A^I-B^{III}-C^{VI}_2), meaning that it is composed of elements from the group I of the periodic table (copper), from the group III (gallium and indium) and from the group VI (selenium and sulfur). Each A-atom (Cu) is bound to four C-atoms (Se or S),

while each C-atom forms a bound with two A-atoms and two B-atoms (Ga or In) [19]. Were the atoms A and B randomly distributed, the crystal would take a cubic zincblende structure. This is not the case, and the CIGSSe superlattice displayed in Figure 2.1 is of chalcopyrite structure with a ratio of the lattice parameters $c/a \sim 2$. Therefore, the quantity $2 - c/a$ gives a value for the tetragonal distortion of the lattice which may arise from the differences in bond length between A-C and B-C. While there is a large literature on the topic, it is not directly important for this thesis.

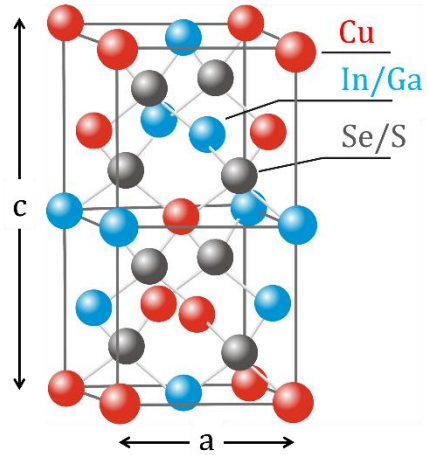

Figure 2.1. Schematic representation of the tetragonal crystal structure of a chalcopyrite $Cu(In,Ga)(S,Se)_2$ compound. The red atoms are Cu, the black ones are S or Se and the blue ones are Ga or In.

2.1.2. Tunability of the band gap

One of the many attractive aspects of the CIGSSe material is the tunability of its band gap E_g. Depending on the concentration of Ga and In, usually indicated by the Ga/(Ga+In) ratio (GGI in short), and the concentration of S and Se, S/(S+Se) ratio (SSSe in short), the band gap can be tuned at will from 1.00 eV to 2.43 eV. Considering X the GGI and Y the SSSe, the band gap (in eV) of the penternary alloy $Cu(In_{(1-X)}Ga_X)(S_YSe_{(1-Y)})_2$ is approximated according to [20,21] by

$$E_g(X,Y) = 1.00 + 0.13X^2 + 0.08X^2Y + 0.13XY + 0.55X + 0.54Y \qquad (2.1)$$

Following Equation (2.1), a band gap of 1.00 eV is achieved for the $CuInSe_2$ compound, when $X = Y = 0$ and a band gap of 2.43 eV corresponds to the ternary alloy $CuGaS_2$, when $X = Y = 1$. A visual representation of Equation (2.1) is depicted in Figure 2.2. The large range of band

gaps available for the CIGSSe alloy makes it, for instance, a very good candidate for tandem application. The ideal band gap for a 2-terminals tandem bottom cell is around 1.0 eV, whereas the one for the top cell should be close to 1.6 eV, leading to theoretical efficiencies as high as 46% [22]. CIGSSe is suitable for both, bottom and top cell.

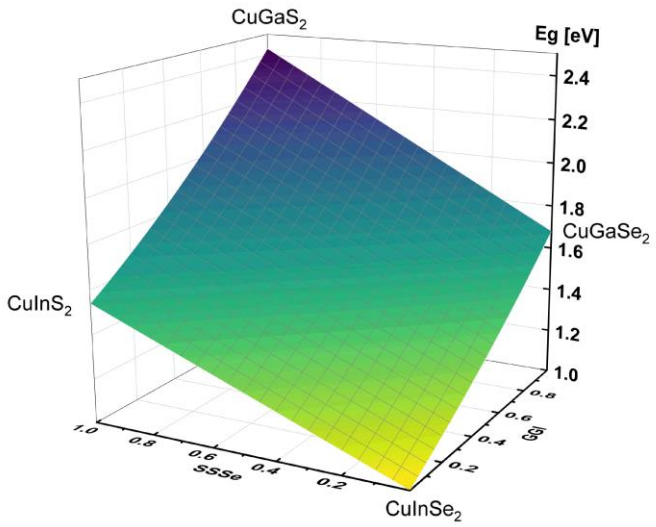

Figure 2.2. 3D representation of Equation (2.1) showing the evolution of the band gap depending on the GGI and the SSSe ratios. The four extreme compositions are indicated: $CuInSe_2$ (1.00 eV), $CuInS_2$ (1.54 eV), $CuGaSe_2$ (1.68 eV) and $CuGaS_2$ (2.43 eV).

Furthermore, the ability to tune the band gap by changing the composition of the alloy has been exploited to grow absorbers with graded GGI, leading to a band gap gradient through the absorber thickness [23–25]. Such a single graded structure leads to an increase of the conduction band towards the back contact and thus prevents the electrons to recombine there non-radiatively before collection. The current record efficiency CIGS solar cell (alloyed with Ag) [26] is based on such "hockey-stick" band gap gradient, i.e., flat for the most part and abrupt at the back. Different absorber architectures involve an additional band gap increase at the front side (double gradient, see Figure 4.1 in chapter 4), meant to reduce undesirable surface recombination and improve the interface absorber/buffer. This gradient may be achieved with a higher Ga content towards the front surface of the absorber or, as is the case in this thesis, by raising the S content at the absorber surface. In addition to an increase in the conduction band, S is known to lower the valence band as well, widening the band gap at the front surface [27].

In either case (single or double gradient), the minimum of the band gap is commonly referred to as "notch". The band gap gradient will be discussed in more details in chapter 4.

The absorbers investigated in this thesis are grown with a Cu/(Ga+In) (or CGI) smaller than unity, typically $0.95 < \mathrm{CGI} < 0.98$. They are therefore referred to as Cu-poor absorbers. In this off-stoichiometry configuration, other phases than the A^{I}-B^{III}-C^{VI}_2 (1:1:2) can form during the crystal growth, such as A^{I}-B^{III}_3-C^{VI}_5 (1:3:5) or A^{I}-B^{III}_5-C^{VI}_8 (1:5:8) [28,29]. These phases are known as ordered vacancy compounds (OVC) or ordered defect compounds (ODC). It is proposed that in the Cu-In-Ga-Se quaternary system, the OVCs arise from the electrically inactive defect complex $M_{Cu} - 2V_{Cu}$, where M stands for In or Ga [28,30,31]. It is still debated, however, whether OVCs play a beneficial or detrimental role for the absorber performance. While the appearance of OVCs (assuming the formation of the complex $M_{Cu} - 2V_{Cu}$) may reduce the density of detrimental M_{Cu} deep defects [30], it is concluded in [32] that they are detrimental and should be avoided. Another work [33] demonstrate that potassium-fluoride (KF) post-deposition treatment in selenides is effective only in the presence of OVCs. In the present work, OVCs are discussed for CIGSSe and ACIGSSe in chapters 4 and 5.

2.1.3. Solar cell structure

While the active material in a solar cell is the absorber, additional layers are necessary to obtain a working device. A schematic representation of a functional p-type CIGSSe solar cell structure and corresponding band diagram under illumination are shown in Figure 2.3. In particular, the structure features (from bottom to top) the soda-lime glass substrate, the Mo back contact, the double graded absorber layer, the buffer layer (ZnOS), the windows layers (intrinsic ZnO and Al-doped ZnO) and finally the metallic front contact (Ni/Al grids). The contacts are not drawn in the band diagram and only the semiconductor layers are represented. The increase in E_C towards the back side is due to the Ga increase, while the E_C increase and E_V decrease towards the front are a result of the higher S content near the front surface. In this configuration, a "spike" – like absorber/buffer interface is obtained, i.e., a positive conduction band offset is forming. This "spike" – like (opposite to "cliff" – like) interface is necessary to prevent electrons to recombine without restraint at the interface. The positive offset, however, should not be too large, less it creates a barrier for the electrons and blocks charge transport. Minemoto

et al. [34] demonstrate that the short-circuit current drops abruptly for an offset larger than 0.4 eV, setting the upper limit for the offset.

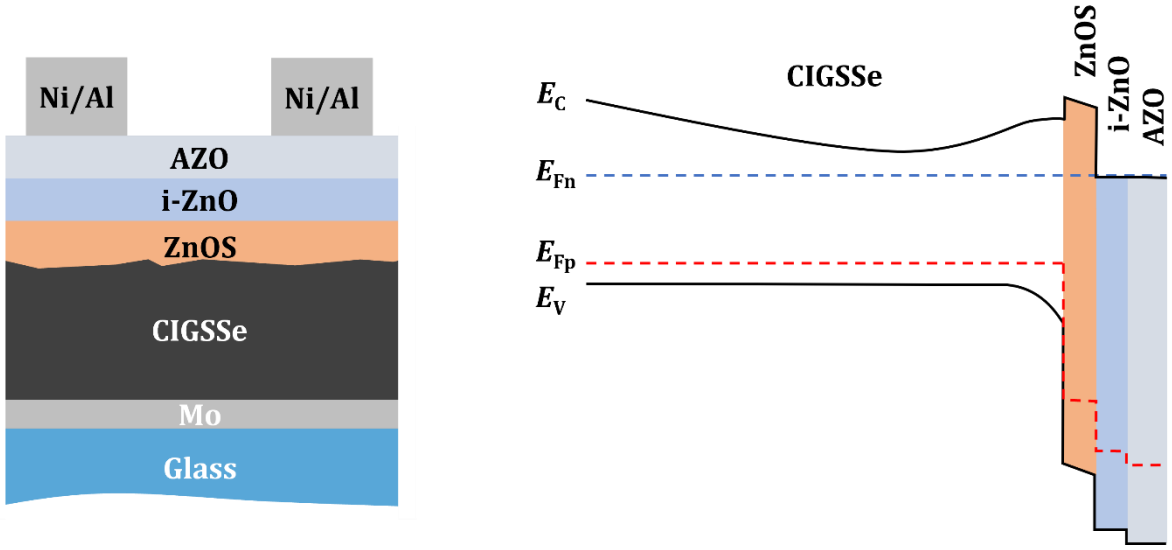

Figure 2.3. Sketch of a solar cell structure (left) and corresponding band diagram under illumination (right). The blue dashed line represents the electron Fermi level and the red dashed one represents the hole Fermi level. The metal contacts are not displayed in the band diagram. The thickness of the different layers are not scaled.

2.2. Basic principles

In the following, important key concepts are introduced, in particular the generation and recombination of charge carriers in a semiconductor, as well as their density in the energy bands.

2.2.1. Charge carriers in semiconductors

The CIGSSe absorber is a direct band gap semiconductor, allowing it to be used for thin film solar cells, typically $1 - 3$ µm thick. While CIGSe can be intrinsically grown n-type (at Ga content below $15 - 19\%$ [35]), it is usually employed as p-type. In a p-type absorber, the electrons are referred to as minority carriers and the holes as majority carriers, for the concentration of holes is considerably larger than that of the electrons. The term p-type, opposite to n-type, means that the semiconductor is doped predominantly with acceptors. In the case of CIGS, the doping results from intrinsic defects such as Cu vacancies V_{Cu} or Cu

antisite Cu_{III} that are reported as shallow acceptors in this material [36]. The density of acceptor states N_A gives a measure of the doping level of an absorber and is typically in the order of $10^{15} - 10^{16}$ cm^{-3} in CIGS [37–40].

In the case of a non-degenerated semiconductor in thermal equilibrium, the density of electrons n_0 in the conduction band follows the Boltzmann approximation

$$n_0 = N_C \cdot \exp\left(-\frac{E_C - E_F}{k_B T}\right) \tag{2.2}$$

where N_C is the effective density of states of the conduction band, k_B is the Boltzmann constant, E_F is the Fermi energy and T is the absolute temperature. Similarly, the density of holes p_0 in the valence band is described by

$$p_0 = N_V \cdot \exp\left(-\frac{E_F - E_V}{k_B T}\right) \tag{2.3}$$

where N_V is the effective density of states in the valence band. In thermal equilibrium, the intrinsic carrier concentration is given by $n_0 \cdot p_0 = n_i^2$. In the case of an intrinsic semiconductor, i.e., undoped ($n_0 = p_0$), the Fermi level lies exactly in the middle of the band gap, equidistant from the conduction and valence band edges (if $N_V = N_C$). However, in the case of an extrinsic semiconductor, the Fermi level moves towards the band containing the largest density of carriers, e.g. the valence band in a p-type semiconductor.

If the thermal equilibrium is broken, for example upon light absorption as discussed in section 2.2.2, charge carriers are generated in the bands and their densities become $n = n_0 + \Delta n$ and $p = p_0 + \Delta p$, where Δn and Δp are the generated carrier densities. In this case, the system cannot be described by a single Fermi level anymore and it splits up into two quasi-Fermi levels, E_{Fn} and E_{Fp} for the electrons and holes, respectively. Equations (2.2) and (2.3) are rewritten accordingly as

$$n = N_C \cdot \exp\left(-\frac{E_C - E_{Fn}}{k_B T}\right) \tag{2.4}$$

$$p = N_{\mathrm{V}} \cdot \exp\left(-\frac{E_{\mathrm{Fp}} - E_{\mathrm{V}}}{k_{\mathrm{B}}T}\right) \tag{2.5}$$

The product of Equations (2.4) and (2.5) leads to

$$n \cdot p = \underbrace{N_{\mathrm{C}}N_{\mathrm{V}} \cdot \exp\left(-\frac{E_{\mathrm{C}} - E_{\mathrm{V}}}{k_{\mathrm{B}}T}\right)}_{n_{\mathrm{i}}^2} \exp\left(\frac{E_{\mathrm{Fn}} - E_{\mathrm{Fp}}}{k_{\mathrm{B}}T}\right) \tag{2.6}$$

where the quasi-Fermi level splitting (qFls) is defined as $\Delta E_{\mathrm{F}} = E_{\mathrm{Fn}} - E_{\mathrm{Fp}}$, as schematized in Figure 2.4. The latter represents a key quantity as it gives the maximal achievable open-circuit voltage (V_{OC}) of a solar cell and thus relates directly to the device performance. The qFls of a bare absorber can be measured by photoluminescence (PL) spectroscopy, which is the focus of section 2.4.2.

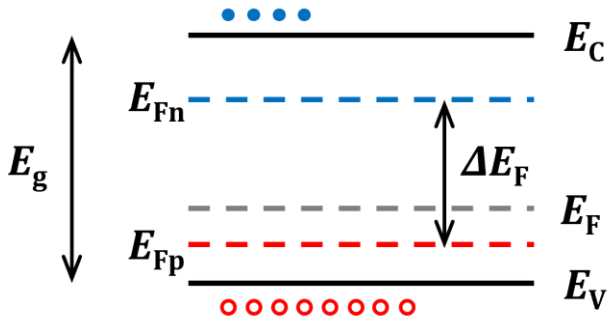

Figure 2.4. Band diagram of a p-type semiconductor in non-equilibrium. The electrons are represented by the blue dots and the holes by the red circles. The blue and red dashed lines correspond to the electron and hole quasi-Fermi levels. In thermal equilibrium, a single Fermi level would be enough to describe the electron and hole concentrations, represented by the gray dashed line.

2.2.2. Absorption of light

As mentioned in the previous section, when light impinges on a semiconductor, it can interact with the material. Light is an electromagnetic wave composed of energy quanta, called photons, each carrying an energy $E_{\mathrm{ph}} = hc/\lambda$, where h is the Planck's constant, c is the speed of light in vacuum and λ is the wavelength of the electromagnetic wave. Only a fraction of the solar spectrum may be used by solar cells, depending on their band gap. Figure 2.5 highlights the fraction of the solar spectrum that is available for a cell of band gap $E_{\mathrm{g}} = 1.05$ eV, which

is a typical value for the absorbers considered in this thesis. Hence, depending on its energy, a photon hitting the surface of a semiconductor can be either transmitted, if $E_{\mathrm{ph}} < E_{\mathrm{g}}$, reflected or absorbed. The first two cases are non-desirable for solar cell application, as they correspond to unavailable energy for power generation.

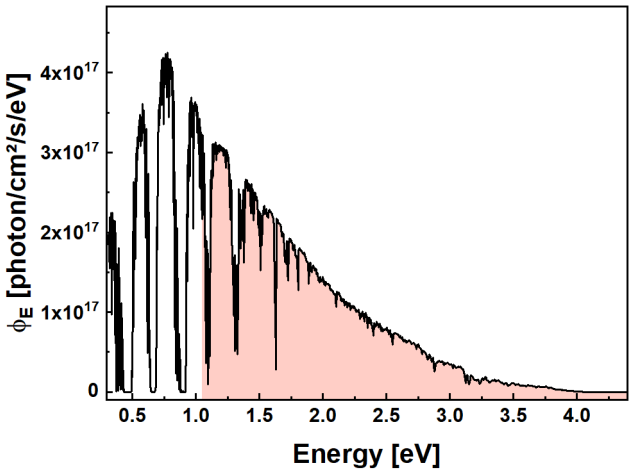

Figure 2.5. AM1.5G solar photon flux density, corresponding to the global solar spectrum reaching the earth surface after crossing a 1.5 atmosphere thickness. It is normalized to a power density of 1000 W/cm^2. The highlighted area represents the share of the spectrum that is available to a solar cell of band gap $E_{\mathrm{g}} = 1.05$ eV. The spectrum is taken from the NREL website [41]

For photons carrying $E_{\mathrm{ph}} > E_{\mathrm{g}}$, the probability of absorption is given by the absorption coefficient α and the intensity $I(z)$ penetrating the material decreases exponentially following the Beer-Lambert's law

$$I(z) = I_0 \cdot e^{-\alpha z} \tag{2.7}$$

where I_0 is the incoming intensity and z is the depth at which the photon is absorbed. Because of their direct band gap, CIGS solar cells possess a high absorption coefficient, in the order of 10^5 cm^{-1} at 660 nm [42]. If a photon is finally absorbed, it transfers its energy to an electron in the valence band, which is excited into an available state in the conduction band, leaving a hole in the valence band. This process is called electron-hole pair generation. When the transferred energy is larger than the band gap energy, the photogenerated carriers thermalize to the respective band edges by phonon emission, i.e., by losing thermal energy to the lattice. The

carrier distribution that results from this quasi-thermal equilibrium is given by Equation (2.4) and (2.5) as discussed in the previous section.

2.2.3. Recombination of the charge carriers

Once electrons are excited, they do not remain in the conduction band indefinitely. In the case of a working solar cell, e.g. at maximum power point (cf. section 2.3), the charges carriers are collected and participate to the current generation. In this section, only the semiconductor layer is considered and therefore no collection is possible. Thus, the recombination process, i.e., the annihilation of an electron-hole pair, happens through one of the three principal mechanisms: band-to-band recombination, defect assisted recombination or Auger recombination (see Figure 2.6). If not stated otherwise, a p-type semiconductor is considered in the following, i.e., minority carriers are electrons and majority carriers are holes.

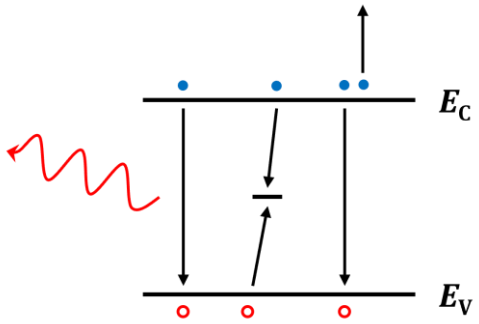

Figure 2.6. Schematic representation of the three principal recombination mechanisms available to a free electron in the valence band. From left to right: band-to-band recombination, defect assisted recombination, Auger recombination.

Band-to-band

Band-to-band recombination corresponds to the situation where a free electron in the conduction band relaxes to the valence band and annihilates with a free hole. A photon of the energy of the transition is released, and hence, such a process is known as radiative recombination. At room temperature, carriers trapped in shallow defects, states close to the band edges, have enough thermal energy to be re-emitted into the respective bands before recombining, therefore making band-to-band recombination the dominant radiative recombination mechanism. Multiple other impurity-related radiative recombination

mechanisms exist in CIGS absorbers but are not relevant for this thesis and will not be discussed.

Since radiative recombination depends on an electron and a hole "finding each other", the net radiative recombination rate, considering the difference of the non-equilibrium recombination rate and the generation rate, increases with the carrier densities and is given by

$$R_{\mathrm{rad}} = B(np - n_{\mathrm{i}}^2) \tag{2.8}$$

where B is the material-specific radiative recombination coefficient. For CIGS, it typically takes a value $B \sim 1 \cdot 10^{-10}$ $\mathrm{cm^3 s^{-1}}$ [43].

In the case of a p-type semiconductor, the density of majority carriers is approximately constant (for reasonably low excitations), i.e., $p \approx p_0 \approx N_{\mathrm{A}}$ and Equation (2.8) can be rearranged as

$$R_{\mathrm{rad}} = BN_{\mathrm{A}}(n - n_0) = BN_{\mathrm{A}}\Delta n \tag{2.9}$$

Often, the recombination rate will be expressed in terms of minority carrier lifetime. For a linear equation as the one for radiative recombination, the lifetime is simply written as

$$\tau_{\mathrm{rad}} = \frac{1}{BN_{\mathrm{A}}} \tag{2.10}$$

Inserting an assumed doping level of 10^{16} $\mathrm{cm^{-3}}$, it yields $\tau_{\mathrm{rad}} \sim 10^{-6}$ s, as predicted for chalcogenides in [14,43]. This value is much larger than the usual measured lifetimes in this material, ranging from a few nanoseconds to a few hundreds of nanoseconds [44–48]. The reason is that, in fact, most of the recombination occurs non-radiatively. A measure of the radiative recombination (and by extension the non-radiative one) is given by the photoluminescence quantum yield Y_{PL}, also abbreviated PLQY. In a PL experiment, it is defined as the ratio between the total emitted photon flux Φ_{PL} and the total incident photon flux Φ_{laser}, $Y_{\mathrm{PL}} = \Phi_{\mathrm{PL}}/\Phi_{\mathrm{laser}}$. As of today, the highest reported PLQY for a solar cell is 35.7%, achieved with a GaAs cell, while CIGSe solar cells typically perform in the range $0.1 - 1.6\%$ [26,49].

Defect assisted: Shockley-Read-Hall

If a recombination occurs without the emission of a photon, it is defined as non-radiative recombination. The transition energy can go into another carrier (Auger) or into phonons, e.g. recombining via defect levels within the band gap. As shown in Figure 2.6, for it to happen, an electron must fall from the conduction band into a defect state and a hole from the valence band must be captured by the same defect. The energy position of the defect plays a critical role, as it has to capture both an electron and a hole. The larger the energy difference between the initial and final states of the carrier, the more phonons are needed for the transition and hence the more unlikely it will happen non-radiatively. Furthermore, when a defect is close to a band edge, the probability of carrier re-emission before recombination is higher. Therefore, defects around midgap will greatly increase the proportion of non-radiative processes and are of the most detrimental kind. This defect assisted mechanism is frequently referred to as Shockley-Read-Hall (SRH) recombination [50,51].

In order to determine the net recombination rate for a specific SRH process, four principal transitions have to be considered: the capture of an electron (i) and a hole (ii), but also the re-emission of an electron (iii) or a hole (iv) before recombination. The expressions for the rates (i)-(iv) can be found in Equation (2.65) from reference [14]. From these, the net recombination rate is derived [52] and can be written as

$$R_{\mathrm{SRH}} = \frac{np - n_{\mathrm{i}}^2}{\tau_{\mathrm{p}}(n + n^*) + \tau_{\mathrm{n}}(p + p^*)} \tag{2.11}$$

with τ_{p} and τ_{n} the hole and electron lifetimes. The quantities n^* and p^* are defined as auxiliary carrier densities, i.e., the electron and hole densities when the Fermi level coincides with the defect energy considered, $E_{\mathrm{d}} = E_{\mathrm{F}}$. Setting $E_{\mathrm{V}} = 0$, the auxiliary carrier densities are given by

$$n^* = N_{\mathrm{C}} \cdot \exp\left(-\frac{E_{\mathrm{g}} - E_{\mathrm{d}}}{k_{\mathrm{B}}T}\right) \tag{2.12}$$

$$p^* = N_{\mathrm{V}} \cdot \exp\left(-\frac{E_{\mathrm{d}}}{k_{\mathrm{B}}T}\right) \tag{2.13}$$

In the case of a low injection level, i.e., when the generated electron concentration is much smaller than the hole concentration ($\Delta n \ll N_\mathrm{A}$), the minority carrier lifetime does not depend on the doping density but on the defect density N_d as

$$\tau_\mathrm{SRH} = \frac{1}{N_\mathrm{d} v_\mathrm{th} \sigma_\mathrm{d}} \tag{2.14}$$

where v_th is the thermal velocity of the minority carriers and σ_d is the capture cross section of the involved defect. In state of the art CIGS solar cells, defect assisted recombination is the limiting process. In addition to bulk defects, surface defects also play a crucial role in carrier recombination. The interruption of the crystal lattice periodicity at the surface generates an interface with its surroundings (e.g., air or other layers), facilitating the formation of defects within this region. These defects act as non-radiative recombination centers.

Auger

The third recombination process displayed in Figure 2.6 is Auger recombination. It is another non-radiative mechanism, during which an electron from the conduction band recombines with a hole from the valence band by transferring its energy to a third particle (electron or hole). For a p-type absorber at low level injection it holds $p \approx N_\mathrm{A}$ and the net recombination rate can be expressed as

$$R_\mathrm{Auger} = C_\mathrm{Auger} N_\mathrm{A}^2 \Delta n \tag{2.15}$$

from which the lifetime of the minority carrier is read

$$\tau_\mathrm{Auger} = \frac{1}{C_\mathrm{Auger} N_A^2} \tag{2.16}$$

where $C_\mathrm{Auger} \approx 10^{-30} - 10^{-31}$ cm^{6}s^{-1} [53,54]. Inserting numbers, it yields $\tau_\mathrm{Auger} \sim 10^{-2}$ s for a doping of 10^{16} cm^{-3} and leads to the conclusion that Auger recombination only plays a role in the minority carrier lifetime in highly doped materials [54], i.e., for $N_\mathrm{A} > 10^{18}$ cm^{-3}.

Finally, the lifetime of the minority carriers is given by the combination of the radiative and non-radiative processes $\tau^{-1} = \tau_\mathrm{rad}^{-1} + \tau_\mathrm{nrad}^{-1}$. The measured lifetime is defined by the limiting mechanism. Depending on the experimental conditions (excitation level, temperature), this

mechanism can change. An extended discussion on the measurement method is provided in section 2.5 and some experimental results are presented in chapter 6.

2.3. Solar cell parameters

While only very few finished solar cells were investigated during the time of this thesis, achieving high power conversion efficiencies (PCE) remains the ultimate goal of solar cell research. This section introduces the cell parameters that define the efficiency of a device. To evaluate the performance of a device, a JV curve is measured, i.e., the solar cell is illuminated and the current density j is measured while swiping across different voltages. Standard test conditions specify a cell temperature of 25°C and an irradiance of 1000 W/m^2, considering the solar spectrum AM1.5. The working principle of a solar cell is based on the photovoltaic effect (hence the name of the technology). In the dark, the diode equation is defined as

$$j = j_0 \left(\exp\left(\frac{qV}{A_{\mathrm{el}} k_B T} \right) - 1 \right) \tag{2.17}$$

where j_0 is the saturation current density, V is the applied voltage and A_{el} is the electrical diode factor (EDF). The latter is further discussed in section 2.4.4. As discussed in the previous sections when light impinges on a solar device, consisting of a p-n junction, it can generate electron-hole pairs. If the photogenerated charges live long enough to be separated by the electric field present in the cell, they can move from the p-side to the n-side, generating a photocurrent density j_{ph} flowing in the opposite direction as the diode current density. Equation (2.17) then becomes

$$j = j_0 \left(\exp\left(\frac{qV}{A_{\mathrm{el}} k_B T} \right) - 1 \right) - j_{\mathrm{ph}} \tag{2.18}$$

Equation (2.18) represents the change of the current density in a device induced by applying a voltage and leads to a typical JV curve as shown in Figure 2.7. Note that for fairer comparison between different cells, the current I is often given as a current density j, in which the area of the cell is taken into account. Considering the fourth quadrant in Figure 2.7, when no voltage is applied, i.e., the device is in short-circuit condition, the current density across the junction is maximized and the photocurrent density reaches a value j_{SC}, known as short-circuit current density. Conversely, when no current is flowing ($j = 0$), the device is in open-circuit condition

and the corresponding applied voltage is known as open-circuit voltage, V_{OC}. The power density achieved by the cell under illumination is given by the multiplication of the current density and the voltage. Somewhere between 0 V and V_{OC} it reaches a maximum known as maximum power point P_{mpp}. As indicated in Figure 2.7, this point is used to find j_{mpp} and V_{mpp}. Since the JV curve is not square, j_{mpp} and V_{mpp} differ from j_{SC} and V_{OC}, and the ratio of their product determines the "squareness", also known as fill factor FF.

$$FF = \frac{j_{mpp} \cdot V_{mpp}}{j_{SC} \cdot V_{OC}} \tag{2.19}$$

Finally, the PCE (or η) is calculated by comparing the total output power with the total input power.

$$\eta = \frac{P_{out}}{P_{in}} = \frac{j_{mpp} \cdot V_{mpp}}{P_{in}} = \frac{j_{SC} \cdot V_{OC} \cdot FF}{P_{in}} \tag{2.20}$$

The last expression of Equation (2.20) is the most common one, as it makes the three quantities j_{SC}, V_{OC} and FF clearly appear.

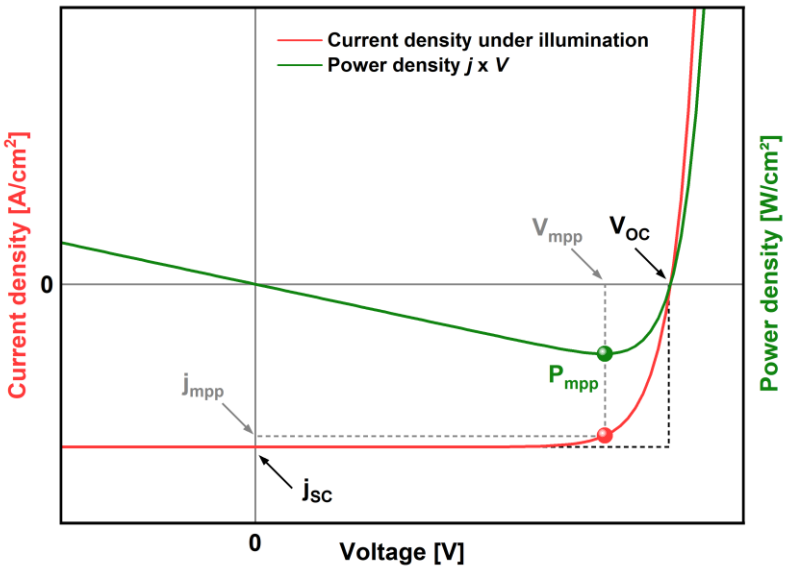

Figure 2.7. Typical JV curve obtained from electrical characterization of a solar under illumination and following Equation (2.18). The maximum power point P_{mpp} is indicated, as well as the related quantities j_{mpp} and V_{mpp}. The short-circuit current density j_{SC} and the open-circuit voltage V_{OC} are identified and labelled accordingly.

Note that by convention the JV curve in Figure 2.7 is displayed in the fourth quadrant and consequently the power appears negative. It is obvious that its absolute value must be considered in this case.

Finally, while the JV parameters can only be measured electrically on a complete solar cell, it is possible to get an idea of their value by performing photoluminescence spectroscopy on the corresponding absorber.

2.4. Steady state photoluminescence spectroscopy

Luminescence designates the emission of photons from a material. The luminescence of a semiconductor may be a spontaneous or stimulated process. If it is triggered by an applied electrical current, it is referred to as *electro*luminescence. If the initial excitation of the material is due to photon absorption, it is identified as *photo*luminescence. While both techniques are often used to characterize semiconductors for solar cell application, the former one requires the handling of a complete cell with electrical contacts. Photoluminescence spectroscopy, however, may be performed at an early stage in the preparation of the cell since the absorber layer alone is needed. Beside the non-destructive aspect of this technique, PL is a quick and easy way to assess for the potential of an absorber to convert efficiently sunlight into usable power, if completed as device. In this section, quantities measurable by PL are introduced, in particular the quasi-Fermi level splitting, the Urbach energy and the optical diode factor.

2.4.1. Photoluminescence emission flux

The luminescence of a semiconductor resemble the one of a black body. The photon emission flux density of a perfect black body (taking the emission cone into account) is given by Planck's law

$$\phi_{\mathrm{BB}}(E) = \frac{2\pi E^2}{h^3 c^2} \cdot \frac{1}{\exp\left(\frac{E}{k_{\mathrm{B}}\mathrm{T}}\right) - 1} \tag{2.21}$$

Since the energies usually considered are $E \gg k_{\mathrm{B}}T \sim 25$ meV (corresponding to the thermal energy at room temperature), the Boltzmann approximation is valid [55] and the -1 in the denominator may be neglected letting Equation (2.21) become

$$\phi_{\mathrm{BB}}(E) = \frac{2\pi E^2}{h^3 c^2} \cdot \exp\left(-\frac{E}{k_{\mathrm{B}}\mathrm{T}}\right) \tag{2.22}$$

While black bodies absorb all incoming radiation (and emit as much), a semiconductor possesses a certain absorptance $A(E)$, characteristic of each sample, which takes the form of a step like function in the Shockley and Queisser theoretical calculation [56], leading to $A(E \geq E_{\mathrm{g}}) = 1$. In reality, absorption extends even below the bandgap as explained in section 2.4.3. The photon flux density of a semiconductor in equilibrium is then given by $\phi_{\mathrm{PL}}^{\mathrm{eq}}(E) = A(E)\phi_{\mathrm{BB}}(E)$. However, in non-equilibrium this expression needs to be corrected for the splitting of the quasi-Fermi levels and the emission flux density of a semiconductor can finally be written as

$$\begin{aligned} \phi_{PL}(E) &= A(E)\phi_{\mathrm{BB}}(E) \exp\left(\frac{\Delta E_{\mathrm{F}}}{k_{\mathrm{B}}\mathrm{T}}\right) \\ \phi_{\mathrm{PL}}(E) &= A(E) \cdot \frac{2\pi E^2}{h^3 c^2} \cdot \exp\left(-\frac{E - \Delta E_{\mathrm{F}}}{k_{\mathrm{B}}\mathrm{T}}\right) \end{aligned} \tag{2.23}$$

Equation (2.23) is commonly referred to as Planck's generalized law. Upon excitation with a continuous wave (CW) laser source of energy larger than the band gap, a quasi-equilibrium is achieved, and quantification of the absorber properties is possible. When the excitation flux Φ_{laser} equals the flux that the absorber would receive from the sun, it allows for direct comparison with the solar cell.

2.4.2. Quasi Fermi level splitting

When PL is measured on an absorber, no charge collection happens since no external circuit is connected. It results that the system is operated at V_{OC} and therefore, provided that the measurement is performed under "one sun", the extracted qFls gives the upper limit of the V_{OC} that a cell based on the investigated absorber may exhibit. The calibration of the PL setup is detailed in section 3.2.2. Two main methods are employed to determine the qFls from a PL spectrum. The first one consists of fitting the high energy slope of the PL spectrum, whereas the second one is based on the PLQY.

QFls determination from the fit

Neglecting the reflectance and assuming that $A(E) = 1$ for energies high enough above the band gap ($\sim E - E_g > 0.1$ eV), this term can be ignored in Equation (2.23) and it can be rewritten as

$$\ln\left(\frac{\phi_{PL} h^3 c^2}{2\pi E^2}\right) = -\frac{E}{k_B T} + \frac{\Delta E_F}{k_B T} \tag{2.24}$$

The only unknown in Equation (2.24) is ΔE_F and it appears evident that by plotting it, the qFls can be deduced from the y-axis intercept of a linear fit at high energies, as shown in Figure 2.8. The slope of the fit is dictated by the absolute temperature. In the best case, T can be left as a free fitting parameter and should return a value equal to the temperature at which the measurement was taken. This is the case in the current example (Figure 2.8) and the fit gives $T = 297$ K and $\Delta E_F = 604$ meV. However, it is often observed that the fitted temperature does not coincide with the experimental temperature (sometimes by more than 150°C), resulting in an underestimation of the qFls [57]. One of the main reasons could be that the original assumption made on the absorptance does not hold. If the fitted temperature is not completely off ($T_{fit} < 330$ K), fixing it to the known temperature can parry the issue and deliver a reliable qFls. If the resulting fit is not reasonable, an alternative determination method should be used, i.e., considering the PLQY.

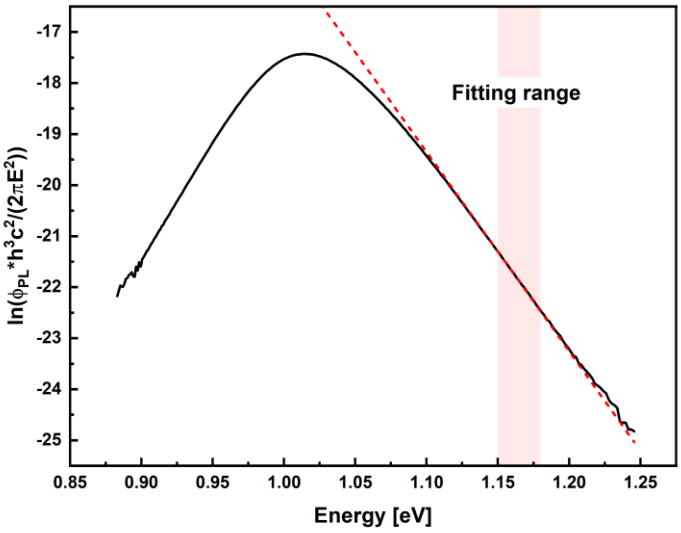

Figure 2.8. Logarithmic representation of a modified PL spectrum of an absorber. The dashed line corresponds to a linear fit according to Equation (2.24). The fitting returns $T = 297$ K and $\Delta E_F = 604$ meV. The fitting range is highlighted between $1.15 - 1.18$ eV. Only one set of diodes in the InGaAs detector is considered (cf. section 3.2.1).

QFls determination from the PLQY

When the fitting method does not produce reliable results, it is encouraged to consider another option. The PLQY relates to the qFls according to

$$\Delta E_F = qV_{OC}^{SQ} + k_B T \cdot \ln(Y_{PL}) \tag{2.25}$$

with qV_{OC}^{SQ} being the Shockley-Queisser (SQ) V_{OC} multiplied by the elementary charge q. The ideal solar cell, governed by the detailed balance theory developed by Shockley and Queisser [56], is defined by the radiative recombination and predicts $\Delta E_F = qV_{OC}^{SQ}$. The quantity qV_{OC}^{SQ} can be calculated from Equation (2.26) where G_{sun} corresponds to the photon flux integrated for energies larger than the band gap, considering the solar spectrum AM1.5G (cf. Figure 2.5). Furthermore, Φ_{eq} represents the thermal photon flux of the semiconductor in equilibrium with its surroundings, and a perfect back side reflector is considered. One can find tabulated values of V_{OC}^{SQ} in the literature, e.g. in reference [58].

$$qV_{\mathrm{OC}}^{\mathrm{SQ}} = k_{\mathrm{B}}T \cdot \ln\left(\frac{G_{\mathrm{sun}}}{\Phi_{\mathrm{eq}}}\right) \tag{2.26}$$

However, in a real solar cell, the dominant recombination occurs non-radiatively, and the SQ limit is reduced by the non-radiative losses, defined as $k_{\mathrm{B}}T \cdot \ln(Y_{\mathrm{PL}})$. For the example given in Figure 2.8, a qFls of 602 meV is obtained, demonstrating the good agreement between the two methods. However, while coherent, both methods underestimate the qFls (by $\sim 10-20$ meV [59]) but for different reasons.

The fitting method uses the assumption that the $A(E) = 1$ well above the band gap. If the absorptance is still increasing over the energy fitting range, it leads to a flattening of the high energy slope of the PL spectrum and consequently to a lower qFls (and apparent higher T). The error on the second method comes from the determination of the band gap, required to calculate $qV_{\mathrm{OC}}^{\mathrm{SQ}}$. In general, the energy of the PL maximum is a good approximation for it and is the value considered in this thesis. However, the determination of the band gap is not straight forward.

On one hand, because the joint density of states is proportional to $\left(E - E_{\mathrm{g}}\right)^{1/2}$ and the distribution of carriers in the bands follows the Boltzmann distribution, $f_{\mathrm{B}} = \exp(-E/k_{\mathrm{B}}T)$, it results that the emission intensity is

$$I(E) \propto \left(E - E_{\mathrm{g}}\right)^{1/2} \exp\left(-\frac{E}{k_{\mathrm{B}}T}\right) \tag{2.27}$$

The maximum of the emission can be calculated by setting the derivative of Equation (2.27) equal to zero, and it reveals that $I_{\max}(E) = E_{\mathrm{g}} + k_{\mathrm{B}}T/2$. The PL maximum is therefore expected to be shifted to higher energy by approximately 13 meV at room temperature. On the other hand, this holds true if the PL emission arises only from band-to-band recombination, considering the step-like absorptance from the SQ model. In reality, the absorption increases gradually and deviates from the step function. This provokes a shift of the PL emission maximum towards lower energy and causes radiative losses, finally reducing the qFls determined considering $E_{\mathrm{g}} = \mathrm{PL}_{\max}$. The gradual increase of the absorption edge is due to sub-band gap recombination through states extending within the forbidden gap, as discussed in the next section.

2.4.3. Urbach energy and band fluctuations

If the temperature of the measurement and the qFls are known, it is possible to rearrange Equation (2.23) to get an expression for the absorptance

$$A(E) = \phi_{PL}(E) \cdot \frac{h^3 c^2}{2\pi E^2} \cdot \exp\left(\frac{E - \Delta E_{\mathrm{F}}}{k_{\mathrm{B}}\mathrm{T}}\right) \tag{2.28}$$

Furthermore, the absorptance relates closely to the absorption coefficient $\alpha(E)$ via the Beer-Lambert's law as

$$A(E) = (1 - R)\left(1 - \mathrm{e}^{-\alpha(E)\cdot d}\right) \tag{2.29}$$

where R is the reflectance of the absorber's surface. Neglecting the reflectance and knowing the thickness d of the absorber, an expression for $\alpha(E)$ can be obtained and it yields

$$\alpha(E) = -\frac{\ln\left(1 - A(E)\right)}{d} \tag{2.30}$$

Considering once more the example from Figure 2.8, the corresponding absorptance and absorption coefficient are plotted in Figure 2.9. From the absorptance spectrum, it can be seen that the assumption $A(E) = 1$ above the band gap, used for the determination of the qFls, is valid in this case (with $R = 0$). The plotted absorption coefficient reflects the density of states that extend below the band gap and shows an exponential behavior. When this is the case, these sub-band gap states, also known as tail states, can be described by

$$\alpha(E) = \alpha_0 \exp\left(\frac{E - E_{\mathrm{g}}}{E_{\mathrm{U}}}\right) \tag{2.31}$$

where α_0 is material-specific and E_{U} is known as the Urbach energy, used to quantify the tail states. In the provided example, a fit according to Equation (2.31) of the absorption coefficient at low energies yields $E_{\mathrm{U}} = 11.5$ meV. It has been demonstrated that each additional meV in Urbach energy (in the range of $10 - 20$ meV) is responsible for an increase of 20 mV in the voltage losses [60].

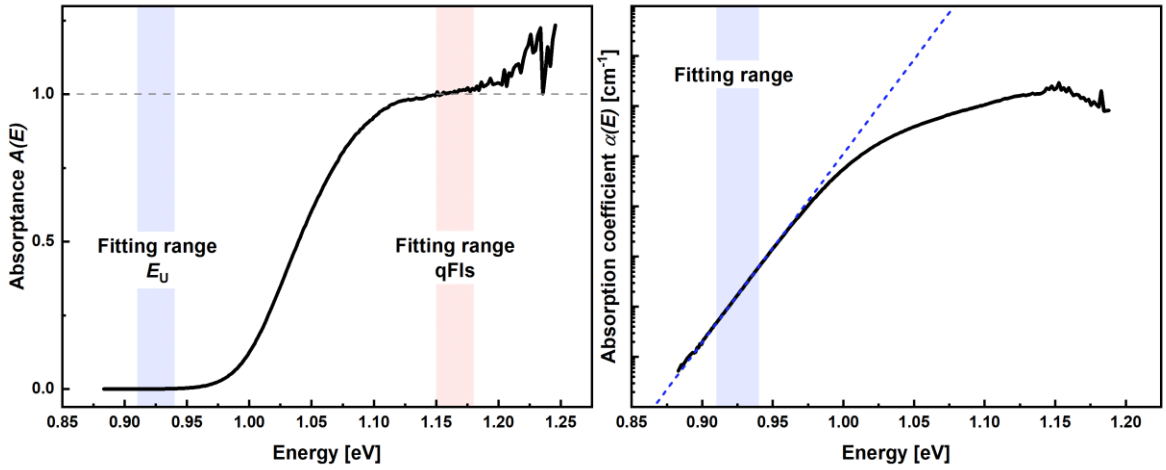

Figure 2.9. Absorptance (left) and absorption coefficient (right) in semi-log scale for the absorber shown in Figure 2.8. The blue dashed line is a fit according to Equation (2.31).The fitting ranges used for the determination of qFls and Urbach energy are highlighted. Only one set of diodes in the InGaAs detector is considered (cf. section 3.2.1).

The tails states arise from thermal and structural disorder that causes the absorber to deviate from the perfect crystal lattice [61]. In CIGS, the disorder is usually due to compositional inhomogeneities, causing fluctuations in the band gap, or to random distribution of charge defects, causing electrostatic potential fluctuations [62]. Both types of fluctuation affect the valence and conduction bands and provide sub-band gap pathways for the charge carriers to recombine, leading to a redshift of the PL maximum and a broadening of the absorption edge. A broadening of the absorption edge is expected as well for absorbers with a band gap gradient, conversely, a sharp absorption edge is expected for absorbers without gradient [63–65]. Assuming a Gaussian distribution of the energy of step-like band gaps, one can fit the derivative of the absorptance and extract the standard deviation (broadening) from

$$\frac{\mathrm{d}A(E)}{\mathrm{d}E} = C_0 + \frac{C_1}{\sigma_{E_g} \cdot \sqrt{2\pi}} \exp\left(-\frac{\left(E - E_g\right)^2}{2\sigma_{E_g}^2}\right) \tag{2.32}$$

where $A(E)$ is the absorptance, E_g corresponds to the mean band gap and σ_{E_g} is the standard deviation from E_g. C_0 and C_1 are fitting constants.

Comparing the Urbach energy and the broadening of the absorption edge for different absorbers may therefore be useful to evaluate for instance how a specific treatment influences the density of states extending below the band gap.

2.4.4. Optical diode factor

As discussed in section 2.3, a fundamental parameter for high efficiency solar cells is the fill factor FF. The latter is strongly influenced by the diode ideality factor, or electrical diode factor A_{el}, as defined in the diode equation (cf. Equation (2.18)). Under illumination, at open-circuit condition ($j = 0$), Equation (2.18) can be rearranged into

$$j_{\mathrm{ph}} = j_0 \left(\exp\left(\frac{qV_{\mathrm{OC}}}{A_{\mathrm{el}} k_B T} \right) - 1 \right) \approx j_0 \exp\left(\frac{qV_{\mathrm{OC}}}{A_{\mathrm{el}} k_B T} \right) \tag{2.33}$$

The approximation in Equation (2.33) is allowed since $qV_{\mathrm{OC}} \gg k_{\mathrm{B}} T$ and A_{el} typically takes a value between 1 and 2, depending on the where the charges recombine. Furthermore, the photocurrent density is proportional to the generation G what leads to

$$j_{\mathrm{ph}} \sim G \sim \exp\left(\frac{qV_{\mathrm{OC}}}{A_{\mathrm{el}} k_{\mathrm{B}} T} \right) \tag{2.34}$$

Although the architecture of a p-n junction has not been discussed in detail in this chapter, it is formed by putting a p-type and an n-type semiconductors in contact. At the interface between the semiconductors, a charge diffusion occurs until an equilibrium is reached, creating the space charge region (SCR). In the bulk of the absorber, the carriers are not affected by the junction and this region is called the quasi-neutral region (QNR). If recombination of the charge carriers occurs dominantly in the QNR, the EDF is expected to be equal to 1. If, however, recombination dominates in the SCR, the EDF increases towards 2.

Considering now a PL spectrum, on the one hand, the total photon flux is obtained by integrating Equation (2.23)

$$\Phi_{\mathrm{PL}} = \int_0^\infty \phi_{PL}(E)\, \mathrm{dE} = C_{\mathrm{BB}} \cdot \exp\left(\frac{\Delta E_{\mathrm{F}}}{k_{\mathrm{B}} \mathrm{T}} \right) \tag{2.35}$$

where C_{BB} corresponds to the integrated black body emission modified by the absorptance. On the other hand, it is empirically found that the total PL flux follows a power law $\Phi_{\mathrm{PL}} \sim G^{A_{\mathrm{opt}}}$, where A_{opt} is referred to as the optical diode factor (ODF). Therefore, combining Equation (2.34) and (2.35) finally leads to

$$G \sim \exp\left(\frac{qV_{\mathrm{OC}}}{A_{\mathrm{el}}k_{\mathrm{B}}T}\right) \sim \exp\left(\frac{\Delta E_{\mathrm{F}}}{A_{\mathrm{opt}}k_{\mathrm{B}}\mathrm{T}}\right) \tag{2.36}$$

Therefore, EDF and ODF can be considered equal [66,67], provided that the optically measured qFls equals to the V_{OC} of the cell. Otherwise, EDF is larger than ODF. The reader's attention is driven to the fact that in a bare absorber no SCR exists and an ODF larger than 1 cannot be explained by recombination in the SCR. Weiss *et al.* [68,69] proposed a model in which in addition to the upwards shift of the electron quasi-Fermi level upon excitation, a downwards shift of the hole quasi-Fermi level is produced. This additional shift arises from metastable defects (like the double vacancy complex $V_{Se} – V_{Cu}$ in CIGS [70]) that changes from donor state into acceptor state under illumination, thus increasing the net acceptor doping.

Consequently, from PL investigation, quantitative information about the ODF may be obtained by excitation dependent measurements. Plotting the integrated PL flux density versus the generation in a double-log scale, one can read the ODF from the slope of a linear fit.

2.5. Time-resolved photoluminescence spectroscopy

Contrary to the steady state PL, time-resolved PL spectroscopy (TRPL) utilizes a pulsed monochromatic light source (with $E_{\mathrm{ph}} > E_{\mathrm{g}}$) rather than a CW source. A pulsed laser sends packets of photons with a certain repetition frequency f_{rep}. The number of photons per pulse is therefore given by

$$\mathrm{photons/pulse} = \frac{P_{\mathrm{average}}}{E_{\mathrm{ph}} \cdot f_{\mathrm{rep}}} \tag{2.37}$$

where P_{average} is the average laser power (which can be measured with a power meter) and E_{ph} is the energy of an emitted photon. Going further, the excess of minority carriers generated per pulse and per volume, considering that each photon is absorbed and creates one electron-hole pair can be estimated with

$$\Delta n = \frac{2 \cdot P_{\text{average}} \cdot \alpha}{E_{\text{ph}} \cdot f_{\text{rep}} \cdot A} \tag{2.38}$$

with A the beam area. In the case of a Gaussian beam, the beam power is half the beam intensity multiplied by the beam area [71], and thus a factor 2 in the numerator of Equation (2.38) is necessary. Because of the pulsed nature of the excitation, the photogenerated carriers recombine before the next pulse and no equilibrium of the charge carrier density can be reached. For this reason, the absorption coefficient α is regarded to define the volume in which the charge carriers are generated as it represents the absorption depth of the excitation photons.

2.5.1. Lifetime and TRPL transients

From the TRPL measurement, one can extract a measure of the minority carrier lifetime. A longer lifetime usually leads to larger V_{OC}, as empirically observed in different thin films such as CdTe [72], CIGSe [73] or industrial CIGSSe [74]. On one hand, the saturation current density j_0 defined in section 2.3 depends inversely on the minority carrier lifetime [75] and on the other hand, rearranging Equation (2.33) shows that $V_{\text{OC}} \sim \ln(j_{\text{ph}}/j_0)$, explaining the experimental trend. Given that the decay of the charge carrier density over time (see Figure 2.10) in low injection can be described by

$$\Delta n(t) = n_0 \, e^{-t/\tau} \tag{2.39}$$

where $n_0 = \Delta n(t = 0)$, one would thus expect a mono-exponentially decaying transient from a time-resolved photoluminescence (TRPL) measurement [76]. However, this is often not the case, and the experimentally measured transients deviate from the expected mono-exponential decay.

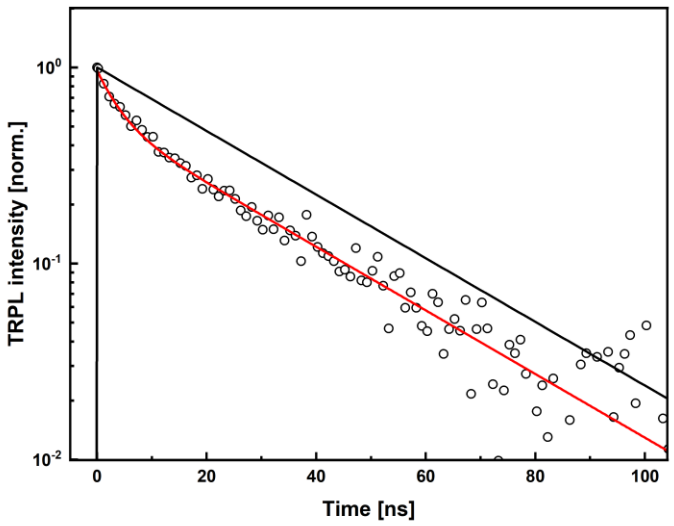

Figure 2.10. Normalized transient decay curve (after background subtraction) showing a bi-exponential behavior. The excitation pulse comes at $t = 0$ ns. The open circles are experimental data points (binned by 5 data points), the red curve is a bi-exponential fit (cf. Equation (2.40)) and the black one is a mono-exponential function of same decay constant $\tau = \tau_2$ as the bi-exponential fit.

In most cases, a bi-exponential fitting is enough to accurately represent the decay of the PL intensity $I_{\mathrm{PL}}(t)$ according to

$$I_{\mathrm{PL}}(t) = y_0 + A_1 e^{-t/\tau_1} + A_2 e^{-t/\tau_2} \tag{2.40}$$

where y_0 is the background signal, τ_1 and τ_2 are the decay components and finally A_1 and A_2 are pre-factors. With such a model, τ_1 describes the part of the decay at short times after the pulse, and the part of the decay at longer times is characterized by τ_2. The interpretation of the decay components is not straight forward as τ_1 and τ_2 can be influenced by a multitude of different phenomena. The most common ones discussed in the literature are introduced in the next section.

For all the TRPL transients showed in this thesis, $t = 0$ is defined as the time of the excitation pulse, also corresponding to the maximum PL intensity. They are systematically fitted with Equation (2.40) and the background signal y_0 is subtracted from both the experimental data points and corresponding fitting curve. For a better display, when too many data points are measured, they are manually binned during the treatment, i.e., every 10 neighboring data points

are averaged into 1. This is purely display related and does not change the extracted the quantities. The binning is indicated in the figures' caption when applied.

2.5.2. Sources of deviation from the mono-exponential decay

This section gives a concise overview of the most commonly suspected physical mechanisms that affect the measured lifetime of the charge carriers in an absorber. In particular, it is discussed how the initial decay, shortly after the pulse, is accelerated.

Injection level

Depending on the doping N_A of the absorber, varying the laser fluence enables to go from low injection condition ($\Delta n \ll N_A$) to high injection condition ($\Delta n \geq N_A$). In the low injection regime, it is expected that all recombination mechanisms depend linearly on the minority carrier density ($\propto n$), leading to a mono-exponential decay [76]. This situation is referred to as monomolecular recombination. However, high injection regime induces bimolecular recombination [77,78], i.e., the densities of both electrons and holes need to be considered (with $n = p$), and the radiative recombination becomes quadratically dependent on the carrier densities ($\propto n^2$) [76]. The high injection regime thus leads to an initial fast decay (not exponential) of the electron population directly after the pulse, followed by a slower exponential decay at later times when the recombination processes become linear with n again. It is therefore preferable to remain, when possible, in the low injection regime to avoid such behaviors. Nevertheless, varying the fluence of the excitation laser may reveal what recombination mechanisms dominate in the absorber and may provide a means to distinguish between some of them [79].

Charge separation and carrier drift

A parallel mechanism to diffusion is carrier drift. Lifetime measurements in the case of a p-n junction (after buffer deposition) are more complicated, due to the presence of a charge-separating field forming from the absorber side to the buffer [45,80]. Generated charge carriers are swiped away from each other by the electric field directly after the excitation pulse, preventing electrons and holes to recombine. This effect hence reduces the measured PL intensity $I_{\mathrm{PL}}(t)$ by kinetics rather than by recombination and leads to a strong initial fast decay in the TRPL transient, at low injection levels. The influence of the charge carrier drift in TRPL

measurement has been experimentally observed and simulated [81]. Maiberg *et al.* [48] find experimentally that the charge separation in CIGS solar cells happens on a time scale of approximately 5 ns. Heise *et al.* [82] compare the TRPL transients of a bare CIGSe absorber, a buffered absorber, and a finished cell under different excitations. They confirm that charge separation only plays a critical role for the buffered absorber and for the cell, at low injection. The influence of the ZnOS buffer layer used in this thesis on the measured decay time is discussed in chapter 6 for a CBD-deposited buffer and for a sputtered one.

Furthermore, Kuciauskas *et al.* [44] demonstrate that carrier drift can also happen in double graded absorbers before any buffer and window layers are deposited, i.e., without a p-n-junction-induced electric field. They measured that after 2.4 ns, the dominant recombination moves from the front side to the notch, due to carrier drift induced by the band gap gradient.

Surface recombination

The time evolution of the carrier concentration profile, and hence the net recombination rate, is affected by front and back surface recombination. Considering for instance defect states at the front surface: directly after the excitation pulse, a substantial number of charge carriers will recombine non-radiatively through the defects (depending on the front surface recombination velocity), leading to an initial fast decay [83,84]. This, furthermore, creates a depletion of charge carriers close to the front side and a bending in the concentration profile, which acts as a driving force for the electrons towards the surface, reducing the carrier lifetime. Observing the effect of the front side recombination depends, however, on the carrier mobility μ. For high enough mobility, the homogenization of the charge carrier concentration happens faster and prevents the appearance of the transient's initial fast decay, as is simulated in Figure 2.11. If the front surface recombination is negligible, back surface recombination results in an upward bending of the transient. Depending on how fast the carriers can reach the back side, the back surface recombination will have a more or less strong impact on the measured transient. In the case of a long bulk lifetime and/or large diffusion length, back surface recombination may become the dominant recombination mechanism and limit the lifetime [17,85].

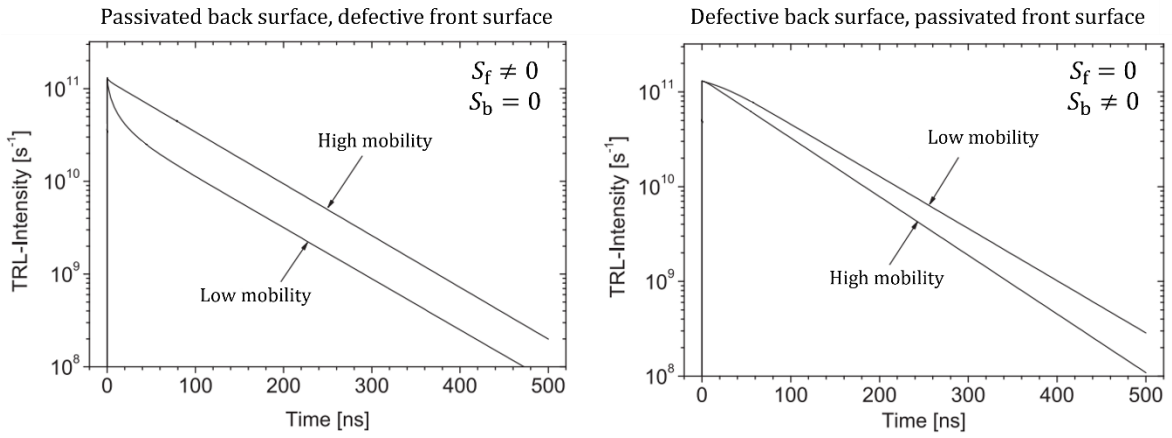

Figure 2.11. Simulated transients of a CIGS absorber with a bulk lifetime of 200 ns in the case of front surface recombination (left) and back surface recombination (right). The effect of high and low carrier mobility on the transient shape is highlighted. The figure adapted from reference [78] with permission.

The lifetime associated to surface recombination (τ_s) strongly depends on the front and back surface recombination velocities, S_f and S_b. A. Sproul [86] discusses two extreme cases, when both S_f and S_b are large ($\geq 10^6$ cm^{2}s^{-1}) and when one of the velocities is large and the second one is low. It leads in the first case to $\tau_s = d^2/D\pi^2$ and to $\tau_s = 4d^2/D\pi^2$ in the second one, where D is the diffusion coefficient and d the sample thickness. In the general case, one has to solve the second order differential equation describing the charge carrier decay [86,87]

$$\frac{\partial \Delta n}{\partial t} = D\nabla^2(\Delta n) - \frac{\Delta n}{\tau} + G \tag{2.41}$$

Considering the adequate boundary conditions (cf. Equation (3) in ref [87]) it is found that $\tau_s = (\alpha_0^2 D)^{-1}$, in which α_0 is the smallest eigenvalue solution of Equation (2.42).

$$\tan(\alpha_0 d) = \frac{D\alpha_0(S_f + S_b)}{D^2\alpha_0^2 - S_f S_b} \tag{2.42}$$

It follows that if S_f, S_b, d and D are known, it is possible to numerically solve Equation (2.42) and determine τ_s. However, direct measurement of the surface recombination velocity is difficult and therefore simulations and modeling are usually used to estimate it [85,88,89].

Trapping

Trapping and detrapping mechanisms can significantly influence the measured carrier lifetime. A trap state differs from a defect state, as described in SRH recombination, by its reemission of a charge carrier being more likely than the capture of the opposite carrier. It does not act as a recombination center. A trap is defined as a shallow defect of capture cross section σ_d that can capture an electron with a capture time τ_c and release it to the conduction band after an emission time τ_e [90]. Consequently, if the capture is fast and the release slow, a trap artificially extends the measured lifetime by delaying the recombination of the charge carriers. Usually, it leads to a slow decay part of the transient at longer times and is used as a possible explanation for bi-exponential decays [91]. Under certain conditions, however, the traps can be neglected. Maiberg *et al.* produced an extensive study of the trapping effects [79] where they simulate the influence of τ_c and τ_e on the transient shape. If the capture time is longer than the lifetime of the carriers, recombination will occur before capture. If the emission time is much shorter than the lifetime and the capture time, the electrons will be directly re-emitted after capture. In both cases, trapping can be neglected, and a mono-exponential decay is expected provided that no other aforementioned mechanisms affects the measurement. Outside these two extreme situations, a short τ_c leads to a strong bi-exponential behavior, impacting both the fast and slow decay parts (at short and long times after the excitation), while a large τ_e affects mostly the slow decay part.

To summarize, the mechanisms presented in this section principally affect the decay at short times after the excitation pulse, leading the measured transients to deviate from a mono-exponential decay. Considering a bi-exponential fitting, τ_1 may reflect the effect of the high injection regime, of charge separation, of front or back surface recombination or of strong trapping. While it is possible to exclude certain effects under specific conditions, such as charge separation in a bare absorber, it is highly probable that the initial fast decay arises from simultaneous mechanisms, thereby complicating the interpretation of τ_1. However, the long decay time, given by τ_2, is not (or less) affected by the mechanisms discussed above and might be viewed as the bulk lifetime. Note that this is only valid if the trapping of charge carriers is negligible. Otherwise, the slow decay part of the transient may also be affected by trapping, especially if the reemission time is long compared to the minority carrier lifetime. This complexifies the interpretation of τ_2 as it becomes the bulk lifetime modified by the dynamics

of the shallow defects. Further physical parameters, such as band gap fluctuations [92] or grain size [75,92] may impact the lifetime measurements as well, and the reader is invited to consult the provided references. Finally, in light of the information provided in this section, it is concluded that τ_2 is the quantity of interest in the determination of the charge carriers lifetime and shall be the decay component considered in the rest of this thesis.

Chapter 3

Experimental

The goal of this chapter is to introduce the industrial growth process of the investigated absorbers, in section 3.1, and to provide experimental details on the different methods used during this thesis. It is evident that over the four years of the thesis, dozens of various techniques were applied at some point and it would not make sense to list them all. Because the main characterization tool employed was photoluminescence spectroscopy, an extensive presentation of the setup, as well as the calibration procedure is given in section 3.2. Characterization techniques such as cathodoluminescence spectroscopy, glow discharge optical emission spectroscopy and Raman spectroscopy contributed significantly to the findings of this work. While not performed by myself, they are presented in sections 3.3, 3.4 and 3.5, respectively.

3.1. Industrial growth of the $Cu(In,Ga)(S,Se)_2$

The absorbers studied is this work are all grown in the pilot line of the industrial partner AVANCIS, Germany. The employed growth method is based on a SEL-RTP process, i.e., stacked element layers followed by a rapid thermal processing [9,93]. A soda lime glass (SLG) is used as substrate. In order to control the amount of Na incorporated into the final absorber, the diffusion of Na from the substrate into the absorber must be prevented. This is achieved by depositing a layer of silicon nitride directly on the SLG. The back electrode consists of double Mo layer with a Se barrier in between. The Na-doped Cu-In-Ga precursor layer is subsequently sputtered on the Mo back contact and a capping Se-layer is thermally evaporated (see Figure 3.1). Finally, the stack is annealed in a S-containing atmosphere using a rapid thermal processing tool, where the desired reaction temperature is reached very quickly before the

absorber is slowly cooled down. This last step finalizes the formation of the CIGSSe absorber. The role of the sulfurization step is to increase the band gap at the front of the absorber, generating a double graded structure. Some of the samples investigated in this thesis don't undergo any further treatments and are measured after this last step. Others receive an additional Na post-deposition treatment (Na-PDT) that is meant to passivate and enhance the quality of the absorber surface. Last but not least, absorbers may be covered with a Zn(O,S) buffer layer, either sputtered at AVANCIS or formed by chemical bath deposition (CBD) at LPV. The buffer deposition is necessary for the formation of a p-n junction and the good functioning of the solar cell. However, since the samples in this work are mainly investigated optically, the buffer is employed as a mean to protect the absorber surface from degradation [94,95]. Prior to the CBD buffer deposition and prior to PL measurements on the bare absorbers (from the front side), a soft potassium cyanide (KCN) etching is performed (30 sec in a 5% concentration solution) to remove residual oxides from the surface and "refresh" the surface. Babbe *et al.* [96] discuss that after such an etching, degraded bare absorbers recover the same qFls as the same absorbers with a buffer layer.

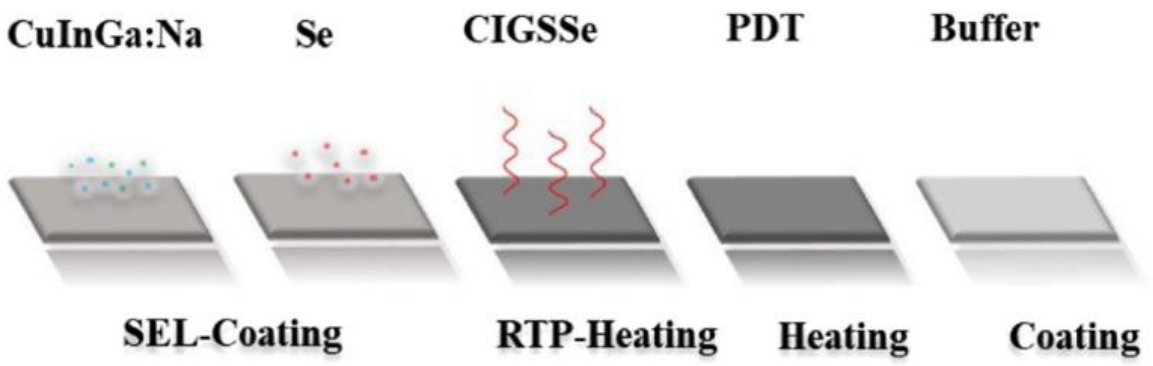

Figure 3.1. Standard pilot line process performed at AVANCIS. The label PDT stands for Na-PDT. The figure is adapted from [9] (CC BY-NC-ND 4.0).

3.2. Photoluminescence spectroscopy

The physical concept of PL and its usefulness in the context of solar cells has been explained already in the previous chapter. While several research groups employ this technique, only few measure absolute fluxes, as this is the case at LPV. This section presents the different components of the steady state and time-resolved PL setups and guides the reader through the principle of the calibration procedure.

3.2.1. Experimental PL setup

At the beginning of this thesis (September 2020), only one steady state PL setup was operational at LPV. I optimized it further, by removing unnecessary components, adjusting existing ones or adding new ones. Furthermore, in accordance with internal discussion, I built a complete second steady state PL setup similar to the first one, allowing for simultaneous users. To complement this second setup, a beam expander is mounted on the laser path to increase the size of the laser beam by up to 10 times. This enables to fully illuminate small solar cells ($\sim 0.5 \times 0.5$ cm^2), which is important to prevent the formation of a current between illuminated and dark areas in a PL experiment (as a consequence of the conductive top layers). However, as no cells are investigated by PL in this thesis, this aspect of the setup will not be further detailed. This section describes only the original (optimized) PL setup.

Since the detection system is very sensitive to external vibrations, the setup is built on an optical table, dampening the vibrations of the surrounding (e.g. other equipment on the table or pumps). For steady state PL, three CW diode lasers (Coherent OBIS LX) are available, with emission wavelength 405 nm ($E_{\mathrm{ph}} = 3.06$ eV), 532 nm ($E_{\mathrm{ph}} = 2.33$ eV) and 660 nm ($E_{\mathrm{ph}} = 1.88$ eV). The choice of the excitation wavelength depends mainly on the band gap of the investigated sample. Here the low band gap phase emits roughly between 1.0 eV and 1.1 eV and the high band gap phase between 1.3 eV and 1.6 eV (cf. chapter 4). Therefore, the red laser (1.88 eV) is used for all measurements shown in this work. In front of each laser, a bandpass filter of bandwidth 10 nm is placed to ensure a narrow spectral emission (see Figure 3.2). The laser beam is guided onto the sample via several silver-coated adjustable mirrors. This coating ensures a good reflectance for the three available wavelengths. Note the use of a dichroic mirror (reflecting $\lambda < 567$ nm and transmitting above) in front of the blue laser that allows for both lasers (red and blue) to shine on the same spot on the sample. While the power of the laser is tunable from 1 mW to 100 mW, the typical power needed for "one sun" illumination is around 2 mW on the sample. Therefore, in order to reach very low excitation levels and vary the incident power over several orders of magnitude, a set of neutral density (ND) filters (from OD0, i.e., no filter, to OD4) is positioned in the laser path. The intensity reduction is given by $I = I_0 \cdot 10^{-\mathrm{OD}}$. Alternatively, a convex lens (of focal length $f_{\mathrm{L}} = 200$ mm) can be added before the sample to focus the beam and shine hundreds of suns on the sample. Finally, the laser beam passes through a hole in an off-axis parabolic (OAP) mirror

and hits the sample, placed on a *xyz*-translation stage, parallel to its normal. The intensity losses along the way, due principally to partial reflectance on the several mirrors, amount roughly to 10% but can be easily balanced with a higher laser power.

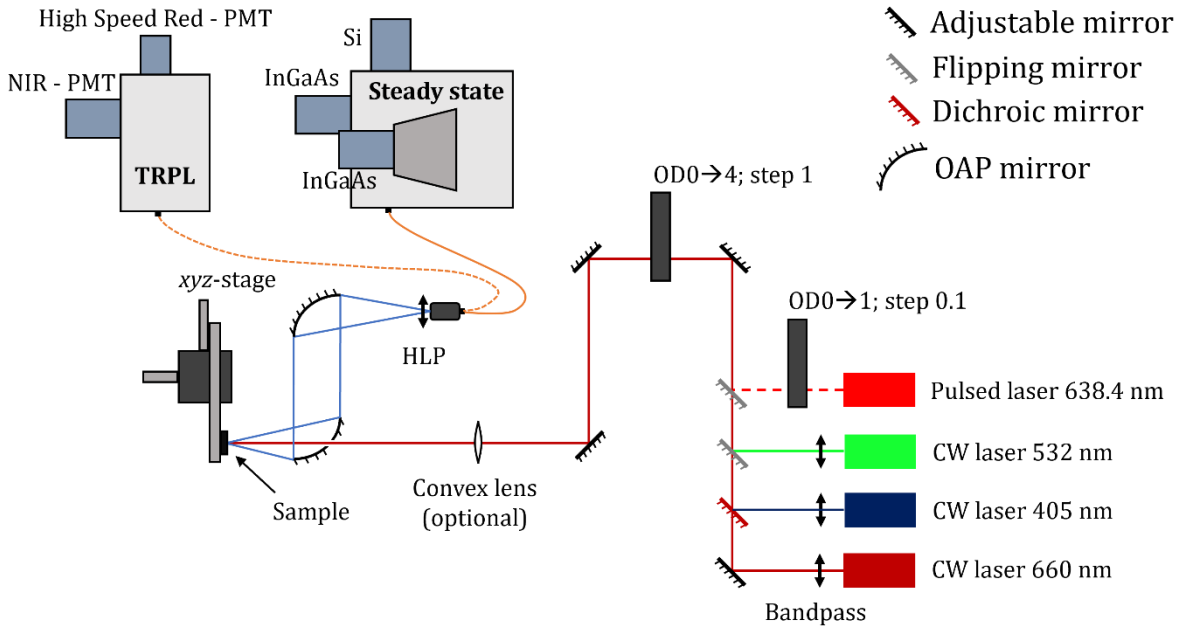

Figure 3.2. Schematic of the experimental PL setup featuring both, the steady state and time-resolved detection systems. Only one of the two orange fibers is connected at a given time, the plain one for steady state or the dashed one for time-resolved PL (TRPL). The blue cones represent the collection by the two off-axis parabolic (OAP) mirrors.

The second part of the optical setup corresponds to the collection part. Once excited, the absorber at the sample position emits light with a characteristic spectrum. The emission of the absorber is not directional but covers the whole upper hemisphere. Therefore, two 90° off-axis parabolic mirrors of diameter $D = 50.8$ mm are used to collect a cone of emission (depicted in blue in Figure 3.2). An aluminum coating provides a flat reflectance profile over a large IR range. The first OAP1 (through which the laser passes) has a focal length $f_{\mathrm{OAP1}} = 2D = 101.6$ mm leading to an angular aperture of $f_{\mathrm{OAP1}}/D = 2$. A high angular aperture (i.e., small f) is preferred to achieve high collection, but a trade-off has to be made to enable easy handling of the sample in front of the OAP, especially when placing the sample inside a cryostat for low temperature measurements (not discussed here). The second mirror OAP2 has a longer focal length $f_{\mathrm{AOP2}} = 3D = 152.4$ mm and is used to focus the signal into a multimode fiber connected to the spectrometer. This focal length corresponds to a half-angle of $\theta_{\mathrm{OAP2}} =$

$\arctan\frac{D}{2f} \approx 9.5°$ (vs. $\sim 14°$ for OAP1) and is required for the signal to adequately couple into the fiber with minimal losses. The fiber used in steady state has a numerical aperture $N = \sin\theta_{\text{fib}} = 0.22$, resulting in a half aperture angle of $\theta_{\text{fib}} = 12.7°$, which effectively captures the signal from OAP2. Furthermore, a high quality longpass filter (HLP) is placed in front of the fiber to prevent any unwanted (and potentially harmful) signals from reaching the detector arrays, e.g. direct reflection of the laser on the sample surface. Generally, an HLP700 (blocking all light below 700 nm) is used in combination with the red laser.

The collected signal is finally coupled into a spectrometer (plain orange fiber in Figure 3.2) and spectrally dispersed by a grating before reaching either a Si-CCD detector (Andor iDus DV420A-OE, efficient from ~ 400 nm to ~ 900 nm) or an InGaAs diode array detector (Andor iDus DU490A-1.7, efficient from ~ 900 nm to ~ 1600 nm). The two detectors are operated at a temperature of -60°C (electrical cooling) to reduce the parasitic thermal noise. With this system and with the combination of a 100 lines/mm grating and the 550 µm core diameter fiber, a spectral resolution of 15 nm is achieved. For each PL measurement with the InGaAs detector, a center wavelength is chosen, and the measurement range extends 200 nm above and below this value. This InGaAs detector has two diodes of slightly different sensitivity. Therefore, in order to reduce the general noise in the PL spectra (and corresponding absorptance), it is sometimes better to consider only one of the two sets of diodes, i.e., every second measured data point is removed. Whenever only one set of diodes is considered, it is indicated in the corresponding figure caption. With the same grating and fiber, the Si detector always "sees" the whole measurable range. Some PL spectra shown in this thesis are measured from 700 nm to 1600 nm ($0.77 - 1.77$ eV) resulting from the merging of three individual spectra taken at different center wavelengths. This is possible because absolutes photon fluxes are measured. An extended detection in the IR may be achieved by a second InGaAs detector operated at -90°C (electrical + water cooling) and covering the $1450 - 2150$ nm spectral range. It has been however very rarely used in this work.

The TRPL setup is discussed in section 3.2.3.

3.2.2. Calibration of the steady state PL

A calibration of the system has to be performed to measure absolute photon flux spectra and achieve a quantitative evaluation of the PL data. The calibration is twofold, it provides on the one hand a spectral correction, and on the other hand an intensity correction.

Spectral correction

The spectral correction is necessary to account for all the optical elements and quantum efficiency limitation of the detectors. A regularly re-calibrated halogen lamp of known spectrum (Avantes AvaLight-HAL-CAL-Mini) is directed onto a spectralon reflector (Lambertian surface with $> 99\%$ diffuse reflectance over the whole UV-VIS-NIR range) placed at the sample position. The spectrum of the lamp is measured under the same experimental conditions as the actual absorbers (same grating, fiber, filters, and ideally same exposure time). The correction function F_{corr} is calculated by dividing the known lamp spectrum $\phi_{\mathrm{Hal.}}^{\mathrm{known}}$ by the measured detector counts $I_{\mathrm{Hal.}}^{\mathrm{meas.}}$

$$F_{\mathrm{corr.}} = \frac{\phi_{\mathrm{Hal.}}^{\mathrm{known}}}{I_{\mathrm{Hal.}}^{\mathrm{meas.}}} \tag{3.1}$$

Each subsequently measured sample emission is then multiplied by this function

$$I_{\mathrm{PL}}^{\mathrm{corr.}} = F_{\mathrm{corr.}} \cdot I_{\mathrm{PL}}^{\mathrm{meas.}} \tag{3.2}$$

Care needs to be taken that $F_{\mathrm{corr.}}$ is not dimensionless but has the unit $\mu W/cm^2$ since the lamp manufacturer provides $\phi_{\mathrm{Hal.}}^{\mathrm{known}}$ in $\mu W/cm^2/nm$ and $I_{\mathrm{Hal.}}^{\mathrm{meas.}}$ (as well as $I_{\mathrm{PL}}^{\mathrm{meas.}}$) is in #/nm. It results in $I_{\mathrm{PL}}^{\mathrm{corr.}}$ having the unit $\mu W/cm^2/nm$. To transform into energy space, a Jacobian transformation [97] is applied following

$$\begin{gathered} y\ [\mu\mathrm{W} \cdot \mathrm{cm}^{-2} \cdot \mathrm{nm}^{-1}] \mapsto y \cdot \frac{x^2}{hc}\,[\mu\mathrm{W} \cdot \mathrm{cm}^{-2} \cdot \mathrm{eV}^{-1}] \\ x\ [\mathrm{nm}] \mapsto \frac{hc}{x}\ [\mathrm{eV}] \end{gathered} \tag{3.3}$$

And finally converting the μW ($= 10^{-6}$ W), a photon flux density in the energy space is obtained by

$$y\ [\mu\mathrm{W}\cdot\mathrm{cm}^{-2}\cdot\mathrm{eV}^{-1}] \mapsto y\cdot\frac{10^{-6}}{q\cdot x}\ [\mathrm{photons}\cdot\mathrm{cm}^{-2}\cdot\mathrm{s}^{-1}\cdot\mathrm{eV}^{-1}] \tag{3.4}$$

Where q is the elementary charge. While providing a physical dimension, this transformation does not make the fluxes absolute, and an intensity correction needs to be done. Therefore, all the PL spectra ($\phi_{\mathrm{PL}}^{\mathrm{corr.}}$) shown in the following chapters are presented in unit photons/cm^2/s/eV if corrected for the intensity, or else are displayed in arbitrary unit (a.u.).

Intensity correction

Using the same spectralon reflector, the laser spectrum ϕ_{laser} (sufficiently attenuated) is directly recorded by the detector and spectrally corrected. Integrating the resulting $\phi_{\mathrm{laser}}^{\mathrm{corr.}}$ the total measured photon flux is obtained. Replacing the spectralon with a photodiode power sensor, the total power of laser is measured, and the actual laser photon flux is calculated via Equation (3.5). The beam spot is recorded with a CMOS camera and the radius r is derived from the Gaussian beam profile where the intensity is reduced by $1/e^2$ ($r \approx 1.11$ mm for the red laser).

$$\phi_{\mathrm{laser}}^{\mathrm{calc.}} = \frac{2P\lambda}{\pi r^2 hc} \tag{3.5}$$

The factor 2 in the numerator is again due to the Gaussian beam profile considered (similarly to Equation (2.38)). Comparing $\phi_{\mathrm{laser}}^{\mathrm{calc.}}$ and $\phi_{\mathrm{laser}}^{\mathrm{corr.}}$ returns the wanted intensity correction factor allowing for absolute photon flux densities.

Knowing the band gap of the studied absorber, it is possible to calculate the photon flux G_{sun} corresponding to a “one sun” illumination (by integrating the solar spectrum, cf. Figure 2.5). By solving Equation (3.5) for P, the laser power required to simulate G_{sun} can be determined. Of course, with a laser source all the photons carry the same energy, but since $E_{\mathrm{ph}} > E_{\mathrm{g}}$ and the solar spectrum is integrated for $E > E_{\mathrm{g}}$, calibrating to the same number of incident photons is valid (assuming that each photon has the chance to create one electron-hole pair).

It should be mentioned that several absorbers investigated in this thesis exhibit an increase in the PL intensity when the excitation laser is turned on. This behavior is not unusual and is

further discussed in chapter 5. The PL intensity generally stabilizes after a couple of minutes under illumination, and only then would the PL measurement be started.

3.2.3. Time-resolved PL

In order to study the temporal recombination dynamics in an absorber (cf. section 2.2.3), steady state PL in not suitable, as charge carrier generation and recombination continuously occur in parallel. The solution is to measure time-solved PL. The same setup as for steady state PL is used, with minor adjustments. A picosecond pulsed diode laser of wavelength 638.4 ± 10 nm and temporal pulse width 87.4 ps (Edinburgh Instrument, EPL – 640) is mounted in the setup (see Figure 3.2). The repetition rate can be varied between 10 presets from 0.02 MHz to 20 MHz and needs to be adjusted depending on the sample's lifetime. While the energy per pulse cannot be modulated, an additional set of ND filters (from OD0 to OD1, in steps of 0.1) is available to attenuate the laser intensity. Combined with the first filters' set, the excitation intensity can be finely attenuated from OD0 down to OD6 in steps of 0.1, although usually any excitation attenuated more than OD3.5 does not lead a detectable sample signal. Without any attenuation, the typical average power at a repetition rate of 10 MHz is $\sim$126 μW at the sample position. In general, the convex lens is added to focus the beam onto the sample. The same OAP mirrors are used to collect the emitted luminescence and directed into a second spectrometer through a second optical fiber ($N = 0.5$ and 200 μm core diameter). A double grating allows for spectral resolution of the emission, i.e., a spectral window of variable bandwidth $\Delta\lambda$ can be chosen to restrain the collection to a certain energy range. As for the steady state PL, two detectors are connected to the spectrometer, covering the visible range (High Speed Red PMT) and IR range (NIR-PMT H10330C-75 operated at -60°C). In this thesis, only the second one is used, as band-to-band emission of the studied absorbers is around 1.05 eV.

Additionally, a second IR detector (NIR-PMT H12397-75, not shown in Figure 3.2) has been briefly used for excitation dependence TRPL measurements (see section 6.2.1). While not connected to any monochromator, i.e., not spectrally resolved, this detector allows for

measurements at relatively low injection levels, thanks to significantly lower dark counts ($5 \cdot 10^3$ s^{-1} vs. $2.5 \cdot 10^5$ s^{-1} for the NIR-PMT H10330C-75).

Time-correlated single photon counting

As mentioned in section 2.2.3, the typical lifetime in CIGS ranges from a few nanoseconds to a few hundreds of nanoseconds, and most of the recombination occurs non-radiatively. The sparseness of the emission makes it near impossible to measure a decay profile from a single excitation-emission cycle. To parry this issue, a time-resolved single photon counting (TCSPC) system [98] is used. The principle of TCSPC is based on the repetitive and precise detection of single photons, as depicted in Figure 3.3. Working with a very low emission rate implies that during most cycles, one or no photon is emitted. The measurement of an event starts with the laser pulse ($t = 0$) and ends with the detection of a photon (or with the next pulse if no photon was emitted). A cycle corresponds to the time period between two laser pulses. The actual measurement then consists of millions of cycles (depending on the repetition rate and measurement time) and the emitted photons, if any, are registered by the fast electronics. A histogram of the photon detection time, organized by time bins, is finally obtained and gives a fair representation the time decay one could have measured from a single-shot time-resolved experiment. The size of the time bin (temporal width) specifies the resolution of the measurement. However, if multiple photons are emitted during 1 cycle, only the first one is registered, leading to an over-representation of the early photons. This effect is known as pile-up and must be avoided. It manifests as a distortion of the measured transient at early times and leads to the decay tail falling below the background level. Usually, keeping a detector count rate (dark counts included) below 5% [98] of the excitation rate ensures the single photon statistics. This can be achieved by (i) increasing the repetition rate, (ii) decreasing the excitation flux or (iii) increasing the detection threshold. The latter point refers to the discriminator level and is explained below.

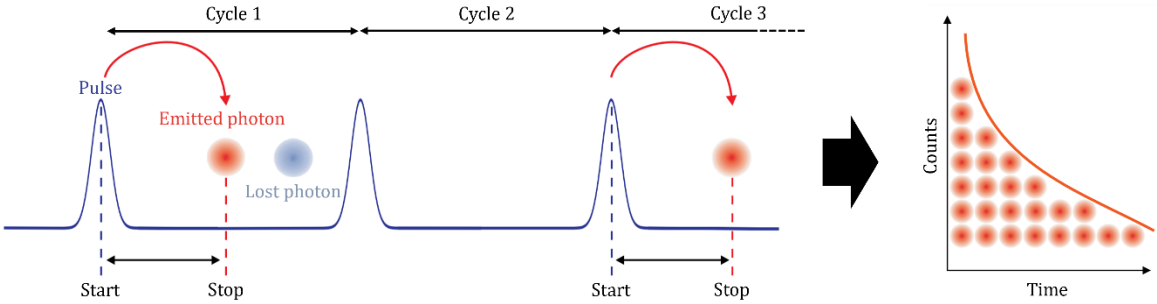

Figure 3.3. Schematic representation of a TCSPC measurement mechanism. In cycles 1 and 3, a photon emission is registered, but not during cycle 2, as it frequently happens. Two photons were emitted during cycle 1, but only the first one is registered. The registered events are grouped by time bins and over many cycles, a histogram is obtained. The figure is adapted from Michael Wahl's work [98] with permission.

Each detected photon should produce an electrical output pulse upon arrival on the detector. In order to achieve it, a near infrared photomultiplier tube (PMT) is used as detector (according to the studied absorbers emitting in this range). When a single photon impinges on the light-sensitive photocathode of the PMT, it produces electrons. These electrons are redirected onto a series of charged electrodes, multiplying the number of electrons at each bounce. Finally, the many electrons reach the anode of the PMT and generate an electrical pulse. The PMT is operated at a constant high voltage (-800 V) where it is most sensitive. Because of the generally still weak output pulse, a pre-amplifier is inserted between the detector and the subsequent electronic components, to boost the signal up to a workable level. The discriminator level mentioned above sets the minimum amplitude a detector pulse must pass to be considered. Increasing this level thus allows to reduce the measured count rate.

General good practice

While acquiring PL decay curves, some precautions must be taken to avoid erroneous transients. First of all, the repetition rate must be selected according to the absorber to measure. It must be low enough, i.e., long enough time period, to contain the whole decay. It is paramount that the absorber is given enough time to relax between two pulses. If not, the tail of one cycle is recorded at early times of the next cycle, leading to distorted transients. At the same time, the repetition rate should be set as high as possible to reduce the probability of pile-

up. If the conditions on the laser repetition rate are met, the decay curve should reach the same background level as before the pulse, as indicated in Figure 3.4 by the dashed line. The background level is not zero because of the "dark counts" that the detector picks up from its surrounding (thermal noise), even when cooled down and shutter closed.

As discussed in section 6.2.2 and detailed in Appendix C.4, the size of the time bin used during the measurement plays an important role is what features can be detected in the transients. A short bin size allows for a more accurate determination of the initial decay (directly after the laser pulse) but leads to a noisier signal at longer decay times, compared to a larger bin size.

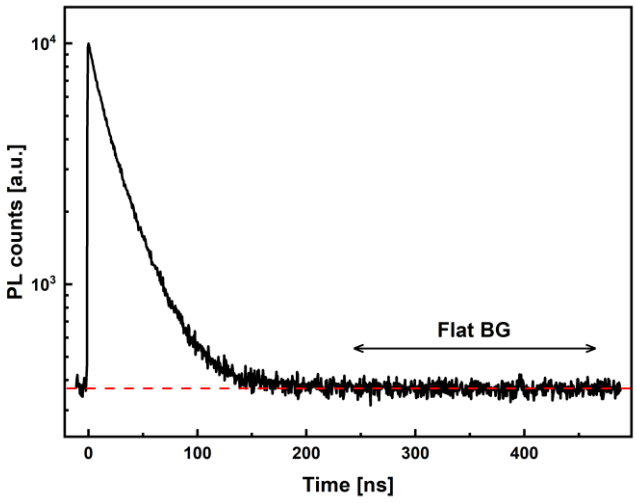

Figure 3.4. Experimental TRPL transient in semi-log scale. The repetition rate of 2 MHz produces a time window of 500 ns. The excitation pulse (and the maximum of the PL counts) is set to $t = 0$. The red dashed line corresponds to the background level.

It has been empirically observed that the dark counts increase over time and need typically a couple of hours after the turning on of the system to stabilize. Therefore, it is recommended to take background measurements before and after the actual absorber measurements to keep track of this evolution. Moreover, to be able to better compare individual transients (recorded on the same day), the total duration of all the measurements is equal (usually 20 min in this thesis), guaranteeing the same background level, independently of the luminescence of the absorber. Furthermore, the sample to noise ratio should be larger than 20%, i.e, $I_{\text{sample}}/I_{\text{BG}} > 0.2$, ensuring that at least every 5^{th} detected photon comes from the sample.

As discussed in detail in Chapter 6, the measured PL decays (and thus carrier lifetime) depend on the generation level. This is why it is strongly encouraged to always vary the excitation intensity and to critically consider any lifetime determination.

3.3. Cathodoluminescence spectroscopy

Cathodoluminescence spectroscopy (CL), similarly to PL, is an optical characterization technique based on photon emission and detection. However, whereas PL employs a laser as excitation source (photons), a focused electron beam is used in CL, involving high energy electrons (typically from a few hundreds of eV to 30 keV). CL allows for mapping of a sample luminescence with nanometer resolution, making this method suitable for detection of non-radiative centers.

Collected signal

In CL, the surface of the investigated sample is scanned by the electron beam, locally exciting the material and generating electron-hole pairs. If the carriers recombine radiatively, the emitted photon can be detected. The emitted signal is collected by a spectrometer and both, a panchromatic image and a hyperspectral data cube are produced as output. A panchromatic image is an integrated intensity map that contains no information about the specific energy of the emission. The hyperspectral data cube however, consists of a collection of individual images of the same region each taken within a different narrow wavelength range, leading to a 3D data cube. Stacking all the images, it produces a full spectrum of the emission in each pixel, as exemplified in Figure 3.5. Furthermore, because of their higher non-radiative recombination rate, grain boundaries appear in this case darker, highlighting the surface morphology of the absorber.

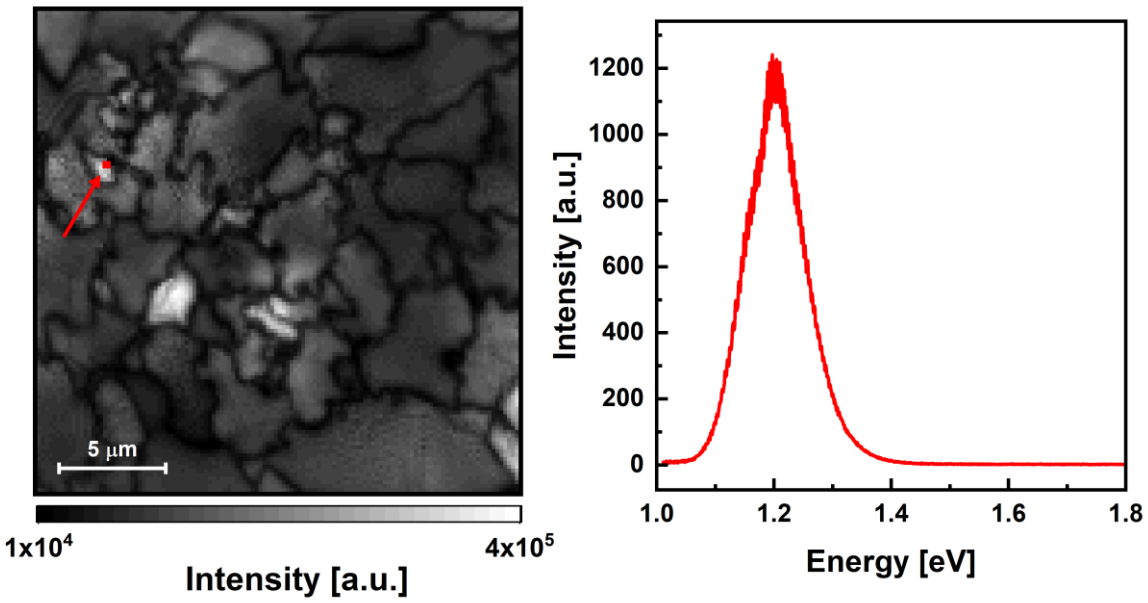

Figure 3.5. Panchromatic image (left) of an absorber's front surface obtained from CL. Each pixel of the panchromatic image contains a full emission spectrum. One pixel is highlighted in red, and the corresponding spectrum is displayed (right).

Measurement resolution

The interaction volume of the electron beam with the material defines the spatial resolution of the measurement. This volume depends strongly on the beam energy and the material density and is typically limited by the area in which electrons lose 90% of their energy. The interaction volume cannot be directly measured but can be numerically approximated by a Monte-Carlo simulation [99]. Furthermore, the acceleration voltage influences how deep the electrons penetrate into the material, i.e., how deep beneath the surface is the sample probed.

Experimental setup

In this thesis, CL spectroscopy was performed by Dr. Gunnar Kusch and Yucheng Hu at the Cambridge Center for Gallium Nitride [100] in a SEM-CL system (Attolight Allalin 4027 Chronos). The microscope is operated at an electron current of $2.5 - 10$ nA and at an acceleration voltage of $5 - 8$ kV. The investigated samples are measured from the front and back sides (after mechanical lift-off from their substrate), as well as from the cross-section.

The hyperspectral data is analyzed using LumiSpy [101], a special Python package for multi-dimensional data analysis (from the HyperSpy library).

3.4. Glow discharge optical emission spectroscopy

To be able to optimize an absorber growth process or to correlate experimental observations with the material composition, an elemental distribution profile is often very valuable. Various techniques such as SIMS (secondary ion mass spectroscopy), TEM (transmission electron microscopy), XPS (X-ray photoelectron spectroscopy) or GDOES (glow discharge optical emission spectroscopy), to cite only a few, may fulfil this purpose [102]. Since GDOES is part of the standard analysis procedure at AVANCIS after the absorber growth, it is the chosen method to produce the depth-resolved composition profiles presented in this work.

GDOES is a rapid depth-profiling technique well-suited for elemental analysis of bulk samples and achieves a depth resolution comparable to that of SIMS [103]. The sample to investigate is introduced into a chamber filled with a low-pressure gas (argon) and placed on a metallic sample holder (cathode). An electric field is applied between the cathode and the anode (placed above the sample) and consequently ionizes the gas, creating a glow discharge plasma. The plasma is used to sputter the surface of the sample and the ejected atoms are excited by the high energy electrons and ions present in the plasma. Upon relaxation, they emit characteristic photons that are detected by a CCD-array. Removing layer by layer, a crater of the size of the anode (2.5 mm) is formed and the depth profile of mass concentration can be determined. In addition to the composition, the thickness of the absorber can be approximated by considering the Mo back contact signal, i.e., as soon as Mo is detected, it means that the whole absorber has been removed.

The system used is a GDA 650 HR, built by Spectruma Analytik in DC excitation mode (constant voltage – constant current mode). The excitation parameters are typically set to 1000 V and 12 mA.

3.5. Raman spectroscopy

It has been discussed in section 2.2.2, that when light interacts with a material it can be absorbed. In Raman spectroscopy, however, information is obtained not from the absorbed

light but from the scattered one. In this case, the excitation photon disturbs the electronic cloud around the nucleus and brings the molecule to a short-lived higher energy state [104]. The new state is not a true one and is called a virtual state. To respect the energy conservation, the scattered photon (which is detected) shifts to a different energy (or frequency) by an amount equal to the energy difference between the final and initial states of the molecule. Each peak in the resulting measured spectrum corresponds to a specific molecular bond vibration. The Raman shift, commonly given in cm^{-1}, and the relative peak intensities produce a unique chemical fingerprint which is then used to identify the material, based on the large data sets available in the literature. If the energy of the excitation laser is close to an electronic transition in the studied material, i.e., the virtual state is close to a true one, the Raman peak intensity of the vibrational mode associated with this specific transition is greatly increased [105]. This phenomenon is known as resonance Raman scattering.

The Raman spectroscopy discussed in chapter 4 has been performed by Dr. Maxim Guc and Robert Fonoll-Rubio at IREC [106], Barcelona, Spain. In particular, the measurements are performed in a backscattering configuration through a probe designed at IREC. Three excitation lasers are available, of wavelengths 442 nm, 532 nm and 785 nm. The last two are used in a macro-Raman configuration, i.e., with a beam spot diameter of ~ 70 μm, whereas measurements done in a micro-Raman configuration, i.e., with a beam spot diameter reduced to ~ 2 μm, utilize the 442 nm excitation laser. Furthermore, the 442 nm and 532 nm excitation lasers are used in association with a fHR 640 monochromator from Horiba Jobin Yvon, coupled with a CCD detector cooled down to -130˚C. However, the 785 nm excitation laser is used with an iHR 320 monochromator from Horiba Jobin Yvon, coupled with a CCD detector cooled down to -70˚C. The excitation power density on the sample is kept below 50 $W \cdot cm^{-2}$ to prevent thermal effects in the measured spectra.

The Raman spectroscopy presented in chapter 5 is performed by Dr. Ricardo G. Poeira at the university facilities. An excitation laser of wavelength 532 nm is used with a Renishaw inVia micro-Raman spectrometer. In particular, a 100× objective lens (with a numerical aperture of 0.85) and a 2400 lines/mm grating is employed.

In both setups, a quick calibration prior to the measurements is systematically performed, measuring a reference monocrystalline silicon sample and imposing its main Raman peak to 520 cm^{-1}.

Chapter 4

Band gap gradient in $Cu(In,Ga)(S,Se)_2$ – the interlacing phases model

The results presented in this chapter are mostly based on the work that has been published in [12]. Certain paragraphs are taken verbatim, with only minor modification, and can be identified by the different font style in which they are written. The graded architecture, widely used in CIGS solar cells, is investigated in industrial absorbers and demonstrated to not be as simple as suggested by compositional profiling. The need for the band gap gradient in CIGS solar cells is extensively discussed in the literature and is introduced in section 4.1. In the case of the graded absorbers considered in this thesis, a second radiative recombination channel is observed in addition to the expected band-to-band one. In section 4.2, it is demonstrated that this second emission comes from the back side and its origin discussed. Section 4.3 focuses on a depth-resolved analysis of the radiative recombination, by cathodoluminescence spectroscopy on the cross-section and by combining photoluminescence with gradual etching of the absorber. It reveals that the band gap gradient is not continuous, but rather that the band gap jumps between grains. This leads to the proposition of an alternative model for the band gap gradient, where two main phases interlace in the bulk, challenging the current belief. The consequences of the new model on the absorber's performance are considered in section 4.4. Finally, the main findings of the chapter are summarized in section 4.5.

4.1. Why the band gap gradient?

The losses of photogenerated charge carriers via non-radiative recombination (SRH recombination) have been discussed in section 2.2.3. With less carriers available, the qFls is

reduced, and consequently so is the V_{OC}, i.e., the ultimate efficiency of a solar cell is decreased. However, non-radiative losses do not only occur in the bulk, and a large contribution could arise from the surfaces if not properly handled (cf. also section 2.5.2). This is especially the case at the back contact interface where the absorber is directly grown on a metal (molybdenum), providing a large number of available states for electrons to recombine. Furthermore, if the carrier diffusion length equals or exceeds the thickness of the absorber, a considerable number of photogenerated carriers are able to reach the back side within their lifetime and the contribution of the back surface becomes even more critical [107]. In high efficiency $CuInSe_2$ solar cells, a diffusion length larger than 3 μm has been estimated [108,109], proving the necessity of considering the back side. For a homogeneous absorber with no special care for the back side recombination, e.g. a pure CISe absorber, the back surface recombination velocity S_b is estimated to be larger than 10^5 cm/s [110]. Various methods to passivate the back surface have been proposed. Jarzembowski *et al.* [111] suggest that alkali post-deposition treatments, in particular NaF, can lead to a reduction of S_b from $> 10^5$ cm/s to $< 10^2$ cm/s in ultrathin CIGSe absorbers. Alternatively, patterned passivating dielectric layers with small openings between the absorber and the back contact show promising reduction of back surface recombination [112,113]. Wang *et al.* [114] propose a new structure featuring a hole selective transport layer between the homogeneous absorber and the Mo back contact, successfully mitigating the back surface recombination and reaching an efficiency close to 17% for an ungraded submicron CIGSe solar cell.

Nevertheless, the most wide-spread solution for reducing back surface recombination in CIGS is to create a band gap gradient towards the back side by increasing the Ga content. Single and double graded absorbers have been developed in the 90s already [115–117], and are still used in high efficiency CIGS solar cells today [9,26,118,119]. The higher concentration of Ga at the back side induces a conduction band gradient, responsible for driving the electrons away from the back contact, thus preventing undesirable non-radiative recombination. The difference between the band gap minimum E_g^{min} and the maximum band gap at the back side E_g^{back} is defined as $\Delta E_g^{back} = E_g^{back} - E_g^{min}$ and represents an activation energy for the back surface recombination velocity $S_b \propto \exp\left(-\Delta E_g^{back}/k_b T\right)$ [120]. Simulations and experiments agree on the improvement in V_{OC} with increasing ΔE_g^{back} [120,121]. In order to mitigate the front surface recombination as well, a front side gradient can also be implemented, as mentioned in section

2.1.2. In the studied CIGSSe absorbers, this is achieved with a higher S content at the front surface of the absorber. As a consequence of the (double) graded structure, the photogenerated carriers are expected to recombine principally at the notch, and therefore produce a single PL emission peak of the energy of the band gap [122], here at approximately 1.05 eV.

4.2. The presence of a second phase

This section reports on the observation of a second emission peak at an energy higher than the expected band-to-band emission. It is measured optically by PL and confirmed by CL. Raman spectroscopy provides further insight on the potential origin of the emission.

4.2.1. Double band gap gradient

Typical GGI profile of the investigated absorbers is shown in Figure 4.1. As already discussed, the Ga content is intentionally increased towards the back side to create the desired band gap gradient. Both profiles, GGI and E_g, display a rather smooth increase over the thickness of the absorber (ignoring the front gradient in the E_g profile). As mentioned in section 2.1.2, the band gap is calculated according to Equation (2.1) and considers the SSSe ratio in addition to the GGI ratio, explaining why the band gap profile does not quite follow the GGI profile. This is especially true at the front surface where a band gap as high as 1.4 eV is calculated. Additionally, based on the GDOES profile, the notch band gap is expected to be close to 1.14 eV, which is 100 meV higher than the measured PL emission peak energy (see Figure 4.4).

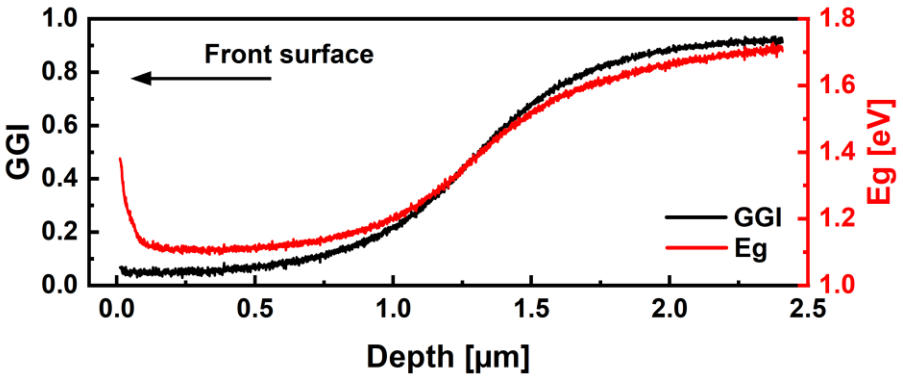

Figure 4.1. Typical GGI (black) and band gap (red) profiles of a "standard" absorber from this study determined from GDOES compositional measurements. The investigated absorbers

are all about 2.4 µm thick. The stronger increase of the band gap from GDOES towards the front is due to the S content, which is higher near the front.

It is observed that the notch energy given by the GDOES profiles systematically leads to higher values compared to other measurements methods. Considering four absorbers of different S contents, $E_{g,min}$ is measured from reflection, EQE, PL and GDOES analysis [20,55,123–125] and compared in Figure 4.2. In the case of reflectance and EQE, the inflection point is used to determine the band gap. For PL, the energy of the notch peak maximum is taken as the band gap, which is expected to be lower than the actual one due to sub-band gap states, as discussed in section 2.4.3. Finally, the E_g from GDOES is obtained by averaging the profile between 200 µm and 500 µm. The comparison reveals that the first three methods agree on $E_{g,min}$, whereas GDOES overestimates it by about 55 meV. A probable reason for this could be that not all of the sulfur is incorporated into the grains, and that non-negligible amounts of it are located at the grain boundaries. Keller *et al.* [126] investigate the atomic structure around grain boundaries in AVANCIS' CIGSSe absorbers by Atom Probe Tomography (APT) and show that S tends to agglomerate at the grain boundaries. Consequently, band gap energies calculated from composition alone are overestimated due to the apparent higher S content. Additionally, as discussed in further detail in section 4.3.1, Raman spectroscopy reveals some S-free areas on the back side of the absorbers. Therefore, the band gap profiles determined from GDOES are considered in a qualitative way only, and often in this thesis the GGI profiles will be directly referred to.

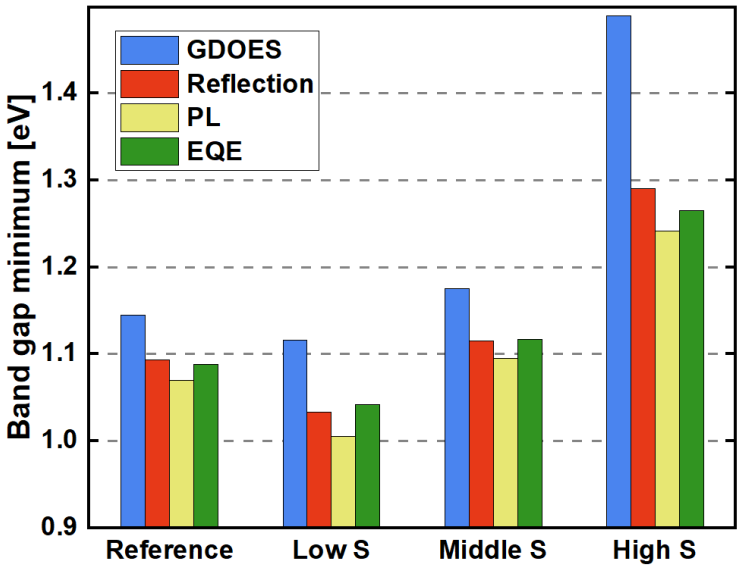

Figure 4.2. Comparison of band gap minimum extracted from GDOES, reflection, PL and EQE for different absorbers of various S content. PL band gap is taken as the energy of the peak maximum, which is lower than the actual band gap (cf. section 2.4.2).

4.2.2. Absorber lift-off

Because of the shape of the gradient, the idea to characterize it is to measure PL from the back side. In order to investigate the recombination activity from the back side, the absorbers are mechanically removed from their substrate and a subsequent analysis of the PL response from the different surfaces is conducted. A two-component epoxy glue (Loctite EA 3421) is spread on the front surface of the samples before a clean glass (SLG) is pressed on it. The pressure is maintained by a clamp for at least 24h to allow the glue to cure. The samples are then mechanically removed from their substrate by applying some force on them. A short dip of the stack in liquid nitrogen (5-10 sec) beforehand has been found to help lifting-off the film more easily. It has been reported [127–129] that the cleavage of such a stack happens at the interface CIGSSe/Mo or within the Mo(S_x,Se_y) layer that forms at the interface. The investigation of the remaining substrate (by X-ray diffraction, not shown) indicates that some residual traces of CIGSSe phase are still present on the substrate, suggesting that the current lift-off procedure does not provide an excellent detachment of CIGSSe from the Mo layer.

In addition, top view SEM images of the front and back sides are provided in Figure 4.3 and allow for comparison of the morphologies between the two surfaces. While the front side displays a very nicely faceted structure, observed in other high quality absorbers [130], the back side appears mostly flat, yet spotted with numerous craters. These craters may have been formed during the absorber growth already or could be a consequence of the lift-off, as it has been proven that absorber's residues are still present on the peeled substrate. It is difficult from the SEM images to estimate the depth of the craters, but some may be deep enough to reach close to front surface, as discussed in the next section.

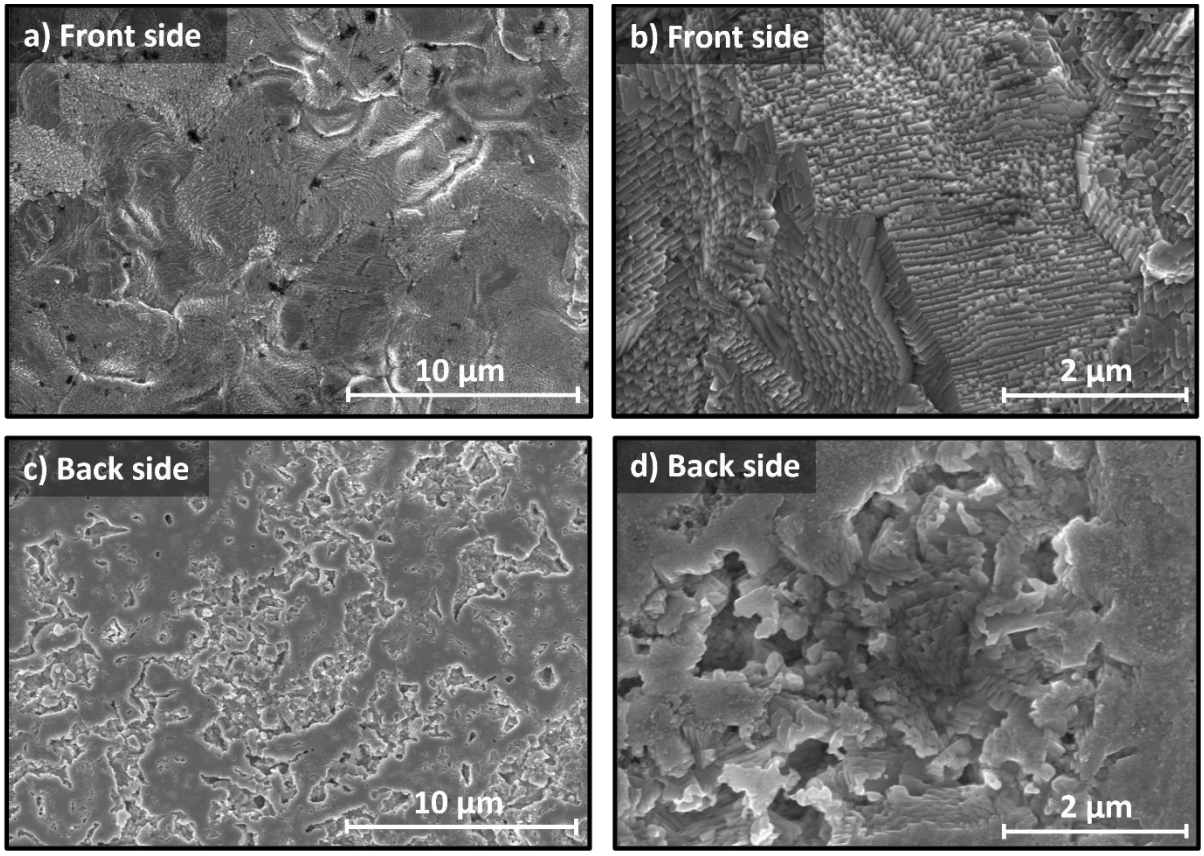

Figure 4.3. SEM top view images of a "standard" absorber from the front side (top row) and back side (bottom row) after lift-off. The micrographs a) and c) show a large view of the sample, while b) and d) are zoomed on specific features (other regions on the sample).

4.2.3. PL on front and back sides

At room temperature, PL measurement with illumination from the front side, before the lift-off (green spectrum in Figure 4.4), reveals only one single contribution at

about 1.04 eV. This PL emission peak corresponds to band-to-band recombination in the notch region [55,122]. The PL spectrum measured from the back side, however, shows two main emission peaks: one peak centered around 1.03 eV and second one in the range of 1.5-1.6 eV (blue spectrum in Figure 4.4). The slight redshift of the notch peak compared with the measurement from the front side is attributed to lattice relaxion after the stress applied by the Mo is removed [122]. The small sharp peak at 0.89 eV is attributed to water absorption [131] and there is a second broader contribution centered around 0.9 eV that is discussed in further detail in section 4.4. The full width half maximum (FWHM) measured for the low energy peak is about 80-90 meV (from the front side) and about 160-180 meV for the high energy peak (from the back side). These values are typical CIGS films [59].

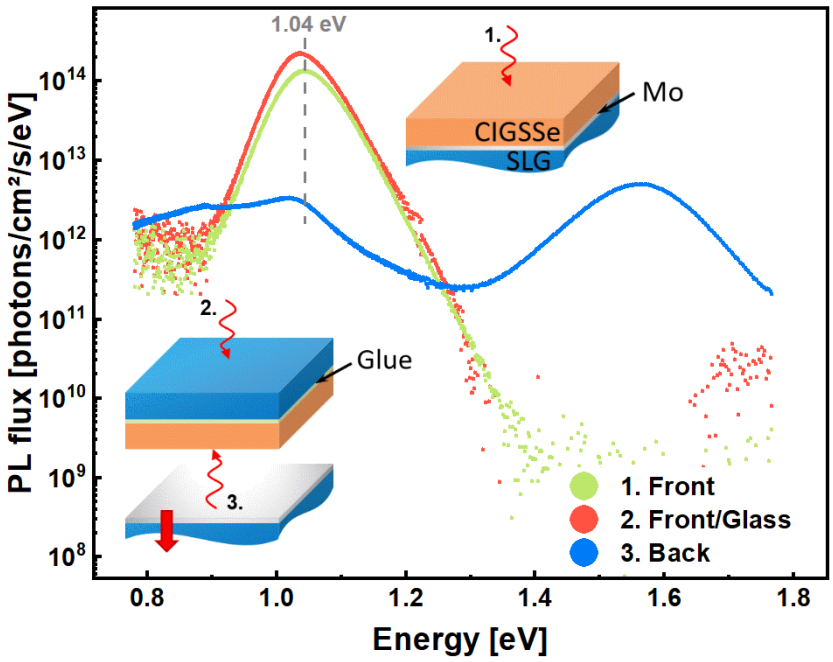

Figure 4.4. Semi-log scale – absolute photoluminescence spectroscopy at the different stages of the lift-off process: under front side illumination before (1.) and after (2.) lift-off and under back side illumination after lift-off (3.). Spectrum 2 has been corrected from the glass emission, see Figure 4.5.

A lower emission energy of 1.03 eV is also measured when illuminating from the front side, after the lift-off. Note however, that in this case the absorber is covered by the glue and the SLG. Under excitation of the red laser, it is found that SLG emits at 1.5

eV, which distorts greatly the PL spectrum of the absorber (see Figure 4.5a). However, taking a PL measurement of the glass alone under the same conditions as the absorber's makes it possible to correct the shape. A simple subtraction of the glass spectrum from the absorber spectrum is performed. The quality of the subtraction can be assessed from the slope of the high energy wing (>0.1 eV above the band gap energy) of the red "corrected" spectrum. In Figure 4.5b, two pieces of glass are glued together with the epoxy glue and the resulting stack emission is compared to that of the glass alone. It demonstrates that the glue does not have any significant emission in this energy range and can therefore be disregarded as potential parasitic signal in PL.

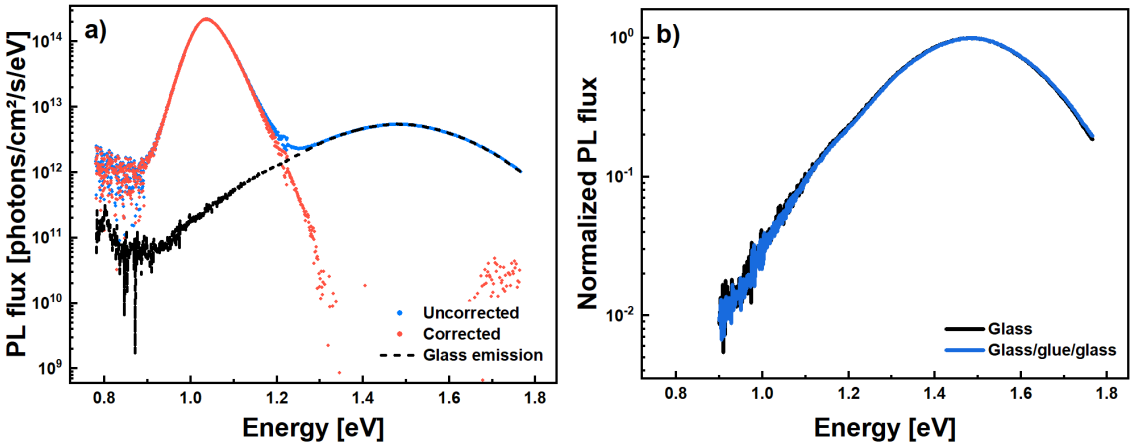

Figure 4.5. Semi-log scale – a) absolute PL of the absorber displayed in Figure 4.4 labeled "Front/glass". The blue spectrum is the uncorrected emission of the absorber affected by the glass emission (black dotted line). The red spectrum is the resulting corrected spectrum after the glass emission is subtracted. b) normalized emission of the glass alone and a stack glass/glue/glass under the red laser excitation.

Based on the common emission from the front and back sides at 1.03 – 1.04 eV, it is argued that independently from the illumination side, significant recombination originates from the band gap notch. After the lift-off, however, the stress applied on the lattice by the molybdenum is released, allowing the lattice to relax. Thus, it is generally observed that the notch PL peak is 10-20 meV lower after lift-off than before, depending on the curing time [122]. The longer the glue cures before the lift-off, the less shift is observed.

Moreover, as shown in Figure 4.4, the notch luminescence is about two orders of magnitude lower when excited and measured from the back side compared to the front side PL. This reduction could originate from various sources. (i) due to the second recombination channel at higher energy, less carriers are available for recombination at the notch. (ii) as seen from Figure 4.1, the notch region extends roughly from ~100 nm to ~700 nm from the front surface. Hence, while illuminating from the back side, the carriers are generated far away from the notch, making it less probable that they reach it to recombine. (iii) it is generally known that the back side of the CIGS absorbers is of lower quality than the bulk [132], offering therefore more non-radiative recombination possibilities, i.e., reducing the overall emission. (iv) finally, due to the imperfect lift-off (cf. Figure 4.3) it is most probable that new non-radiative recombination centers are created.

4.2.4. The origin of the high energy PL peak

The band gap profile from Figure 4.1 cannot explain why only two peaks are detected from PL. If one assumes that the high energy peak originates from the band gap gradient at the back side, then all of the intermediate band gaps should also be visible in PL, and result in one single very broad peak. Unexpectedly, the high energy peak can be detected from the front side as well, but only at low temperatures (in the range of 10 – 80 K in Figure 4.6). At low temperatures, a decrease of the photogenerated carriers' mobility is expected and therefore the recombination is more likely to occur at the generation site. Moreover, the absorber is excited with a laser of wavelength 660 nm having a penetration depth in the material of about 100 nm. It suggests that within the first few hundreds of nanometers from the front surface, the second recombination channel already exists, emitting at 1.5 - 1.6 eV. While appearing as a good candidate for explaining the second luminescence peak, it is demonstrated in the following that the front side gradient is not responsible for it. According to Figure 4.1, the front gradient is very localized to the front surface and carriers generated in this region might still be able to reach the notch, even at low temperature.

The redshift of the high energy peak with increasing temperature detected in Figure 4.6 is a commonly observed phenomenon that is addressed in detail in several works [133–135]. It relates to the potential fluctuations of the energy bands, and while important for solar cells, a deepened

analysis of this behavior falls outside the scope of this thesis. The sharp emission peak highlighted in Figure 4.6 (red dashed line) is several orders of magnitude weaker than the low energy peak and is not present in all measurements. As will be explained by the proposed model in section 4.3, it may correspond to a third recombination channel present close to the surface.

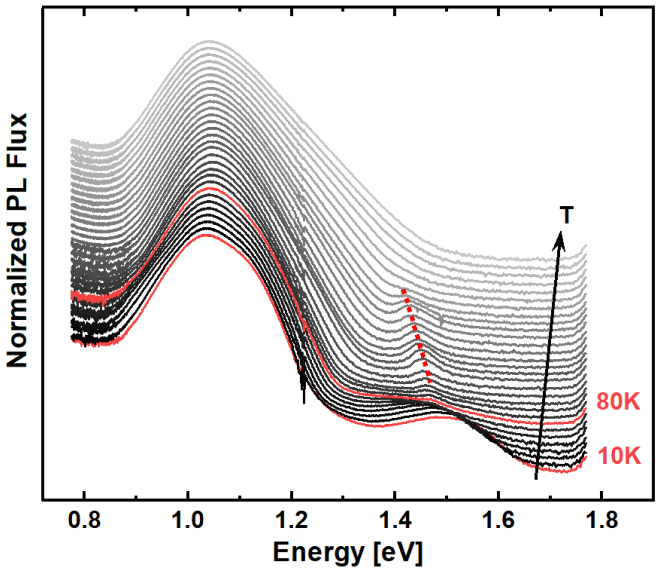

Figure 4.6. Semi-log scale – Temperature dependent PL measurement from the front side from 10 K up to 300 K. The data is normalized to the low energy peak and manually shifted for better display. In addition to the low energy peak, a second recombination channel is detected at high energy for temperatures between 10 K and 80 K. The red dashed line highlights an additional peak discussed in the text.

It is suspected that the high energy peak is related to the larger band gap close to the back side of the absorber. In order to verify it, a series of absorbers with varying GGI at the back side is prepared. As mentioned in section 4.2.1, it is believed that the sulfur is not entirely incorporated in the grains and therefore the back side GGI is employed as a guide to compare the band gap energy trends between the samples. Note that this does not provide an exact value for the expected band gaps. Figure 4.7a shows the relation between the position of the high energy PL peak measured from the back side and the back side GGI averaged over the last 400 nm of the GDOES profiles. Samples in region III present small changes in back side GGI, ranging from 0.85 to 0.93 and only a loose correlation is observed for the corresponding high

energy PL peak, which varies from 1.50 eV to 1.56 eV. Samples in region II have a significantly reduced back side GGI of 0.71 to 0.77. The same PL peak energy is observed within errors, except for one sample with slightly lower peak energy (and lower back side GGI). Lastly, the samples in region I have the lowest back side GGI (0.66 and 0.52) and show the lowest peak energies (1.38 eV and 1.30 eV). This demonstrates that the PL emission at high energy strongly depends on the GGI at the back side of the absorber. In a previous work on co-evaporated CIGSe absorbers from ZSW, Wolter *et al.* [122] detected a similar high energy peak in addition to the notch peak when measuring from the back side. These samples were grown with a back side GGI of about 0.6 and the high energy peak was detected at 1.31 eV, correlating with the trend observed in Figure 4.7a. Figure 4.7b provides examples of back side PL spectra for decreasing GGI. In most cases, as the high energy PL peak redshifts, the relative intensity of the notch emission increases. Additionally, the contribution at energies below 1 eV (purple and green spectra) gradually disappears with the reduction of the back side GGI, suggesting a close relation between the two.

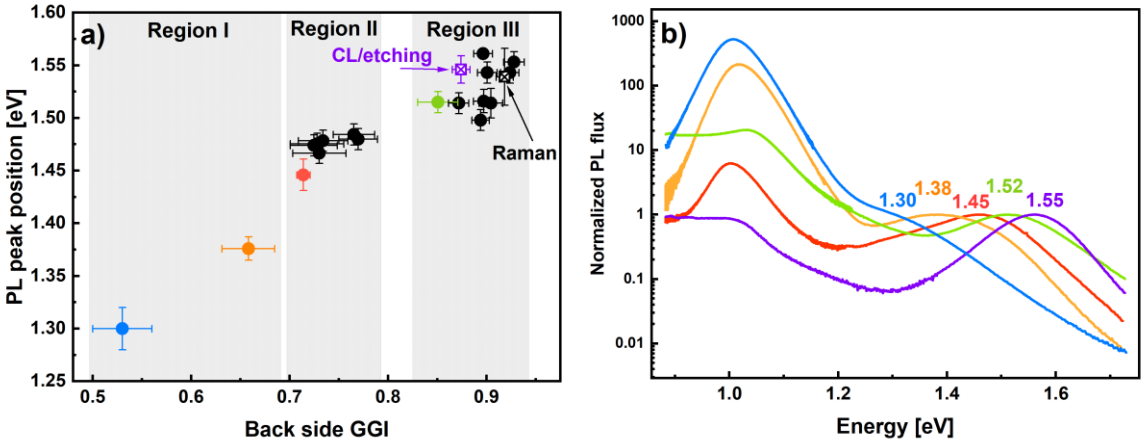

Figure 4.7. a) Collection of 20 different samples of varying back side GGI. For each of them, the position of the high energy peak is measured by PL from the back side. The error in PL energy is due to inhomogeneities and is determined from different measurements on the same sample. The back side GGI is determined from an average over the last 400 nm of the corresponding GGI profile. The standard deviation is taken as the error. The samples labeled "CL/etching" and "Raman" are referred to in the text. b) PL spectra from the back side of five

chosen absorbers, color-highlighted in a). They are normalized to the second peak, and the energy of the peak maximum is indicated.

Based on these results, it is argued that there is no continuum of band gaps through the material (which should result in a continuous emission spectrum), as suggested by the GDOES profile in Figure 4.1, but rather that there are distinct phases of discrete band gaps coexisting throughout the whole thickness of the material.

4.3. A new model for the band gap gradient

Before establishing a new model, further characterization of the suspected phases forming must be done and their distribution within the depth of the absorber better evaluated. This is achieved by Raman spectroscopy together with a combination of cross-sectional CL and depth-resolved PL.

4.3.1. Raman spectroscopy investigation

Investigation by Raman spectroscopy of both the front and back sides of the absorbers is conducted to assess whether the different phases are due to different CIGSSe compositions or due to secondary phases. As mentioned in section 3.5, these measurements are performed at IREC [106], in macro and micro configurations and are discussed in this section.

Four different absorbers are measured (all from region III in Figure 4.7a) in a macro-Raman configuration and Figure 4.8a and b summarize the normalized Raman spectra of the sample indicated in Figure 4.7a. As no significant differences could be observed between the samples, the other measurements are added in the Appendix A.1. A 532 nm laser excitation is used in this case and up to 25 spots are measured on each surface, which provides representative information for the whole sample. This excitation wavelength is close to the band gap of pure $CuGaS_2$ [136], which leads to resonant Raman scattering and a strong intensity increase of some peaks is observed (indicated by the green dashed lines in Figure 4.8a and b). The main peaks, observed from the front side, are associated to the Se-Se and S-S vibrational modes at 178 cm^{-1} and 288 cm^{-1}, respectively [137,138]. When measuring from the back side, a

slight blueshift of these peaks to 185 cm^{-1} and 307 cm^{-1}, respectively, is observed (cf. Figure 4.8b). This can be explained by the increase in S and Ga content towards the back of the absorbers [137,139]. The associated increase in the band gap also leads to additional resonant behavior of the spectra measured from the back side. The peaks marked by the gray dashed lines, at 170 cm^{-1}, 238 cm^{-1}, and 252 cm^{-1}, are attributed to a $MoSe_2$ phase detected at the back side of the absorbers [140]. This is an expected secondary phase at the Mo-CIGSSe interface [141,142]. All other peaks result from CIGSSe phases and no obvious secondary phases are observed. An investigation of the remaining substrate after lift-off reveals some traces of CIGSSe phases, providing further evidence of the imperfect removal of the absorber from its substrate (see Appendix A.1).

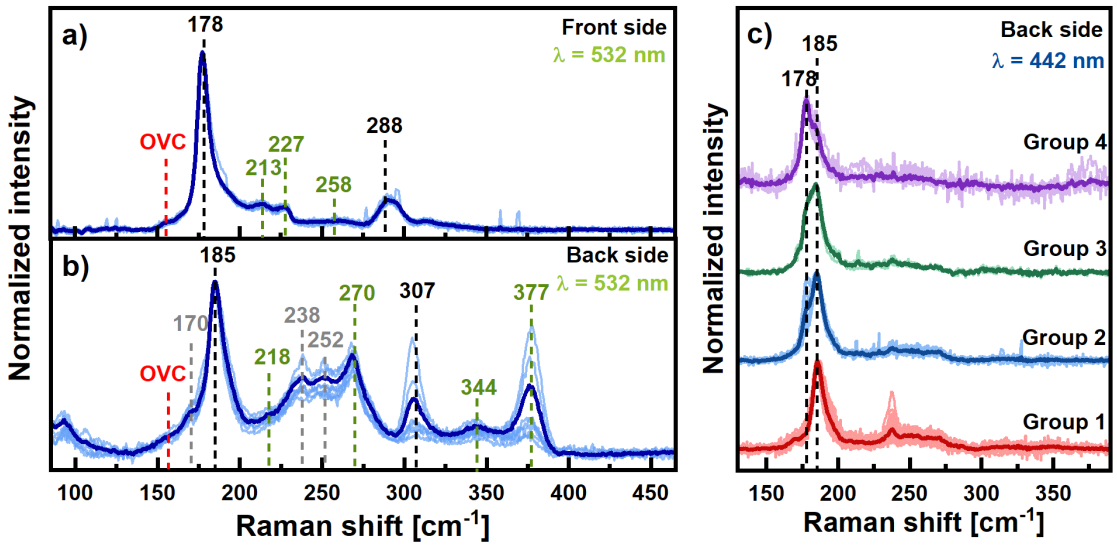

Figure 4.8. Typical Raman spectra measured from a) the front side before lift-off and b) the back side after lift-off in a macro-Raman configuration. A 532 nm wavelength laser is used as an excitation source. c) Micro-Raman on a 3 × 3 mm^2 area from the back side using a 442 nm wavelength laser as excitation source. Individual measurements are ordered in group 1 to 4 depending on the dominant peak. Pale lines in all figure parts are individual measurements taken on different positions and normalized to the peak related to Se-Se vibrations (178 cm^{-1} and 185 cm^{-1}). Darker lines are the resulting averaged spectra.

Additionally, a small peak of an OVC phase is visible from both sides, appearing as a shoulder on the low frequency side of the Se-Se peak [143], as highlighted by the red

dashed lines in Figure 4.8a and b. As shown in Figure 4.9, under excitation of a 785 nm laser (in macro-Raman configuration), more of the OVC peaks are detected from both sides. Because this wavelength is closer to the band gap of the OVC phases, e.g. $CuIn_3Se_5$ [144], it provides conditions close to resonance and therefore more of the vibrational modes can be detected. However, from the back side, a strong PL signal is measured and prevents a clear Raman measurement.

Nevertheless, despite the detection of OVC phases, it is believed that the high energy PL peak originates from a high GGI CIG(S)Se phase, as it shows a strong correlation with the back side GGI. Furthermore, based on the peak ratio OVC/(1:1:2) in Figure 4.8, the volume fraction of OVCs is low compared to the 1:1:2 phase, and could not produce such a strong PL emission at high energy as detected (for instance) in Figure 4.4.

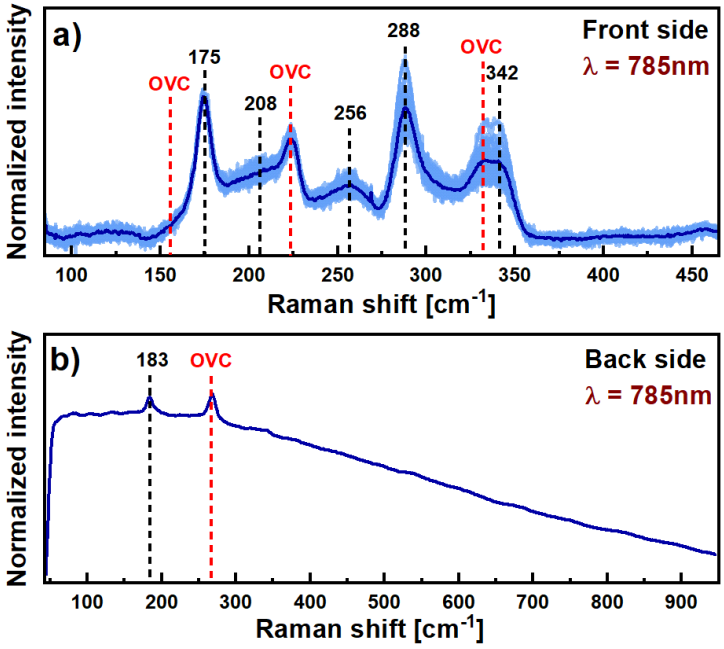

Figure 4.9. Raman spectra measured from the a) front and b) back sides under an excitation wavelength of 785 nm. Note the scale difference between the two graphs. From the back side, the background noise is quite high due to the photoluminescence signal under this excitation wavelength which prevents its correction by standard methods.

Furthermore, the pale lines in Figure 4.8 and Figure 4.9 represent individual measurements performed on different positions on the absorber. They can be used

as an indication of the lateral homogeneity, in terms of chemical composition, of the absorbers' surfaces. Considering Figure 4.8a and b, it follows that absorbers are very homogeneous from the front side, whereas significant variation is observed between the individual measurements from the back side, suggesting larger inhomogeneities. In particular, the back side of the absorber is scanned over an area of 3 × 3 mm^2 with a 442 nm excitation wavelength in a micro-Raman configuration (see Figure 4.8c). This excitation wavelength has been chosen for being far from resonant with pure $CuGaS_2$, $CuGaSe_2$ and $CuIn_3Se_5$ OVC phases [136,144,145] and has a penetration depth shorter than 100 nm. Within the small area, 64 positions are measured which enables a grain to grain analysis. From this measurement it can be concluded, based on the absence of the 307 cm^{-1} peak, that some sulfur-free areas are present on the back side. More interestingly, grains with significantly different Ga amount are detected. Two distinct $Cu(In,Ga)Se_2$ phases are distinguished when measuring from the back side, one more Ga-rich and the other more In-rich, yielding the peaks at 185 cm^{-1} and 178 cm^{-1}, respectively. For clarity, the individual measurements are divided into four groups depending on the dominating phase. The Ga-rich phase strongly dominates in groups 1 and 2, whereas the In-rich one dominates the spectra in group 4. Group 3 regroups spectra where the two phases compete. From the position of the Raman peak and assuming a linear dependence of the peak position with the GGI [139], it is possible to estimate the GGI of the observed phases. Considering the peak positions for pure $CuInSe_2$ at 175 cm^{-1} and for pure $CuGaSe_2$ at 186 cm^{-1}, it yields a GGI of 0.3 for the 178 cm^{-1} Raman peak and a GGI of 0.9 for the 185 cm^{-1} peak. While a GGI of 0.9 correlates well with the GGI profile towards the back side, the GGI of 0.3 is larger than the expected one for the notch. However, this approximation does not consider the potential presence of S and could lead to an overestimation. The micro-Raman investigation, again, hints towards the coexistence of two distinct phases.

It is important to note that because of the aforementioned imperfect lift-off (cf. Figure 4.3), the crystal layers are broken in some places and therefore, measuring from the back side, it is possible to penetrate deeper in the material and "see" grains from the bulk/front interface of the absorber. Nevertheless, as seen from CL in the next section, some low band gap phases are indeed located close to the back surface.

4.3.2. Cross-sectional cathodoluminescence spectroscopy

Complementary information on the variation of the band gap from grain to grain is obtained from CL-SEM. In particular, CL is performed on the cross-section of an absorber similar to the one in Figure 4.8 and Figure 4.9 (and highlighted in Figure 4.7a). As mentioned in section 3.3, in each pixel of the CL map, a spectrum is measured making it possible to follow the evolution of the band gap from the front surface down to the back side. Figure 4.10a shows a secondary electron (SE) cross-section image of the region where CL is performed. SE images are recorded under conditions optimized for CL imaging, which often has opposite imaging requirement (largest aperture vs smallest aperture, high current vs low current, fixed working distance due to fixed focal point of light collection optics). This explains the rather low quality of the image and the latter only provides a guide to follow where the CL signal is coming from. Furthermore, the acceleration voltage in the microscope is set in such a way as to probe deeper in the material and reduce the influence of the cleaved surface. Therefore, a one-to-one correlation between the energy map and the micrograph is not possible. Figure 4.10b reports the energy of the maximum of each individual spectrum. It is important to mention that this representation gives only a simple view of the band gap energies, as some spectra, especially close to the back side, are too noisy to identify peaks. As the sample is slightly tilted, not only the cross-section's emission is visible, but also the very front surface. The latter is dominated by a low band gap phase with emission at about 1.13 eV (dark blue color) that relates to the low energy peak in the PL spectra, centered at 1.04 eV. Energy differences between the two measurement methods is attributed to the decreased quantum efficiency at such low energies of the Si-camera used in CL. A comparison of the CL emission captured with a Si-detector and with an InGaAs-detector is provided in Appendix B.1.

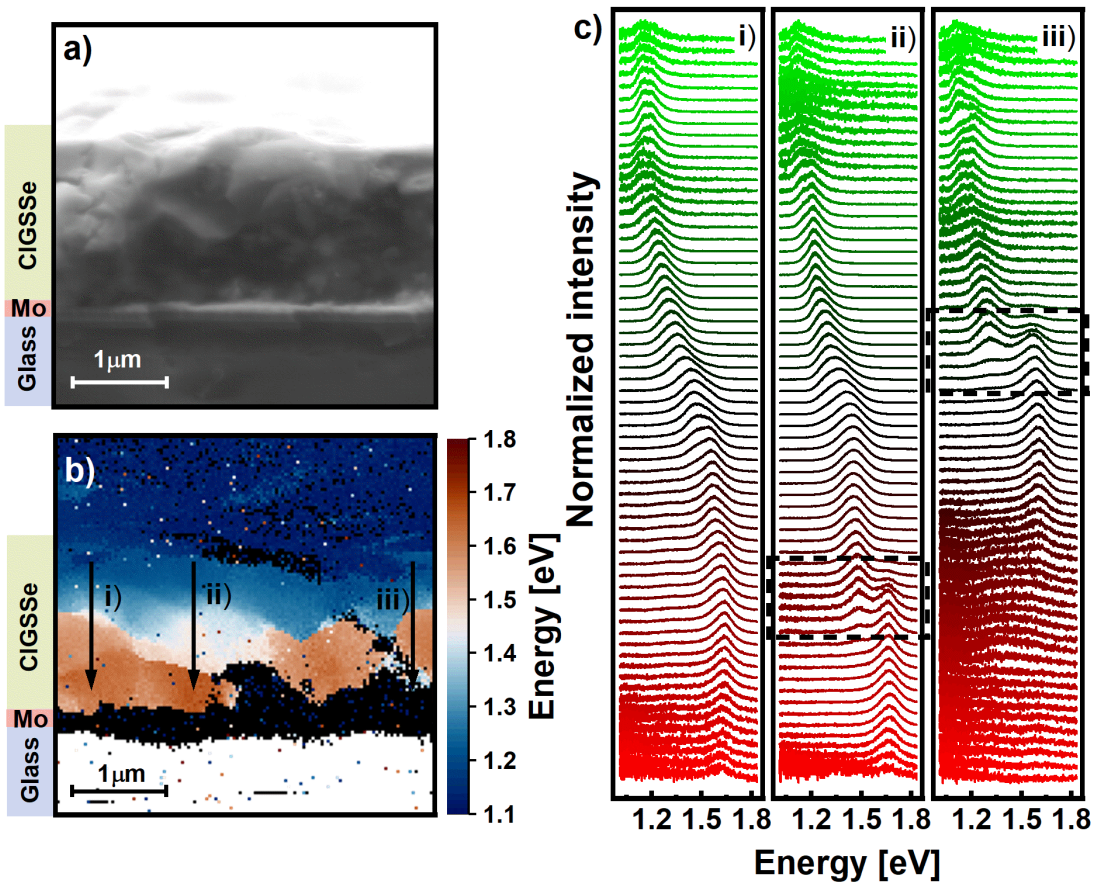

Figure 4.10. a) SE cross-section image of the region of interest where the CL is performed. b) Colormap of the energy of the maximum of the CL emission. Dark red corresponds to the high band gap phase, white/light blue to the intermediate one and dark blue to the low band gap phase. The white region at the bottom is glass and the black regions are either molybdenum (see left legend) or too noisy to identify peaks. c) Individual spectra along the lines i-iii) shown in b). The dashed boxes indicate the coexistence regions.

Considering individual line profiles from top to bottom along the cross-section of the film, as indicated in Figure 4.10b by the vertical arrows, three scenarios are identified. i) two-phases region with a smooth transition from the front surface towards the back side. ii) three-phases region with a smooth transition at intermediate depth from the low band gap phase to an intermediate band gap phase. Closer to the back side, a coexistence of the intermediate band gap phase and the high gap phase is observed. iii) two-phases region with a coexistence of the low band gap and high band gap phases at intermediate depth.

Individual spectra along the three lines are plotted in Figure 4.10c. In case i), mostly a single emission peak is detected at each depth, gradually increasing from 1.15 eV to 1.62 eV towards the back side. It should be noted, however, that in the transition region the peak broadens compared to the front and back regions. Cases ii) and iii) feature distinct areas where multiple phases are simultaneously observed (dashed boxes in Figure 4.10c). In case ii), a gradual increase similar to the one from i) is observed from 1.13 eV until 1.48 eV, but a sharp transition from 1.48 eV to 1.67 eV then occurs, and two peaks appear in the corresponding spectra. The low energy peak loses in intensity as the higher energy one takes over. This abrupt transition from one recombination channel to another is observed in the colormap (Figure 4.10b) as an abrupt change of color. The line profile iii) is another example of such an abrupt change of recombination energy, happening however closer to the front surface, changing the dominant recombination from 1.28 eV to 1.61 eV. From a larger set of CL measurements performed on the same sample and on a second one with an additional sodium treatment (see Figure 4.11 and Appendix A.2), it is concluded that scenario i) is not the most probable, but that generally, one or two abrupt transitions occur, indicating two or three discrete phases. In Figure 4.11, two energy maps (and corresponding SE images) are shown; one of the absorber discussed in Figure 4.10 (without Na-PDT) but from a different region, a of a similar absorber after an additional Na-PDT. As described above, several abrupt color transitions, i.e., band gap jumps, are observed in both cases. In addition, close to the back side (cf. Figure 4.11a), emission from a lower band gap is detected. Conversely, close to the front side (cf. Figure 4.11b), a patch of high band gap emission is measured. This highlights the fact that the low (high) band gap phase is not solely confined to the front (back) of the absorber.

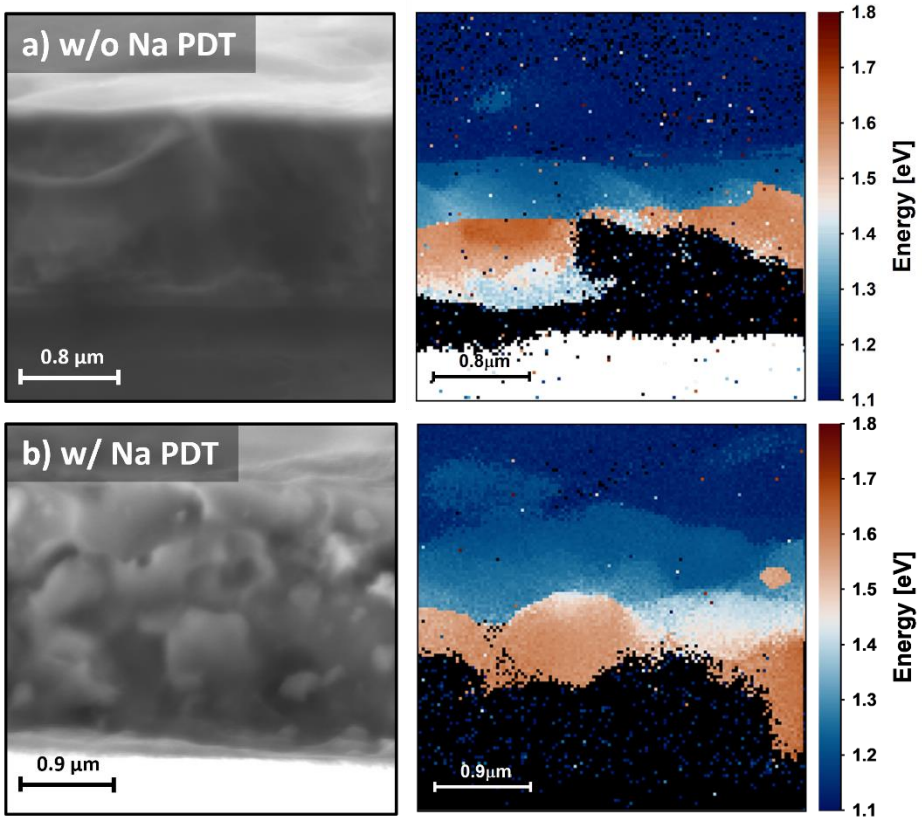

Figure 4.11. Cathodoluminescence on the cross-section of the absorber from Figure 4.10 (without Na-PDT) a) and of a similar absorber which received an additional Na-PDT b). The SE images (left) are given as a guide to estimate where the signal is coming from. The energy maps of the maximum of the emission (right) indicates the energy of the dominant recombination.

While it is generally impossible to see a direct correlation between the morphology of the SE image and the CL emission (because of the different probing depth and the image quality), it is possible to relate the panchromatic images with the corresponding energy maps. The panchromatic images provide the intensity of the emission, which is indicative of the radiative recombination. With this reasoning, brighter areas could correspond to grains and darker ones to grain boundaries. Combining the panchromatic image and the energy map, the relation between the morphology and the emission energy is highlighted (Figure 4.12). Although it is a very indirect way to look for grain boundaries, a certain correlation between the morphology and the color is observed, associating one color with one “hill”.

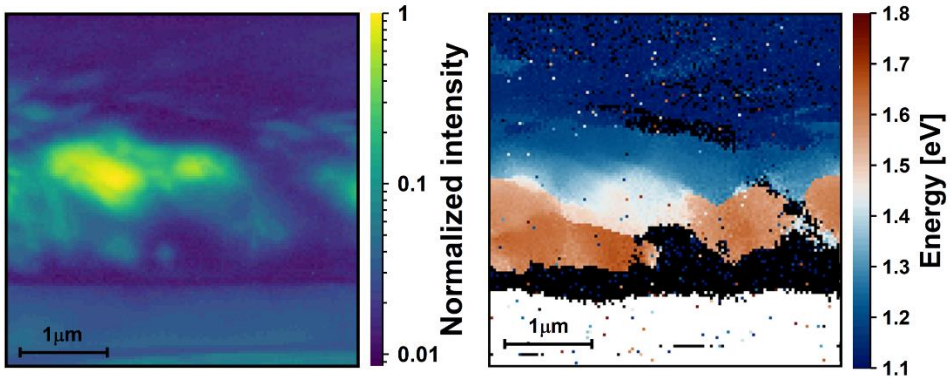

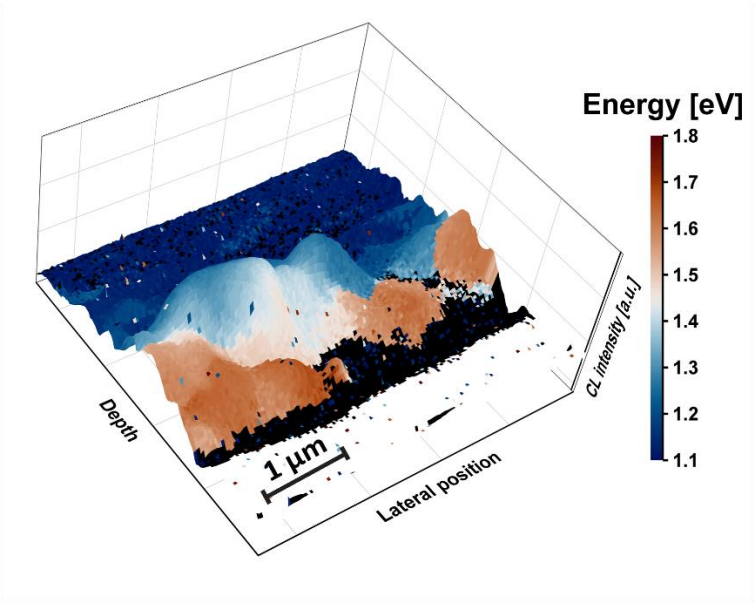

Figure 4.12. Panchromatic image (top left) displaying the normalized intensity of the CL emission (in logarithmic scale) of the absorber without Na-PDT. Energy map reproduced from Figure 4.10b (top right). The bottom image is a combination of the top images: the morphology is given by the intensity and the color by the emission energy. It is assumed that a hill is associated to a grain, while a valley relates to a grain boundary.

Until now, it appears that the gradual increase of the band gap from the front side towards the back side, observed by GDOES elemental analysis, seems not to accurately represent the gradient profile. Raman and CL point rather towards the coexistence of a low and a high band gap phases. However, these two techniques only consider small regions, and the question remains how general this behavior is. As discussed in the next section, a depth-resolved PL investigation of the absorbers demonstrates that this behavior is observed even on larger scales.

4.3.3. Depth-resolved photoluminescence spectroscopy

To verify the hypothesis that the bulk of the absorber is made of interlaced distinct phases, depth-resolved photoluminescence spectroscopy is performed, after sequential etching of the absorber. To this purpose, a bromine etching routine has been developed. An aqueous bromine solution of concentration 0.1 M is prepared by diluting liquid bromine (Br_2) (0.3 mL) into distilled water (60 mL) and finally adding potassium bromide (KBr). The absorbers are dipped into the etching solution for 40s to 4 min depending on the desired etching depth. The remaining thickness of the etched absorbers is measured by cross-sectional SEM imaging. The etched surface generally presents an unequal roughness and therefore the error in the measurement of the thickness is estimated to be ±0.2 µm. The etching is either performed on absorbers before the lift-off, to remove the front part of the absorber, i.e., the low GGI area, or performed after the lift-off, to remove the back part, i.e., the high GGI area.

In this section, only the absorber highlighted in Figure 4.7a is discussed. Two additional absorbers from region III are included in Appendix A.3. Following the etching, the PL spectra at different depths throughout the thickness are measured, thus providing information about the depth distribution of the different phases. Figure 4.13 summarizes the results from the two faces. Note that these two measurements (front and back etching/PL) are independent from each other and performed under different experimental conditions. Because of the lower signal from the back side, the excitation intensity for the back side measurement is set higher than for the front side. The spectra are all spectrally corrected but are not corrected in intensity (cf. section 3.2.2). The measured PL flux is thus not absolute, but a relative comparison between the spectra within the same graph is reliable.

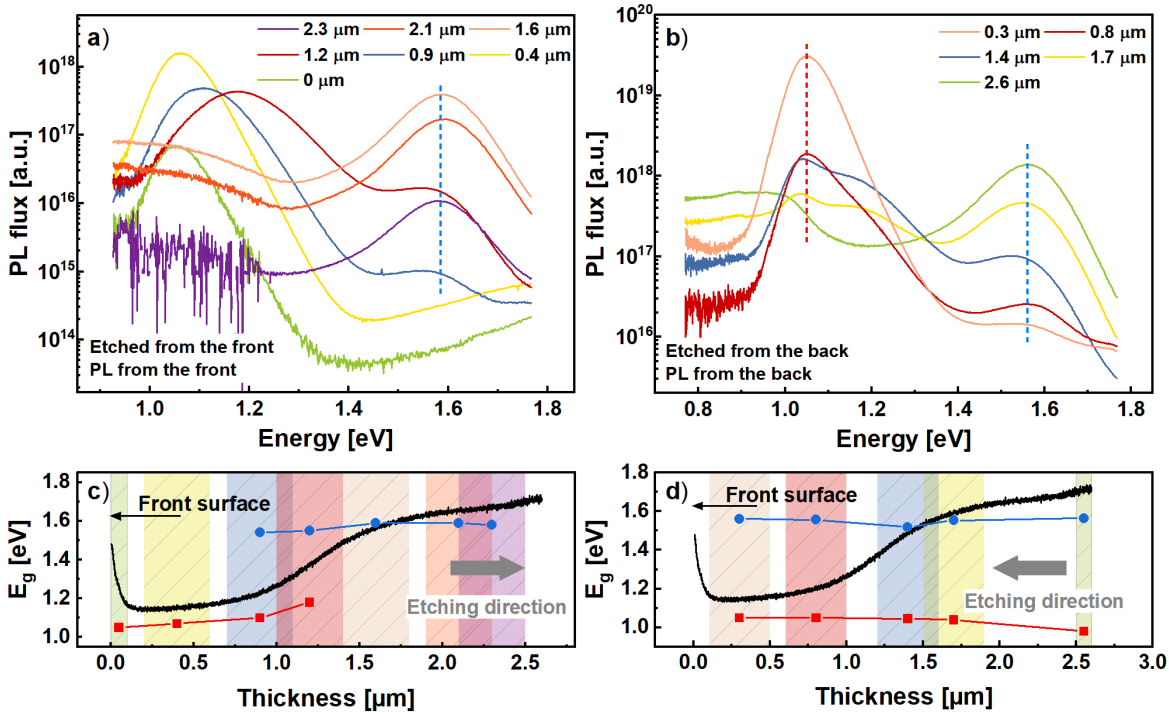

Figure 4.13. Top: semi-log scale, non-absolute PL spectra at different depths after the absorber is gradually etched, from a) the front side and b) the back side. The legend indicates the depth relative to the front surface at which PL is performed (0 µm corresponds to the front surface and 2.6 µm to the back). The dashed lines represent the peaks' position, also reported in c) and d). Bottom: band gap profile determined from GDOES (black) and energies of the measured PL notch peak (red) and high energy peak (blue) at the different etching steps, from the front side c) and the back side d). The colored bars indicate the etching depth, including errors.

After the first etching step from the front side, about 400 nm of material is etched and the notch peak intensity increases by one order of magnitude. The low intensity of the non-etched absorber is attributed to the degraded surface after air exposure, which is a region of non-radiative recombinations [95,96]. Empirically, it is observed that a buffered absorber remains stable for months, whereas a bare one oxidizes in a few hours in the air, resulting in a decrease of the PL intensity by up to two orders of magnitude. It should also be noted that even though there is a steep band gap increase at the very front surface of the absorbers (although no indication of it has been detected in CL), the expected recombination, when no etching is performed, is still at the band gap minimum, due to carrier diffusion. As more of the material is

removed, the peak related to the notch recombination reduces in intensity, broadens and blueshifts slightly before disappearing entirely (see Figure 4.13a). This behavior correlates well with the trend in the band gap profile shown in Figure 4.13c. With the etching of the front side, most of the low band gap phase, which dominated the recombination before etching, is removed. Hence, recombination via phases of larger GGI becomes detectable, leading to the blueshift and broadening of the PL peak. On the other hand, before the notch peak disappears, the high energy peak, centered at 1.56 eV, is detected after 0.9 µm of the absorber is etched and remains at constant energy until only 300 nm of material are left. This is in contradiction to the smooth profile indicated by GDOES and in agreement with the CL observations which have already shown that some high band gap material is present in the bulk of the absorber and not solely at the back side.

To gain a better understanding of which contribution comes from what depth, the etching (as well as the PL measurement) is performed from the back side, thus conserving the notch at all times, and removing only the back part (see Figure 4.13b and d). Therefore, no shift of the notch emission peak is observed, as expected. In a similar manner as from the front side, as more of the material is etched away, the high energy peak remains at constant energy. Additionally, it gradually loses in intensity, while the notch peak's intensity increases, confirming that the high band gap phase is more present towards the back side of the absorber.

Moreover, an additional PL peak at about 1.2 eV is detected at intermediate depth, in the absorber's bulk (at depths 1.7 µm and 1.4 µm), as it can be seen in Figure 4.13b (yellow and blue spectra). This peak is attributed to a third phase of intermediate band gap, as already seen in CL spectroscopy (Figure 4.10, line profile ii)). In addition, the broadening of the notch peak (at depths 0.9 µm and 1.2 µm), when measuring from the front side, is another indication of the presence of this phase.

While CL provides information on the different band gaps present throughout the absorber on a micrometer scale, PL collects signal from a few hundred grains at once. Therefore, depth-resolved PL spectroscopy gives an average of the three

scenarios discussed in Figure 4.10, showing that mainly two or three individual phases with different GGI ratio are formed within the material. Transmission electron microscopy coupled with energy-dispersive X-ray spectroscopy (TEM-EDX) investigation has been conducted by Dr. Andrea Griesi and Dr. Giorgio Divititi at IIT [146], Genoa, Italy, on lamellae of the same sample as investigated by CL (cf. Figure 4.10). The experimental data was denoised using a non-negative matrix factorization (NMF) algorithm yielding results with high contrast and distinct spatial distribution of the key elements, in particular In and Ga. A sharp transition between a Ga-rich region (at the back) and an In-rich region (at the front) is observed in Figure 4.14. However, over the ~ 4 µm wide investigated cross-section, the frontier between the Ga-rich and In-rich regions is not flat (see blue dashed line in Figure 4.14b), supporting the idea of two distinct phases of different band gap coexisting at a given depth, as observed from CL and PL.

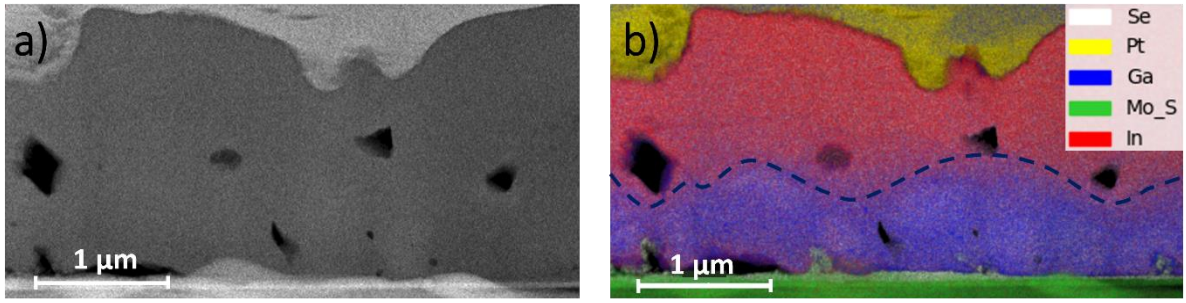

Figure 4.14. TEM image of the same sample as investigated by CL a). An overlay of the atomic composition (from EDX) is shown is b). In particular, the Ga (blue) and In (red) distributions dominate. Se (white) is homogeneously distributed. The S (sparse in the bulk) and Mo (back contact) have indissociable signals (green). Pt (yellow) is used as coating for reducing the charging effect during the measurement. The dashed blue line is a guide to the eye, following the separation between the Ga-rich and In-rich regions.

4.3.4. Challenging the current belief

As emphasized in section 4.1, most CIGS solar cells are based on a graded structure and a gradual increase of the band gap from the front side towards the back side is assumed, as provided by any depth-resolved elemental analysis. In the current study, the GDOES-based band gap profile (considering the GGI) would lead to a band gap gradient model as depicted in Figure 4.15a.

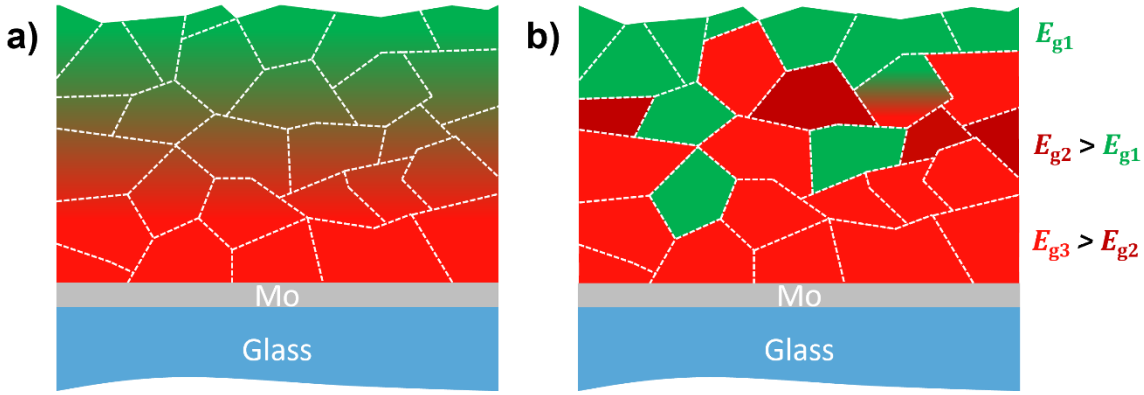

Figure 4.15. Model (not scaled) for band gap gradient a) as suggested from the GDOES profile (omitting the front gradient, in agreement with CL), and b) as proposed in this work, based on various characterization techniques. Green indicates a low band gap phase (E_{g1}), dark red an intermediate band gap phase (E_{g2}) and light red a high band gap phase (E_{g3}).

However, as demonstrated in the previous sections, a situation as depicted in Figure 4.15b seems more reasonable. In this representation, one grain shows one phase, with a few exceptions. A large density of high band gap phase (with E_{g3} dictated by the back side GGI) forms close to the back contact of the absorber. Contrastingly, a low band gap phase forms in high density towards the front side, generating the "notch" part of the absorber. In the bulk of the material, these two phases coexist, in different densities, giving rise to an apparent gradient in the GDOES profile. In addition to the two main phases, a sparse phase of intermediate band gap could be detected in the bulk, represented by the dark red color in Figure 4.15b. Finally, as observed by CL, some rare regions show a smooth band gap gradient as highlighted in Figure 4.15b.

The high band gap phase forming at the back side of the absorber, however, is of lower quality than the low band gap one and appears detrimental to the overall performance of the absorber, as is discussed in the next section.

4.4. Influence of the high band gap phase

Considering Figure 4.13b, as the back side of the absorber is etched past the steep Ga gradient and most of the high band gap phase is removed (last etching step from

the back side, at depth 0.3 µm), the notch peak's intensity increases by one order of magnitude. This strongly indicates that the non-radiative losses decrease when the back part is removed, i.e., that this part of the absorber provides undesirable recombination paths that are detrimental to the performance. A similar observation has been made based on carrier lifetime in graded CIGSe absorbers [132]. In fact, an increase of one order of magnitude in PL intensity translates into an increase of approximately 60 meV in quasi Fermi level splitting. Among the undesirable recombination paths, a broad PL contribution centered at about 0.9 eV is detectable from the back side, and from the front side after sufficient etching. Other chalcopyrite thin films studies reported on a PL emission at such low energy. Niki *et al.* [147] observe a broad peak at about 0.85 eV in Cu-poor and Cu-rich $CuInSe_2$ films. Mansfield *et al.* [148] conclude that in standard Cu-poor $Cu(In,Ga)Se_2$ a band-to-defect emission is detectable by PL spectroscopy at 0.79 eV. More recently, Siebentritt *et al.* [149] show that similar deep defect is also detected in sulfide chalcopyrites. Spindler *et al.* [36] report on a defect transition in $Cu(In,Ga)Se_2$ around 0.7 eV to 0.8 eV, for high GGI and low GGI, respectively. However, similarly to the observations in [147], they show that the transition is more pronounced in Cu-rich films than in Cu-poor samples. They also discuss deep broad transitions around 1.10 eV and 1.24 eV in $CuGaSe_2$ at 10 K that they tentatively attribute to Ga_{Cu} and $[Ga_{Cu}\text{-}2V_{Cu}]$, respectively [150]. In the present work, the 0.9 eV defect emission could be a combination of the 0.8 eV and 1.10 eV defects. Most importantly, this defect emission disappears as the back part of the absorber is etched away, hinting that these defects are associated to the high band gap phase, present in higher density at the back side. This disappearing of the defect emission could be the cause of the increase in PL intensity observed in Figure 4.13b after the last etching step. The two additional absorbers from Appendix A.3 have been gradually etched from the back as well, but with shorter etching steps past the steep Ga gradient. It shows more clearly that the low energy PL peak intensity gradually increases as the back side is etched away.

Nevertheless, alternative reasons for the PL intensity increase should not be excluded. In particular, according to the proposed model, the low and high band gap

phases intermix in the bulk, leading to a large interface area. When etching enough of the back side, less high band gap material is left in the remaining absorber, reducing therefore the number of interfaces between the two phases. This could in turn increase the PL intensity of the low energy peak, considering the interfaces to be prone to non-radiative recombination.

To quantify further the influence of the high band gap phase on the radiative efficiency of the absorbers, a large number of different CIGSSe absorbers is investigated. For all of them, absolute PL from both sides is measured (without etching). On the one hand, based on the measurements conducted on the front side, the non-radiative losses, $k_b T \ln(Y_{\mathrm{PL}})$, as defined in section 2.4.2, are calculated. On the other hand, based on the measurements from the back side, the relative contribution of the high energy peak to the notch peak is determined. In other words, the ratio of the integrated PL emission of the high energy peak and of the notch peak is calculated, as demonstrated in Figure 4.16b. It is referred to as "peaks ratio" in Figure 4.16a.

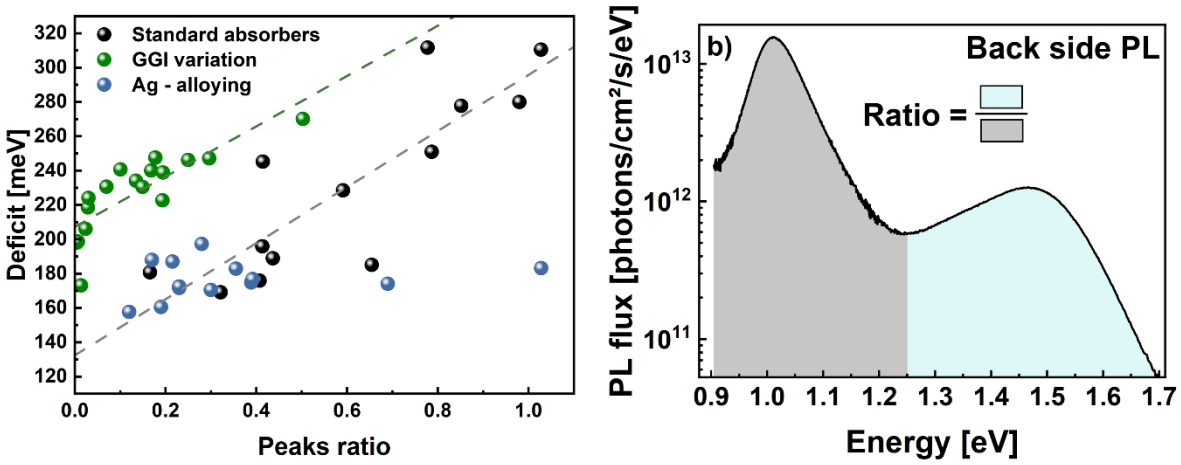

Figure 4.16. a) Non-radiative losses vs. peaks ratio for different CIGSSe absorbers. The gray dashed line is a linear fit of the "standard" absorbers (black data points), whereas the green dashed line is a fit of the "GGI variation" absorbers (green data points). The green and blue data points are added compared to [12]. The peaks ratio is calculated as the ratio of the integrated PL fluxes of the high energy peak and of the low energy peak, from measurements from the back side, as shown in b).

Non-radiative losses through Shockley-Read-Hall recombination have a direct impact on Y_{PL}. As a consequence, both, qFls and V_{OC}, are reduced by the same quantity $kT\ln(Y_{PL})$ [59]. Based on absolute PL investigation on absorbers, it is therefore possible to predict the losses in the device's performance.

Considering at first only the black data points in Figure 4.16a, a linear relation between the non-radiative losses and the peaks ratio is obtained (gray dashed line), demonstrating the negative impact of the high band gap phase on the absorber performance. High non-radiative losses are usually associated with high peaks ratio, and according to the fit, reducing the peaks ratio could lower these losses by up to 180 meV. However, as shown in Figure 4.17 for 5 representative "standard" absorbers from Figure 4.16, the intensity variation of the high energy peak is less strong than that of the notch peak. In the given example, between the peaks ratio 0.17 (black spectrum) and 0.79 (pink spectrum) the intensity of the high energy peak increases by a factor ~ 2, while the intensity of the notch peak decreases by a factor ~ 3. This indicates that the increase in the PL notch intensity participates strongly to the trend observed in Figure 4.16. Therefore, the origin of this behavior might not be solely related to the high band gap phase, but also to the quality of the low band gap phase.

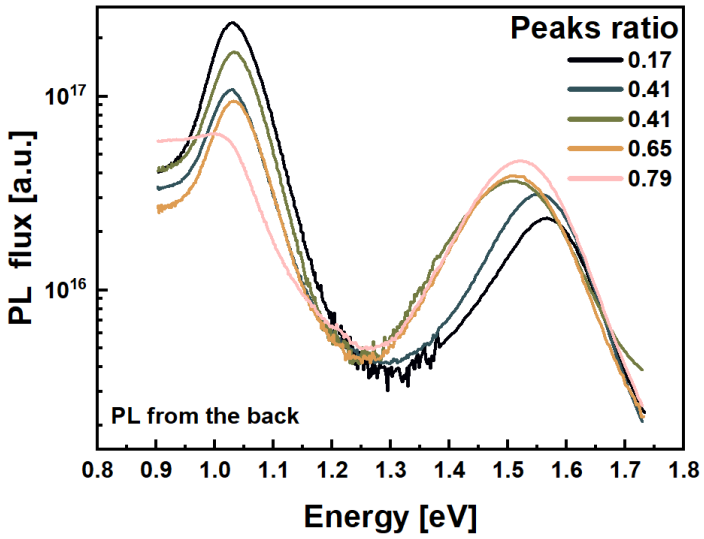

Figure 4.17. Non-absolute PL spectra of 5 "standard" absorbers from Figure 4.16a, measured from the back side after lift-off. The measurements are taken on the same day under the same experimental conditions and can therefore be compared. The peaks ratio (cf. Figure 4.16b) is indicated in the legend.

Now these statistics, as mentioned, are only based on the black data points, which represent the data available at the time of the corresponding publication [12]. These samples are based on "standard" absorbers, but with or without Na-PDT and with or without buffer. In general, the Na-treated absorbers have a lower peaks ratio and lower deficit, while the buffer tends to increase the measured deficit. The distinction between them is discussed in Appendix A.4. All the other data points in Figure 4.16a are bare absorbers and correspond to samples with GGI variations in the elemental stack (green data points) or alloyed with Ag (blue data points). While the Ag-alloyed samples follow the trend given by the "standard" absorbers, the samples with varying GGI fall on a line $60 - 70$ meV above the "standard" absorbers (indicated by the green dashed fit). It is reminded that the deficit is measured from the front side PL, largely dominated by the notch emission, and hence the quality of the low band gap phase dictates mainly the deficit. The "GGI variation" absorbers are not as optimized as the "standard" ones, what may be a reason for the higher deficit. It is important to note also that because the peaks ratio is defined from the back side PL after the lift-off, the quality of the latter, e.g. the cracks in the layer, can affect how much of the low band gap phase is detected. Therefore, while the back side has been undoubtedly proven to be detrimental to the absorber performance, it is not the sole origin of an overall higher deficit.

4.5. Summary

In this chapter, the common view of the band gap gradient in CIGS absorbers has been challenged. In particular, industrial $Cu(In,Ga)(S,Se)_2$ absorbers were investigated and based upon to design a new gradient model. It has been demonstrated that the back side (and/or the interface between the different phases) of graded CIGSSe absorbers is a source of non-radiative recombination and therefore a limiting parameter for the absorber performance. Depth-resolved photoluminescence spectroscopy reveals that two main radiative recombination paths compete: one at about 1.04 eV, corresponding to recombination in the low band gap phase and one around 1.56 eV, attributed to recombination in the high band gap phase. At intermediate depth into the bulk of the absorber, a third recombination path may sometimes be detected, indicating the presence of a sparse phase of band gap around 1.2 eV. Raman and cathodoluminescence spectroscopy confirm the formation of multiple phases and

locate the low (high) band gap phase close to the front (back) side. It is therefore proposed that the band gap gradient is not a gradual band gap increase from the front side towards the back side, but rather that two main phases of low and high band gap form, with the low band gap phase predominantly near the front and the high band gap phase predominantly near the back. The interlacing of these two phases in the bulk of the material produces the apparent gradient one can measure from an elemental profile, e.g. by GDOES.

In addition, a broad defect band centered around 0.9 eV is detected and associated with the high band gap phase. A tentatively proposed origin is a combination of two deep defects, one around 0.8 eV, commonly observed in selenide and sulfide chalcopyrites, and another one around 1.1 eV, as detected in CGSe. By etching the back side of the absorber until most of the high band gap phase is removed, a strong increase of one order of magnitude in the PL intensity of the notch peak is achieved, which translates into an increase of 60 meV in quasi Fermi level splitting. Furthermore, the non-radiative losses correlate linearly with the relative intensity of the high energy PL peak compared to the notch PL peak. While the peaks ratio is influenced by many parameters (quality of the low band gap phase, density of the high bandgap phase, lift-off quality), it is shown that in the "standard" absorbers, a decrease of the non-radiative losses of up to 180 meV could be expected by reducing this ratio.

As discussed in the next chapter, Ag-alloying affects the elemental redistribution in the absorbers and can influence the band gap gradient, leading to a smoother transition from the low band gap phase towards the high band gap one.

Chapter 5

Improved sequentially processed $Cu(In,Ga)(S,Se)_2$ by Ag-alloying

It has been demonstrated in the previous chapter that industrial CIGSSe absorbers grown at AVANCIS feature band gap jumps, rather than a smooth transition from a low to a high band gap. In this chapter, it is discussed how Ag-alloying in such absorbers helps to smoothen the band gap gradient. Most of the presented results have been previously published in reference [13]. Certain paragraphs are taken verbatim, with only minor modification, and can be identified by the **different font style** in which they are written. **While previous research predominantly focuses on selenide absorbers, the literature on sulfur-selenide absorbers alloyed with Ag remains to this day relatively sparse. The aim here is to bridge this gap by investigating how Ag incorporation affects the elemental composition and performance of $Cu(In,Ga)(S,Se)_2$ absorbers**. A brief review of the current state of the art in ACIGS solar cells is given in section 5.1. The consequences of Ag on the absorbers' morphology are investigated in section 5.2, while section 5.3 deals with the resulting enhanced elemental interdiffusion. Finally, the performance improvement (or not) of the bare absorbers is discussed in section 5.4 by absolute PL and complemented by IV measurements on the corresponding finished cells. A summary of the chapter's main results is provided in section 5.5.

5.1. State of the art

At the time of writing this thesis, the best PCE for CIGS solar cells is achieved with a $Cu(In,Ga)Se_2$ absorber, in which 19% of the Cu is replaced by silver (Ag) [26], commonly

referred to as ACIGS. It is generally observed that Ag improves the optoelectronic quality of the CIGS solar cells [151], in particular leading to V_{OC} increase. As reported in previous studies [152,153], alloying CIGS with Ag leads to a downshift of both the conduction band minimum (CBM) and the valence band maximum (VBM) compared to the pure Cu-based absorbers. This property, combined with an appropriate tuning of the GGI, offers the possibility to accurately design the band edges position, i.e., modify the electron affinity, in order to optimize the interface absorber/buffer while conserving the desired band gap. As discussed in section 2.1.3, a small "spike" – like interface between the conduction bands of the absorber and the buffer is preferred. First-principles calculations from [152] predict the band gap and band edges evolution for a selection of GGI and AAC ([Ag]/([Ag]+[Cu])) ratios (see Figure 5.1). As shown in Figure 5.1b, the VBM decreases first slower than the CBM until a certain AAC is reached and the opposite happens. Hence, for a given GGI, as displayed in Figure 5.1a, this results in a decrease of the band gap for low AAC followed by an increase for higher AAC. Depending on the GGI, the change in band gap is more or less pronounced. According to the calculations shown in Figure 5.1, a relatively small amount of Ag (AAC < 0.25) has a stronger effect (decrease of E_g) on a wide band gap material than on a lower band gap one, whose E_g is barely affected at low AAC. Boyle *et al.* [154], however, determine experimentally (from optical transmission measurements) the band gap of several ACIGSe absorbers with varying Ga and Ag contents and show that for AAC $\leq$ 0.27, the band gap of absorbers with GGI $\leq$ 0.5 slightly increases ($\Delta E_g < 0.05$ eV), whereas it slightly decreases for GGI $\geq$ 0.8. From a multiple linear regression of their experimental data, the authors do not expect any significant decrease of the band gap, even at low AAC and high GGI, as suggested from the first-principles calculation shown in Figure 5.1.

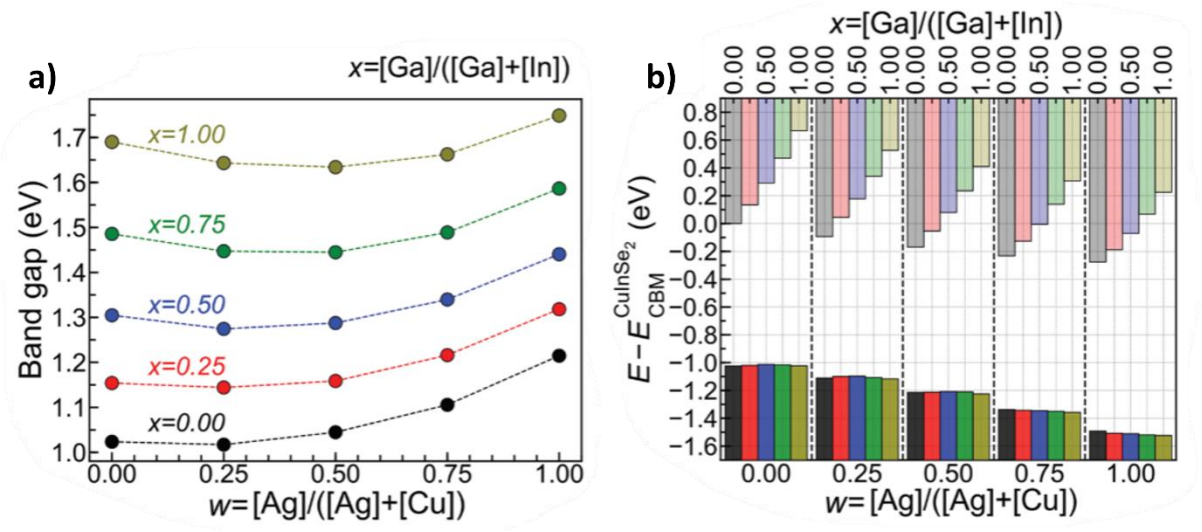

Figure 5.1. First-principles calculations of a) the band gap of ACIGS absorbers depending on the GGI and AAC ratios and b) the corresponding energy of the conduction band minimum (CBM) compared to the one of pure CISe (GGI = AAC = 0). The figure is reproduced from [152] with permission.

Growing Ag-based solar cells has been done for nearly two decades already. In 2005, Nakada *et al.* [155] achieved a 9.2% PCE for a 1.7 eV band gap Ag(In,Ga)Se_2 solar cell. More recently, several studies reported on alloying Ag with wide band gap Cu(In,Ga)Se_2 (ranging from $E_g = 1.24$ eV to $E_g = 1.46$ eV) during co-evaporation [32,156–159], improving the performances mostly by increasing the V_{OC}, compared to Ag-free CIGS of similar band gap. Improving such wide gap material would be interesting for multi-junction devices. At the same time, the effect of Ag-alloying is also actively investigated in lower band gap Cu(In,Ga)Se_2 [130,160–163] (ranging from $E_g = 1.02$ eV to $E_g = 1.18$ eV), showing promising performance.

Leading to a lower melting temperature than the pure Cu compounds for both selenides and sulfides [19], alloying with Ag offers the possibility to process the absorbers at lower temperature, which represents a great advantage from an industrial point of view. Alternatively, growing at similar temperatures as the Ag-free compound, the grain size can be increased [159] and lattice distortion may be reduced, as simulated by Zhang *et al.* [164] in selenides. The presence of Ag in the crystal lattice has the following reported effects: deep defects may be passivated in low band gap absorbers [165], an improved morphology is widely observed, translated

into an increase of the grain size [159] and a smoother surface [130,163] is commonly obtained. The latter point could be a consequence of the increase in grain size, that leads to larger flat surface areas. In the case of Ag-PDT [130], it is speculated that the decrease in surface roughness results from the generation of the liquid Ag – Se phase during the PDT. In addition, a reduction of the doping – hole density – as well as an improved current collection are systematically reported and attributed to a widening of the space charge region [162]. However, there exists no universal recipe for alloying CIGS absorbers with Ag. For instance, Ag may be introduced as PDT, co-evaporated at different stages in the growth process or as sputtered elemental precursor (as is the case here); all methods potentially leading to substantial improvements. Also, the optimum amount of Ag depends strongly on the composition of the host material, i.e., the GGI and the ([Ag]+[Cu])/([Ga]+[In]) (or I/III) ratios. Therefore, large discrepancies are observed in the literature regarding the nominal composition of the reported best performing cells, e.g. AAC $= 0.045$ in [165], AAC $= 0.16$ in [156] or AAC $= 0.5$ in [152].

Mori *et al.* [166] reported on Ag-alloying in pure sulfide Cu(In,Ga)S_2 absorbers (of band gaps ranging from 1.54 eV to 1.66 eV). Their best performing cell, compared with the Ag-free reference of same band gap, showed an improved absorber morphology and larger short circuit current (J_{SC}), but also a lower V_{OC}, which ultimately led to a decreased cell efficiency. Cheng *et al.* [167] tried a different approach and first prepared a (Ag,Cu)(In,Ga)Se_2 solar cell that showed better crystal structure and larger band gap compared to the Ag-free reference ($E_g = 1.02$ eV vs $E_g = 0.98$ eV) and subsequently sulfurized the absorber, forming (Ag,Cu)(In,Ga)$(S,Se)_2$ which further improved the performance (and led to $E_g = 1.22$ eV).

In the following sections, industrial CIGSSe absorbers with different (low) amounts of Ag, introduced as precursor in the elemental stack, are prepared as indicated in section 3.1. Some absorbers are grown with the same elemental stack precursor but differ in the introduced amount of Ag, and further absorbers are produced with a fixed AAC but slightly different GGI. Nevertheless, the I/III ratio is kept constant at ~ 0.96 for all variations. While the precise atomic percentage of Ag cannot be disclosed, the AAC remains below 0.1, even for the highest Ag content (AAC-3 in Table 5.1). Two series are considered (cf. Table 5.1). The first one

contains eight absorbers, three of them (samples Ag-1, Ag-2 and Ag-3) are grown with the same elemental stack GGI as the reference (Ref-1) but with increasing Ag content. In addition, four samples of intermediate Ag content (AAC-2) but lower GGI are prepared (samples Ag-2.1 – Ag-2.4). Reducing the GGI has been demonstrated beneficial in other studies (cf. chapter 4) and leads to further improvement in the present one, as discussed in section 5.4. The GGI in the precursor stack of sample Ag-2.1 is lower than the one of the reference and is further reduced for the samples Ag-2.2, Ag-2.3 and Ag-2.4. Samples Ag-2.2 and Ag-2.3 are identical from a composition point of view, but the temperature of the RTP of the second one is reduced. Finally, the sample Ag-2.4 is grown with a reduced Na content in the precursor stack. Encouraged by the low non-radiative losses measured in samples Ag-2.2 and Ag-2.3 (see section 5.4 below), a second series has been developed, based on the lowest GGI in the precursor stack. Ref-2* does not contain any Ag and samples Ag-1* – Ag-3* have similar AAC variation as the first series (cf. Table 5.1). The investigation of this second series is new to this chapter, i.e., not part of the aforementioned publication [13].

Table 5.1. List of the samples from this chapter. Two series are prepared, the ([Ag]+[Cu])/([Ga]+[In]) ratio of the first one is kept constant for all samples at I/III ~ 0.96. The second series present the same

three Ag variations as series 1 but with the lowest GGI ratio in the precursor stack. Samples Ag-2.2 and Ag-2* should be identical.

Series	Sample	GGI	AAC	Description
Series 1	Ref-1	**GGI-3**	**No Ag**	Reference
	Ag-1		**AAC-1**	Lowest AAC
	Ag-2		**AAC-2** > AAC-1	Intermediate AAC
	Ag-3		**AAC-3** > AAC-2	Highest AAC
	Ag-2.1	**GGI-2** < GGI-3	**AAC-2**	Intermediate AAC Intermediate GGI
	Ag-2.2	**GGI-1** < GGI-2		Intermediate AAC Lowest GGI
	Ag-2.3			Intermediate AAC Lowest GGI Lower process temperature
	Ag-2.4			Intermediate AAC Lowest GGI Lower Na in elemental stack
Series 2	Ref-2*	**GGI-1**	**No Ag**	Reference
	Ag-1*		**AAC-1**	Lowest AAC
	Ag-2*		**AAC-2**	Intermediate AAC
	Ag-3*		**AAC-3**	Highest AAC

5.2. Absorber morphology

As reported in the literature [166,168], the absorber's morphology is affected by the presence of Ag in the crystal. SEM imaging of the top surface and cross-section of the samples allows for visualization of these changes. Figure 5.2 shows the SEM images for the reference sample and the samples Ag-1 and Ag-3 (lowest and highest Ag content). From the cross-section images (Figure 5.2 bottom) an overall increase in the grain size is observed as more Ag is added, compared to the reference sample. With the highest Ag content, grains larger than 2 µm (laterally) are obtained. As mentioned already, this is expected since Ag has a lower melting point than Cu and thus growing $(Ag,Cu)(In,Ga)(S,Se)_2$ at similar temperature as the pure Cu-compound results in larger grains [19]. Moreover, in the reference sample, a layer of fine grains is present near the back contact. With larger amounts of Ag, the size of these fine

grains increases until no strong contrast between them and the bulk ones is visible anymore. This is consistent with the observations reported by Wang *et al.* [130].

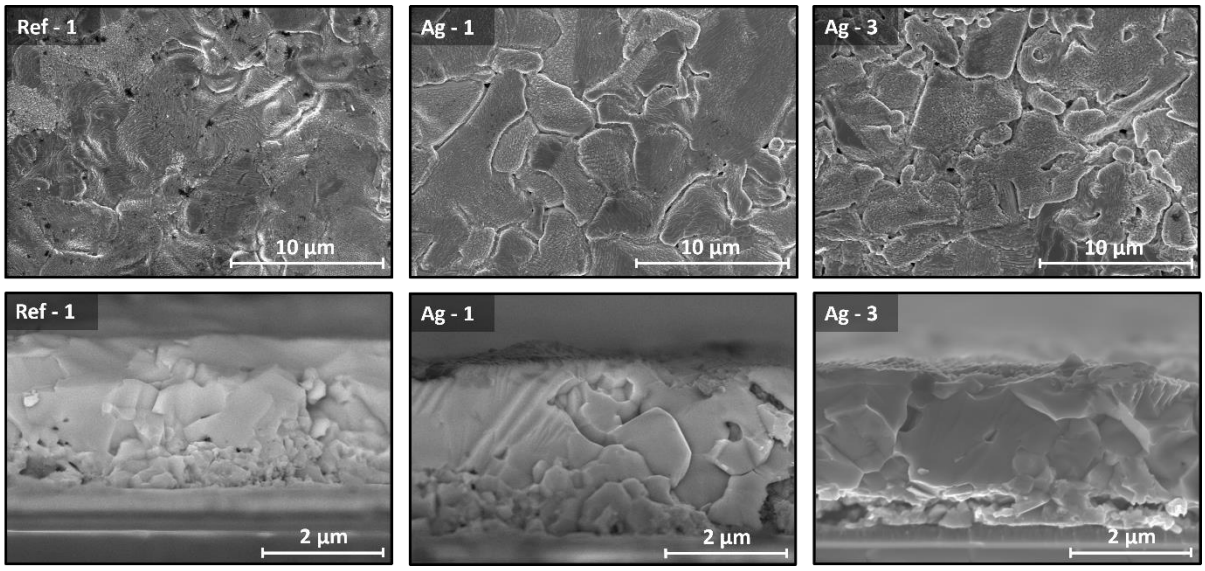

Figure 5.2. Scanning electron microscopy (SEM) images of top view (top) and cross-section (bottom) of the reference absorber, containing no Ag, and two absorbers from series 1 with low Ag content (Ag-1) and high Ag content (Ag-3). The sample Ag-3 is slightly detached from the substrate, most probably due to imperfect cleaving.

The top view SEM images (Figure 5.2 top) also reveal morphology modifications with added Ag. The reference sample exhibits a relatively smooth surface. However, with the lowest Ag content (Ag-1), crevices appear on the surface and further adding Ag (Ag-3) leads to an increased density of these crevices. Essig *et al.* [169] reported similar features in co-evaporated (Ag,Cu)(In,Ga)Se_2 absorbers, speculating that these crevices are related to the agglomeration of Ag on the surface during deposition. However, they show that the crevices remain shallow or inexistant for low Ag contents (AAC ~ 0.05) and do not impact the cell performance. Would the crevices be deep enough to connect with the back contact, the shunt resistance would tend to zero and the device would not work at all. With the low Ag contents used in this thesis, the crevices are relatively shallow (~ 600 nm deep) as shown in Figure 5.3 for the samples Ag-1 and Ag-2. Furthermore, they seem to be non-detrimental to the bare absorber performance, as evaluated by calibrated PL (see section 5.4.1).

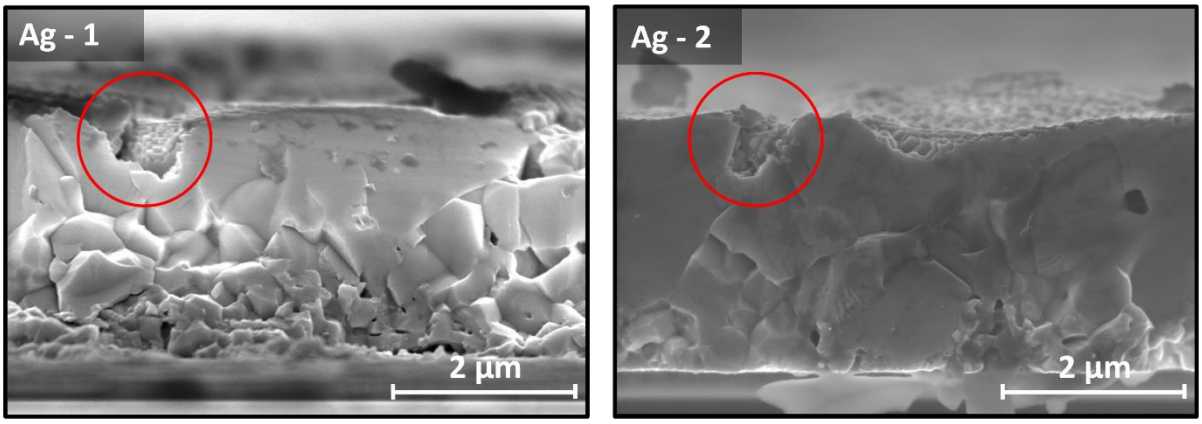

Figure 5.3. SEM cross-section images of the samples Ag-1 and Ag-2 featuring crevices (circled in red) as mentioned in the text. The crevices are about ~ 600 nm deep in these two examples.

As mentioned in chapter 4 section 4.2.2, the lift-off of the absorbers from their substrate leads to an imperfect back surface. Back surface SEM images of samples displayed in Figure 5.2 are shown in Figure 5.4. From the bottom row micrographs in Figure 5.4 it can be seen that the grain size significantly increases in sample Ag-3, supporting the previous statement that the fine grains at the back side of absorbers are reduced when adding Ag. The long cracks present on the back side of sample Ag-3 (Figure 5.4 top right) are believed to arise following the lift-off rather than originating from the crevices on the front surface, as no particular shunting of the cell has been observed.

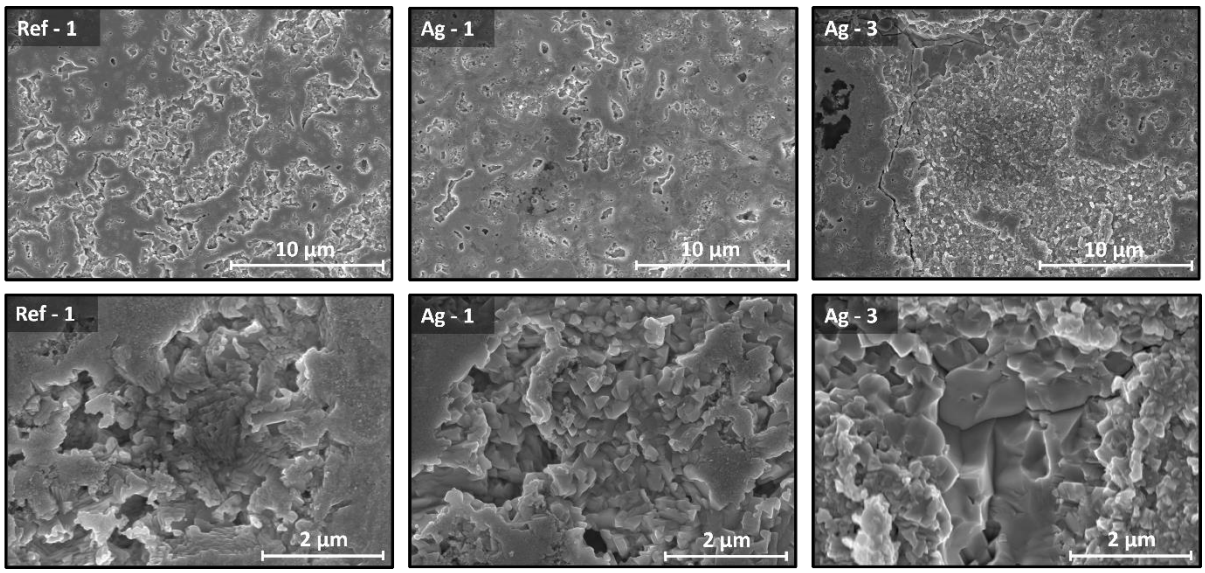

Figure 5.4. SEM top view images from the back side of samples Ref-1, Ag-1 and Ag-3 after lift-off. The top row shows a large view of the back side of the absorbers, while the bottom row provides a closer view (of a different region), as indicated by the scale bars.

5.3. Elemental interdiffusion

In this section, the enhanced vertical interdiffusion of In and Ga upon Ag alloying is discussed based on a compositional analysis by GDOES and further supported by PL and CL measurements. Nevertheless, despite the smoother band gap gradient resulting from the elemental interdiffusion, a significant lateral inhomogeneity is observed in the Ag-alloyed absorbers.

5.3.1. Effect on GGI

The in-depth composition of the absorbers has been investigated by GDOES and the GGI profiles of the four first samples from the series 1 and the series 2 (cf. Table 5.1) are reported in Figure 5.5a and b. The absorbers from each series shown in Figure 5.5 have all the same GGI in the precursor stack. It is observed that upon addition of Ag, the GGI profiles flatten. The overall GGI at the notch position ($E_{\mathrm{g,min}}$, from ~ 100 nm to ~ 700 nm) increases from about 0.10 to 0.20 for the two series while the GGI at the back (averaged over the last 400 nm) decreases from about 0.89 to 0.77 for the series 1 and from 0.80 to 0.75 for the series 2. Such flattening of the GGI profiles

has been reported in low and high band gap Ag-alloyed chalcopyrites [152,163]. This suggests that Ag enhances the interdiffusion of Ga and In, as reported in [170]. According to the gradient model proposed in chapter 4, no gradual evolution of the band gap exists in the absorber, but instead two phases of low and high band gap form at the front and back sides and interlace in the bulk. Therefore, comparing the GGI profiles of the Ag-alloyed absorbers with the respective reference (Figure 5.5a and b), a low band gap phase of higher E_g is expected towards the front surface, and a high band gap phase of lower E_g is expected near the back contact. This is discussed in more details in sections 5.3.2 and 5.3.3. The absorbers from series 1 have been probed on four different spots, while the ones from series 2 on only two different spots. They all yield very similar profiles, attesting to the homogeneity of the samples. Exception is the sample Ag-3 from series 1 for which the greatest discrepancies have been observed, as shown in Figure 5.5c. Since no such inhomogeneity (based on two spots) has been observed in the sample Ag-3* (with the same AAC as Ag-3 but lower GGI), it is difficult to conclude if higher Ag content generally reduces the lateral homogeneity or if specifically sample Ag-3 presents a strong lateral inhomogeneity.

It has been demonstrated that diffusion of Ga and In in CIGSe occurs through Cu vacancies [171,172]. Based on the diffusion model proposed by D. Colombara [173], atom diffusion (in particular, Ga and In) may be enhanced or hindered by the presence of dopants, depending on the concentration of dopant and of vacancies. Because Ag occupies the same sites as Cu, it may reduce the concentration of copper vacancies V_{Cu} (provided that the I/III ratio changes) and, in too great amounts, alter the diffusion, leading to compositional inhomogeneities, as observed in Ag-3. As indicated in section 5.1, however, no significant change in the I/III ratio is measured from XRF, suggesting that the inhomogeneities arise from a different origin.

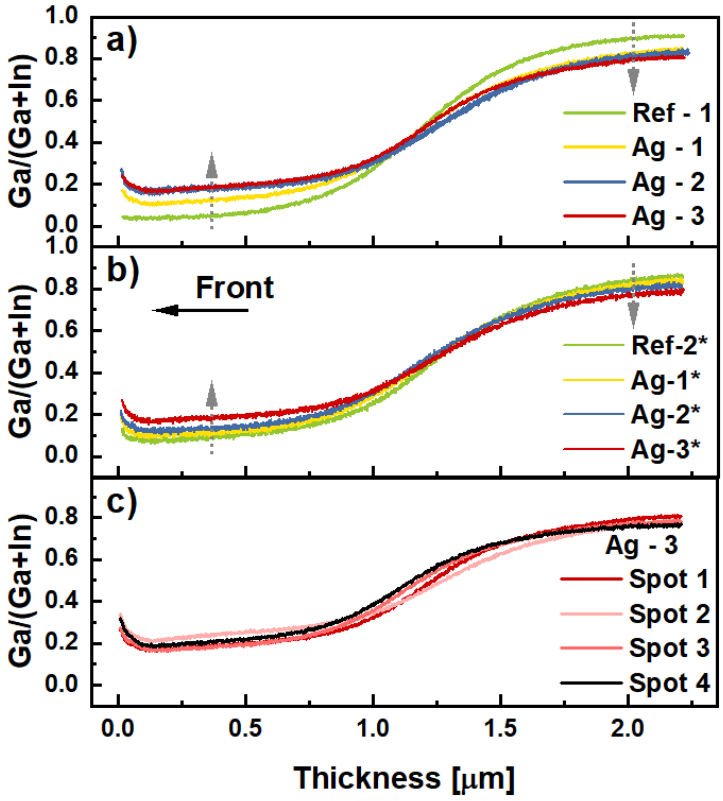

Figure 5.5. GGI profiles as measured by GDOES for the first four absorbers of the series 1 a) and of the series 2 b). With increasing Ag content, the profiles flatten. c) GGI profiles for the sample Ag-3 (series 1), taken on four different spots, labelled spot 1 – 4. Spot 1 is the one shown in a). All the other absorbers showed nearly superposable profiles on the four (or two for series 2) different probing spots.

The lateral inhomogeneity of the sample Ag-3 is confirmed by Raman spectroscopy. Figure 5.6 displays the spectra obtained from the front side of the samples Ag-1 (b), Ag-2 (c) and Ag-3 (d) on different spots, compared to the reference sample Ref-1 without Ag (a). The latter shows two main peaks, associated to the A-like symmetry modes of the Se-Se and S-S vibrations, at 179 cm^{-1} and 292 cm^{-1}, respectively [137,138]. The samples Ag-1 and Ag-2 (lowest and intermediate Ag contents) yield the same two peaks, showing no significant difference to the reference sample, although a very low intensity of the S-S related peak is registered for Ag-2. The very small shift of the Se-Se peak in sample Ag-2 may be attributed to the measurement's uncertainty. However, in the case of the sample Ag-3 (highest Ag content), the two peaks are shifting significantly in energy between different positions while scanning the

surface. No significant broadening of the peaks is measured, hence giving no indication of potential double peaks. The Se-Se peak shifts from 179 cm^{-1} to 184 cm^{-1} together with the S-S peak from 292 cm^{-1} to 298 cm^{-1}. Such a shift is usually associated with increased Ga content [144]. Thus, this observation could indicate the formation of ACIGSSe phases of higher Ga content close to the surface in addition to the same low gap phase as the reference (producing the peaks at 179 cm^{-1} and 292 cm^{-1}). The formation of phases of higher band gap contributes to the increase in the GGI ratio observed towards the front side, at least for the sample Ag-3.

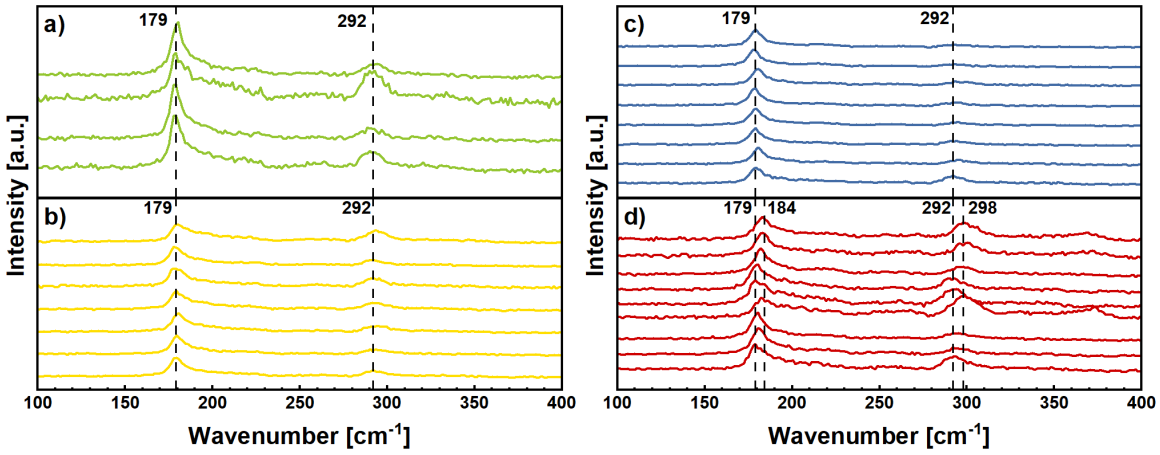

Figure 5.6. Raman spectroscopy performed from the front side of the reference sample (series 1) a) and the samples Ag-1 to Ag-3 b) – d). Each spectrum corresponds to a different spot (of diameter 2 µm) on the sample (considering an area of ~ 100×100 μm^2). The spectra are normalized to the Se-Se peak and manually shifted for clarity.

It is usually observed that (Ag,Cu)(In,Ga)Se_2 solar cells have a low tolerance to (Ag,Cu)-poor off-stoichiometry composition [174] leading to the formation of OVC. Keller *et al.* show that OVCs form for I/III ratios < 0.97. Above this value, other secondary phases start appearing as stoichiometry is approached. Both OVC and secondary phases are detrimental to the device performance [32]. In this study, despite the relatively low I/III ratio (~ 0.96), no OVC signature (at 155 cm^{-1}) in the Raman spectra is present in either sample.

5.3.2. PL spectra evolution upon Ag-alloying

The bare absorbers from the two sample series are investigated by absolute PL from the front and back sides (see Figure 5.7a – c). While five spots are measured from the front side and three are measured from the back side, only one spectrum for each sample is shown in Figure 5.7a – c, as no major difference exists between the different spots. The discussed values, such as the qFls, are averaged over the various spots and the standard deviation is taken as the error. A soft KCN etching is performed before measuring from the front side to remove oxides and refresh the surface after the absorbers have been exposed to air (cf. section 3.1). The back side is accessed after performing the lift-off of the absorber from its substrate, thus providing a fresh back surface and does not require any additional etching. PL spectra provide information about the recombination activity in the material. The reference sample from series 1 (Ref-1) is a CIGSSe absorber with a band gap around 1.05 eV. Therefore, a dominant PL peak is expected at this specific energy and is attributed to band-to-band recombination. As already deduced from the Raman analysis, the Ag-alloyed samples have the same low band gap phase as the reference. The PL analysis confirms it since the similar emission around 1.05 eV is observed for the samples of series 1 from the front side (see Figure 5.7a and b). This is coherent with the theoretical band gap predictions for selenides computed in [152] for both low Ga and low Ag contents. Only the sample Ag-2 (series 1) shows a band-to-band emission of substantially higher energy (1.080 eV). This specific sample, of intermediate AAC, behaves as an outlier and is the only one that exhibits no improvement in the non-radiative losses compared to the reference sample (cf. section 5.4.1). On the other hand, according to the GGI profiles in Figure 5.5 it is expected that with added Ag the notch energy increases. For the sample Ag-3, which has similar PL notch energy as the sample Ref-1, the larger notch GGI can be attributed to the presence of the high band gap phase close to the front surface (as seen from Raman). However, no such inhomogeneities have been observed for the sample Ag-2 and thus hints that the low band gap phase forming close to the front side (cf. chapter 4 section 4.3.4) has a larger band gap energy than the other absorbers form series 1.

Having a lower GGI in the precursor stack, the reference sample from the series 2 (Ref-2*) shows a band-to-band PL emission peak around 1.04 eV. Contrary to the series 1, the emission peak blueshifts upon Ag alloying to 1.05 eV, 1.06 eV and 1.08 eV, respectively (cf. Figure 5.7c), in line with the GGI profiles from Figure 5.5b.

Additionally, for the highest Ag content of series 1 (Figure 5.7a, Ag-3), a shoulder is detected at higher energies (~ 1.25 eV) from the front side and suggests the presence of an alternative recombination channel. The possibility of forming OVCs and/or secondary phases is discussed extensively for high band gap ACIGSe in [174], reporting principally the formation of 1:3:5 OVCs ($(Ag,Cu)(Ga,In)_3Se_5$) at the front and back interfaces for I/III off-stoichiometry absorbers. Close to stoichiometry, the authors observed the formation of sparse Ag_9GaSe_6 grains, which are, however, mainly expected for above stoichiometry compounds. In the present case, despite the relatively low I/III ratio, only (A)CIGSSe phases and no OVC phases were detected from Raman spectroscopy, suggesting that the shoulder in the PL comes from an (A)CIGSSe phase of higher GGI than the low band gap phase. The formation of this additional phase reinforces the statement that Ga diffuses more with Ag alloying. No such shoulder is observed from the front side for the series 2, for which the overall GGI is reduced. Nevertheless, from the backside, in addition to the low and high energy peaks, a third emission peak at ~ 1.32 eV is measured in the sample Ag-3*, indicating the possibility of the formation of intermediate phases at higher Ag content.

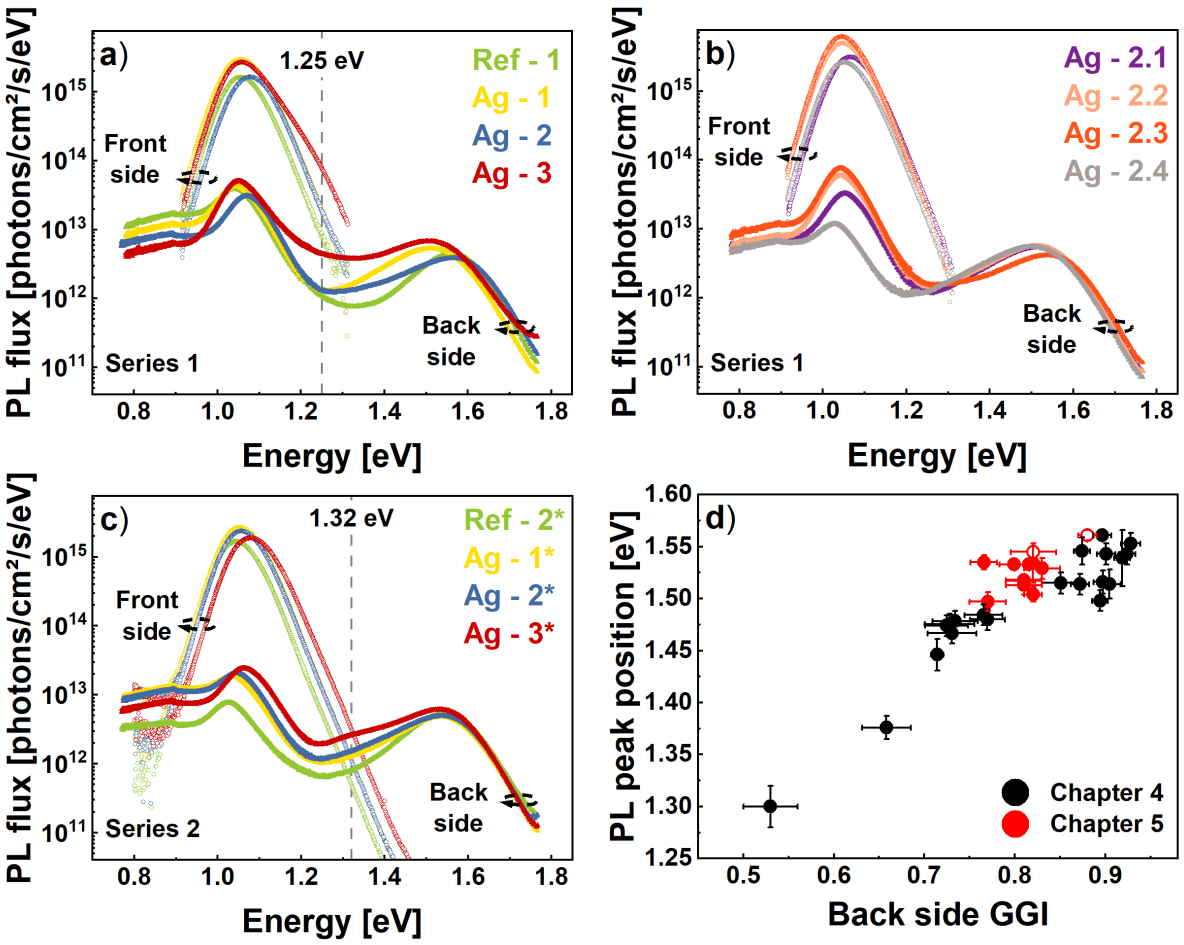

Figure 5.7. Absolute PL measured from the front (open circles) and back (full triangles) sides of the two series of absorbers (cf. Table 5.1). The scales in a) – c) are identical allowing for better comparison. No high energy peak is observed from the front side and the part where $E > 1.3$ eV is not measured for the series 1. The peak position of the high energy emission vs. the back side GGI is given in d). The black dots are data points from chapter 4 and the red ones are from the present series 1 and 2. The open red dots are the reference samples Ref-1 and Ref-2*.

All measurements from the back side reveal two main emission peaks. The one at low energy corresponds to the notch emission, similarly as from the front side measurement. For both series, it is detected at the same energy from both the front and back sides of a given absorber, indicating a common origin, i.e., the low band gap phase. The second PL peak (at higher energy) arises from the high band gap phase forming principally near the back side (cf. chapter 4). The notch PL intensity is lower by almost 2 orders of magnitude compared to the front side, what could be explained with the same arguments as provided in section 4.2.3 (second recombination

channel, imperfect lift-off, back side generally of lower quality). Although the four absorbers in Figure 5.7a were grown with the same amount of Ga and In precursors, the band gap of the high gap phase, dependent on the GGI at the back side, reduces with increasing Ag content (from 1.56 eV to 1.49 eV). Furthermore, the valley between the two main peaks becomes shallower for higher Ag content and the same shoulder at ~ 1.25 eV is detected for the sample Ag-3. This supports the earlier claim that the diffusion of Ga is enhanced by Ag alloying and additional evidence is provided by CL in the next section. The relation between the back side GGI and the PL maximum of the high band gap phase follows well the trend previously observed in chapter 4 (see Figure 5.7d). The four absorbers from the series 2, despite the different Ag contents, do not show significant changes in the emission energy of the second peak (from 1.55 eV to 1.53 eV), nor in the depth of the valley, suggesting a weaker influence of Ag on the high band gap phase in this series.

The same broad PL contribution is observed below 0.9 eV (from the back side) in all cases and attributed to deep defects associated to the high band gap phase, as discussed in section 4.4.

5.3.3. Smoothening of the band gap gradient

In the previous sections, interdiffusion of Ga and In, as well as lateral inhomogeneity arising upon Ag alloying have been discussed. This section focuses on CL performed on the cross-section of the absorbers (of series 1) Ag-3 and Ag-1 (in Figure 5.8 and Figure 5.9, respectively) and provides further evidence of the above-mentioned observations. A CIGSSe absorber similar to the reference Ref-1 has already been investigated in chapter 4 and some of the major results are reproduced in Figure 5.8. A spectrum is measured for each pixel in the CL measurement, creating the hyperspectral dataset. The corresponding panchromatic emission intensity is depicted in Figure 5.8b and the emission energy of the intensity maximum is reported in Figure 5.8c. It is important to repeat that the CL measurements were performed using an uncorrected silicon CCD detector. This detector is characterized by a significant reduction in detection efficiency towards the lower measured energies.

Measurement performed by an InGaAs diode array, with enhanced sensitivity at the low energy scale is provided in Appendix B.1 and shows a brighter front side and lower emission energy, as expected. This explains the lower intensity of the signal near the front surface (Figure 5.8b), as well as the discrepancy between CL and PL about the energy of the luminescence maximum of the low band gap phase (1.05 eV from PL and 1.15 eV from CL) since PL utilizes a spectrally corrected InGaAs detector in this range. When measured with the suitable detector (Si for visible and InGaAs for IR), the CL emission energy agrees with the one measured from PL.

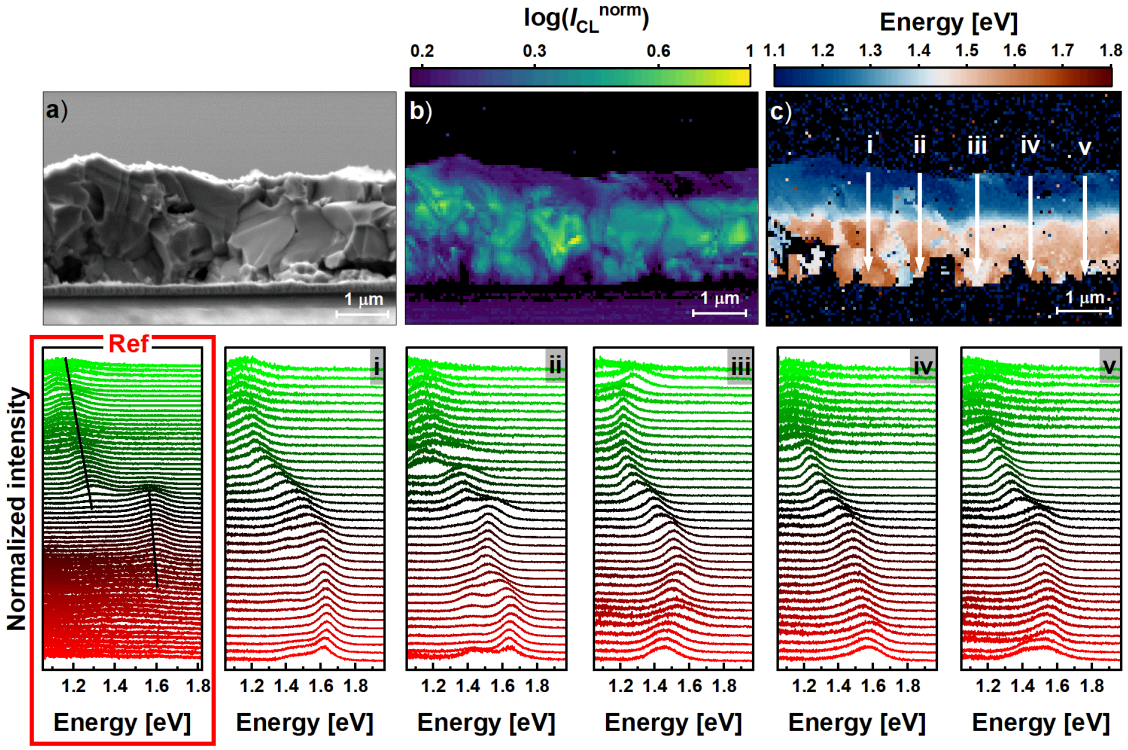

Figure 5.8. Cathodoluminescence spectroscopy on the cross-section of the sample Ag-3 (series 1). The top row shows the SE image of the region of interest a), the normalized intensity map of the panchromatic luminescence in logarithmic scale b) and the colormap of the energy of the maximum of the CL emission c). The bottom row displays the individual spectra along the lines i-v drawn in c). The leftmost graph in the bottom row is reproduced from Figure 4.10 (line profile iii) and corresponds to the most typical emission observed in the reference sample. The black lines are a guide to the eye. All the spectra are normalized to the maximum of the emission and shifted for clarity.

Although each pixel in the colormaps is of one single color, the transition from one E_g to the other is often not sharp and two peaks are visible, but only the energy of the dominant one is displayed.

A sudden jump in emission energy from the low band gap phase to the high band gap phase has been the most frequent observation in section 4.3.2 and an example is given in Figure 5.8 (red-framed graph). From the front surface towards the back contact, E_g increases only slightly until a certain depth in the bulk where a jump to a higher E_g occurs. It is visible from the two peaks present in the spectra at this depth and highlighted by the black lines. This led to the conclusion that in graded absorbers, there is no smooth band gap gradient, but instead that a low band gap phase forms towards the front, a high band gap phase forms towards the back, and the two phases interlace in the bulk of the material. Similar behavior is observed for the line profile ii in Figure 5.8, although it is not the most common situation. Indeed, the line profiles i and iii-v reveal a smoother gradient from the front side to the back side, suggesting that Ag improves the gradient behavior, i.e., less energy jumps and smoother shifts, likely by Ga and In interdiffusion. However, close to the back side, several line profiles (e.g. line profile **iii**) display a reversed gradient: the band gap reduces when reaching the Mo back contact. This is especially bad since such a gradient would drive the electrons towards the back side, instead of driving them away from it.

As seen in Figure 5.9, the reverse gradient is also detected in some line profiles of the sample Ag-1 (lowest Ag content). However, this sample shows more of the jump-like gradient, e.g. line profiles **v** and **vi** in Figure 5.9. In addition, areas of different band gaps within very small distances indicate a certain inhomogeneity, also highlighted by the many spectra featuring double peaks along the line profiles. While this vertical inhomogeneity seems to be reduced with higher Ag content (only few double peaks observed in Figure 5.8), both samples Ag-1 and Ag-3 display a lateral inhomogeneity, especially close to the back side (stark intermittence of red and blue, i.e., high and low E_g). Additional cross-section measurements on these two samples are provided in Appendix B.2 which support the observed lateral inhomogeneity. Additionally, the first few hundreds of nanometers from the front surface show a mix of dark and lighter blues, indicating the variation of band gaps as observed from

Raman. In particular, patches of higher band gap material are present near the front surface (also visible in the top spectra from the line profiles iii in Figure 5.8 and ii in Figure 5.9).

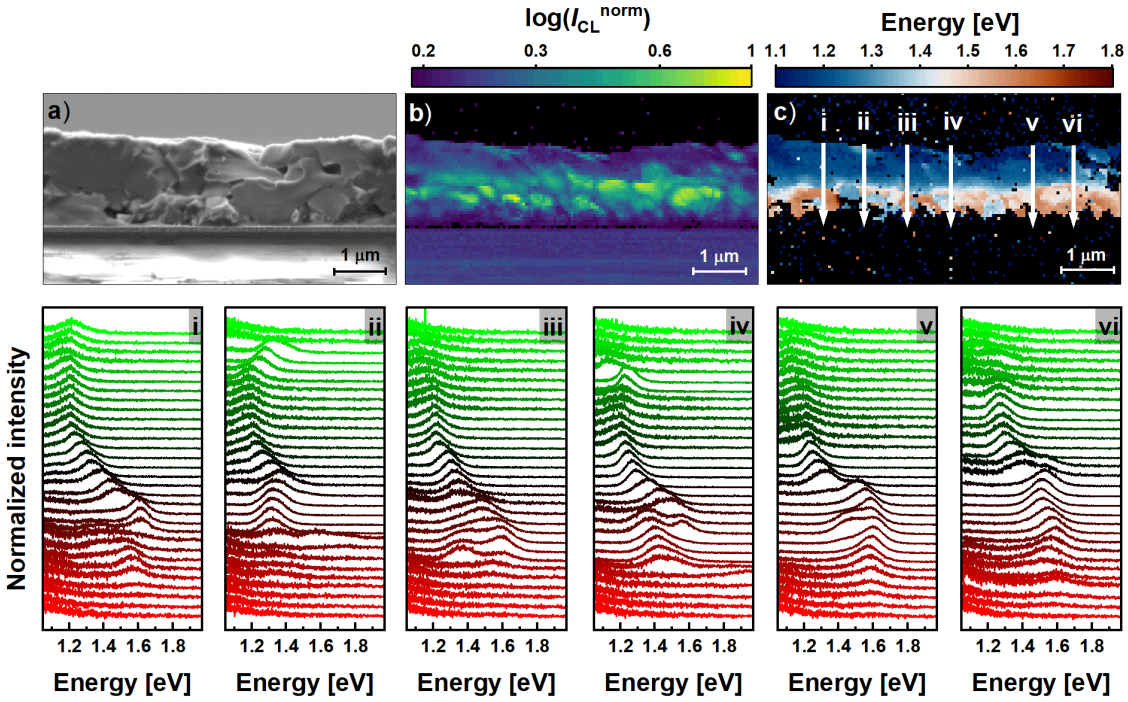

Figure 5.9. Cathodoluminescence spectroscopy on the cross-section of the sample Ag-1 (series 1). The top row shows the SE image of the region of interest a), the normalized intensity map of the panchromatic luminescence in logarithmic scale b) and the colormap of the energy of the maximum of the CL emission c). The bottom row shows the individual spectra along the lines i-vi drawn in c). All the spectra are normalized and shifted for clarity.

Comparing the colormaps from Figure 5.8, Figure 5.9 and Appendix B.2, it appears that the high band gap phase remains more localized at the back side in sample Ag-1 whereas it spreads closer to the front side with added Ag. This contrast is particularly visible on the energy maps taken with the InGaAs detector in Appendix B.1. Taken together, the cathodoluminescence results support the increased diffusion of Ga from the back side towards the front side of the absorber as suggested by the variation of band gaps near the two surfaces. This in turns, provides the explanation for the flattening of the GGI profiles observed by GDOES. With the formation of higher (lower) band gap phases near the front (back) surface, the average GGI in this region is expected to

increase (decrease). Moreover, with increasing Ag content, a smoother band gap gradient is achieved, despite a certain lateral inhomogeneity and reversed band gap gradient near the back contact.

5.4. Performance enhancement

It has been demonstrated that the morphology, as well as the gradient profile, may be improved by addition of Ag in the absorbers. In this section, the effect on the bare absorbers and correspond finished cells' performance is discussed.

5.4.1. Absorber improvement

As introduced in section 2.3, information about qFls, tail states and ODF can be obtained from absolute PL measurement on the front side. QFls gives an upper limit to the V_{OC} [55] and is therefore a very useful quantity to anticipate how good a finished cell can be. Fitting the high energy part of the PL spectrum, sufficiently far above the band gap – where it is assumed that the absorptance is equal to 1 – one can get a measure of the qFls [59]. However, because of the shoulder in this range for one of the samples (cf. Figure 5.7a), an evaluation of the qFls based on the PLQY following Equation (2.25) is preferred. Moreover, the quantity $|kT \cdot \ln(Y_{PL})|$ represents the non-radiative losses and, contrary to the qFls, does not depend on the band gap of the material, allowing for a comparison of absorbers with different band gaps, provided that the "one sun" excitation is correctly adapted to each absorber.

Figure 5.10 summarizes the results from the front side PL measurements for the two series of samples. An increase as large as 30 meV is observed in terms of qFls between the samples Ag-2 (intermediate Ag content) and Ag-3* (high Ag content) and their respective reference sample (light gray bars). Although it may look like a great improvement, the non-radiative losses remain unaffected within error (black bars). The higher qFls in these cases comes from the band gap increase, as indicated at the bottom of Figure 5.10, and not from any material improvement. In both series, the highest non-radiative losses are recorded for the reference samples (Ref-1 ~ 188 eV and Ref-2* ~ 183 meV). The Ag-alloyed absorbers from series 2, despite having larger qFls (and larger E_g) than the reference sample, do not show any

significant decrease of the non-radiative losses (lowest losses achieved for the sample Ag-1* with ~ 175 meV) and would therefore be expected to perform equally good if finished into solar cells. The series 1 leads to more promising results. Growing absorbers with a lower GGI in the elemental precursors stack (series 2), requires a new optimization of the process which is not straight forwards to achieve, probably explaining the performance difference between the two series. **Considering the series 1, alloying with Ag reduces the non-radiative losses by ~ 15 meV in the case of the samples Ag-1, Ag-3, Ag-2.1 and Ag-2.4 and a decrease by as much as 30 meV is achieved for the samples Ag-2.2 and Ag-2.3. Similar improvement would therefore be expected in the V_{OC} of a cell made from these absorbers and is discussed in section 5.4.3.**

It should be noted that samples Ag-2.2 (series 1) and Ag-2* (series 2) should be identical, with the same low GGI in the precursor stack and the same intermediate AAC (cf. Table 5.1). However, these two samples yield quite different results in terms of E_g, qFls and non-radiative losses, questioning the reproducibility of the process, or the homogeneity of the absorbers. Nevertheless, the starting point of the series 1 is close to the "standard" recipe, i.e., the growth process is the most optimized, and conclusions can be drawn from the results of this series. A third series of samples was prepared, with the same Ag variation, but a precursor stack GGI even lower than the series 2. Unfortunately, something went wrong with the process and the absorbers exhibited worse performance than the reference sample. This specific series is thus only briefly discussed in the Appendix B.3.

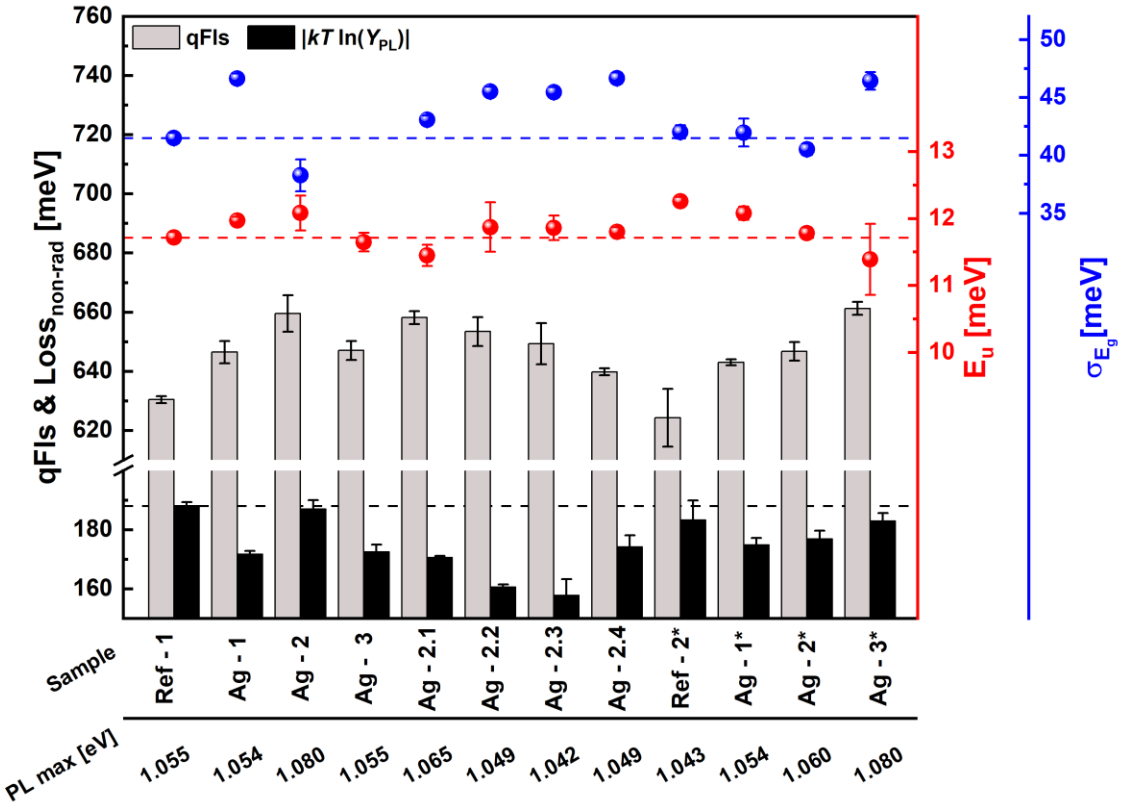

Figure 5.10. Summary of the PL results for the series 1 and 2 (the results for the series 2 are added compared to the publication [13]). The samples Ag-2.1 – Ag-2.4 are samples with the same intermediate Ag content as Ag-2 but with variations in the growth process (cf. Table 5.1). The left axis is the qFls and the non-radiative losses defined by $|kT \cdot \ln(Y_{\mathrm{PL}})|$. The first right axis (red) is the Urbach energy and the second one (blue) is the standard deviation from the mean band gap as defined in Equation (2.32). The dashed lines set the reference level for the different quantities based on Ref-1. The energy of the PL peak maximum (used to calculate the qFls) is given for each sample below the bottom axis.

As introduced in section 2.4.3, the low energy part of the PL spectrum, far below the band gap, can be used to measure the tail states [57]. Tail states have a direct detrimental impact on V_{OC} [60,62,175] and can be described by the Urbach energy E_{U}. A reduction of the Urbach energy upon incorporation of Ag is observed in wide band gap CIGSe [151,156], but the opposite is reported for low band gap CIGSe [163]. In the present study, no significant change is observed for the series 1; the measured E_U ranges from 11.4 meV to 12.0 meV and $E_U^{\mathrm{Ref}} = 11.7$ meV. The samples from series 2 show a decreasing E_{U} trend with increasing Ag content, from 12.3 meV down to 11.4 meV, with

however a large error on Ag-3*, making the difference hardly significant. This suggests that the tail states are not strongly affected by the (low) Ag incorporation.

Another parameter linked to the alloy disorder is the sharpness of the absorption edge, as discussed in section 2.4.3. The absorptance is obtained from the PL measurement (cf. Equation (2.28)) and is plotted in Figure 5.11 for Ref-1. The standard deviation for each of the samples from series 1 and 2 is reported in Figure 5.10. The smallest one is obtained for the sample Ag-2 (38 meV) and increases up to 47 meV for the samples Ag-1, Ag-2.4 and Ag-3* (three different Ag contents). Due to the shoulder at 1.25 eV in the PL spectrum, the absorptance of the sample Ag-3 – which showed the largest inhomogeneity in the GGI profile and in the Raman spectra – could not be extracted. Such low spreading in the standard deviation (< 10 meV) is not significant and does not support firm conclusions. It appears that the changes observed in the band gap gradient are too small to have an effect on the broadening of the absorption edge. Other effects seem to be more important.

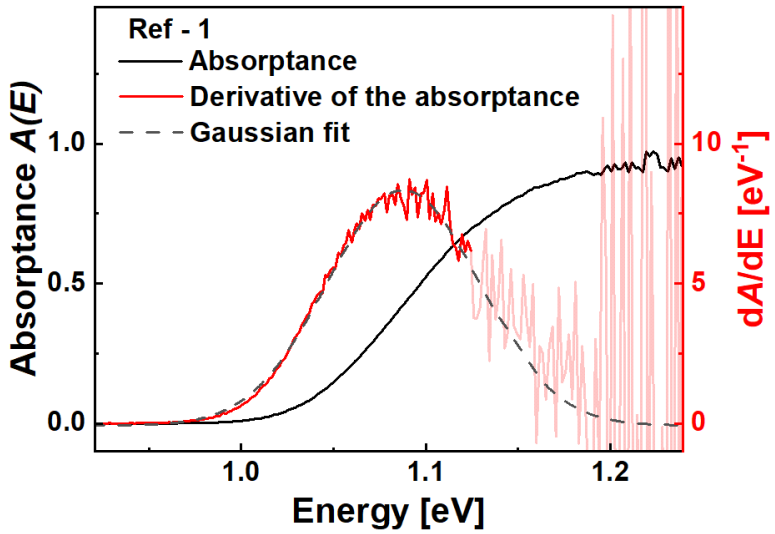

Figure 5.11. Absorptance obtained from a PL measurement on the reference sample Ref-1 (black curve) and its derivative (red curve). The derivative is fitted according to Equation (2.32) (dashed line) over the highlighted range ($0.90 - 1.14$ eV). The high energy part of the derivative is disregarded because of the high noise. Only one set of diodes in the InGaAs detector is considered (cf. section 3.2.1).

5.4.2. Optical diode factor with and without Ag-alloying

As discussed in section 2.4.4, a decisive parameter for solar cell efficiency is given by the fill factor. While it obviously cannot be determined from PL on bare absorbers, the optical diode factor, however, can be measured. The value of the latter has a direct influence on the FF; high ODF leads to lower FF [68,69], i.e., for a good FF the ODF has to be as close to 1 as possible. As mentioned, in the case of bare absorbers, an ODF larger than 1 is attributed to the presence of metastable defects.

Absorbers without Ag

The ODF of the "standard" bare absorbers discussed in chapter 4 is measured and takes a value in the range of $1.22 - 1.28$, as shown in Figure 5.12b (first panel). Furthermore, it has been observed with these CIGSSe absorbers that a Na-PDT usually increases the ODF by $\sim 0.1 - 0.2$ (cf. Figure 5.12b, second panel). Na is reported to increase the metastable behavior in CIGS absorbers [176,177], but according to Wang *et al.* [85] this would lead to an increase in the net doping density upon illumination (enhancing the radiative recombination) and consequently to a decrease of the ODF. However, Na-PDT may also improve the defect and surface passivation [178,179] which may lead to a decrease of the surface recombination (contributing to the non-radiative recombination) and a subsequent increase in the ODF [85]. It is further observed that after buffer deposition (sputtered ZnOS), the ODF of the "standard" absorbers increases significantly, up to 1.89 (Figure 5.12b, third panel). A better surface passivation can be achieved with a buffer, providing an explanation for the increase in the ODF. Despite the buffer layer being relatively thin (~ 65 nm), the formation of a shallow SCR cannot be excluded, and could potentially participate to the ODF increase as well (cf. section 2.4.4). In fact, from TRPL measurements on the buffered absorbers, a fast initial PL decay is observed and could be attributed to the formation of a SCR, as discussed in chapter 6, section 6.3.2.

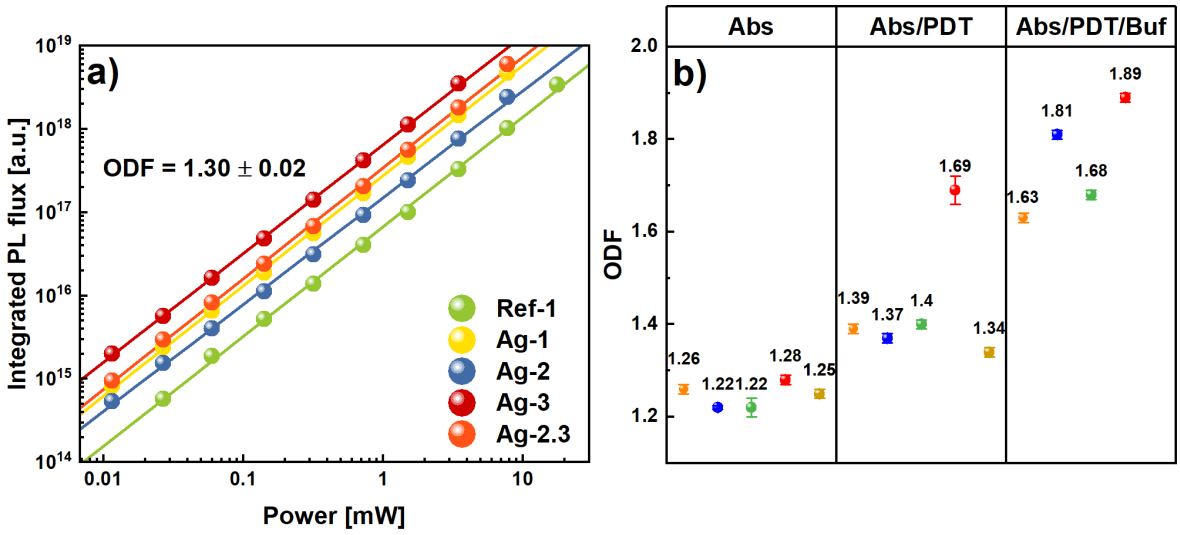

Figure 5.12. a) Integrated PL flux vs. laser power at the sample position from an excitation dependent PL measurement for five samples of series 1. The plain lines are a linear fit to the data and the slope, i.e., the ODF, is indicated. b) A collection of measured ODF for the "standard" absorbers from chapter 4. The left panel is for bare absorbers, the middle one for absorbers with a Na-PDT and the right one for absorbers with a Na-PDT and a sputtered ZnOS buffer layer. The color differentiates the individual absorbers.

Absorbers with Ag

The ODF of five selected samples from series 1 (the reference sample, the three samples with different AAC and the absorber with the lowest non-radiative losses) is measured. It is reminded that these samples are all bare absorbers, with no Na-PDT. Upon Ag incorporation, regardless of the Ag content (which is generally low for all the present variations), the ODF of the absorbers remains unchanged and equals the one of the reference sample, ODF = 1.30 ± 0.02. This value is slightly larger than what is measured in the "standard" bare absorbers. The current record ACIGS solar cell (with a much higher AAC than in this work) also has an ideality factor of 1.30 [26]. However, Weiss *et al.* [69] observed a decrease in ODF for ACIGS absorbers compared to CIGS absorbers (both grown at ZSW), leading to a larger *FF*. Here, because no change in ODF is measured, it is reasonable to expect a similar *FF* for all the cells prepared from these absorbers, provided that the subsequent deposited layers (buffer, window layers) are not affected by the different Ag contents themselves. The amount of Ag used in the

present absorbers being small, no significant change of the band alignment is expected [152]. Furthermore, beside the absence of change in the ODF upon Ag incorporation, a slight increase in PL intensity is detected (cf. Figure 5.7a and b). This could be interpreted as a reduction of surface recombination (which can increase the ODF), together with an increased doping (which can reduce the ODF).

As mentioned already, a possible explanation for an ODF larger than 1 could be the presence of metastable defects that convert from donor to acceptor upon illumination, leading to an increase of the net doping and a resulting increased PL intensity. In the absorbers investigated in this work, once the excitation laser is turned on, the integrated PL flux increases logarithmically with time and reaches a plateau after about 5 min under illumination, as shown in Figure 5.13. This is much longer than the few seconds reported in [68] for a metastable transition in CIGSe, which suggests that different defects with different transition rates might be at work here. Although only the sample Ag-1** is shown in Figure 5.13 as an example for the increasing PL intensity, all the absorbers from series 1 and 2 exhibit this behavior (more or less pronounced). Moreover, it is not only observed in the Ag-alloyed absorbers, but also in some "standard" absorbers. Whenever the samples show this behavior, a short time (~ 5 min) is waited between the turning on of the laser and the actual PL measurement. Similarly, it is a standard procedure to perform light soaking of the finished cells before measuring the IV parameters.

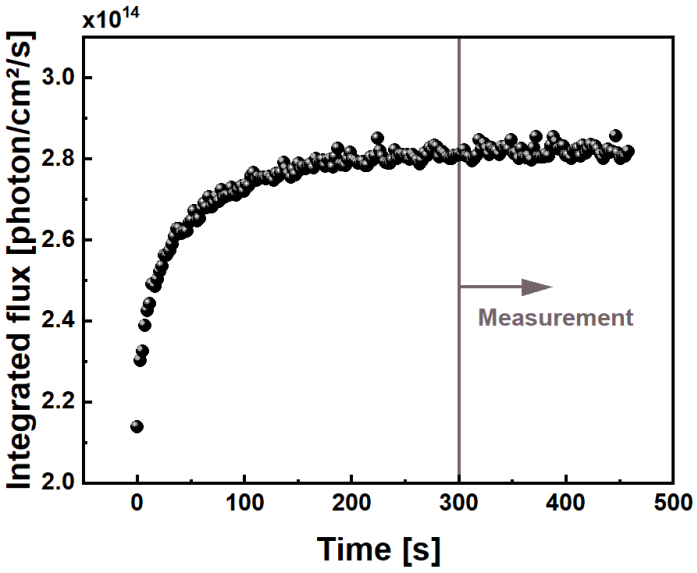

Figure 5.13. Temporal evolution of the integrated PL flux measured from the front side of the sample Ag-1**. $t = 0$ corresponds to the turning on of the laser, $t = 300$ s denotes the time waited before a steady state PL measurement is taken. The laser excitation is set to simulate a "one sun" illumination.

5.4.3. Cell improvement

In this section, the electrical performance of the solar cells based on the absorbers from series 1 are measured. Before being processed into cells, the absorbers receive a Na-PDT. Provided that all the absorbers react the same way to the Na-PDT, the trends observed from the electrical measurements should be comparable with the ones from PL. The results of the IV characteristics (measured at AVANCIS) are reported in Figure 5.14. For the sake of data confidentiality, all the values are normalized according to the reference sample Ref-1, and a relative comparison to it is discussed.

As shown in Figure 5.14d, an increase in the V_{OC} is generally obtained (within error) for cells based on the investigated absorbers. However, the V_{OC} improvement does not always correlate with the reduction of the non-radiative losses measured on the bare absorbers by PL (cf. Figure 5.10). In particular, when comparing the two samples with the lowest non-radiative losses from PL, the V_{OC} improvement for the sample Ag-2.2 is less than the expected one and no improvement for the sample Ag-2.3 is measured. This implies that additional losses may occur while finishing the cell. It is important to note at this point that while the measurements of the bare absorbers

are performed on inch by inch samples (cut from larger absorbers), the IV parameters are measured on 10 cm by 10 cm encapsulated submodules. The potential effect of Ag on the buffer and window layers is not investigated in this work but could contribute to the discrepancies between PL and IV results.

Furthermore, the highest V_{OC} is measured for the sample Ag-3 (relative improvement of 6.5% compared to the reference sample's V_{OC}) and even exceeds the corresponding qFls. Such behavior has been previously reported in [59] for the "standard" absorbers/cells discussed in chapter 4. It was demonstrated that the V_{OC} and qFls strongly depend on the wavelength of the excitation; measurements performed under a blue illumination leading to a qFls up to 30 meV larger than under red illumination. The origin of this behavior, not commonly observed in CIGS, is not fully understood yet, but it is likely that metastable defects are involved in it. Alternatively, the larger V_{OC} measured in this case could be a consequence of the Na-PDT provided before the cell-making.

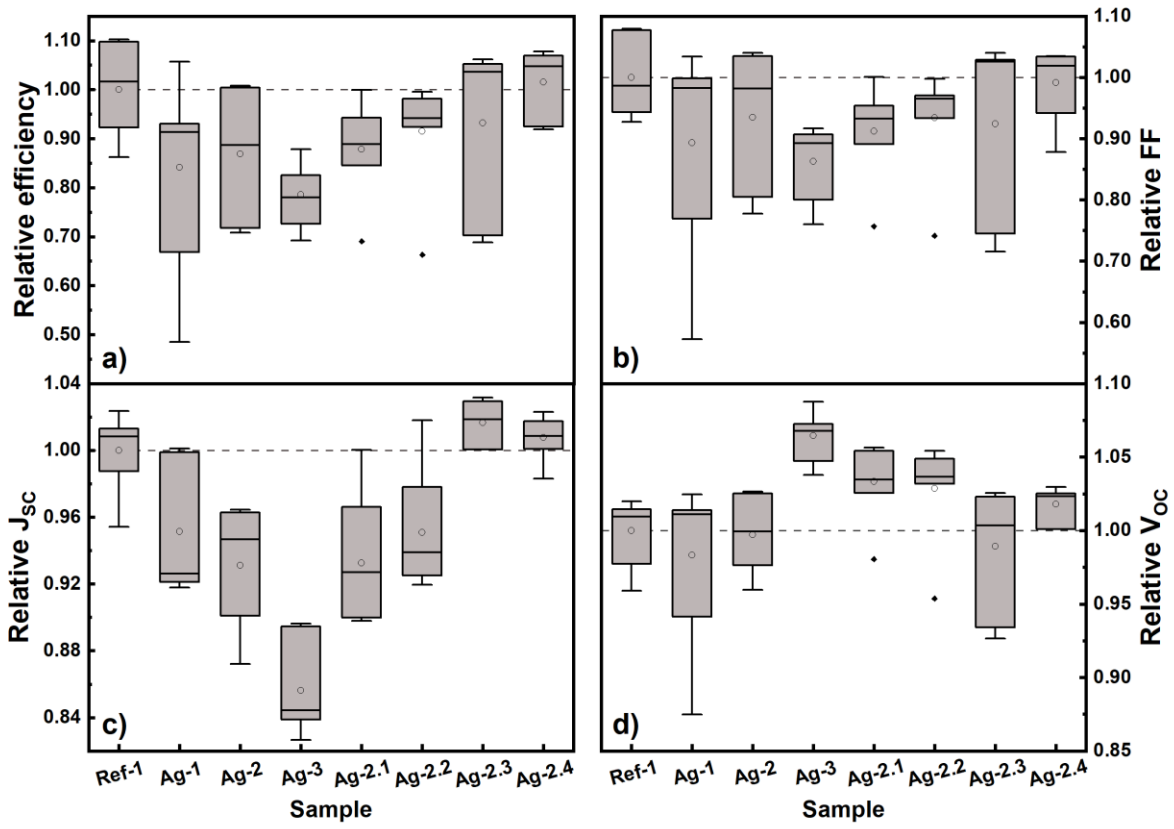

Figure 5.14. Relative IV parameters for the cells based on the absorbers discussed in the text. The data is normalized to the mean value of the reference sample. The efficiency a), the FF b), the J_{SC} c) and the V_{OC} d) are displayed. For each of the samples, seven different cells are measured. The box limits are given by the 1st and 3rd quartiles (Q1 and Q3) and the whiskers by the minimum and maximum values. The open dot inside is the mean value and the line is the median. Any data point falling outside 1.5·IQR is considered an outlier and shown as black dot. IQR is defined as IQR = Q3-Q1 and stands for inter-quartile range.

Despite the higher V_{OC}, the cells did not show significant improvement in efficiency, mostly due to a reduction of the short circuit current density J_{SC} (Figure 5.14c), leading to a lower product $J_{SC} \cdot V_{OC}$. The current losses may arise from the higher band gap observed at the front side, as discussed from CL in section 5.3.3. The best performing Ag-alloyed cell (based on absorber Ag-2.4: lowest GGI in the elemental stack, intermediate AAC and lower Na content) shows a relative improvement of 1.6% in average efficiency compared to the reference (slight improvement in V_{OC} and J_{SC} but decrease in FF).

While the improvement in cell efficiency is not drastic, the absorbers alone show encouraging performance. It can thus be expected that further optimization of the industrial process for Ag containing absorbers and adaptation of the cell process will make full use of the reduced non-radiative recombination and result in improved efficiencies.

5.5. Summary

In this chapter, industrial (Ag,Cu)(In,Ga)$(S,Se)_2$ absorbers with various (low) Ag contents in the elemental precursor stack have been investigated. It is found that the crystal morphology improves with Ag, in particular showing an increased grain size, in line with the available literature. Despite the appearance of shallow crevices on the front surface of the Ag-alloyed absorbers, improvement in the absorbers' and cells' performance could be achieved.

Upon Ag-alloying, a stronger interdiffusion of Ga and In is observed, resulting in a flattening of the GGI profiles. The decrease of the back side GGI correlates with a redshift of the high energy peak measured by photoluminescence from the back side of the absorbers. As the back side GGI decreases, the front side GGI increases. However, in most of the cases, only a small blueshift of the notch PL peak is measured, not enough to explain the higher GGI measured at the front side from GDOES. From cathodoluminescence, areas of higher energy emission are located near the front surface and are attributed to the formation of (A)CIGSSe phases of higher Ga content, which is confirmed by Raman spectroscopy. This provides a tangible explanation for the observed front side GGI. In addition, a certain lateral compositional inhomogeneity is noted close to the two surfaces (front and back), especially in the sample with the highest AAC (series 1). CL on the cross-section of the samples supports the lateral inhomogeneity, but also indicates that a smoother band gap gradient (with no/fewer band gap jumps) is achieved after Ag incorporation compared to the model proposed in chapter 4. However, in several locations, a decreasing band gap is observed near the back contact in the two Ag-alloyed absorbers investigated by CL. This situation could be extremely detrimental as it would promote non-radiative recombination at the back contact and should be avoided. Nevertheless, according to the measured performance, this reversed gradient seems to be sparse enough to not cause extreme losses. In fact, a promising reduction of the non-radiative losses of up to 30 meV is measured for the bare absorber with low precursor stack GGI and intermediate AAC (series 1). It is further demonstrated that even grown at a reduced process temperature, good

performing absorbers can be produced, which is very interesting from an industrial point of view. Unfortunately, solar cells based on the series 1 absorbers did not show as much improvement in efficiency as what could have been expected from the optical characterization. While in most cases a V_{OC} increase is obtained, the J_{SC} decreases in all but two samples, ultimately leading to no or slight efficiency increase. The best reported cell efficiency corresponds to a relative increase of 1.6% compared to the reference sample. Nevertheless, further optimization of the growth and cell-making processes would maximize the benefits of the absorber improvement demonstrated by absolute photoluminescence. Another parameter reflecting the quality of an absorber is how long the photogenerated carriers can live before recombining. The lifetime of the charge carriers can be determined optically via time-resolved photoluminescence, as discussed in the next chapter.

Chapter 6

Time-resolved photoluminescence

In the previous chapters, it has been discussed that the band gap gradient in the investigated CIGSSe absorbers features in fact band gap jumps, rather than a gradual change. Furthermore, replacing a small part of the Cu by Ag during the growth led to a smoother gradient, and the Ag-alloyed absorbers showed promising performance improvement. This final chapter discusses how Ag-alloying and Na-PDT affect the carriers' lifetime and doping of the absorbers. It regroups a collection of experimental observations and interpretations of decay transients measured by time-resolved photoluminescence. In particular, the dependence of the decay times on the excitation intensity and on the sample temperature are investigated. The aim of this chapter is twofold: it offers possible explanation for the experimental measurements, but also discusses the do's and don'ts when measuring TRPL. Section 6.1 presents current theories and models from the literature about excitation and temperature dependence of the minority carriers' lifetime. The most relevant experimental results on Ag-alloyed and Na treated absorbers and their discussion in light of the models introduced in section 6.1 are shown in section 6.2. Comparing different thicknesses and deposition methods, the influence of the buffer layer on the TRPL transients is investigated in section 6.3. Finally, section 6.4 concludes on the findings of the present chapter.

6.1. General interpretation of the transient decays

The bi-exponential fit used to describe the TRPL transients and extract the decay components τ_1 and τ_2 is discussed in section 2.5 and shall not be re-introduced in this section. However, it is stressed again that τ_2 is the parameter that is here considered as a combination of bulk and

surface lifetime (provided that no significant trapping effect dominates the transient) and that is evaluated in this chapter.

6.1.1. Excitation dependence of the SRH lifetime

Considering recombination via defects, the SRH recombination rate has been defined in section 2.2.3. In the case of a p-type semiconductor, it holds $p_0 \approx N_\mathrm{A}$ and $n = n_0 + \Delta n \approx \Delta n$. Considering further $\Delta p \approx \Delta n$, it follows $p \approx N_\mathrm{A} + \Delta n$. The excitation dependent SRH lifetime τ_SRH is hence given in this case by [50,51,180]

$$\frac{1}{\tau_\mathrm{SRH}} = \frac{N_\mathrm{A} + \Delta n}{\tau_\mathrm{p}(n^* + \Delta n) + \tau_\mathrm{n}(N_\mathrm{A} + p^* + \Delta n)} \tag{6.1}$$

where n^* and p^* are the auxiliary carrier densities defined by Equation (2.12) and (2.13). When considering a deep defect level, the auxiliary densities are negligible compared to the doping density. Equation (6.1) leads to two plateau lifetimes, at low and high injection levels, i.e., for $\Delta n \ll N_\mathrm{A}$ and $\Delta n \geq N_\mathrm{A}$. Therefore, at high injection, the expected SRH lifetime is given by $\tau_\mathrm{SRH} = \tau_\mathrm{p} + \tau_\mathrm{n}$, while at low injection it asymptotically reaches $\tau_\mathrm{SRH} = \tau_\mathrm{n}$ [181] (in the case of a single deep recombination center). The low injection level lifetime depends on the position of the involved defect. As mentioned in section 2.2.3, defects at midgap are the most detrimental and τ_n has its smallest value in this case. For defects closer to the band edges, τ_n becomes larger [181]. Figure 6.1 shows an example of the SRH lifetime dependence for a n-type Si semiconductor (the minority carriers are holes) of band gap 1.11 eV and doping density of $n_0 = 5 \cdot 10^{13}$ cm^{-3}. The defect considered as recombination center is placed at midgap ($E_\mathrm{r} = 0.555$ eV), above midgap ($E_\mathrm{r} = 0.8$ eV) and below midgap ($E_\mathrm{r} = 0.3$ eV). The influence of the ratio between the majority carrier lifetime and minority carrier lifetime (here $\zeta = \tau_\mathrm{n}/\tau_\mathrm{p}$) is highlighted in Figure 6.1 as well.

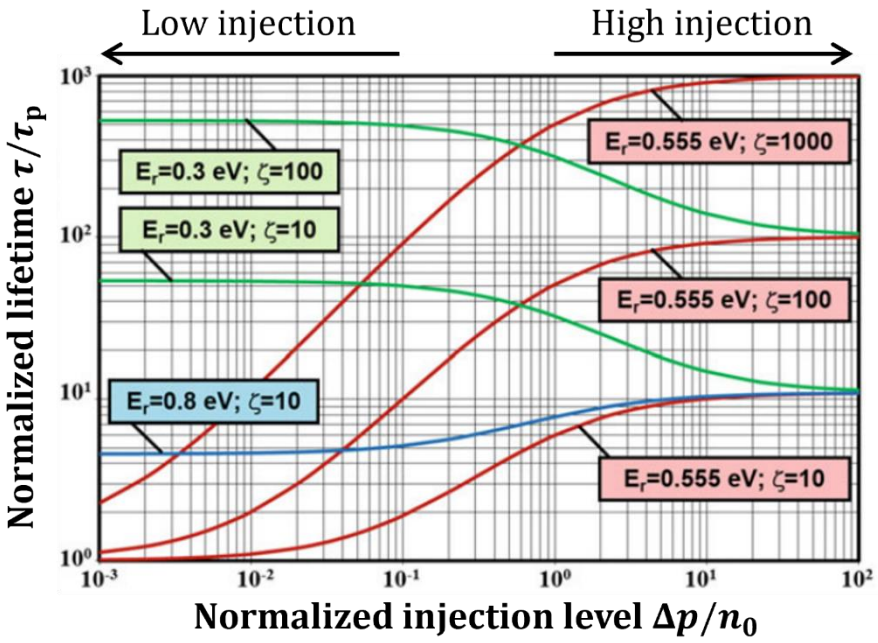

Figure 6.1. Normalized lifetime τ/τ_p (considering the midgap defect) vs normalized injection level $\Delta p/n_0$ in double logarithmic scale for a n-type Si semiconductor (holes are minority carriers) of doping $n_0 = 5 \cdot 10^{13}$ cm^{-3}. The defect energy position is varied between $E_r = 0.555$ eV (at midgap, red curves), $E_r = 0.8$ eV and $E_r = 0.3$ eV (above and below midgap, green and blue curves, respectively). The ratio $\zeta = \tau_n/\tau_p$ takes the value $10, 100, 1000$ as indicated. The figure is adapted from [181].

From Figure 6.1 it can be seen that the lifetime can either increase or decrease with the excitation, depending on the defect level [182,183]. As mentioned, the latter has a direct influence on the auxiliary carriers' densities. For a shallow defect state (very close to one of the bands), n^* (for a shallow acceptor state) or p^* (for a shallow donor state) can become comparable or larger than the doping density and therefore cannot be neglected at low injection level in Equation (6.1) anymore. This leads to the low injection plateau $\tau = \tau_p(n^*/N_A) + \tau_n$ for a shallow acceptor and $\tau = \tau_n(1 + p^*/N_A)$ for a shallow donor [183], which can be larger than the high injection plateau depending on n^* and N_A (green curves in Figure 6.1). This SRH lifetime dependence on the injection level emphasizes the importance of varying the excitation in order to derive any reliable lifetime values. There exists a rich literature on Si solar cells using this dependence to determine the doping density, the energy and density of the involved defect and the charge carriers' lifetimes [182,184–188].

However, while this lifetime dependence appears to be well-known in the Si community, its study and interpretation is only sparsely covered for thin films and diverges between the different reports. Cheng *et al.* [189], similarly as in the Si solar cells studies, numerically fit the measured excitation dependence of the decay time and locate a donor state in a CdTe solar cell. In CdSeTe absorbers, Moseley *et al.* [190] measure a decreasing τ_2 with increasing injection level and discuss that τ_2 may represent the bulk lifetime only under specific conditions of doping and laser fluence. Shirakata *et al.* [191] report on an increasing lifetime (considering τ_1 from the bi-exponential fit) of a CIGSe solar cell with increasing injection level but admit that the physical meaning of the behavior remains unclear. Maiberg *et al.* [192] investigate several CIGSe absorbers and measure both decreasing and increasing decay times for increasing injection level. They attribute the decrease to a reduction of the trapping effect (through traps saturation, i.e., the electron supply from the trap states becomes negligible compared to the photogenerated electrons) and the increase to the SRH lifetime dependence given by Equation (6.1), considering deep defects. They conclude that both effects act on similar time scale and can potentially compensate each other. Finally, Metzger *et al.* [45] consider a CIGSe absorber before and after deposition of the top layers (CdS and ZnO) and demonstrate that with higher injection level, the lifetime of the bare absorber decreases, whereas it increases for the CIGS/CdS/ZnO stack. The authors conclude that the lifetime measurements strongly depend on the experimental conditions and that the lifetime correlates with the surface quality.

In this thesis, it is shown by technology computer-aided design (TCAD) simulation that the decay time can become longer at high excitation due to "hole limited" recombination, in the context of SRH recombination (cf. section 2.2.3). At high excitation, many electrons (minority carriers in p-type semiconductors) are generated and because of their large capture cross section, they are quickly captured by the deep defects. However, due to the asymmetric capture cross section, the holes are captured at a slower rate and the recombination time is thus limited by the hole capturing and becomes $\tau_\mathrm{n} + \tau_\mathrm{p}$, as discussed above. Conversely, at low excitation, the density of holes is much greater than the one of electrons and therefore the recombination via deep defects depends on the electron capturing, leading to a lower decay time τ_n. In a TRPL experiment, due to the pulsed nature of the excitation, a large density of electrons are generated directly after the pulse and the recombination is "hole limited", i.e., $\tau = \tau_\mathrm{n} + \tau_\mathrm{p}$. At later times, once a substantial number of carriers have recombined already, there are only few electrons

remaining (compared to the holes) and the recombination becomes "electron limited", i.e., $\tau = \tau_n$. Figure 6.2 simulates the TRPL transients under various excitation levels and for different defect energies. In each case, at the lowest excitation, the decay is mono-exponential. As the excitation is increased, however, the initial decay time becomes longer, reflecting the "hole limited" recombination, before returning to the "electron limited" recombination at later times, creating a bowing of the transients. This bowing becomes less pronounced as the defect is moved closer to the conduction band (Figure 6.2b and c), as it can start acting as a trap as well.

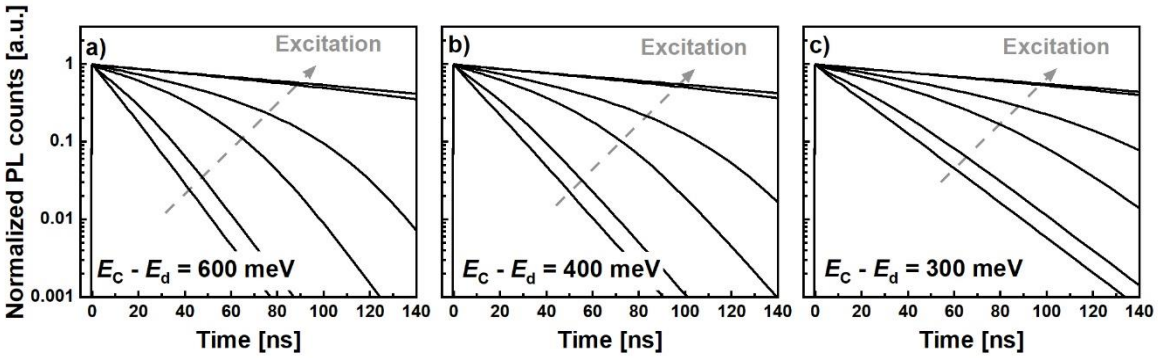

Figure 6.2. TRPL transient simulation for three different defect energies: 600 meV below the conduction band a), 400 meV b) and 300 meV c). A double band gap gradient is considered following the GGI profile from Figure 4.1. The transients are normalized to the maximum of the emission in each case. The highest excitation corresponds to an excess carrier density $\Delta n = 6 \cdot 10^{15}$ cm^{-3} and the transients are simulated at $0.1, 1, 5, 10, 50$ and 100% of this excitation.

These simulations provide a possible explanation for the observed behavior of the experimental transients discussed in section 6.2. However, due to time limitation, no experimental data was fitted with this model. Nevertheless, it is quite certain that one can find an adequate combination of defect density, defect energy, capture cross section and doping density for which the simulations are in line with the experiments.

6.1.2. Temperature dependence of the measured lifetime

Beside the excitation dependence of the measured lifetime, a temperature dependence is also commonly observed in semiconductors. Various explanations for the strong temperature dependence of the measured carriers' lifetime are proposed in the literature and discussed here.

Trapping – detrapping hypothesis

As discussed in section 2.5.2, carrier traps present in the material may artificially extend the measured lifetime. A possible interpretation for a shorter measured lifetime at temperatures higher than RT is therefore the thermally enhanced detrapping of the minority carriers [192], i.e., an increased reemission of the carriers from the trap state to the conduction band. In such a situation, the decay time follows Equation (6.2) [193], where the exponential part describes the detrapping and the power law represents the temperature dependence of the lifetime.

$$\tau \sim T^{-b} \cdot \exp\left(\frac{E_\mathrm{d}}{k_\mathrm{B}T}\right) \tag{6.2}$$

It is important to clarify that from the SRH recombination theory, the charge carriers' lifetimes τ_n and τ_p do depend on the temperature as they are inversely proportional to the thermal velocity and to the involved defect's capture cross section σ_d (cf. Equation (2.14)). While the thermal velocity is known to vary with $\sim T^{1/2}$ (see e.g. [194]), the thermal dependence of the capture cross section is not well established. Maiberg *et al.* assume $\sigma_\mathrm{d} \sim T$ in [79] but find via simulation $\sigma_\mathrm{d} \sim T^{4.5}$ and $\sigma_\mathrm{d} \sim T^{2.5}$ in [192] for various CIGS. Levcenko *et al.* [195] fit the temperature dependence of the PL emission for CZTS and find $\sigma_\mathrm{d} \sim T^{0.8}$. Tyagi *et al.* [196] report for Si that $\sigma_\mathrm{d} \sim T^{a}$ where the exponent a takes values from 0.5 to 3.4. However, some reports on Si [185] also demonstrate increasing lifetimes at temperatures higher than RT, attributed to a decrease in the capture cross section with increasing temperature, $\sigma_\mathrm{d} \sim T^{-0.3}$.

Maiberg *et al.* perform excitation and temperature dependent measurements and simulations on CIGS and CZTS [192,193] and use Equation (6.2) to determine the energy position of a trap state in these materials. Connelly *et al.* [197] measure the carriers' lifetime in a GaInSb superlattice over a wide temperature range ($11 - 300$ K) and discuss three temperature regions. The measured (low injection) lifetime decreases first from 11 K to 100 K before increasing until 250 K and finally decreases again above 250 K. The authors are able to reliably fit this lifetime behavior using a model similar to Equation (6.2) considering a single defect state close to the valence band.

Multiphonon theory

A second plausible explanation for the decreased decay time at higher temperatures is provided by the multiphonon theory. As discussed in section 2.2.3, instead of recombining radiatively

by photon emission, charge carriers may alternatively recombine non-radiatively by emission of multiple phonons (SRH recombination). Although band-to-band recombination occurring by phonon emission is very unlikely because the bands have essentially the same energy dependence on the configuration coordinate diagram (i.e., no overlap between E_C and E_V), it is reasonable to assume that recombination through deep defects may happen by multiphonon emission [198]. Figure 6.3a schematizes a configuration coordinate diagram which is used to understand the concept of multiphonon recombination. The upper and lower parabolas, i.e., potential energy surfaces, represent the CBM and VBM states, while the red parabola corresponds to an available defect state within the band gap. In general, the minimum of the defect state is shifted on the configuration coordinate axis compared to the two other states. Considering an electron in the conduction band state, it can transition via phonon emission to the defect state, provided that the lowest energy vibrational wavefunction of the conduction band parabola overlaps with a vibrational wavefunction of the defect parabola [198,199] as represented in the inset of Figure 6.3b. The higher the overlap, the more probable the transition is. The same process holds for the transition from the defect state to the valence band state. The energy difference between the initial and final state is given by ΔE. The transition from the upper to the lower parabola may be thermally activated. Since recombination via phonon emission is a non-radiative process, it results that the non-radiative recombination rate increases with increasing temperature, ultimately leading to a shorter measured lifetime.

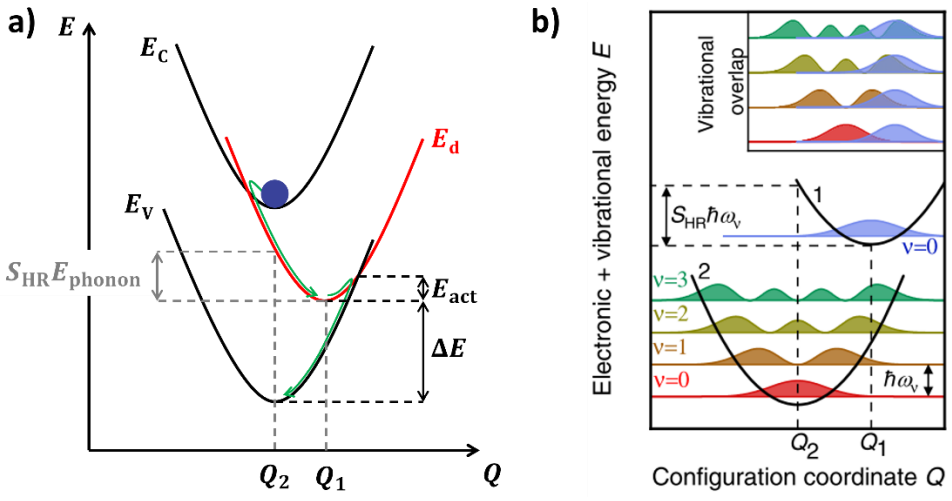

Figure 6.3. a) Schematic representation of a configuration coordinate diagram showing two multiphonon transitions (green arrows) involving a deep defect. The black parabolas represent the CBM and VBM with an equilibrium position Q_2. The red parabola corresponds to the defect state (Q_1) and

its energy difference with the valence band is given by ΔE. The blue dot symbolizes an electron. b) configuration coordinate diagram representing two electronic states and the absolute square of the first vibrational wavefunctions (i.e., probability of finding these states) identified by the vibrational quantum number ν. The inset highlights the overlap between the ground vibrational state of the upper parabola and the first four vibrational states of the lower parabola. Part b) is reproduce from [198] with permission.

The multiphonon transition rate, which has been derived by T. Markvart [200], demonstrates the complex dependence of the process on the ratio l/S_{HR}, where $l = \Delta E/E_{\mathrm{phonon}}$ is the number of phonons (of energy E_{phonon}) involved in the transition and S_{HR} is the Huang-Rhys factor. The latter describes the electron-phonon coupling, i.e., the relative shift between the two parabolas; it is defined based on the position difference of the two parabola minima (Q_1 and Q_2) as indicated in Figure 6.3. If the shift is large, S_{HR} approaches $\Delta E/E_{\mathrm{phonon}}$ and the transition rate is maximized [199]. Inversely, if the shift is small, the multiphonon transition becomes unlikely.

Henry & Lang [201] show that at high temperatures, the capture cross section of deep defects, possibly responsible for multiphonon emission, is given by

$$\sigma_{\mathrm{d}} = \sigma_{\infty} \cdot \exp\left(-\frac{E_{\infty}}{k_{\mathrm{B}}T}\right) \tag{6.3}$$

where σ_{∞} is a constant that depends on the product $S_{\mathrm{HR}}E_{\mathrm{phonon}}$ and $E_{\infty} = E_{\mathrm{act}} - kT_{\mathrm{R}}$. E_{act} is the activation energy required for the multiphonon transition (as indicated in Figure 6.3a) and $kT_{\mathrm{R}} = 25$ meV is the thermal energy at room temperature. Furthermore, A. Schenk [202] derives the low and high temperature limits of the SRH lifetime, assuming multiphonon processes and neglecting the temperature dependence of the trap energy. In the high temperature approximation it is furthermore assumed that $k_{\mathrm{b}}T \gg E_{\mathrm{phonon}}$ and the lifetime is given by

$$\tau \sim \frac{1}{\mathrm{T}} \cdot \exp\left(\frac{C}{k_{\mathrm{B}}T}\right) \tag{6.4}$$

with C a constant dependent on the activation energy. At low temperature, $k_{\mathrm{b}}T \ll E_{\mathrm{phonon}}$ is assumed and it is found that the SRH lifetime follows a power law as [202]

$$\tau \sim T^{-3/2} \tag{6.5}$$

The choice of the high or low temperature approximation is defined by the phonon energy. However, when $k_{\mathrm{b}}T$ is in the range of E_{phonon}, the threshold between the two approximations is not entirely clear.

Front side barrier model

Lastly, Weiss *et al.* [47] propose another possible mechanism for the measured decay time temperature dependence in double graded CIGS solar cells. As discussed in section 2.1.2, a common band gap architecture in CIGS features a double band gap gradient, towards the back side and towards the front side. While in sulfur-free absorbers the front side gradient is obtained with a higher Ga content (similarly as for the back side), in the case of the CIGSSe absorbers studied in this work, it is achieved with a higher S content (although no indication of it is observed from CL, cf. chapters 4 and 5). Both types of gradient lead to an increase of the conduction band (S mostly shifts the valence band down, but also a bit the conduction band up), and therefore act as a barrier for the excess electrons, confining them in the notch and limiting surface recombination. As the temperature increases, the electrons may gain enough thermal energy to overcome the barrier and recombine non-radiatively at the front surface, yielding a decrease of the TRPL measured decay time. Weiss *et al.* [47] simulate the influence of the barrier height on the measured decay time for various front surface recombination velocities and successfully modeled the temperature dependence of the measured decay time (assuming SRH to be temperature independent). They find that a high enough front side gradient effectively reduces the impact of the surface recombination, even for S_{f} as high as 10^6 cm/s. Therefore, when measuring the temperature dependence of the decay time in CIGS absorbers, it is important to consider the presence of a front side gradient, or to ensure a good passivation of the front surface.

6.2. Experimental TRPL transients' behavior

In order to observe significant enough variations and draw conclusions from the transient decays, it is necessary to cover a wide enough range of experimental conditions. While a small increase of the sample temperature ($\Delta T = 30 \sim 40$°C) is usually enough to detect significant changes in the measured lifetime [192,193], the excitation must be varied over several orders of magnitudes to include high and low injection levels. For both temperature and excitation dependent measurements, the measurable range depends strongly on the experimental setup.

A temperature increase and/or a lower injection level lead to a weaker PL emission, and therefore the setup's detection efficiency will define the lower bound. The highest injection level, however, is given by the laser's performance and the various intensity enhancements added to the setup, e.g. focusing lens. If not specified otherwise, the intensity dependence is performed using the low dark counts H12397-75 detector and the temperature dependence using the H10330C-75 one (cf. section 3.2.3). For each sample, i.e., all transient decay curves within one graph, the signal is acquired over the same duration, typically $10-20$ minutes. Moreover, contrary to the PL measurements, TRPL measurements have been performed on a single spot for each sample discussed in this chapter. A relatively good homogeneity of the samples is assumed based on the PL investigation.

6.2.1. Excitation dependence measurements

Excitation dependent photoluminescence decays of bare absorbers from Chapter 5, in particular samples Ag-1, Ag-3 and Ag-2.3 (cf. Table 5.1), have been measured over several orders of magnitude of laser fluence. The transients and the corresponding extracted decay times (τ_2 from a bi-exponential fit) are shown in Figure 6.4. The lowest excitation, in each case, corresponds to the weakest measurable signal and varies from sample to sample depending on the respective PL intensity. The sample Ag-3 (Figure 6.4c) is characterized at all excitations by a strong bi-exponential decay with a sharp fast initial decay. Based on the discussion in section 2.5.2 and from the surface morphology and inhomogeneities of the sample Ag-3 demonstrated in Chapter 5, the initial fast decay of the transients may be attributed to surface recombination. The long decay time (τ_2) increases with the excitation as plotted in Figure 6.4d. While the long decay time also increases with the excitation for the samples Ag-1 and Ag-2.3 (Figure 6.4a and e), the initial decay is not as pronounced as for sample Ag-3. In fact, some of the transients measured at intermediate excitations (light green to light orange transients) cannot be well represented by a bi-exponential function, as can been seen from the fitting curves in Figure 6.4 (black lines). As the excitation increases, the detected PL counts increase, and the transients deviate from the bi-exponential behavior. At the same time, the risk to measure pile-up increases as the detected PL counts grow above the recommended 5% of the excitation rate (cf. section 3.2.3). Therefore, an OD1.3 filter is added after the sample to attenuate its signal. However, this also reduces the signal-to-noise ratio to some extend (still fulfilling the condition $I_{\mathrm{sample}}/I_{\mathrm{BG}} > 0.2$) and the tail of the decay that does not follow the bi-

exponential behavior may be disappearing in the noise. The comparison of a measurement with and without the attenuation is discussed in Appendix C.2 and shows that in the two cases the decay time returned by a bi-exponential fit (τ_2) is similar. Here, the OD1.3 filter has been used systematically at high excitations when the condition for pile-up was not fulfilled anymore (indicated in Figure 6.4b, d and f by the shaded areas). At lower excitations, which are of prime interest, as discussed in the following, no attenuation of the PL emission is required and the fittings appear reliable.

It should be mentioned that the repetition rate has been kept constant (0.5 MHz) for all excitations only for sample Ag-1. It has been demonstrated for perovskites that the measured decay time shows a strong dependence with the laser repetition rate [203,204] (longer decay time for low repetition rates). This effect is usually attributed to the uncomplete depopulation of trap states between two pulses at high repetition rates, thus masking the actual trap density. In CIGS, it is not clear how much the repetition rate influences the measured decay times, especially when it is ensured that the decay ends before the next pulse, i.e., reaches the background level. It is however still better to keep the repetition rate constant for all measurements to avoid this uncertainty, provided that the measured decay ends before the next pulse, even for the highest excitations. Due to the limited experience with TRPL at the time of the measurements, the repetition rate for the samples Ag-3 and Ag-2.3 was decreased from low to high excitation. For sample Ag-3, the repetition rate has been set to $f_{\mathrm{rep}} = 0.5$ MHz and reduced to $f_{\mathrm{rep}} = 0.2$ MHz only for the highest excitation. For sample Ag-2.3, the repetition rates $f_{\mathrm{rep}} = \{5, 2, 1, 0.5\}$ MHz have been used. While the observed transient's trends seem to be coherent with the expectations despite the different f_{rep}, the PL intensity decreases slightly at lower f_{rep} (for a given excitation, and always measuring over the same duration). This explains why the intensity of the two highest excitations for sample Ag-3 (Figure 6.4c dark red and black) are comparable, even though there is a factor 2.5 difference in the excitation. Similarly, for the sample Ag-2.3 at low excitations, the PL intensity is lower for the third transient (Figure 6.4e blue) compared to the second one (purple), despite the higher excitation. Regardless of f_{rep}, according to the SRH lifetime excitation dependence discussed in section 6.1.1, a longer decay time is expected at higher excitations.

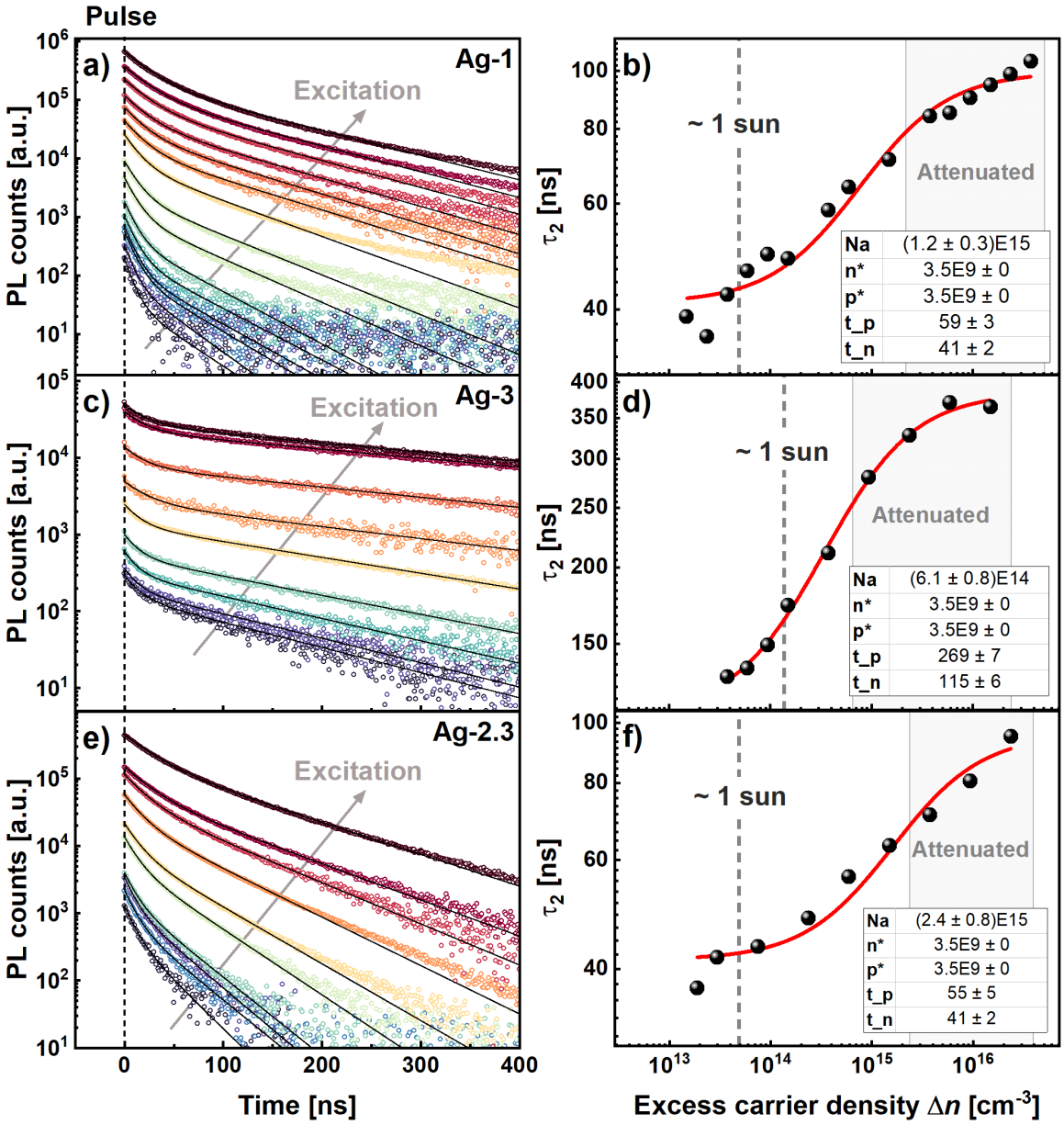

Figure 6.4. TRPL transients measured under different excitations plotted in semi-logarithmic scale after background subtraction for a) sample Ag-1, c) sample Ag-3 and e) Sample Ag-2.3. The data is binned by 10 data points. The time scale is identical for all three graphs, but the intensity is in arbitrary unit, not comparable from one graph to another. The transients are fitted (before background subtraction) with a bi-exponential function (black line) and τ_2 at each excitation is extracted and displayed in b), d) and e) associated respectively to a), c) and e). The shaded areas highlight the cases when an OD1.3 filter was used to attenuate the sample emission. The excess charge carriers scale is identical for all three graphs and the steady state "one sun" carrier generation is indicated by the gray dashed line for each sample. A fit according to Equation (6.1) is performed and the fit parameters are reported in the

corresponding table. The auxiliary carrier densities n^* and p^* are fixed to $n^* = p^* = n_\mathrm{i} = 3.5 \cdot 10^9$ cm^{-3}.

The laser excitation power is converted into an excess carrier density Δn considering the small volume defined by the absorption coefficient, according to Equation (2.38). To give a comparison, it is possible to estimate the steady state "one sun"-equivalent carrier generation, considering the thickness of the absorber $d = 2.4$ µm (instead of the absorption coefficient) to define the generation volume and the electron lifetime obtained from the fit in Figure 6.4. Taking a band gap of 1.04 eV, the "one sun" carrier generation (cf. Equation (C.1) in Appendix C.1) for each absorber from Figure 6.4 is estimated and indicated in the corresponding graph. It can be seen that the measured decay time at this value does not necessarily correspond to the minority carrier lifetime as it is not in the low injection plateau range (especially for sample Ag-3).

For all three samples, the slow decay time increases with the injection level, as observed in Figure 6.4b, d and f. For the samples Ag-1 and Ag-2.3, τ_2 grows by about ~ 60 ns over almost 4 orders of magnitude, whereas it grows by ~ 230 ns for the sample Ag-3 over only 3 orders of magnitude. Moreover, at a given Δn, decay times considerably larger are measured for sample Ag-3 compared to the two others. While the τ_2 excitation dependence for sample Ag-1 (Figure 6.4b) seems to follow a power law (straight line in a double logarithmic plot), the dependence for samples Ag-3 and Ag-2.3 shows more of an "S-shape" behavior, similar to the one expected for the SRH lifetime excitation dependence discussed in section 6.1.1. The red curve in Figure 6.4b, d and f represents a fit to the data according to Equation (6.1), where the doping density N_A and the carriers' lifetime τ_p and τ_n are left as fitting parameters. The auxiliary densities, however, are fixed and approximated by $n^* = p^* = n_\mathrm{i}$. The intrinsic carrier density is calculated based on the definition given in Equation (2.6), assuming a band gap of 1.05 eV and the effective masses $m_\mathrm{e}^* = 0.1 m_0$ and $m_\mathrm{h}^* = 0.7 m_0$ for the electrons and holes [205], where the free electron mass is $m_0 = 9.1 \cdot 10^{-31}$ kg, leading to $n_\mathrm{i} = 3.5 \cdot 10^9$ cm^{-3}. The fit returns similar values for the carriers' lifetimes in the case of samples Ag-1 and Ag-2.3, $\tau_\mathrm{n} \approx 40$ ns and $\tau_\mathrm{p} \approx 60$ ns, while longer lifetimes are measured in sample Ag-3 (with the highest AAC), $\tau_\mathrm{n} \approx 115$ ns and $\tau_\mathrm{p} \approx 270$ ns. These values are in the range of what is typically reported in the literature as discussed in section 2.2.3. The longer lifetimes measured for the sample Ag-3 go in pair with a lower doping extracted from the fit, $N_\mathrm{A} \approx 6 \cdot 10^{14}$ cm^{-3},

compared to the one of samples Ag-1 and Ag-2.3, $N_A \approx 1.5 \cdot 10^{15}$ cm^{-3}. The doping difference between the samples is most probably a consequence of the larger Ag content in sample Ag-3, as commonly observed in ACIGS solar cells (cf. chapter 5). Nevertheless, the doping densities extracted from the fit in all cases is about one order of magnitude lower than the expected ones (from CV) for these samples. Table 6.1 summarizes the doping densities (first three columns) and electron lifetimes (last two columns) for the three samples obtained from different methods. In addition to the doping density measured by CV and obtained from the fit shown in Figure 6.4, an estimation of N_A based on the band gap and qFls measured by absolute PL and τ_n (from the fit) is provided. A graphic comparison of the doping densities is provided in Figure 6.5. The last two columns of Table 6.1 give values for the electron lifetime, one returned by the fit of the decay times and the other calculated based on the electrical measurements, i.e., considering the V_{OC} (instead of qFls) measured by IV and the doping obtained from CV. The calculation of the doping from TRPL/PL and lifetime from CV/IV is possible assuming that in a p-type semiconductor the non-equilibrium hole density (cf. Equation (2.4)) is approximately equal to the doping density ($p \approx N_A$). The detailed calculation of the doping and the lifetime, and corresponding error, can be found in Appendix C.1.

While the doping density obtained from the fit of the TRPL decay time is surprisingly low, the ones measured by CV and calculated from the TRPL/PL measurements are in the same range. It is important to stress that CV measurements are performed on encapsulated submodules (i.e., after buffer and window layers deposition and undisclosable optimization treatments), whereas the TRPL/PL measurements are performed on absorbers (bare or with a buffer layer). Moreover, the absorbers received a Na-PDT before being completed into solar cells and measured electrically. As discussed in chapter 5, this may be a reason for discrepancies observed between the two measurement methods, in particular for the sample Ag-3 for which a qV_{OC} significantly larger than the qFls has been measured.

Table 6.1. Doping obtained from CV measurements, from the fit of the TRPL decay time and from the calculation shown in Appendix C.1 based on PL (qFls and E_g) and TRPL measurements (τ_n from fit). The last two columns give the electron lifetime calculated based on the CV doping and the measured V_{OC} as shown in Appendix C.1, and obtained from the decay time fit. The results for the samples Ag-

1, Ag-3 and Ag-2.3 (from Figure 6.4) and for samples 1, 2 and 3 (absorbers with or without Na-PDT, cf. Figure 6.7) are reported. No CV nor IV data is available for the sample 2.

	Doping from… [cm^{-3}]			τ_n from… [ns]	
Sample	**CV**	**Fit**	**TRPL/PL**	**CV/IV**	**Fit**
Ag-1	$(2.0 \pm 0.6) \cdot 10^{16}$	$(1.2 \pm 0.3) \cdot 10^{15}$	$(2.8 \pm 0.5) \cdot 10^{16}$	20 ± 28	41 ± 2
Ag-3	$(2.2 \pm 1.1) \cdot 10^{16}$	$(6.1 \pm 0.8) \cdot 10^{14}$	$(8.5 \pm 1.1) \cdot 10^{15}$	134 ± 89	115 ± 6
Ag-2.3	$(1.5 \pm 0.7) \cdot 10^{16}$	$(2.4 \pm 0.8) \cdot 10^{15}$	$(4.3 \pm 1.2) \cdot 10^{16}$	50 ± 56	41 ± 2
Sample 1	$(5.1 \pm 0.1) \cdot 10^{16}$	$(3.1 \pm 0.6) \cdot 10^{15}$	$(1.5 \pm 0.2) \cdot 10^{16}$	63 ± 49	21 ± 1
Sample 2		$(5.1 \pm 1.2) \cdot 10^{15}$	$(2.8 \pm 0.4) \cdot 10^{16}$		23 ± 1
Sample 3	$(3.9 \pm 0.1) \cdot 10^{16}$	$(1.1 \pm 0.3) \cdot 10^{15}$	$(3.6 \pm 1.2) \cdot 10^{16}$	82 ± 64	26 ± 2

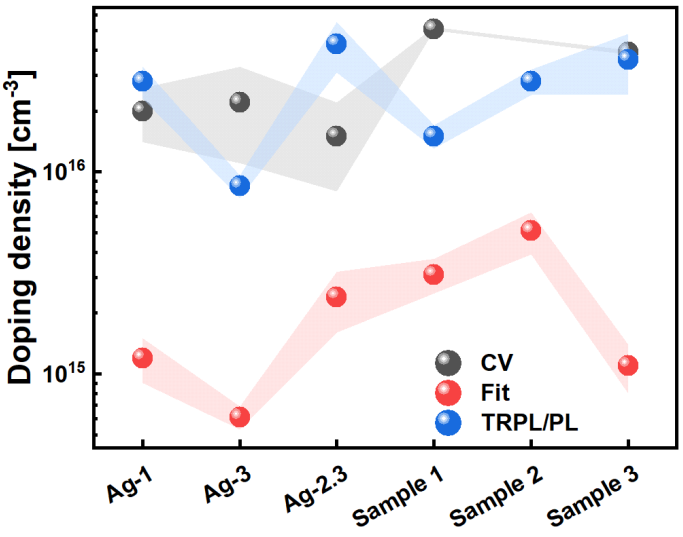

Figure 6.5. Graphic representation of the doping densities reported in Table 6.1 for the three different determination methods: from CV measurements on cells (black), from the fit of the measured decay time on absorbers (red) and from the combination of the TRPL and PL quantitative analysis (blue). The shaded areas represent the error on the doping densities.

However, comparing the doping densities obtained from the two optical measurements (fit and TRPL/PL), despite the difference in the values, the trend for the Ag-alloyed samples is similar. It is hence legitimate to question the accuracy of the excess carrier density determination. If

the actual Δn is one order of magnitude larger than the calculated one, the doping density from the fit would be one order of magnitude larger and match the expected one. Considering Equation (2.38) in section 2.5 which is used to define the excess carrier density, the main source of error would come from the determination of the beam radius, but it would require than the measured radius r is ~ 3 times larger than the actual one in order to account for difference in the excess carrier density since $\Delta n \sim r^{-2}$. It is hardly believable that such an error is made on the beam radius, considering the generally very good agreement observed between the absolute PL and IV measurements. This suggests that the low fitted doping density is due to other phenomena or to too simple considerations. In fact, this fitting assumes a single defect state and does not consider any metastabilities, which are known to exist in this material and are responsible for increasing the net doping upon illumination. The measurements were performed starting at low excitation and ending at high excitation. It could therefore be argued that the doping density is not constant throughout the whole experiment and that the model used to fit the data cannot trustfully represent the situation. Jensen *et al.* [206] discuss how the presence of metastable defects reduces the electron lifetime due to an increase in the doping density. López Salas *et al.* [207], combining experiment and simulation, further demonstrate that in CIGS it is the increase in the doping density (after light soaking) that has the strongest influence on the measured decay times. Considering here Equation (6.1), a very naïve model is derived considering that the doping density varies with the excess carrier density as $\Delta N_{\mathrm{A}} \sim \Delta n^{X}$. As can be seen in Figure 6.6, it is found that with fixed charge carriers' lifetimes $\tau_{\mathrm{n}} = 115$ ns and $\tau_{\mathrm{p}} = 300$ ns, letting the doping density increase from $N_{\mathrm{A}} \approx 4 \cdot 10^{14}$ cm^{-3} to $N_{\mathrm{A}} \approx 2 \cdot 10^{15}$ cm^{-3} (with $X = 0.16$), a reasonably good representation of the experimental data is obtained. While really simple, it shows that in the presence of metastabilities, similar behavior of the measured decay time could be expected. This may contribute to the very low doping densities returned by the fit.

However, for one of the samples (Ag-2.3), the reversibility of the measurement has been verified, i.e., after the highest excitation has been reached, it was gradually reduced to the lowest one following the same excitation steps (see Appendix C.2). No significant change in the decay time could be observed between the two measurements, suggesting that the

metastable defects are converted from donors to acceptors already at the lowest excitations, or faster than the measurement time.

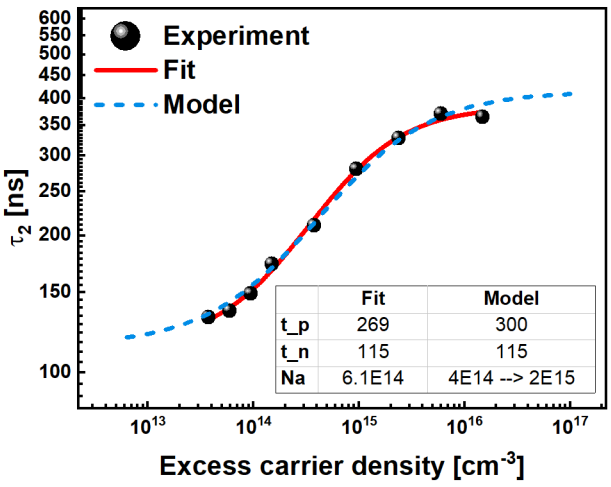

Figure 6.6. TRPL decay time measured at different excitations for the sample Ag-3 as shown in Figure 6.4. The red line is the fit according to Equation (6.1) while the dashed blue line models the experimental data considering a variable doping density. The parameters of the fit and used for the model are indicated in the floating table.

Finally, as shown in Appendix C.1, it is possible to estimate the minority carrier lifetime based on the cell's electrical characterization. However, due to the non-negligible measured V_{OC} variation (over seven different measurements for each of the "Ag" samples, cf. Figure 5.14), the error on the calculated lifetime is extremely large, as seen in Table 6.1. It is thus complicated to have a meaningful comparison of the two methods in terms of electron lifetime, although the lifetime calculated from CV/IV is generally in the same range as the one measured from TRPL (for samples Ag-1, Ag-3 and Ag-2.3). On one hand, from both methods (CV/IV and TRPL) the electron lifetime becomes longer for the highest Ag content (sample Ag-3), which is good for obtaining higher V_{OC}. On the other hand, from the optical measurements, the doping density seems to decrease for this specific sample compared to the two others, which would lead to a lower V_{OC}. However, after the submodule completion (including additional layers and treatments), the doping density of the sample Ag-3 measured from CV is slightly

larger than the two others, demonstrating the beneficial effect of the treatments performed during the cell-making process.

Using the same approach as for the Ag-alloyed absorbers, a second set of samples is investigated to determine the influence of a Na post-deposition treatment on the doping density and on the minority carrier lifetime. For this purpose, three samples are prepared: a reference absorber receiving no Na-PDT (sample 1), an absorber receiving no Na-PDT (sample 2) but undergoing an annealing in S-containing atmosphere and an absorber receiving a Na-PDT in a S-containing atmosphere (sample 3). All samples already have Na in the precursors stack, the Na-PDT provides additional Na. Furthermore, a ZnOS buffer layer is deposited by CBD at LPV and prevents oxidation of the absorbers' surface over time. The effect of the buffer on the measured decay time is addressed in more details in section 6.3. The laser repetition rate has been changed from 2 MHz to 1 MHz at high excitations for samples 1 and 2, while four different f_{rep} were used for the sample 3 ($f_{\mathrm{rep}} = \{5, 2, 1, 0.5\}$, similarly to sample Ag-2.3).

The TRPL decay time (τ_2) at different excitation levels is plotted in Figure 6.7 for each of the samples and a fit according to Equation (6.1) is performed. The parameters of the fit are reported in the floating table in Figure 6.7 and the doping densities and electron lifetimes are summarized in Table 6.1, along with the corresponding CV measurements. Unfortunately, no CV nor IV data is available for the sample 2. The results for the samples 1 and 2, with no extra Na-PDT, are very similar, leading to comparable carriers' lifetimes ($\tau_{\mathrm{p}} \approx 61$ ns and $\tau_{\mathrm{n}} \approx 22$ ns) and comparable doping densities ($N_{\mathrm{A}} \approx (3-5) \cdot 10^{15}$ cm^{-3}). The sample 3, which received the Na-PDT, exhibits barely significant longer carriers' lifetimes ($\tau_{\mathrm{p}} \approx 72$ ns and $\tau_{\mathrm{n}} \approx 26$ ns) and a slightly lower doping density ($N_{\mathrm{A}} \approx 1.1 \cdot 10^{15}$ cm^{-3}). The latter point is surprising since it is commonly reported that Na incorporation increases the net doping density [208–211]. However, the doping densities obtained from the fit are again about one order of magnitude lower than the ones calculated from TRPL/PL (see Table 6.1 and Figure 6.5). Moreover, from TRPL/PL, the highest doping density is found for the Na treated sample, more in line with the literature. The larger computed value is a result of the larger qFls measured for the sample 3 following the Na-PDT ($\Delta E_{\mathrm{F}} \approx 640$ meV vs. $\Delta E_{\mathrm{F}} \approx 610$ meV for sample 1, both having the same band gap). CV measurements on cells made from samples 1 and 3 yield doping densities of $N_{\mathrm{A}} \approx 5.1 \cdot 10^{16}$ cm^{-3} and of $N_{\mathrm{A}} \approx 3.9 \cdot 10^{16}$ cm^{-3}, respectively, contradicting the trend of the calculated doping density from TRPL/PL. It should be noted that contrary to the

"Ag" samples, a single CV measurement has been done on samples 1 and 3, leading to no statistical results. Based on the CV doping density and V_{OC} measured on these cells (not shown) electron lifetimes of $\tau_n \approx 63$ ns (sample 1) and $\tau_n \approx 82$ ns (sample 3) are obtained and are about a factor 3 larger than from the fit (again with a significant error on the value). This could be attributed to the presence of metastable defects. The laser excitation during PL and TRPL measurements may trigger the conversion of metastable donors into acceptors, leading to an increase in the doping density and to a decrease in the electron lifetime. Contrastingly, the CV measurements are performed in the dark and might not induce the metastable conversion, provided that the applied voltage does not shift E_{Fn} over the transition point.

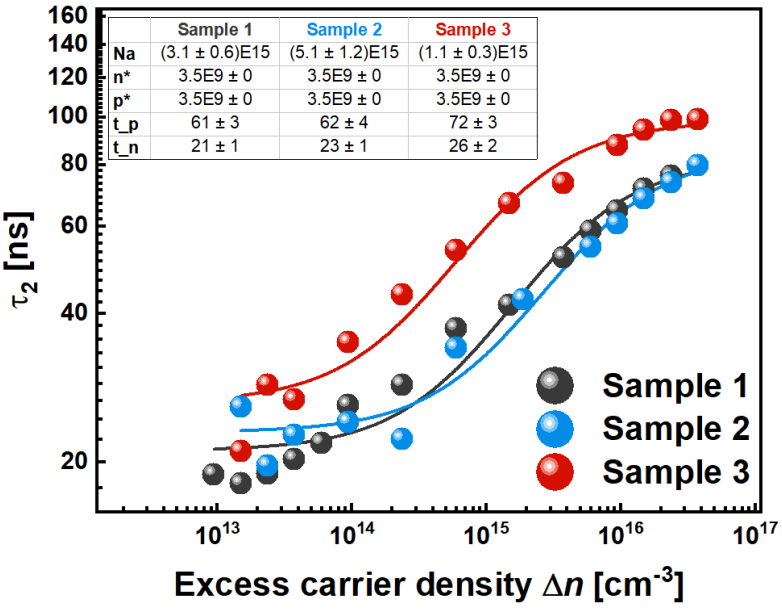

Figure 6.7. Measured decay time at different laser excitations for the samples 1, 2 and 3. These samples have a ZnOS buffer (deposited by CBD). A fit according to Equation (6.1) is performed and the fit parameters are reported in the floating table for each sample. The auxiliary carrier densities n^* and p^* are fixed to $n^* = p^* = n_i = 3.5 \cdot 10^9$ cm^{-3}.

In summary, both measurement methods (optical and electrical) may indicate that with a Na-PDT (sample 3) the electron lifetime slightly increases. It is speculated that Na passivates grains boundaries and defects in CIGS absorbers [178,209,211] and hence measuring a longer minority carrier lifetime is coherent with the expectations. Sample 2, which received a heat treatment but no Na, shows only minor differences from sample 1, suggesting that the changes observed in sample 3 come from the additional Na and not from the heat treatment. However,

no significant trend in the doping density is obtained when comparing the two methods, one reason for it probably being the lack of statistics.

6.2.2. Temperature dependence measurements

On one hand, as discussed above, excitation dependent TRPL measurements allow for reliable carriers' lifetime determination, and combined with absolute PL investigation, lead to an estimation of the doping density. On the other hand, it is proposed that temperature dependent TRPL measurements may be used for defect analysis, returning the shallow defect state's energy that acts as a charge carrier trap [192,193]. Using a Peltier stage to heat up the samples, TRPL transients are measured for samples 1 and 3 (i.e., without and with Na-PDT) at 23°C, 33°C, 44°C and 53°C. To verify that no temperature-induced degradation is provoked, and that the measurement is reversible, the sample 1 (with ZnOS) is allowed to cool back down to 23°C and is measured again under the same conditions after 1h and the next day. The same long decay time as the initial measurement is recovered in both cases, hinting that no long term changes are induced in the absorber.

For each temperature, the transients and the corresponding τ_2 are shown in Figure 6.8 for the samples 1 and 3. Not only the buffered absorbers discussed in section 6.2.1 are investigated, but also the corresponding bare absorbers – after a soft KCN etching. The respective long decay times are plotted in Figure 6.8b and d. The decay times measured for the bare absorbers are much lower than the ones of the buffered absorbers. This difference is attributed to the surface degradation of the samples over time (cf. section 3.1), since the measurements were performed about 6 months after the growth and even a 5% KCN etching hardly recovers the initial absorber quality. The excitation level is kept constant at all temperatures and is approximately the same as the highest one used in Figure 6.7, i.e., $\Delta n \approx 4 \cdot 10^{16}$ cm^{-3}. A measurement of the sample 1 at lower excitation ($\Delta n \approx 4 \cdot 10^{15}$ cm^{-3}) is provided in Appendix C.3. The measured decay time is shorter, as expected from the previous section, and a similar temperature dependence as for the higher excitation is observed. In Figure 6.8, the measured decay time for the sample 3 at 23°C ($\tau_2 = 224$ ns) differs significantly from the one reported in Figure 6.7 ($\tau_2 = 99$ ns) at similar excitation ($\Delta n \approx 4 \cdot 10^{16}$ cm^{-3}). The reason behind this unexpected discrepancy is the different time bin sizes used for these two measurements. In the previous section, the bin size has been set to 0.2 ns whereas a bin size of 19.5 ns has been used

in Figure 6.8c. With a larger time bin, the transient features at early times (initial fast decay) are less pronounced and the bi-exponential fit returns different values for the fit parameters. A transient comparison of the sample 3 with different time bin sizes can be found in Appendix C.4. It shows that a fit of the long decay part of the transients (ignoring the early times) leads to similar decay times regardless of the binning used for the measurement. In this section, the important information is the dependence of τ_2 on the temperature, rather than its actual value. Regardless of its value at RT, τ_2 decreases as the temperature increases (also for the lower excitation shown in Appendix C.3). Based on the discussion in section 6.1.2, the decay time evolution can be due to thermal detrapping as described by Equation (6.2), or to multiphonon emission as described by Equation (6.4). Mathematically, the difference between the two models is that the exponent b which defines the power law dependence of the temperature, is a fit parameter in Equation (6.2), while it is fixed to $b = 1$ in Equation (6.4). In Figure 6.8b and d, the solid gray lines represent the fit assuming thermal detrapping (free b) and the red dashed lines the fit considering multiphonon processes ($b = 1$). The two models essentially lead to the same fit (overlap of the gray lines and red dashed lines). Furthermore, due to the small temperature range ($T_{\max} - T_{\min} \approx 30$ K) and the sparse data points, it is difficult to obtain a reliable fit. It follows that in the first case (free b), the derived trap energy E_{d} varies from 0.1 meV to 130 meV away from the conduction band with errors larger than $10 \cdot E_{\mathrm{d}}$, as reported in Table C.1 in Appendix C.3. Similarly, the exponent b takes values between 0.6 and 7 and the error is again many times larger than the value itself. In the second case (fixed b), the fit parameter C from Equation (6.4) varies from 89 meV to 206 meV (cf. Table C.1). According to the theory, it is related to the activation energy necessary to trigger the multiphonon processes.

While in the two cases the values themselves are contained in a reasonable range, drawing any conclusions from such fits does not make sense. Therefore, although the temperature dependence of the measured decay time is evident, its interpretation is more ambiguous. Based solely on TRPL investigation, and especially with such a small temperature range, it seems impossible to determine the origin of the dependence. Nevertheless, combining with the CV measurements performed in the dark, one might speculate on the dominating process. Assuming the lifetime determined from CV (τ_{CV}) to be the "real" minority carrier lifetime, a comparison with the one measured from (excitation dependent) TRPL (τ_{n}) leads to three

scenarios. (i) $\tau_n > \tau_{CV}$, the measured lifetime is longer than the "real" one, indicating electron trapping, and the temperature dependence may be interpreted as thermal detrapping. (ii) $\tau_n = \tau_{CV}$, the measured lifetime is the "real" one, and thus the temperature dependence is likely to arise from thermally activated multiphonon processes and/or recombination at the front surface, if the absorber is grown with a conduction band gradient at the front side, as discussed in section 6.1.2. (iii) $\tau_n < \tau_{CV}$, the measured lifetime is shorter than the "real" one, suggesting that the net doping is significantly different between the two measurements, and hence points towards metastable defects (cf. section 2.4.4) in addition to one of the effects discussed in (i) and (ii). In the present study, the measured TRPL lifetime is shorter than the one from CV ($\tau_n < \tau_{CV}$), hinting at the presence of metastable defects.

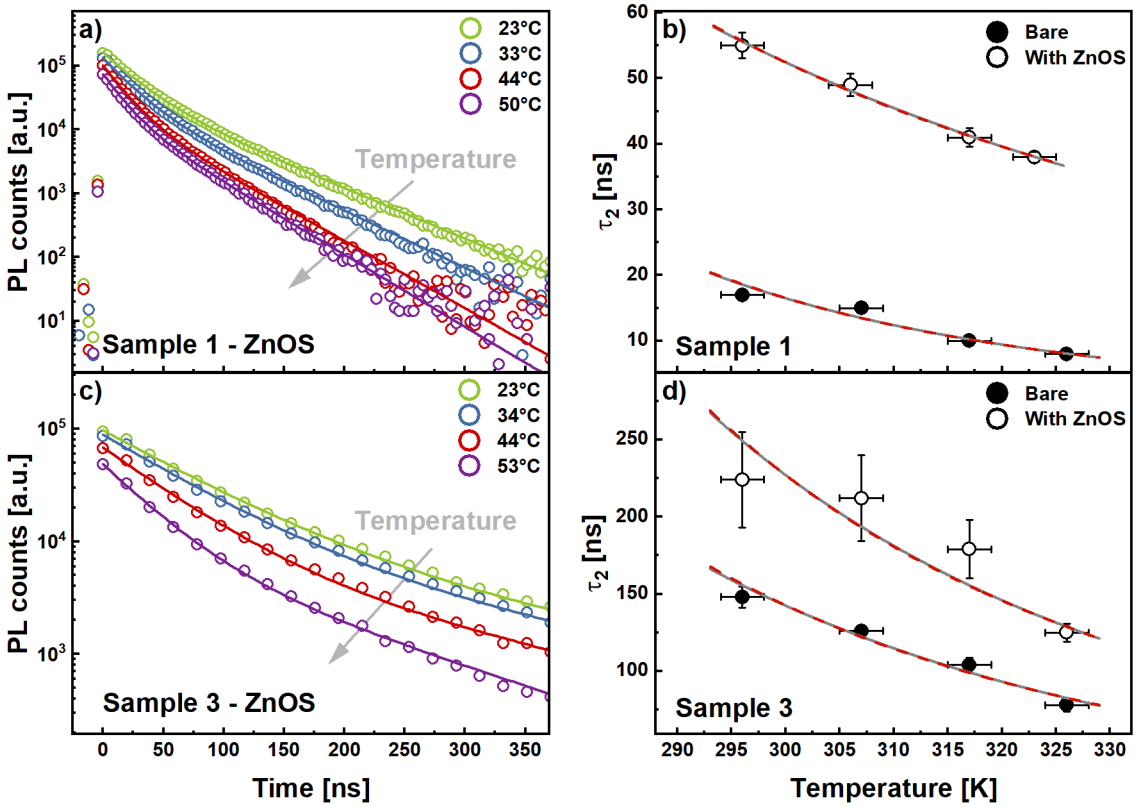

Figure 6.8. TRPL transients for the samples 1 and 3 with a ZnOS buffer (cf. section 6.2.1), at different temperatures above RT, as indicated by the legend in a) and c). The data points are experiment and the plain lines represent the bi-exponential fit. The transients for the bare absorbers are not shown, but the long decay time (τ_2) is reported for each temperature in b) and d) for both cases, KCN etched bare absorbers (full dots) and absorbers covered with ZnOS (open dots). The solid gray lines are a fit to the data according to Equation (6.2) while the dashed red ones are a fit according to Equation (6.4). The

error on the temperature is empirically estimated at ± 2 K and the error on τ_2 is taken from the bi-exponential fit.

To summarize, observing a temperature dependence of the measured lifetime is not sufficient to conclude that carrier trapping is occurring and hence, extracting trap energies from this dependence may be misleading. Combining with CV measurement may help differentiate between trapping and multiphonon processes.

6.3. The effect of the buffer layer

Until this point, no real difference in the transient shape (particularly at short times after the excitation pulse) has been observed between the samples with a ZnOS buffer (from CBD) and the bare ones, whether in the excitation nor in the temperature dependence of the decay time. In this section, the influence of the buffer thickness on the decay time is investigated and a comparison between the CBD-deposited ZnOS buffer and a sputtered ZnOS buffer is made.

6.3.1. Independence of the buffer thickness

When the n-type buffer is deposited onto the p-type absorber, a SCR forms at the junction. In PL and TRPL, the presence of the SCR is usually ignored due to the small buffer thickness. To verify it, four different ZnOS buffer thicknesses are deposited by CBD on a "standard" CIGSSe absorber. The thickness is not precisely controlled, but by interrupting the process at different times, variation of the thickness is ensured (confirmed by the different colors in Figure 6.9). From experience, based on the deposition time and the color, the thicknesses are estimated to range from ~ 20 nm to above 50 nm (but most probably < 70 nm). It is expected that the thicker the buffer is, the larger the SCR becomes and therefore charge separation effects could take place.

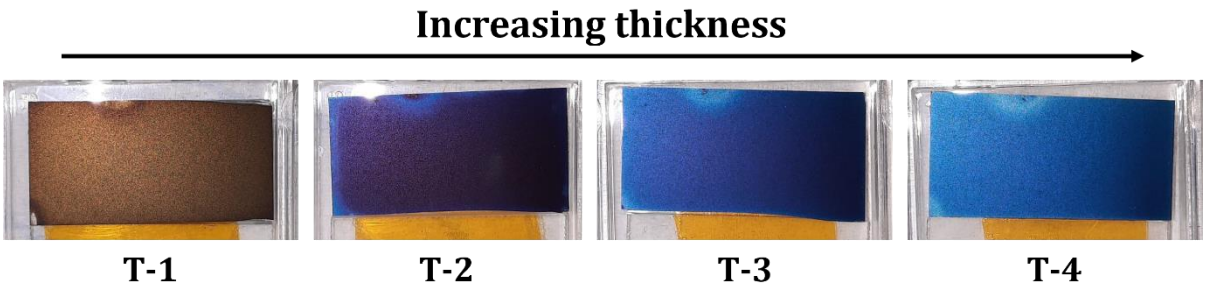

Figure 6.9. Optical image of the four samples after buffer deposition by CBD. The thickness increases from sample T-1 (brown) to sample T-4 (light blue).

The excitation is varied over one order of magnitude, from $\Delta n \approx 4.7 \cdot 10^{15}$ cm^{-3} to $\Delta n \approx 4.7 \cdot 10^{16}$ cm^{-3} and the transients are compared in Figure 6.10a. The detector NIR-PMT H10330C-75 (cf. section 3.2.3) has been used for these measurements. For any given excitation, no significant change in the transient shape is detected from the thinnest to the thickest buffer. As discussed in section 2.5.2, charge separation, if happening, would impact the initial part of the decay, leading to a faster decay time shortly after the pulse. In the present case, all the samples display a slight bi-exponential behavior at low excitations (squares and circles in Figure 6.10a) and tend towards a mono-exponential decay at higher excitations (up and down triangles). The decay times returned by the bi-exponential fit are plotted in Figure 6.10b. As observed in section 6.2.1, higher excitation leads to longer τ_2 and each sample shows similar increase. The differences in the measured decay times between the samples do not follow the thickness changes. In fact, the longest τ_2 is registered for the sample T-1 and the shortest one for the sample T-2, with $\tau_2^{"T-2"} \approx 0.77 \cdot \tau_2^{"T-1"}$ at all excitations. Therefore, it is concluded that even with a thicker buffer layer (deposited by CBD), no charge separation is detected from a TRPL investigation and that neither the fast nor the slow decay times are not significantly impacted. However, the situation is different with the sputtered ZnOS buffer layer.

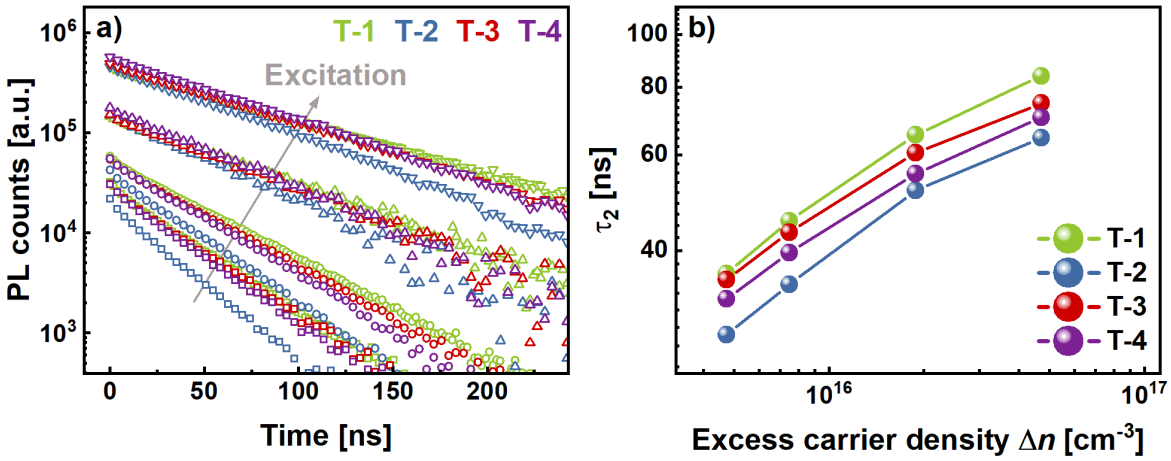

Figure 6.10. TRPL measurements of the samples T-1 to T-4 at four different excitations. The transients are plotted in a) and the long decay time is reported in b). The error on τ_2 given bit the bi-exponential fit of the transient is smaller than the size of the dots. The samples are identified by the color code.

6.3.2. Comparison between CBD-deposited and sputtered ZnOS buffer

One of the "standard" CIGSSe absorbers (with Na-PDT) on which a ZnOS buffer layer of thickness ~ 65 nm has been sputtered (at AVANCIS), is investigated in this section. The excitation is varied over about one order of magnitude, covering the range $\Delta n \approx 3.7 \cdot 10^{15}$ cm^{-3} to $\Delta n \approx 4.7 \cdot 10^{16}$ cm^{-3} and the repetition rate is kept constant at all excitations $f_{\mathrm{rep}} = 0.2$ MHz. As expected, the sample emission intensity increases with the excitation, but contrary to the samples with the CBD buffer, the decay time becomes shorter at high excitation. Figure 6.11 shows the transients' evolution for the various excitations, as well as the extracted long decay time. Although this absorber is very similar to the ones investigated in the previous sections, the measured decay times are much longer – hundreds of nanoseconds vs. tens of nanoseconds for the bare absorbers or absorbers covered with a CBD buffer. Such long decay times may be an indication of charge carrier trapping. Sugiyama *et al.* [212] demonstrated by impedance spectroscopy that the sputtering of the buffer can damage the interface between the buffer and the absorber, which may generate such defects responsible for carrier trapping. While no plateau of the decay time is observed over the small measured range, according to the SRH-lifetime excitation dependence (cf. section 6.1.1) a decreasing decay time is associated to shallow defect. Moreover, the decreasing decay time fits with the simulations by Maiberg *et al.* [79], where the authors suggest that the average trap occupation increases with higher excess carrier density, and consequently the influence of the electron capture on the

decay time decreases. Therefore, the TRPL results may indicate the formation of shallow defects during the sputtering of the buffer layer.

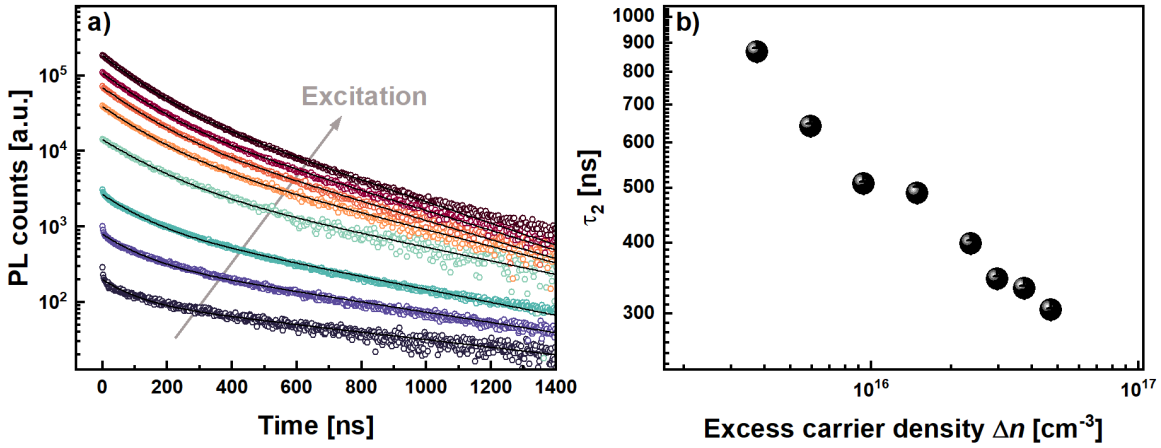

Figure 6.11. Excitation dependence TRPL measurement of a "standard" absorber (with Na-PDT) with a sputtered ZnOS buffer layer. The transients and the respective bi-exponential fit are displayed in a). The data is binned by 10 data points. The corresponding long decay time is reported in b). The error is taken from the fit.

Furthermore, a striking feature of the transients in Figure 6.11a is the very sharp decay that happens over the first 5 ns for the three lowest excitations. This initial decay cannot be fitted by the bi-exponential function, as can be seen from the fitting curves. As the excitation is further increased, the initial fast decay disappears. Heise *et al.* [82] report on similar behavior and attribute it to charge separation. As discussed in section 6.3.1, no charge separation effect could be detected for the samples with a CBD-deposited buffer over the same excitation range, regardless of the buffer thickness. It is therefore speculated that the sputtered ZnOS is more doped than the CBD-deposited one, generating a larger SCR, detectable in the TRPL transients. This hypothesis is supported by a larger ODF (cf. section 2.4.4) in the case of the sputtered buffer. The same "standard" absorber, with and without additional Na-PDT, receives a ZnOS buffer layer by CBD and by sputtering. As shown in Figure 6.12, independent of the Na treatment, the sample with the sputtered buffer exhibits an ODF about 0.2 larger than the one with the CBD buffer. As discussed in section 2.4.4, if a SCR is formed, recombination in this region leads to a larger diode factor, as observed in the present case.

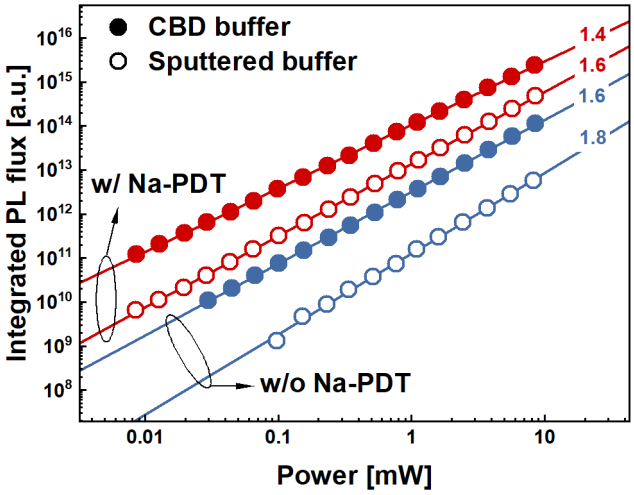

Figure 6.12. Integrated PL flux vs. laser power at the sample position from an excitation dependent PL measurement of a "standard" absorber. Samples with no Na-PDT are in blue and with an additional Na-PDT in red. The full dots correspond to the CDB-deposited ZnOS and the open ones to the sputtered ZnOS.

6.4. Summary

In this chapter, the potential of time-resolved photoluminescence measurements has been presented. Investigating various CIGSSe absorbers, Ag-alloyed, with or without additional Na-PDT and with or without buffer layer, it is found that TRPL can be used as a quantification method for the charge carriers' lifetime and doping density. Provided that a wide enough excitation range is covered (4 – 5 orders of magnitude appears ideal for these samples) and that a good signal can be detected at very low excitation, it is possible to obtain a reliable estimation of the charge carriers' lifetime. Following the excitation dependence of the SRH lifetime, a fit of the measured decay time returns the electron and hole lifetimes. It is found that the carriers' lifetime is significantly longer in the absorber with the highest Ag content, while the Na-PDT seems to increase it only slightly. Combining the measured lifetime with absolute PL measurements, the doping density can be calculated, yielding values comparable to that from CV measurements. Without exception, the doping density obtained from the fit of the decay time is about one order of magnitude lower than the expected one. As of now, it is uncertain if this results from an underestimated excess carrier density or if it is due to too many

approximations in the model. For instance, the presence of metastable defects, converting from donors into acceptors upon illumination, has been ignored.

A preliminary investigation of the temperature dependence of the measured decay time has been conducted. Because of the rather small temperature range experimentally covered, no conclusion about the origin of the dependence could be drawn. Three possible hypotheses are discussed, thermal detrapping, thermal activation of multiphonon recombination and surface recombination in the case of a conduction band gradient at the front side of the absorber. It is proposed that combining temperature and excitation dependent TRPL measurements, a distinction between the three mechanisms can be made, although no direct evidence could be provided in this chapter.

Finally, it is demonstrated that in the case of a CBD-deposited ZnOS buffer layer, the thickness of the buffer (< 70 nm) does not affect the TRPL transients. However, absorbers receiving the standard sputtered ZnOS buffer processed at AVANCIS exhibit charge separation features in the transients. It is speculated that this buffer is more doped, leading to the formation of a non-negligible space charge region. A larger optical diode factor supports the explanation. Moreover, absorbers with the sputtered buffer show a significantly longer decay time that decreases with increasing excitation. The latter behavior is attributed to trapping and detrapping of the charge carriers. An excitation dependent investigation over a larger excess carrier density range (~ 4 orders of magnitude) and a complementary temperature dependent measurement could provide additional evidence of shallow defects.

To conclude, this chapter explores the possibilities offered by TRPL. An excitation dependence of the measured lifetime is expected for SRH recombination and it is necessary to measure over several orders of magnitude of excitation in order to extract charge carriers' lifetime. The measured temperature dependence of the lifetime is not necessarily due to detrapping (in particular when the decay time increases with excitation) but may arise from multiphonon processes. When measuring a buffered absorber, an initial fast decay is likely due to the formation of a SCR.

Chapter 7

Summary and outlook

The aim of this thesis was to characterize industrial $Cu(In,Ga)(S,Se)_2$ absorbers, principally by photoluminescence. The absorbers studied in this work were all provided by AVANCIS, within the scope of the POLCA project, and grown with the typical double graded architecture of their standard process. Different sets of absorbers were investigated to determine the influence of the precursor stack GGI, the Na-PDT and the Ag-alloying on the performance and band gap gradient. To complement the absolute PL and time-resolved PL measurements performed at LPV, various collaborations with European research groups were organized. These collaborations significantly contributed to the findings of this thesis, providing experimental results from measurement techniques such as cathodoluminescence spectroscopy, Raman spectroscopy or TEM-EDX investigation.

From a depth-resolved compositional analysis of the absorbers (by GDOES, on a relatively large area – spot diameter of ~ 2.5 mm), the GGI profile is obtained, showing a relatively flat part until ~ 700 nm from the front surface before gradually increasing towards the back contact. Although S should affect the band gap energy of the CIGSSe absorbers – particularly defining the front side gradient – the question arises whether S is actually introduced into the crystal lattice or simply accumulating at the grain boundaries. For this reason, the GGI profile alone is considered in this work to describe the band gap gradient. While the GGI profile suggests a gradual band gap change through the thickness of the absorber, it is demonstrated that in fact, principally two CIGSSe phases of low and high band gaps form close to the front and back sides, respectively. In the bulk of the absorber, these two phases coexist in different densities at a given depth, leading to an apparent smooth band gap gradient. On a sub-micron scale, CL reveals that there exist jumps in the band gap energy. Furthermore, combining a gradual etching of the absorber and PL measurements from the front and back sides at different

depths, it is concluded that this behavior holds for larger scales as well (collecting signal from hundreds of grains at once). Finally, Raman spectroscopy indicates the simultaneous presence of low and high GGI phases on the back side of the absorbers over a small area (3×3 mm^2). Taken together, a novel model for the band gap gradient in graded chalcopyrite solar cells is proposed, featuring the interlacing of two phases of different band gaps leading to an apparent gradual band gap change, as expected from a compositional analysis. At a later stage, cross-sectional TEM-EDX investigation was performed, providing experimental results in line with the proposed model.

The "standard" absorbers, i.e., prepared following the optimized growth process at AVANCIS, exhibit good performance, yielding efficiencies as high as 17.6% for submodules made out of the investigated absorbers (with anti-reflection coating). Nevertheless, depth-resolved PL measurements (through sequential etching of the absorbers) demonstrate that the high band gap phase is of lower quality than the low band gap one, in particular due to the formation of deep defect(s) with a broad PL emission peak around 0.9 eV. Improving the quality of this high band gap phase should therefore be of major interest in order to reach higher efficiencies. Reducing the GGI in the precursor stack results in a lower band gap of the high band gap phase, which in turns makes the deep defects shallower, possibly diminishing their detrimental impact on the cell performance. It would be interesting, as further investigation, to isolate the high band gap phase and perform defect analysis, e.g. measuring PL at low temperatures, to identify the defect origin and find ways to remove it. This would require optimizing the etching process (aiming for homogeneous etching of the surface) and removing the front side of the absorbers until most of the low band gap phase is gone.

In the fifth chapter of this thesis, the impact of Ag-alloying on the absorber morphology and performance is studied. A relative efficiency improvement of 1.6% compared to a "standard" reference submodule could be achieved by reducing the GGI in the precursor stack and alloying the absorber with a low Ag amount. Two series of ACIGSSe absorbers were prepared, varying the AAC and GGI in the elemental stack and modifying the growth temperature, as well as the Na content in the elemental stack. In general, it is shown by absolute PL investigation on the bare absorbers that in all but one of these absorbers lower non-radiative losses can be achieved compared to the Ag-free reference sample. In the best case, a reduction of the non-radiative losses by 30 meV is recorded, corresponding to the absorber with a reduced process

temperature. This result is very interesting from an industrial point of view, as growing at lower temperature could decrease the production costs. In addition, further optimization of the Ag-alloyed cell-making process would allow for full use of the reduced non-radiative losses and lead to higher improvement of the submodules. The already observed improvement may result from the larger grains (i.e., less grain boundaries) obtained upon Ag-alloying, in particular close to the Mo back contact. In addition, an enhancement of the interdiffusion of Ga and In is demonstrated, leading to a flattening of the GGI profile with increasing Ag content. Cross-sectional CL measurements reveal that with the highest Ag content (which is still relatively low) fewer band gap jumps are observed, compared to the Ag-free sample investigated in chapter 4. However, while a more gradual band gap increase from the front side towards the back side is obtained, the band gap decreases again close to the back contact in some regions. Such "reverse" band gap gradient is bad for solar cells as it would increase the back surface recombination, and consequently the non-radiative losses. Moreover, close to both surfaces (front and back) a certain lateral inhomogeneity is observed. The growth of ACIGSSe absorbers at AVANCIS is a new process still under development and the results from chapter 5 indicate that despite the already achieved performance improvement, special attention should be paid to the back interface.

Finally, an investigation of the dynamics of charge carriers, in particular the change of the lifetime with different treatments, such as Ag-alloying or Na-PDT, is performed in the last chapter of this thesis. From intensity dependent time-resolved photoluminescence measurements, the PL decay time of various absorbers is plotted for different excess carrier densities. In general, it is observed that the decay time becomes longer with increasing laser excitation. Considering that in chalcopyrites the lifetime is limited by SRH recombination (defect-assisted), it is possible to fit the decay time intensity dependence with the expected SRH-lifetime intensity dependence. From this model, reasonable charge carriers' lifetime can be estimated, and combined with absolute PL measurements lead to calculated doping densities similar to the ones measured by capacitance-voltage on the corresponding submodules. Because of the excitation dependence, measuring TRPL at a single excitation flux is not very meaningful and could lead to quite arbitrary numbers. It is found that the electron lifetime may increase upon Ag-alloying and with Na-PDT, which would be beneficial for achieving larger V_{OC}. Due to large uncertainty on the values, no significant trend in doping density can be concluded.

Furthermore, a short investigation of temperature dependent TRPL is conducted. While no quantitative information could be gathered, it is argued that the obvious temperature dependence of the measured decay time is not necessarily an indication of charge carriers trapping. In fact, thermally activated multiphonon processes would lead to similar behavior. Two temperature dependence models are proposed in the literature, dominating either at high or low temperatures. Therefore, future investigation, such as TRPL at low temperatures, could help defining the temperature range in which each model is relevant.

As mentioned in chapter 3 and 6, most of the excitation dependent TRPL measurements in this work are performed using a detector with low dark counts (which only worked for about two months before needing repair), allowing for measurements at low injection levels. However, in none of the investigated absorbers, the expected SRH-lifetime plateau at low injection level is clearly reached. Playing with the detection threshold of the system, one could probably measure the transient decays at even lower injection level than in this work, and experimentally observe the decay time plateauing. One step further could combine excitation and temperature dependent measurements (both over sufficiently large ranges of excitation fluxes and temperatures) to evaluate the potential trapping of the charge carriers. Furthermore, as observed in some samples, the transient decay curves move away from the bi-exponential function at high excitations and the origin of such behavior remains unclear at this point.

To conclude, a lot could be understood from the investigation of industrial high quality CIGSSe absorbers. Combining various optical characterization methods, a new band gap gradient model was proposed. Furthermore, an optical and electrical quantitative analysis showed that performance improvement could be achieved upon Ag-alloying in both, the absorbers and the submodules. Finally, it is demonstrated that reasonable lifetime and doping determination is possible from time-resolved photoluminescence on bare absorbers, provided that a wide enough range of excitation fluxes is covered.

Appendices

A. Appendix of Chapter 4

A.1. Raman spectroscopy on additional absorbers

As mentioned in section 4.3.1, Raman spectroscopy has been performed on more than one absorber. The three absorbers shown in Figure A.1 are "standard" absorbers and complement the Raman analysis discussed in the main text. They all have received an additional Na-PDT, but this treatment does not significantly affect the Raman signal, as demonstrated in Figure A.2. Nevertheless, while the same Raman peaks are observed at the same positions for all the samples, the homogeneity of the red-colored sample (in Figure A.1) is lower than the other, as hinted by the individual measurements (pale lines). This specific sample showed generally lower qFls, and might be of lower quality, correlating with the stronger inhomogeneities.

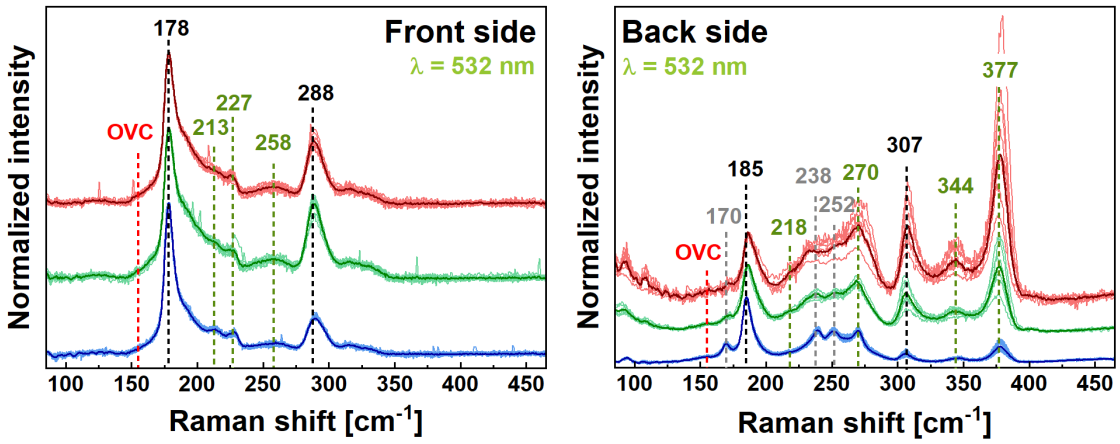

Figure A.1. Raman spectra (normalized to the Se-Se related peak) on three additional "standard" absorbers measured from the front side (left) before lift-off and from the back side (right) after lift-off. A 532 nm wavelength laser is used as excitation source. The black label are associated with the chalcopyrite phases, the green ones with resonance behavior and the gray ones with $MoSe_2$.

Further investigation on the effect of Na-PDT has been conducted and the corresponding Raman analysis is reported in Figure A.2. Comparing the red (without Na-PDT) and blue (with Na-PDT) spectra, no difference can be made from the front side (on which the PDT is performed). Small variations are visible from the back side, but not significant enough to be conclusive. Especially, no shift in the Se-Se related peak (178 cm^{-1} and 185 cm^{-1}) nor in the S-S related one (290 cm^{-1} and 306 cm^{-1}) is reported, suggesting that the GGI remains unchanged upon Na surface treatment.

In addition, a Raman investigation is performed on the remaining substrate after lift-off. Mostly, signals associated with $MoSe_2$ are detected, as expected. However, a small peak at 185 cm^{-1} is still observable and suggests that some CIGSSe residuals are present on the substrate.

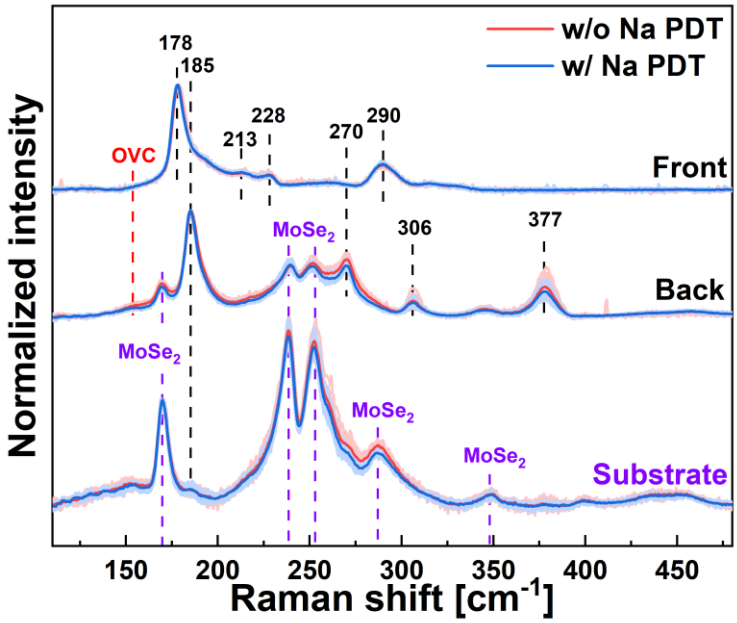

Figure A.2. Raman spectroscopy on the front and back sides of a "standard" absorber with (blue) and without (red) Na-PDT. Raman on the remaining substrate after lift-off in the two cases is also provided and the $MoSe_2$ related peaks are marked.

A.2. Cathodoluminescence on cross section

In total, two absorbers were investigated by CL in this chapter, one without any Na-PDT, and another one with a Na-PDT. To complement the analysis discussed in the main text, additional

energy maps obtained from CL on cross section are provided in Figure A.3 (sample without Na-PDT) and Figure A.4 (sample with Na-PDT). The SE images are of poor quality, but again, the parameters needed for good CL imaging are opposite to the ones required for good SE imaging. From the different energy maps, several abrupt color changes are observed, supporting the claim from section 4.3.2, that the dominant recombination jumps from one energy to another. This implies the coexistence of the low and high band gap phases at a given depth.

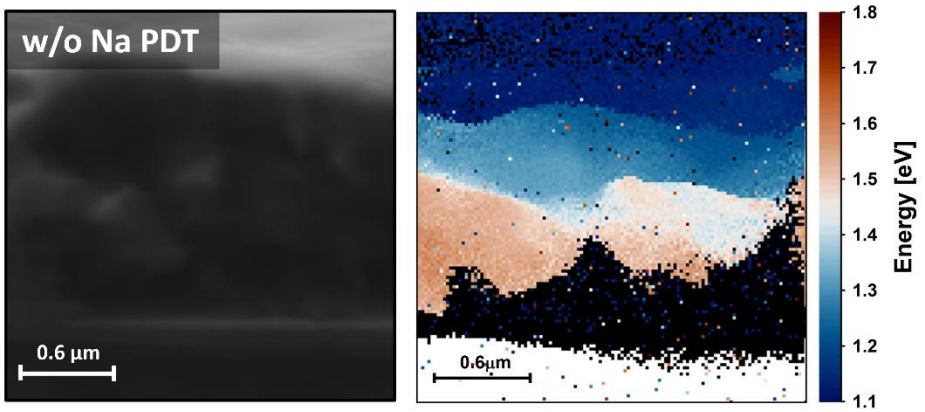

Figure A.3. Cathodoluminescence on the cross-section of the absorber without Na-PDT. The region displayed here is different from the ones shown in Figure 4.10 and Figure 4.11. The SE image (left) is given as a guide to estimate where the signal is coming from. The energy map of the maximum of the emission (right) indicates the dominant recombination energy.

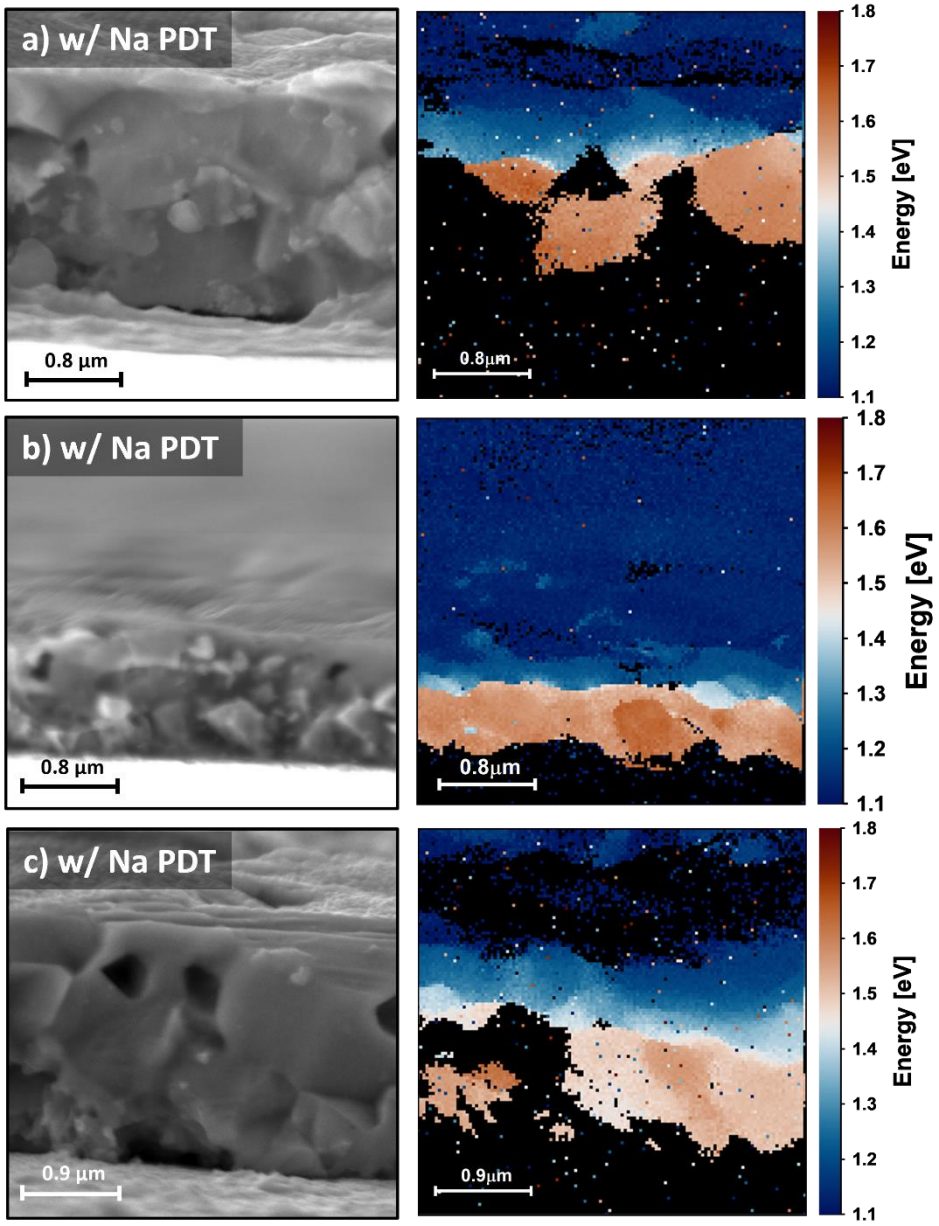

Figure A.4. Cathodoluminescence on the cross-section of the absorber with an additional Na-PDT. Three different regions a), b) and c) of the sample are displayed (also different from the one shown in Figure 4.11). The SE image (left) is given as a guide to estimate where the signal is coming from. The energy map of the maximum of the emission (right) indicates the dominant recombination energy.

A.3. Bromine etching from the back side

In a similar manner as explained in section 4.3.3, two additional absorbers from region III (cf. Figure 4.7) are etched from the back side and PL is measured at the resulting depth. The PL of the second absorber (Figure A.5b) has been measured by Felix Dingwell during his bachelor

thesis at LPV. As shown in Figure A.5, the etching steps have been narrowed around the steep band gap change (as expected from GDOES). Although the etching is not perfectly controllable, the trend discussed in the main text is confirmed by the complementary measurements. Once most of the back side is etched away, the PL notch emission gradually increases and the 0.9 eV defect emission disappears, highlighting the detrimental effect of the high band gap phase.

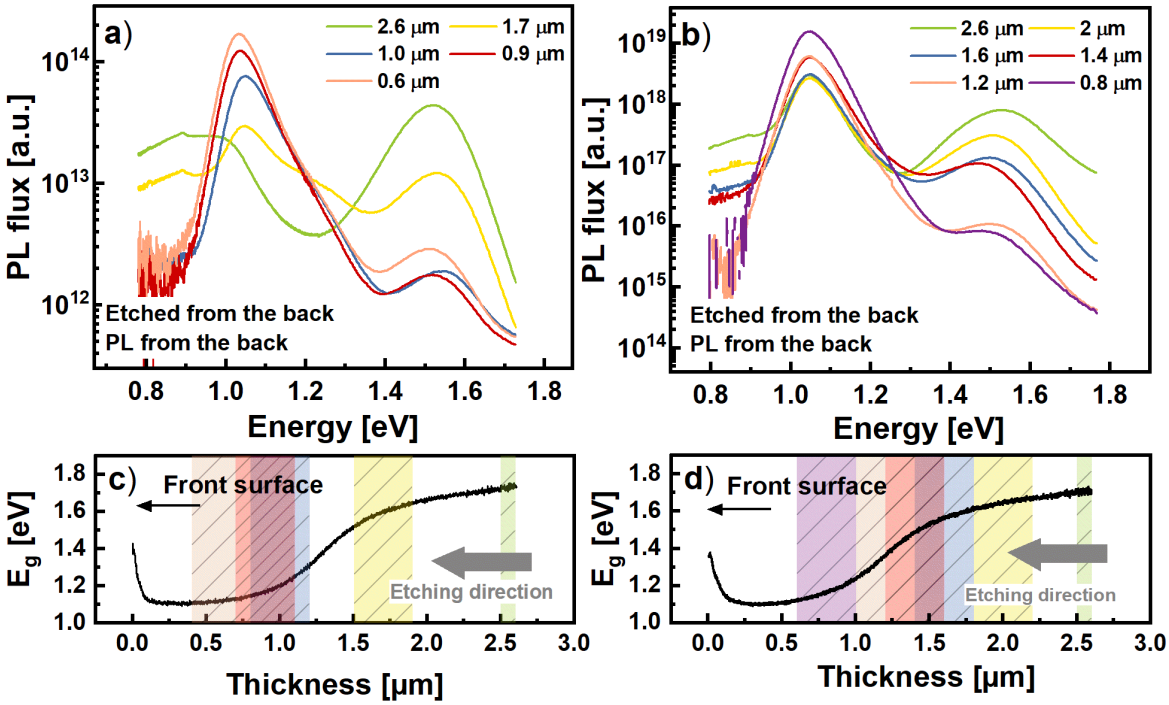

Figure A.5. Top: non-absolute PL spectra at different depths after the absorber is gradually etched from the back side. a) and b) correspond to two absorbers from region III in Figure 4.7a. The legend indicates the depth relative to the front surface at which PL is performed (0 µm corresponds to the front surface and 2.6 µm to the back). Bottom: band gap profiles determined from GDOES. The colored bars indicate the etching depth, including errors. Only one set of diodes in the InGaAs detector is considered (cf. section 3.2.1).

A.4. Deficit vs peaks ratio

Figure 4.16 from the main text shows the relation between the deficit (calculated from a PL front side measurement) and the high and low energy peaks ratio (calculated from a PL back side measurement). The quantitative analysis is based on the black data points. These points are a collection from four "standard" absorbers and are distinguished from each other in Figure

A.6. Each absorber is considered in three different states: bare, with a Na-PDT and with a Na-PDT and a ZnOS buffer layer. Only the absorber #4 also has the state buffer alone, i.e., without the Na-PDT. Considering the bare absorbers (squares), it shows that not all the absorbers perform equally good, based on the deficit. Nevertheless, the surface treatment (triangles) appears to reduce both, the peaks ratio and the deficit, except for one case (abs#7), which is the absorber showing the greatest inhomogeneities from Raman (cf. Figure A.1). Surprisingly, the buffer deposition (by sputtering) also affects the deficit leading to a deficit increase (> 70 eV for abs#4) in all cases, but one (abs#7).

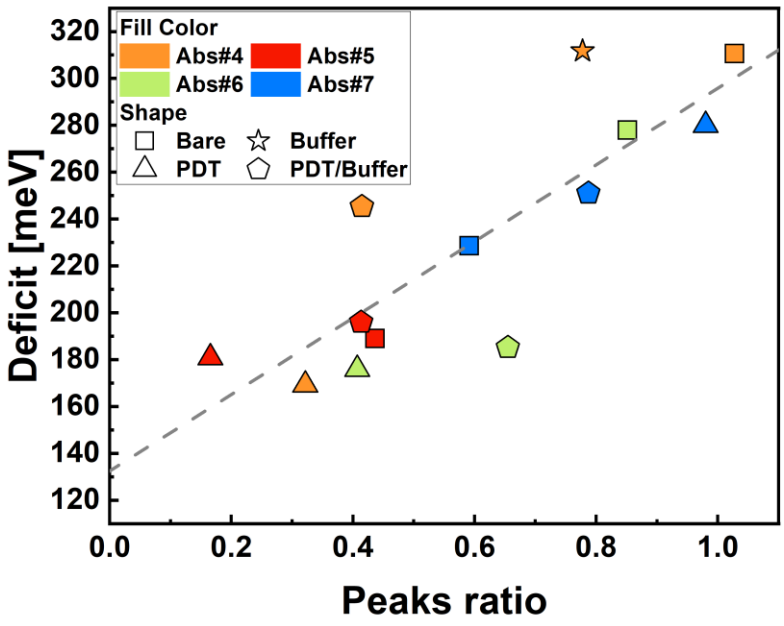

Figure A.6. Non-radiative losses vs. peaks ratio for the “standard” CIGSSe absorbers, displayed as black points in Figure 4.16a. The dashed line is a linear fit to the data points. The peaks ratio is calculated as indicated in the main text. The color code differentiates between the four samples and the shape indicates the state of the sample.

B. Appendix of Chapter 5

B.1. CL spectroscopy with an InGaAs detector

It is argued in chapters 4 and 5 that the generally lower intensity of the front side measured by CL is due to the low quantum efficiency of the Si detector in this range. Since the low band gap phase is mostly present close to the front side and its emission is measured around 1.05 eV from PL, it is expected that the Si detector is not suited for this energy range. Therefore, Figure B.1 provides cross-sectional cathodoluminescence measurements on samples Ag-1 and Ag-3 (cf. Table 5.1) performed with an InGaAs diode array detector (similar to the one used for PL). The intensity maps (panchromatic) reveal indeed a higher emission intensity close to the front side while mostly no signal is detected from the back (note the logarithmic scale). This results from the drop in quantum efficiency of the InGaAs detector at $E > 1.3$ eV, and therefore, the energy maps (Figure B.1, rightmost column) display only noise close to the back side. Nevertheless, an emission of $E \sim 1.05$ eV is detected close to the front side in sample Ag-1, which is coherent with the PL measurements.

The sample Ag-3, on the other hand, shows strong emission around $1.2 - 1.3$ eV close to the front side. This supports the observed flattening of the GGI profiles and the proposition that Ag helps smoothen the band gap gradient across the absorber depth.

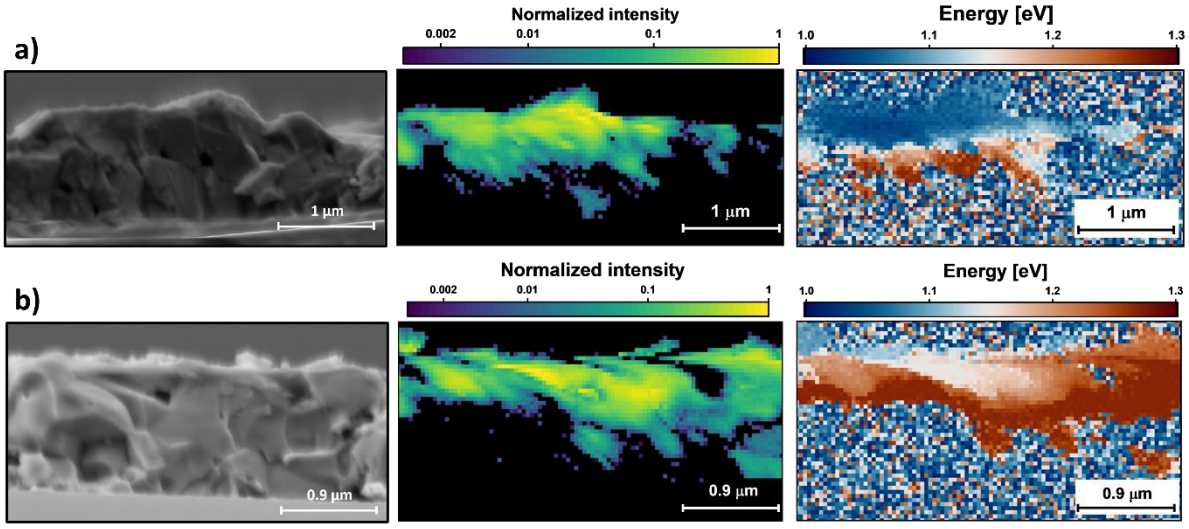

Figure B.1. SE images of the region of interest (left) and corresponding normalized panchromatic intensity map (middle) and dominant emission energy colormap (right) of the samples Ag-1 a) and Ag-3 b), measured by CL with an InGaAs diode array instead of the usual Si detector. This detector cannot detect emission with $E > 1.3$ eV, and only noise is measured close to the back side. The blur in the SE images comes from a shift during the measurement.

B.2. Cathodoluminescence on cross-section – Ag series 1

To complement the CL measurements shown in Figure 5.8 and Figure 5.9, additional cross-section SE images and the corresponding energy colormaps are provided in Figure B.2. The lateral inhomogeneity, in particular close to the back side, is highlighted by the intermittence of the red and white/blue color.

In addition, it is observed for the sample Ag-3 (Figure B.2b) that the high band gap phase (red) is present in lesser density than in the sample Ag-1, and a more gradual transition to the low band gap phase (blue) is achieved, supporting the smoother gradient behavior discussed in section 5.3.3 and Appendix B.1.

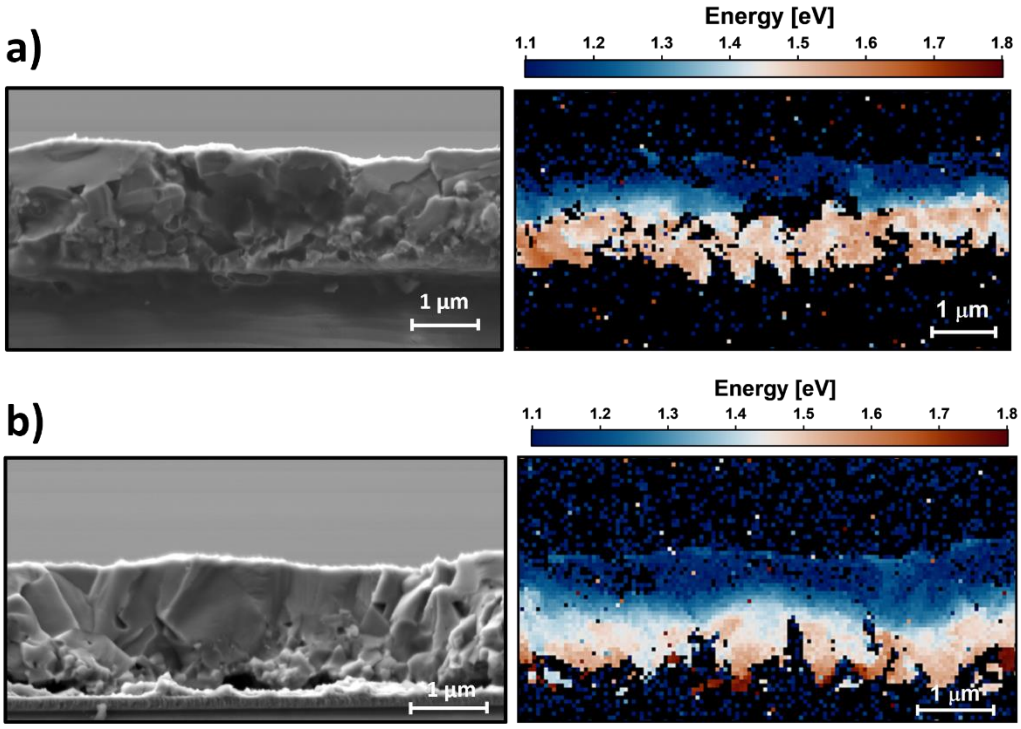

Figure B.2. Complementary SE image of the region of interest (left) and corresponding energy colormap (right) for the samples Ag-1 a) and Ag-3 b).

B.3. A third series of Ag-alloyed samples

Motivated by the generally low deficit of the absorbers grown with reduced GGI in the precursors stack (series 1) and considering the detrimental impact of the high back side GGI (cf. chapter 4), a third series of Ag-alloyed absorbers is prepared. This series 3 is grown with an even lower precursor stack GGI < GGI-1 than the series 2 and the usual AAC variations are applied (Ref-3** contains no Ag, and samples Ag-1** – Ag-3** have similar AAC-1 – AAC-3 than series 1 and 2). Figure B.3 regroups the absorbers' performance, similarly as in Figure 5.10. The reference sample Ref-1 from the first series is added for comparison. The band gap (taken as the PL peak maximum) of the sample Ref-3** is significantly lower than the one of Ref-1, reflecting the lower GGI ratio. As the AAC is increased, the notch PL peak blueshifts, particularly for the highest AAC (Ag-3**). However, the qFls does not increase accordingly, but remains comparable to that of the series' reference (all qFls are in the range $586 - 599$ meV). This is explained by the larger non-radiative losses (up to 229 meV for Ag-3** vs. 197 meV for Ref-3**). In addition, the Urbach energy increases substantially for the samples Ag-

2** and Ag-3**, indicating a larger sub-band gap recombination activity, and reducing the overall performance.

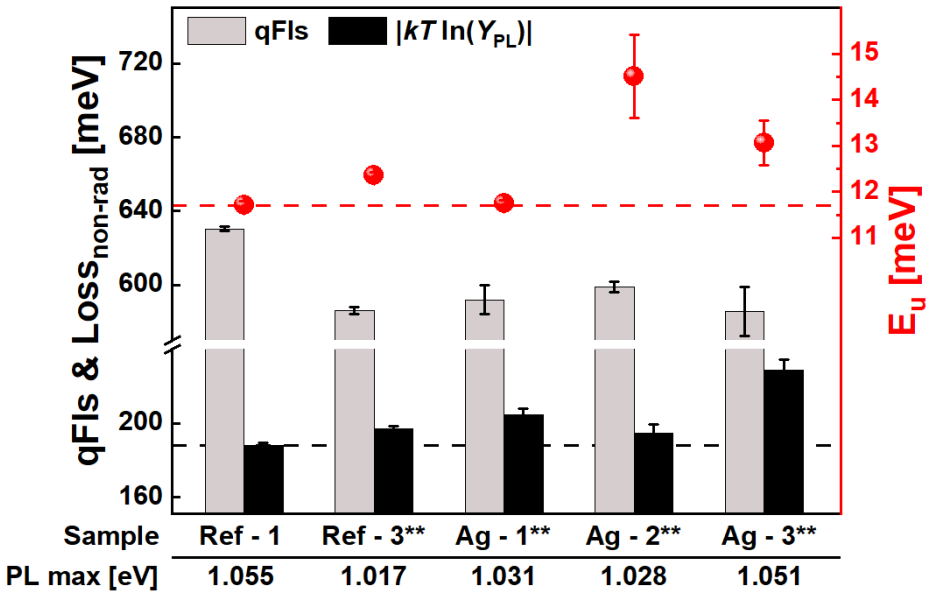

Figure B.3. Summary of the PL results for the series 3. The sample Ref-1 (series 1) is added for comparison. The left axis is the qFls and the non-radiative losses and the right one is the Urbach energy. The dashed lines set the reference level based on Ref-1. The energy of the PL peak maximum (used to calculate the qFls) is given for each sample below the bottom axis.

In addition to the sub-band gap recombination, more than the two main expected recombination channels (low and high band gap phases) are detected by PL, as shown in Figure B.4 and Figure B.5. In addition to the notch PL peak, a second peak is detected in samples Ag-2** and Ag-3** around 1.13 eV from the front and back sides. However, it is important to note that the PL intensity measured from the back side is comparable to the one from the front side, most probably because of the low contribution of the high band gap phase (1.35 eV) at such low GGI. In fact, the emission from the deep defects associated to the high band phase (around 0.9 eV, cf. section 4.4) is not detectable from the back side.

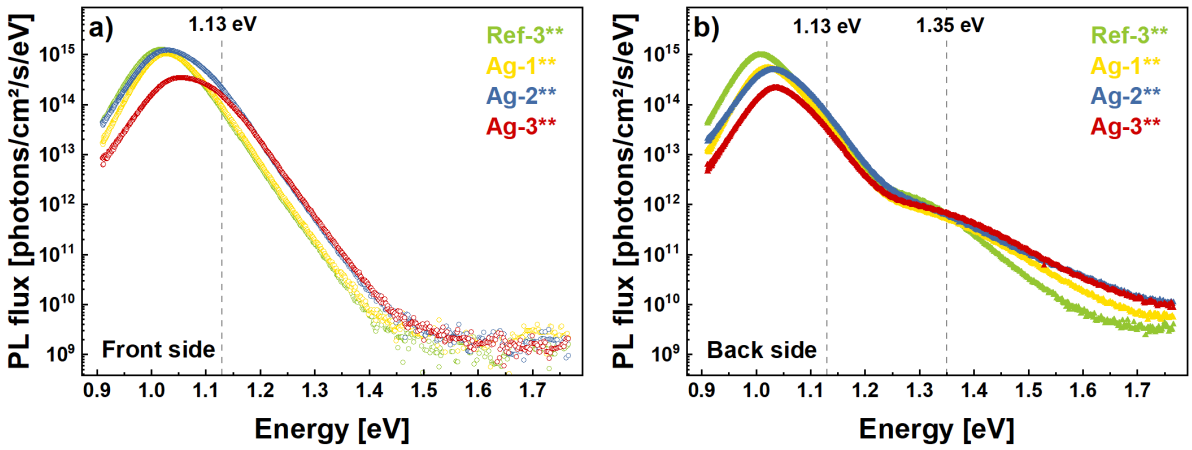

Figure B.4. Absolute PL from a) the front side and b) the back side of the samples from series 3. The (semi-log) scales are identical to allow for direct comparison. The dashed lines indicate peaks other than the notch peak.

The spectra plotted in Figure B.4 are not entirely representative of the emission of these absorbers. The samples Ag-2** and Ag-3** (having large AAC) display a strong inhomogeneity from both the front and back sides. Figure B.5 shows an example for the Ag-2** measured from the front side. In addition to the notch peak at 1.03 eV and to the high band gap phase emission at 1.35 eV, as detected from the back side, peaks at 1.13 eV and 1.50 eV are measured. This suggests that close to the front surface (laser penetration depth being roughly ~ 100 nm) large compositional inhomogeneities are present. This support the claim that Ag enhances the interdiffusion of Ga and In and promotes lateral inhomogeneity in the absorbers, here leading to detrimental effect.

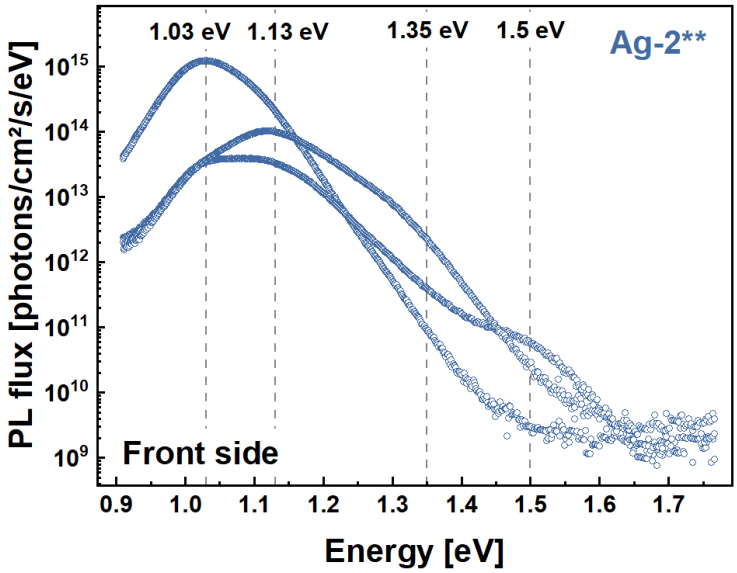

Figure B.5. Absolute PL from the front side of the sample Ag-2**. Each spectrum is taken on a different spot, highlighting the strong inhomogeneity of the PL emission.

C. Appendix of Chapter 6

C.1. Doping and lifetime calculation

Combining absolute PL performed at a "one sun" excitation (typically the generation flux is $\Phi_{\text{laser}} = 2.85 \cdot 10^{17}$ photons/cm^2/s for a band gap of 1.04 eV) with the lifetime extracted from TRPL, it is possible to estimate the doping density of an absorber. Similarly, combining IV measurements with the doping density obtained from CV, it is possible to estimate the minority carriers' lifetime.

Doping from TRPL/PL

A set of relations is considered here. The charge carriers densities in non-equilibrium p and n as given by Equation (2.4) and (2.5) from section 2.2.1, the dependence of the electron density on the excitation flux Φ_{laser} as given by Equation (C.1), and finally an expression for the band gap E_{g} as defined by Equation (C.2).

$$n = \Phi_{\text{laser}} \cdot \frac{\tau_{\text{n}}}{d} \tag{C.1}$$

$$E_{\text{g}} = (E_{\text{C}} - E_{\text{Fn}}) + \Delta E_{\text{F}} + (E_{\text{Fp}} - E_{\text{V}}) \tag{C.2}$$

To calculate the electron density in steady state (Equation (C.1)) it is assumed that the charge carrier density homogenizes over the whole absorber thickness d, which is therefore considered in the equation. The thickness is known, the electron lifetime τ_{n} is measured/fitted by TRPL, the qFls comes from absolute PL and the band gap is taken as the energy of the PL peak maximum. As shown in Figure 4.2 (chapter 4), depending on the determination method, e.g. PL, EQE or reflection, the band gap may vary by about $15 - 30$ meV. To remain consistent in this thesis, the PL band gap is considered here and the uncertainty on it, as compared to the other methods is ignored. Combining all the above equations yields the doping $N_{\text{A}} \approx p$ in a p-type absorber

$$N_{\text{A}} = \frac{d \cdot N_{\text{v}} N_{\text{c}}}{\Phi_{\text{laser}} \cdot \tau} \cdot \exp\left(\frac{\Delta E_{\text{F}} - E_{\text{g}}}{k_{\text{B}} T}\right) \tag{C.3}$$

Furthermore, the error on the doping is calculated considering the error on the measured lifetime (from the fit of the excitation dependent measurement) and on the qFls (from different measurements spots). Writing σ_X the error on variable X, the error on $N_{\mathrm{A}}(\tau, \Delta E_{\mathrm{F}})$ is defined using the partial derivatives

$$\sigma_{N_{\mathrm{A}}} = \sqrt{\left(\frac{\partial N_{\mathrm{A}}}{\partial \tau}\sigma_{\tau}\right)^2 + \left(\frac{\partial N_{\mathrm{A}}}{\partial \Delta E_{\mathrm{F}}}\sigma_{\Delta E_{\mathrm{F}}}\right)^2} \tag{C.4}$$

Lifetime from IV/CV

From the electrical measurements the doping and the V_{OC} are known. Since the V_{OC} is also measured under "one sun", the same generation flux can be used. Taking the same band gap from the PL and replacing ΔE_{F} by V_{OC} in the set of equations given above, the lifetime is calculated as

$$\tau = \frac{d \cdot N_{\mathrm{v}} N_{\mathrm{c}}}{\Phi_{\mathrm{laser}} \cdot N_{\mathrm{A}}} \cdot \exp\left(\frac{V_{\mathrm{OC}} - E_{\mathrm{g}}}{k_{\mathrm{B}} T}\right) \tag{C.5}$$

Similarly, the error on the calculated lifetime is determined by the error on the doping density and on the V_{OC}

$$\sigma_{\tau} = \sqrt{\left(\frac{\partial \tau}{\partial N_{\mathrm{A}}}\sigma_{N_{\mathrm{A}}}\right)^2 + \left(\frac{\partial \tau}{\partial V_{\mathrm{OC}}}\sigma_{V_{\mathrm{OC}}}\right)^2} \tag{C.6}$$

C.2. Complement on the excitation dependent TRPL

Transient's distortion at high excitations

It has been observed that as the PL emission of a sample increases (when going to higher injection levels) the transient moves away from the bi-exponential behavior. As mentioned in section 3.2.3, it is important that the emission counts rate remains below 5% of the excitation rate lest pile-up may occur. To respect this condition, an OD1.3 filter is placed before the detector to attenuate the PL signal at high excitations and remain below the recommended threshold. This, however, also reduces the signal-to-noise ratio, as can be seen in Figure C.1,

and the decay disappears in the noise before it can deviate from the bi-exponential behavior. Figure C.1 provides two examples that illustrate the effect of the attenuation, specifically for sample Ag-2.3 at excitation of $\Delta n \approx 1.5 \cdot 10^{16}$ cm^{-3} (top row) and $\Delta n \approx 3.7 \cdot 10^{15}$ cm^{-3} (bottom row). In the first case, the signal-to-noise ratio of the attenuated transient is still largely above the recommended threshold of 20% (cf. section 3.2.3), but in the second case the ratio becomes critically low. In both cases, the non-attenuated and attenuated transients are fitted with a bi-exponential function displayed in a semi-logarithmic scale (a and c) and in double logarithmic scale (b and d). While both R^2 are very good, the fit of the attenuated transients looks much better. Nevertheless, the slow decay time returned by the fit, τ_2, is equal between the non-attenuated and attenuated transients at low excitation (cf. floating table in Figure C.1c), and still comparable at higher excitation (cf. floating table in Figure C.1a), despite the inaccuracy of the bi-exponential fit.

Note that since the signal has been attenuated by an OD1.3 filter, the attenuated transients' intensity is multiplied by $10^{1.3}$ during the data treatment, explaining the large difference in the background signal.

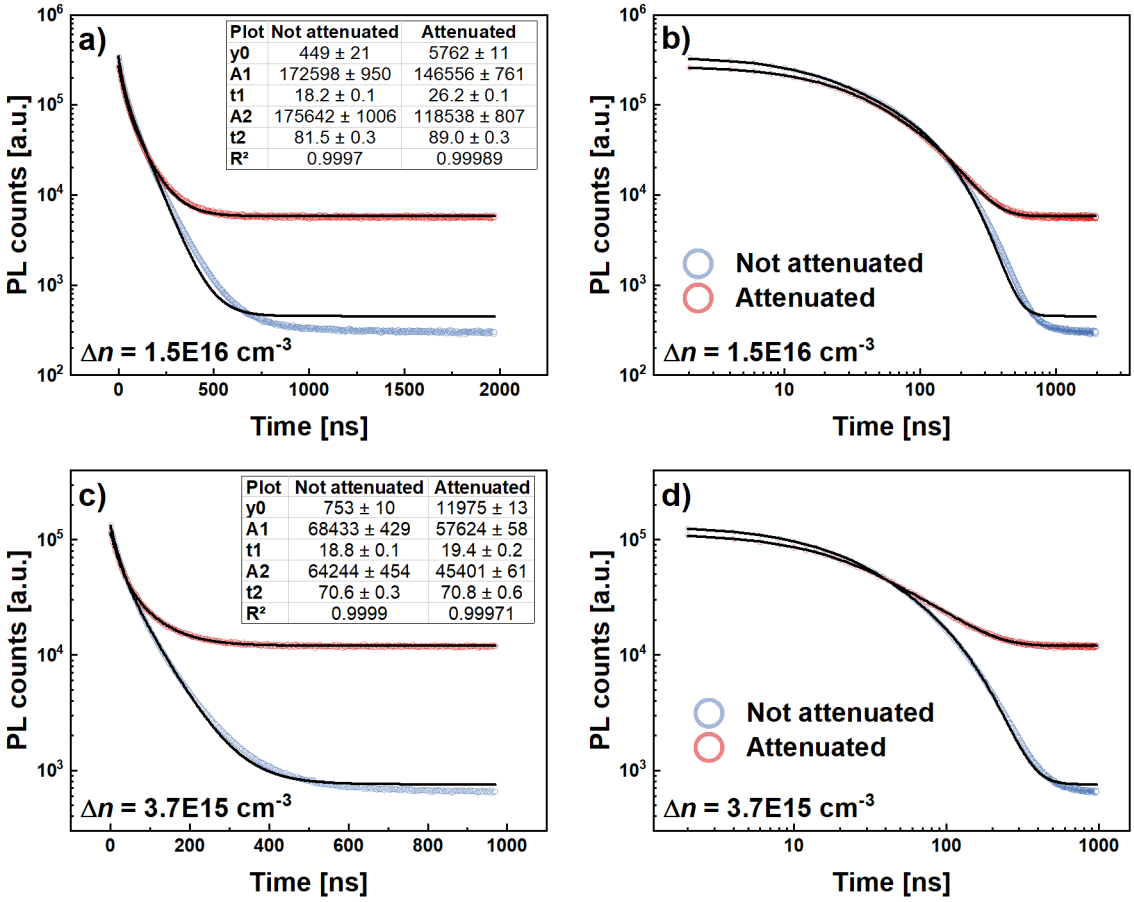

Figure C.1. TRPL measurement of the sample Ag-2.3 at an excitation corresponding to $\Delta n = 1.5 \cdot 10^{16}$ cm^{-3} (top row) and to $\Delta n = 3.7 \cdot 10^{15}$ cm^{-3} (bottom row). Each row display the same data in semi-logarithmic scale a) and c), and in double logarithmic scale b) and d). The data is binned by 10 data points. Within a graph, the same acquisition parameters are used but in one case (red circles) the emission from the sample is attenuated by an OD1.3 filter, while the full signal intensity is registered in the other case (blue circles). The displayed attenuated transients' intensity is multiplied by $10^{1.3}$ to account for the OD filter used during the measurement. The transients are fitted with a bi-exponential function and the fit parameters are reported in the associated floating table.

Reversibility of the measurements

The excitation dependent TRPL measurements shown in chapter 6 are taken starting at the lowest excitation and gradually increasing it. The reversibility of this process has been assessed for the sample Ag-2.3. Directly after the measurement at the highest excitation, a second measurement is taken on the same spot under the same conditions before the laser intensity is reduced again, following the same excitation steps. Note that the transient measured again at

the lowest excitation was too noisy to achieve a reliable fit. As shown in Figure C.2, the two sets of measurements agree on the decay time, with a maximum deviation of 6 ns at $\Delta n = 7.5 \cdot 10^{13}$ cm^{-3}. This deviation is negligible considering that the two measurements at the highest excitation, performed one after the other differ already from 3 ns. The fit according to Equation (6.1) leads to $\tau_n = 35 \pm 2$ ns from high to low excitation which is comparable to $\tau_n = 41 \pm 2$ ns obtained from low to high excitation. The fitted doping densities are equal within error, $N_A = (1.8 \pm 0.4) \cdot 10^{15}$ cm^{-3} (high to low) vs. $N_A = (2.4 \pm 0.8) \cdot 10^{15}$ cm^{-3} (low to high). It is therefore concluded that no irreversible change is done to the sample, even at high excitation, or that the metastable transition occurs faster than the measurement time. It also indicates that if metastable defects are present (which is suspected), they either revert to their original state over a time as short as the measurement, or that they are converted from donors to acceptors at low excitations already and remain in their metastable state during the whole measurement. The latter explanation is the most probable.

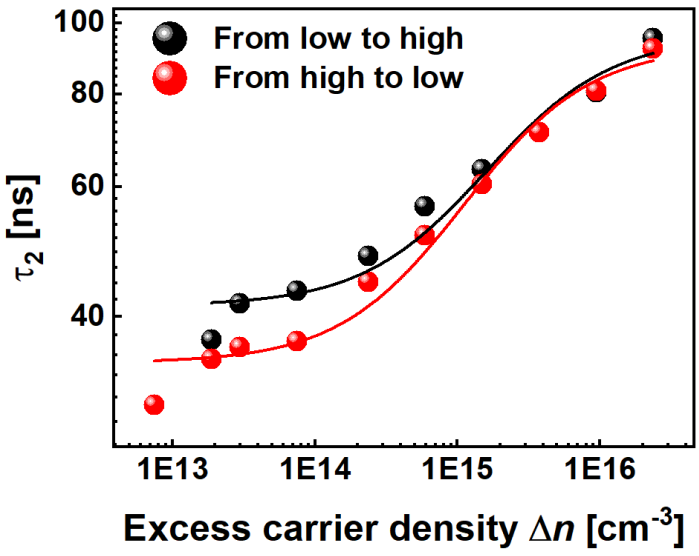

Figure C.2. Extracted τ_2 from a bi-exponential fit of the TRPL transients of sample Ag-2.3 at different excitations. The black data points correspond to a measurement from low to high excitation and the red ones from high to low excitation on the same spot. The plain lines are a fit according to Equation (6.1).

C.3. Complement on the temperature dependent TRPL

Because the measured lifetime depends on the excitation level, the temperature dependent measurement of the sample 1 (with ZnOS buffer) is repeated at a lower excitation as compared

to section 6.2.2. The results for the two excitations are compared in Figure C.3 and the fit parameters are reported in Table C.1 along with the fit parameters from Figure 6.8. As expected, the decay time is shorter at lower excitation, and similar temperature dependence is observed.

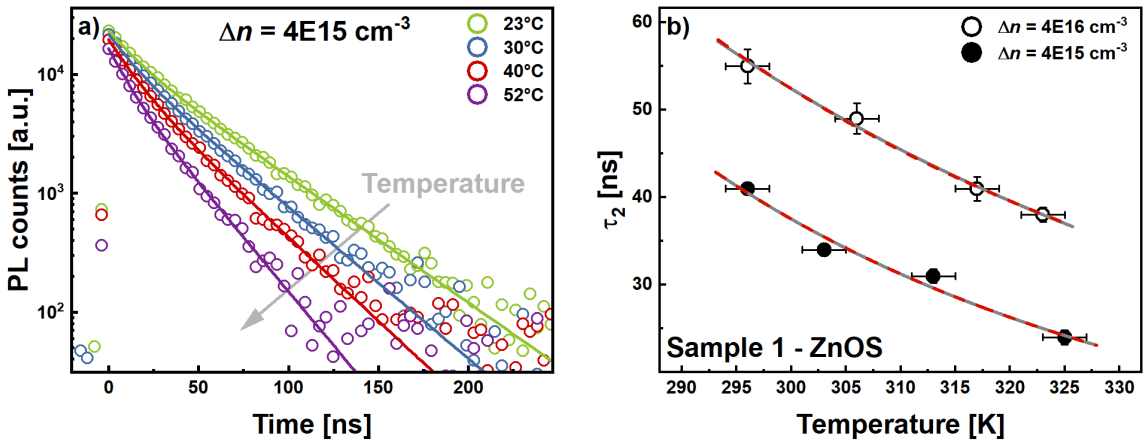

Figure C.3. a) TRPL transients for the sample 1 with a ZnOS buffer, at different temperatures above RT (as indicated by the legend). A lower excitation is used compared to the one in Figure 6.8a. The data points are experiment and the plain lines correspond to the bi-exponential fit. The long decay time (τ_2) is reported for each temperature in b), for both excitations, $\Delta n \approx 4 \cdot 10^{16}$ cm^{-3} as shown in Figure 6.8 (open dots) and $\Delta n \approx 4 \cdot 10^{15}$ cm^{-3} (full dots). The solid gray lines are a fit to the data according to Equation (6.2) while the dashed red ones are a fit according to Equation (6.4). The error on the temperature is empirically estimated at ± 2 K and the error on τ_2 is taken from the bi-exponential fit.

Table C.1. Fit parameters of the decay time temperature dependence according to Equation (6.2) and (6.4) for samples 1 and 3, with and without buffer layer. The results for sample 1 at lower excitation are also included. The data and fitting are shown in Figure 6.8 and Figure C.3.

	$\tau \sim T^{-b} \cdot \exp\left(\frac{E_\mathrm{d}}{k_\mathrm{B}T}\right)$		$\tau \sim \frac{1}{\mathrm{T}} \cdot \exp\left(\frac{C}{k_\mathrm{B}T}\right)$
Sample	$\boldsymbol{b}$	$\boldsymbol{E_\mathrm{d}}$ **[meV]**	$\boldsymbol{C}$ **[meV]**
Sample 1 (bare)	5 ± 204	94 ± 5476	206 ± 40
Sample 1 (ZnOS)	4 ± 26	5 ± 690	89 ± 6
Sample 1 (ZnOS) Lower excitation	0.6 ± 59	130 ± 1584	120 ± 18
Sample 3 (bare)	7 ± 165	0.1 ± 4476	150 ± 27
Sample 3 (ZnOS)	5 ± 182	62 ± 4901	157 ± 4

C.4. Influence of the time bin size in a TRPL measurement

As discussed in section 6.2.2, the transient shape (especially the initial decay part) is influenced by the time bin size used during the data acquisition. For the same measurement duration (20 minutes in Figure C.4), a small bin size allows for a more precise detection of the early time features, but leads to a noisier long decay part, compared to a larger bin size. It results that fitting with a bi-exponential function may lead to discrepancies in the fit parameters as τ_1 and τ_2 are not fitted over the same time range. Figure C.4 illustrates the situation. The sample 3 with a ZnOS buffer (cf. sections 6.2.1 and 6.2.2) is measured twice in a row, on the same spot and with the same acquisition parameters, but once with a bin size of 4.9 ns (blue circles in Figure C.4) and once with a bin size of 19.5 ns (red circles). With the smaller bin size, the (blue) transient shows an initial fast decay over the first ~ 50 ns after the laser pulse. This initial decay is not detected with a larger bin size (red transient). Therefore, the experimental data is not fitted the way with a bi-exponential fit (gray dashed line in Figure C.4). In the first case (bin size of 4.9 ns), τ_1 represents the part of the transient from 0 ns to ~ 50 ns and leads to a τ_2 of 97 ns. In the second case (bin size of 19.5 ns), τ_1 describes the part from 0 ns to ~ 150 ns what leads to $\tau_2 = 217$ ns. However, if the fit is performed over the same time range, the two measurements agree better. In Figure C.4, a mono-exponential fit is performed between

$t = 250$ ns and $t = 400$ ns (solid black line), corresponding to the long decay part of the transients and returns $\tau = 102 \pm 7$ ns for the bin size 4.9 ns and $\tau = 123 \pm 8$ ns for the bin size 19.5 ns. This highlights the importance of the choice of the time bin size and of the fitting range.

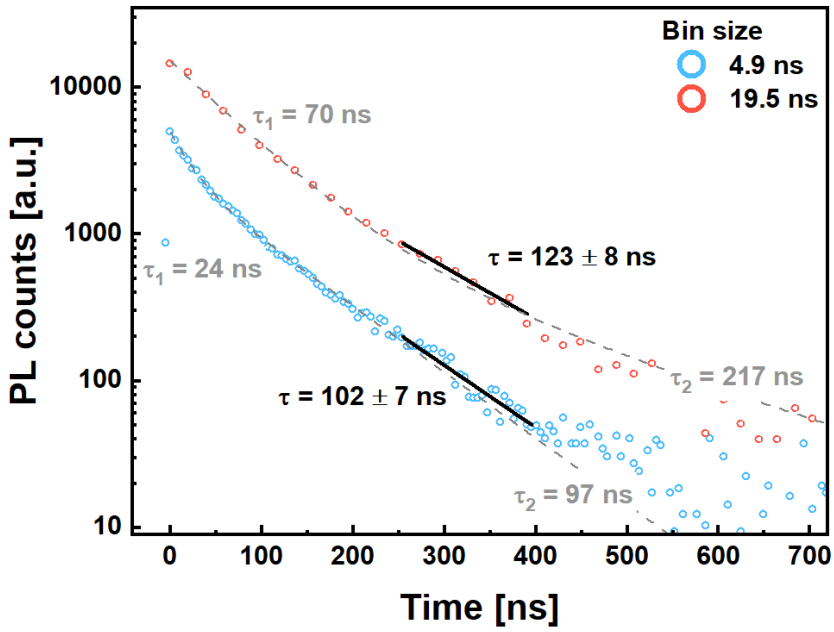

Figure C.4. TRPL transients measured on the same spot (sample 3 with a ZnOS buffer) with all the same acquisition parameters, but different time bin sizes. The blue transient has a bin size of 4.9 ns while the red one has a bin size of 19.5 ns. The gray dashed lines represents a bi-exponential fit and the time components τ_1 and τ_2 are indicated. The background signal (returned by the bi-exponential fit) has been subtracted. The solid black lines represent the mono-exponential fit over the time range $250 - 400$ ns and the time component τ is indicated.

List of publications

1. A. JC. M. Prot, M. Melchiorre, F. Dingwell, A. Zelenina, H. Elanzeery, A. Lomuscio, T. Dalibor, M. Guc, R. Fonoll-Rubio, V. Izquierdo-Roca, G. Kusch, R.A. Oliver, and S. Siebentritt, "Composition variations in Cu(In,Ga)(S,Se) 2 solar cells: Not a gradient, but an interlaced network of two phases," APL Mater. **11**, 101120 (2023).

2. A. JC. M. Prot, M. Melchiorre, T. Schaaf, R.G. Poeira, H. Elanzeery, A. Lomuscio, S. Oueslati, A. Zelenina, T. Dalibor, G. Kusch, Y. Hu, R.A. Oliver, and S. Siebentritt, "Improved Sequentially Processed Cu(In,Ga)(S,Se)2 by Ag Alloying," Solar RRL, (2024).

3. S. Siebentritt, U. Rau, S. Gharabeiki, T.P. Weiss, **A. Prot**, T. Wang, D. Adeleye, M. Drahem, and A. Singh, "Photoluminescence assessment of materials for solar cell absorbers," Faraday Discuss, (2022).

4. O. Ramírez, J. Nishinaga, F. Dingwell, T. Wang, **A. Prot**, M.H. Wolter, V. Ranjan, S. Siebentritt, O. Ramírez, F. Dingwell, T. Wang, A. Prot, M.H. Wolter, V. Ranjan, S. Siebentritt, and J. Nishinaga, "On the origin of tail states and VOC losses in Cu(In,Ga)Se2," Solar RRL **7**(13), (2023).

5. R.G. Poeira, A. Pérez-Rodríguez, **A. JC. M. Prot**, M. Alves, P.J. Dale, and S. Sadewasser, "Direct fabrication of arrays of Cu(In,Ga)Se2 micro solar cells by sputtering for micro-concentrator photovoltaics," Mater Des, 111597 (2023).

6. T. Wang, L. Song, S. Gharabeiki, M. Sood, **A. JC. M. Prot**, R.G. Poeira, M. Melchiorre, N. Valle, A.-M. Philippe, S. Glinsek, E. Defay, P.J. Dale, and S. Siebentritt, "Shifting the paradigm: a functional hole selective transport layer for chalcopyrite solar cells," Solar RRL 8(9), (2024).

Collaborative contributions

During this thesis, some of the major results and conclusions were achieved thanks to various collaborations with European research groups. First of all, the R&D department of AVANCIS provided all the absorbers investigated in this work. Moreover, the regular discussions with Dr. Anastasia Zelenina, Dr. Hossam Elanzeery, Dr. Alberto Lomuscio, Dr. Souhaib Oueslati and Dr. Thomas Dalibor contributed greatly to the understanding and interpretation of the experimental results. The cathodoluminescence measurements presented in chapters 4 and 5 were performed at the Cambridge Center for Gallium Nitride by Dr. Gunnar Kusch and Yucheng Hu. The Raman spectroscopy shown in chapter 4 was done at IREC by Dr. Maxim Guc and Robert Fonoll-Rubio and the one from chapter 5 was conducted at the University of Luxembourg by Dr. Ricardo G. Poeira. All of the SEM measurements were performed at the University of Luxembourg by Dr. Michele Melchiorre. Finally, the TEM/EDX investigation shown in chapter 4 was conducted at IIT by Dr. Andrea Griesi and Dr. Giorgio Divititi. The TCAD simulations shown is chapter 6 were done by Dr. Matthias Maiberg from the University of Halle, Germany.

I would like to extend a great thank you to all the aforementioned contributors to my research project.

Acknowledgements

I had heard four years ago that pursuing a PhD was not an easy task…today I can confirm that it is true. Fortunately, that does not mean one cannot enjoy the experience. In fact, during my time at LPV, I have grown a lot, both scientifically and personally, and I appreciate the person I have become. This transformation, however, did not happen on its own, and I have many people to thank for it.

First of all, my biggest thanks goes to my supervisor, Susanne, for placing her trust in me when I was still a Master student, stuck in Grenoble during the first Covid lockdown. Susanne, I think we never thank you enough for what you do. It has been an absolute pleasure to work with you. You always made time to discuss my results, ideas, or any misunderstandings, and you guided me whenever I needed it. Thank you also for being one of the most caring and kind people I know. It is clear that our well-being is important to you, and you make sure that everyone feels welcome and comfortable in your group, despite the stressful nature of our work. Vielen lieben Dank für alles, Susanne!

I would like to extend my thanks to Thomas Dalibor and Daniele Brida for their support as part of my CET, as well as Thomas Kirchartz and Romain Carron for their participation in my defense committee. Additionally, I am grateful to all the AVANCIS members (and future colleagues!) who actively participated in the numerous project meetings we held during these four years of close collaboration. Thank you, Anastasia, Hossam, Alberto, Souhaib, Mohit and Thomas.

I would like to thank every member of the LPV and LEM teams, the ones who left during my PhD, as well as the new ones who joined later to replenish the ranks. It was very valuable to benefit from the bits of knowledge and expertise that each of you provided. A special thanks goes to my close friends and colleagues Ricardo, Taowen and Omar, without whom my PhD experience would never have been the same. Thank you for the precious advice and helpful scientific discussions (yes, we did have some – I think), and, above all, for the countless moments we shared outside of the office. Naturally, I thank you too, Patricia, for without your flawless management I would never have been able to attend conferences, place (and receive!) orders or secure meeting rooms at such short notice. I also want to express my gratitude to you,

Michele, for your constant kindness and availability (I honestly don't know how you manage to squeeze our every baseline need into your calendar), you rock! Talking about rock, thank you, Thomas, for your invaluable help with any kind of machine or device I struggled with. I hope to meet you one day on the Graspop site!

Promovieren ist jedoch mehr als nur im Labor zu arbeiten und mit den Kollegen zu diskutieren. Es ist eine Reise, die sowohl professionelle als auch persönliche Aspekte umfasst. Ich bin von Herzen dankbar an die Mozartstraße-WG, wo ich ein zweites Zuhause gefunden habe. Danke an Euch, Annika, Loan, Daki, Yildiz und Meziyet, dass Ihr mich akzeptiert habt (obwohl Ihr nicht immer die Wahl hattet…). Besonderer Dank gilt Dir, Annika, mein Schatz. Deine Unterstützung, ob in guten oder schlechten Zeiten, hat mir unendlich viel bedeutet. Du hast meine Liebe zum Lesen wiedererweckt und mir damit eine Ausgangstür aus der oft stressigen wissenschaftlichen Welt geöffnet. Dich zu haben, hat meinen Alltag einfach leichter und schöner gemacht. Ich freue mich auf unser zukünftiges gemeinsames Leben und all die Abenteuer, die vor uns liegen, ich liebe Dich.

Forcément, quelques remerciements en français sont également nécessaires. Merci à vous deux, Wayhlan et Zacknir (aka Virgile et Lionel) pour ces soirées du mercredi. Avoir ce rendez-vous (plus ou moins) hebdomadaire a rythmé une bonne partie de mon doctorat et m'a aidé à rester motivé, surtout lors de la phase d'écriture de cette thèse. Merci à tout le reste de la troupe de Décibulles (désolé, trop de prénoms), avec qui j'ai partagé des moments mémorables lors des festivals, mais pas que !

Un immense merci à mes parents, Papa et Maman, et à mes frères et mi cuñada, Thomas, Rebeca, Simon et Gautier pour votre soutien continu. Peu importe le niveau de stress dans lequel je me trouvais, passer du temps avec vous ou vous avoir en visio a toujours été un moment de détente. Je n'oublie bien sûr pas mes tantes et leurs compagnons, Françoise, Gérard, Lucienne, Mireille et Farid. Merci de vous être intéressés à mon travail et d'avoir su m'accompagner tout au long de cette aventure.

Finally, I would like to express my sincere gratitude to you, dear Reader, for taking the time to read my thesis in its entirety or in parts. I hope that you could learn something, and if not, I recommend starting from page 1 (again).

Bibliography

[1] R. Lindsey, L. Dahlman, “Climate Change: Global Temperature,” can be found under https://www.climate.gov/news-features/understanding-climate/climate-change-global-temperature, **2024**.

[2] *Climate Change 2023: Synthesis Report. Contribution of Working Groups I, II and III to the Sixth Report of the Intergovernmental Panel on Climate Change*, Geneva, **2023**.

[3] Climate Change Institute, University of Maine, “Climate Reanalyzer,” can be found under https://climatereanalyzer.org/clim/t2_daily/?dm_id=world, **2024**.

[4] Government of Canada, “Canada’s record-breaking wildfires in 2023: A fiery wake-up call,” can be found under https://natural-resources.canada.ca/simply-science/canadas-record-breaking-wildfires-2023-fiery-wake-call/25303, **2024**.

[5] J. Kimutai, F. Masambaya, J. Arrighi, E. Raju, F. Otto, M. Zachariah, *Urban Planning at the Heart of Increasingly Severe East African Flood Impacts in a Warming World*, **2024**.

[6] UNFCCC, “The Paris Agreement,” can be found under https://unfccc.int/process-and-meetings/the-paris-agreement, **2015**.

[7] Energy Institute, *Statistical Review of World Energy*, **2023**.

[8] Fraunhofer Institute for Solar Energy Systems, *Photovoltaics Report* , **2024**.

[9] H. Elanzeery, M. Stölzel, P. Eraerds, P. Borowski, H. Aboulfadl, A. Lomuscio, D. Helmecke, C. Schubbert, S. Oueslati, M. Hála, J. Röder, F. Giesl, T. Dalibor, *IEEE J Photovolt* **2023**, *14*, 107.

[10] S. P. Bremner, M. Y. Levy, C. B. Honsberg, *Progress in Photovoltaics: Research and Applications* **2008**, *16*, 225.

[11] “Avancis GmbH,” can be found under https://www.avancis.de/en, **2024**.

[12] A. JC. M. Prot, M. Melchiorre, F. Dingwell, A. Zelenina, H. Elanzeery, A. Lomuscio, T. Dalibor, M. Guc, R. Fonoll-Rubio, V. Izquierdo-Roca, G. Kusch, R. A. Oliver, S. Siebentritt, *APL Mater.* **2023**, *11*, 101120.

[13] A. J. M. Prot, M. Melchiorre, T. Schaaf, R. G. Poeira, H. Elanzeery, A. Lomuscio, S. Oueslati, A. Zelenina, T. Dalibor, G. Kusch, Y. Hu, R. A. Oliver, S. Siebentritt, *Solar RRL* **2024**, DOI 10.1002/solr.202400208.

[14] R. Scheer, H. W. Schock, *Chalcogenide Photovoltaics Physics, Technologies, and Thin Film Devices*, Wiley-VCH Verlag GMbH & Co, Weinheim, **2011**.

[15] P. Würfel, *Physics of Solar Cells*, Wiley-VCH, Weinheim, **2005**.

[16] J. Bisquert, *The Physics of Solar Cells: Perovskites, Organics, and Photovoltaic Fundamentals*, CRC Press, Boca Raton, **2018**.

[17] D. Abou-Ras, T. Kirchartz, U. Rau, *Advanced Characterization Techniques for Thin Film Solar Cells*, Wiley-VCH, Weinheim, **2011**.

[18] D. A. Neamen, *Semiconductor Physics and Devices : Basic Principles*, McGraw-Hill, New York, **2012**.

[19] J. L. Shay, J. H. Wernick, *Ternary Chalcopyrite Semiconductors: Growth, Electronic Properties, and Applications*, Pergamon Press, New York, **1975**.

[20] M. Bär, W. Bohne, J. Röhrich, E. Strub, S. Lindner, M. C. Lux-Steiner, C. H. Fischer, T. P. Niesen, F. Karg, *J Appl Phys* **2004**, *96*, 3857.

[21] H. Landolt, R. Börnstein, K. H. Hellewege, D. Bimberg, M. Schultz, H. Weiss, O. Madelung, *Landolt-Börnstein Numerical Data and Functional Relationships in Science and Technology*, Berlin, **1982**.

[22] G. E. Eperon, M. T. Hörantner, H. J. Snaith, *Nat Rev Chem* **2017**, *1*, DOI 10.1038/S41570-017-0095.

[23] M. A. Contreras, J. Tuttle, A. Gabor, A. Tennant, K. Ramanathan, S. Asher, A. Franz, J. Keane, L. Wang, R. Noufi, *Solar Energy Materials and Solar Cells* **1996**, *41–42*, 231.

[24] M. Bodegård, O. Lundberg, J. Malmstrom, L. Stolt, A. Rockett, *Conference Record of the Twenty-Eighth IEEE Photovoltaic Specialists Conference* **2000**.

[25] A. M. Gabor, J. R. Tuttle, M. H. Bode, A. Franz, A. L. Tennant, M. A. Contreras, R. Noufi, D. G. Jensen, A. M. Hermann, *Solar Energy Materials and Solar Cells* **1996**, *41–42*, 247.

[26] J. Keller, K. Kiselman, O. Donzel-Gargand, N. M. Martin, M. Babucci, O. Lundberg, E. Wallin, L. Stolt, M. Edoff, *Nat Energy* **2024**, DOI 10.1038/s41560-024-01472-3.

[27] M. Turcu, I. M. Kötschau, U. Rau, *J Appl Phys* **2002**, *91*, 1391.

[28] S. B. Zhang, S.-H. Wei, A. Zunger, *Phys. Rev. Lett.* **1997**.

[29] K. Sato, H. Katayama-Yoshida, in *AIP Conf Proc*, American Institute Of Physics Inc., **2014**, pp. 150–155.

[30] B. Huang, S. Chen, H. X. Deng, L. W. Wang, M. A. Contreras, R. Noufi, S. H. Wei, *IEEE J Photovolt* **2014**, *4*, 477.

[31] J. Pohl, K. Albe, *Phys Rev B Condens Matter Mater Phys* **2013**, *87*, DOI 10.1103/PhysRevB.87.245203.

[32] J. Keller, P. Pearson, N. Shariati Nilsson, O. Stolt, L. Stolt, M. Edoff, *Solar RRL* **2021**, *5*, DOI 10.1002/solr.202100403.

[33] T. Lepetit, S. Harel, L. Arzel, G. Ouvrard, N. Barreau, *Progress in Photovoltaics: Research and Applications* **2017**, *25*, 1068.

[34] T. Minemoto, T. Matsui, H. Takakura, Y. Hamakawa, T. Negami, Y. Hashimoto, T. Uenoyama, M. Kitagawa, *Solar Energy Materials & Solar Cells* **2001**, *67*, 83.

[35] O. Ramírez, E. M. Lanzoni, R. G. Poeira, T. P. Weiss, R. Leturcq, A. Redinger, S. Siebentritt, *APL Mater* **2022**, *10*, DOI 10.1063/5.0091676.

[36] C. Spindler, F. Babbe, M. H. Wolter, F. Ehré, K. Santhosh, P. Hilgert, F. Werner, S. Siebentritt, *Phys Rev Mater* **2019**, *3*, DOI 10.1103/PhysRevMaterials.3.090302.

[37] N. Christoforou, J. D. Leslie, S. Damaskinos, *Solar Cells* **1989**, *26*, 215.

[38] J. T. Heath, J. D. Cohen, W. N. Shafarman, *J Appl Phys* **2004**, *95*, 1000.

[39] F. Werner, F. Babbe, J. Burkhart, C. Spindler, H. Elanzeery, S. Siebentritt, *ACS Appl Mater Interfaces* **2018**, *10*, 28553.

[40] F. Werner, B. Veith-Wolf, M. Melchiorre, F. Babbe, J. Schmidt, S. Siebentritt, *Sci Rep* **2020**, *10*, DOI 10.1038/s41598-020-64448-9.

[41] "NREL Solar Ressource Data & Tools," can be found under https://www.nrel.gov/grid/solar-resource/spectra-am1.5.html, **2024**.

[42] H. I. Abdalmageed, M. Fedawy, M. H. Aly, in *J Phys Conf Ser*, IOP Publishing Ltd, **2021**.

[43] J. H. Werner, J. Mattheis, U. Rau, in *Thin Solid Films*, **2005**, pp. 399–409.

[44] D. Kuciauskas, J. V. Li, M. A. Contreras, J. Pankow, P. Dippo, M. Young, L. M. Mansfield, R. Noufi, D. Levi, *J Appl Phys* **2013**, *114*, DOI 10.1063/1.4825211.

[45] W. K. Metzger, I. L. Repins, M. A. Contreras, *Appl Phys Lett* **2008**, *93*, DOI 10.1063/1.2957983.

[46] S. Shirakata, T. Nakada, *Thin Solid Films* **2007**, *515*, 6151.

[47] T. P. Weiss, R. Carron, M. H. Wolter, J. Löckinger, E. Avancini, S. Siebentritt, S. Buecheler, A. N. Tiwari, *Sci Technol Adv Mater* **2019**, *20*, 313.

[48] M. Maiberg, C.-Y. Song, M. Morawski, F. Neduck, H. Kempa, J. Damm, D. Hariskos, W. Witte, R. Scheer, *Phys Rev Appl* **2024**, *21*, 034051.

[49] M. A. Green, A. W. Y. Ho-Baillie, *ACS Energy Lett* **2019**, *4*, 1639.

[50] W. Shockley, W. T. Read, *Physical Review* **1952**, *87*, 835.

[51] R. N. Hall, *Physical Review* **1952**, *87*, 387.

[52] C.-T. Sah, R. N. Noyce, W. Shockley, *Proceedings of the IRE* **1957**, *45*, 1228.

[53] A. Richter, S. W. Glunz, F. Werner, J. Schmidt, A. Cuevas, *Phys Rev B Condens Matter Mater Phys* **2012**, *86*, DOI 10.1103/PhysRevB.86.165202.

[54] D. Baek, *Journal of the Korean Physical Society* **2015**, *67*, 1064.

[55] S. Siebentritt, T. P. Weiss, M. Sood, M. H. Wolter, A. Lomuscio, O. Ramirez, *JPhys Materials* **2021**, *4*, DOI 10.1088/2515-7639/ac266e.

[56] W. Shockley, H. J. Queisser, *J Appl Phys* **1961**, *32*, 510.

[57] G. Rey, C. Spindler, F. Babbe, W. Rachad, S. Siebentritt, M. Nuys, R. Carius, S. Li, C. Platzer-Björkman, *Phys Rev Appl* **2018**, *9*, DOI 10.1103/PhysRevApplied.9.064008.

[58] S. Rühle, *Supporting Information Tabulated Values of the Shockley-Queisser Limit for Single Junction Solar Cells*, **n.d.**

[59] S. Siebentritt, U. Rau, S. Gharabeiki, T. P. Weiss, A. Prot, T. Wang, D. Adeleye, M. Drahem, A. Singh, *Faraday Discuss* **2022**, DOI 10.1039/d2fd00057a.

[60] M. H. Wolter, R. Carron, E. Avancini, B. Bissig, T. P. Weiss, S. Nishiwaki, T. Feurer, S. Buecheler, P. Jackson, W. Witte, S. Siebentritt, *Progress in Photovoltaics: Research and Applications* **2021**, DOI 10.1002/pip.3449.

[61] S. John, C. Soukoulis, M. H. Cohen, E. N. Economou, *Phys Rev Lett* **1986**, *57*.

[62] O. Ramírez, J. Nishinaga, F. Dingwell, T. Wang, A. Prot, M. H. Wolter, V. Ranjan, S. Siebentritt, O. Ramírez, F. Dingwell, T. Wang, A. Prot, M. H. Wolter, V. Ranjan, S. Siebentritt, J. Nishinaga, *Solar RRL* **2023**, *7*.

[63] U. Rau, J. H. Werner, *Appl Phys Lett* **2004**, *84*, 3735.

[64] J. Mattheis, U. Rau, J. H. Werner, *J Appl Phys* **2007**, *101*, DOI 10.1063/1.2721768.

[65] S. Gharabeiki, T. Schaaf, F. Lodola, T. Wang, M. Melchiorre, S. Siebentritt, *(In preparation)* **2024**.

[66] T. Trupke, R. A. Bardos, M. D. Abbott, J. E. Cotter, *Appl Phys Lett* **2005**, *87*, DOI 10.1063/1.2034109.

[67] F. Babbe, L. Choubrac, S. Siebentritt, *Solar RRL* **2018**, *2*, DOI 10.1002/solr.201800248.

[68] T. P. Weiss, F. Ehre, V. Serrano-Escalante, T. Wang, S. Siebentritt, *Solar RRL* **2021**, *5*, DOI 10.1002/solr.202100063.

[69] T. P. Weiss, O. Ramírez, S. Paetel, W. Witte, J. Nishinaga, T. Feurer, S. Siebentritt, *Phys Rev Appl* **2023**, *19*, DOI 10.1103/PhysRevApplied.19.024052.

[70] S. Lany, A. Zunger, *J Appl Phys* **2006**, *100*, DOI 10.1063/1.2388256.

[71] B. Saleh, M. Teich, *Fundamentals of Photonics*, Wiley, **2019**.

[72] A. Kanevce, D. Kuciausskas, T. A. Gessert, D. H. Levi, D. S. Albin, *38th IEEE Photovoltaic Specialists Conference* **2012**, 848.

[73] B. Ohnesorge, R. Weigand, G. Bacher, A. Forchel, W. Riedl, F. H. Karg, *Appl Phys Lett* **1998**, *73*, 1224.

[74] J. Palm, V. Probst, F. H. Karg, *Solar Energy* **2004**, *77*, 757.

[75] W. K. Metzger, D. Albin, D. Levi, P. Sheldon, X. Li, B. M. Keyes, R. K. Ahrenkiel, *J Appl Phys* **2003**, *94*, 3549.

[76] T. Kirchartz, J. A. Márquez, M. Stolterfoht, T. Unold, *Adv Energy Mater* **2020**, *10*, DOI 10.1002/aenm.201904134.

[77] M. Maiberg, R. Scheer, *J Appl Phys* **2014**, *116*, DOI 10.1063/1.4896483.

[78] M. Maiberg, R. Scheer, *J Appl Phys* **2014**, *116*, DOI 10.1063/1.4896484.

[79] M. Maiberg, T. Hölscher, S. Zahedi-Azad, R. Scheer, *J Appl Phys* **2015**, *118*, DOI 10.1063/1.4929877.

[80] W. K. Metzger, R. K. Ahrenkiel, J. Dashdorj, D. J. Friedman, *Phys Rev B Condens Matter Mater Phys* **2005**, *71*, DOI 10.1103/PhysRevB.71.035301.

[81] M. Maiberg, C. Spindler, E. Jarzembowski, R. Scheer, *Thin Solid Films* **2015**, *582*, 379.

[82] S. J. Heise, J. F. López Salas, *Thin Solid Films* **2017**, *633*, 35.

[83] Y. I. Ogita, *J Appl Phys* **1996**, *79*, 6954.

[84] K. L. Luke, L. J. Cheng, *J Appl Phys* **1987**, *61*, 2282.

[85] T. Wang, F. Ehre, T. P. Weiss, B. Veith-Wolf, V. Titova, N. Valle, M. Melchiorre, O. Ramírez, J. Schmidt, S. Siebentritt, *Adv Energy Mater* **2022**, *12*, DOI 10.1002/aenm.202202076.

[86] A. B. Sproul, *J Appl Phys* **1994**, *76*, 2851.

[87] T. Otaredian, *Solid State Electron* **1993**, *36*, 153.

[88] R. K. Ahrenkiel, S. W. Johnston, *Solar Energy Materials and Solar Cells* **2009**, *93*, 645.

[89] R. Kniese, M. Powalla, U. Rau, *Thin Solid Films* **2009**, *517*, 2357.

[90] R. K. Ahrenkiel, N. Call, S. W. Johnston, W. K. Metzger, *Solar Energy Materials and Solar Cells* **2010**, *94*, 2197.

[91] R. Scheer, A. Pérez-Rodríguez, W. K. Metzger, *Progress in Photovoltaics: Research and Applications* **2010**, *18*, 467.

[92] M. Maiberg, F. Bertram, M. Müller, R. Scheer, *J Appl Phys* **2017**, *121*, DOI 10.1063/1.4976102.

[93] J. Palm, T. Dalibor, R. Lechner, S. Pohlner, R. Verma, R. Dietmüller, A. Heiß, H. Vogt, F. Karg, in *29th European Photovoltaic Solar Energy Conference and Exhibition*, **2014**.

[94] W. K. Metzger, I. L. Repins, M. Romero, P. Dippo, M. Contreras, R. Noufi, D. Levi, *Thin Solid Films* **2009**, *517*, 2360.

[95] D. Regesch, L. Gütay, J. K. Larsen, V. Deprédurand, D. Tanaka, Y. Aida, S. Siebentritt, *Appl Phys Lett* **2012**, *101*, DOI 10.1063/1.4752165.

[96] F. Babbe, L. Choubrac, S. Siebentritt, *Appl Phys Lett* **2016**, *109*, DOI 10.1063/1.4961530.

[97] A. M. Mathai, *Jacobians of Matrix Transformations and Functions of Matrix Argument*, World Scientific Pub., Singapore, **1997**.

[98] M. Wahl, *The Principle of Time-Correlated Single Photon Counting*, PicoQuant GmbH, Berlin, **2014**.

[99] D. Drouin, A. Réal Couture, D. Joly, X. Tastet, V. Aimez, R. Gauvin, *CASINO V2.42-A Fast and Easy-to-Use Modeling Tool for Scanning Electron Microscopy and Microanalysis Users*, **2007**.

[100] "Cambridge Center for Gallium Nitride," can be found under https://www.gan.msm.cam.ac.uk/, **2024**.

[101] J. Lähnemann, J. F. Orri, E. Prestat, D. N. Johnstone, N. Tappy, "LumiSpy/lumispy: v0.2.1," DOI 10.5281/ZENODO.7274897can be found under https://zenodo.org/record/7274897, **2022**.

[102] D. Abou-Ras, R. Caballero, C. H. Fischer, C. A. Kaufmann, I. Lauermann, R. Mainz, H. Mönig, A. Schöpke, C. Stephan, C. Streeck, S. Schorr, A. Eicke, M. Döbeli, B. Gade, J. Hinrichs, T. Nunney, H. Dijkstra, V. Hoffmann, D. Klemm, V. Efimova, A. Bergmaier, G. Dollinger, T. Wirth, W. Unger, A. A. Rockett, A. Perez-Rodriguez, J. Alvarez-Garcia, V. Izquierdo-Roca, T. Schmid, P. P. Choi, M. Müller, F. Bertram, J. Christen, H. Khatri, R. W. Collins, S. Marsillac, I. Kötschau, *Microscopy and Microanalysis* **2011**, *17*, 728.

[103] J. Angeli, A. Bengtson, A. Bogaerts, V. Hoffmann, V. D. Hodoroaba, E. Steers, *J Anal At Spectrom* **2003**, *18*, 670.

[104] E. Smith, G. Dent, *Modern Raman Spectroscopy: A Practical Approach*, John Wiley & Sons Ltd., **2019**.

[105] W. Kauschke, M. Cardona, *Phys. Scr* **1989**, *T25*, 201.

[106] "Institut de Recerca en Energia de Catalunya (IREC)," can be found under https://www.irec.cat/, **n.d.**

[107] U. Rau, H. W. Schock, *Appl. Phys. A* **1999**, *69*, 131.

[108] L. Stolt, J. Hedström, J. Kessler, M. Ruckh, K. O. Velthaus, H. W. Schock, *Appl Phys Lett* **1993**, *62*, 597.

[109] R. Scheer A', M. Wilhelm, H. J. Lewerenz, H. W. Schock, L. Stolt, *Solar Energy Materials and Solar Cells* **1997**, *49*, 299.

[110] T. P. Weiss, B. Bissig, T. Feurer, R. Carron, S. Buecheler, A. N. Tiwari, *Sci Rep* **2019**, *9*, DOI 10.1038/s41598-019-41716-x.

[111] E. Jarzembowski, F. Syrowatka, K. Kaufmann, W. Fränzel, T. Hölscher, R. Scheer, *Appl Phys Lett* **2015**, *107*, DOI 10.1063/1.4928187.

[112] T. Schneider, J. Tröndle, B. Fuhrmann, F. Syrowatka, A. Sprafke, R. Scheer, *Solar RRL* **2020**, *4*, DOI 10.1002/solr.202000295.

[113] B. Vermang, J. T. Wätjen, V. Fjällström, F. Rostvall, M. Edoff, R. Kotipalli, F. Henry, D. Flandre, *Progress in Photovoltaics: Research and Applications* **2014**, *22*, 1023.

[114] T. Wang, L. Song, S. Gharabeiki, M. Sood, A. JC. M. Prot, R. G. Poeira, M. Melchiorre, N. Valle, A.-M. Philippe, S. Glinsek, E. Defay, P. J. Dale, S. Siebentritt, *Solar RRL* **2024**, *8*.

[115] M. Contreras, J. Tuttle, D. Du, Y. Qi, A. Swartzlander, A. Tennant, R. Noufi, *Appl Phys Lett* **1993**, *63*, 1824.

[116] M. A. Contreras, A. M. Gabor, A. L. Tennant, S. Asher, J. Tuttle, R. Noufi, *Progress in Photovoltaics: research and application* **1994**, *2*, 287.

[117] A. Dhingra, A. Rothwarf, in *Proc. 23rd IEEE Photovoltaic Specialists Conf.*, **1993**, pp. 475–480.

[118] M. Nakamura, K. Yamaguchi, Y. Kimoto, Y. Yasaki, T. Kato, H. Sugimoto, *IEEE J Photovolt* **2019**, *9*, 1863.

[119] F. Karg, in *Energy Procedia*, **2012**, pp. 275–282.

[120] T. Dullweber, O. Lundberg, J. Malmström, M. Bodegard, L. Stolt, U. Rau, H. W. Schock, J. H. Werner, *Thin Solid Films* **2001**, *387*, 11.

[121] T. Klinkert, M. Jubault, F. Donsanti, D. Lincot, J. F. Guillemoles, *Journal of Renewable and Sustainable Energy* **2014**, *6*, DOI 10.1063/1.4866255.

[122] M. H. Wolter, B. Bissig, E. Avancini, R. Carron, S. Buecheler, P. Jackson, S. Siebentritt, *IEEE J Photovolt* **2018**, *8*, 1320.

[123] J. Tauc, R. Grigorovici, A. Vancu, *phys. stat. sol* **1966**, *15*, 627.

[124] E. A. Davis, N. F. Mott, *Philosophical Magazine* **1970**, *22*, 903.

[125] R. Carron, C. Andres, E. Avancini, T. Feurer, S. Nishiwaki, S. Pisoni, F. Fu, M. Lingg, Y. E. Romanyuk, S. Buecheler, A. N. Tiwari, *Thin Solid Films* **2019**, *669*, 482.

[126] J. Keller, R. Schlesiger, I. Riedel, J. Parisi, G. Schmitz, A. Avellan, T. Dalibor, *Solar Energy Materials and Solar Cells* **2013**, *117*, 592.

[127] S. Lange, F. Giesl, V. Naumann, C. Hagendorf, P. Eraerds, *Surface and Interface Analysis* **2022**, DOI 10.1002/sia.7081.

[128] L. Weinhardt, O. Fuchs, A. Peter, E. Umbach, C. Heske, J. Reichardt, M. Bär, I. Lauermann, I. Kötschau, A. Grimm, S. Sokoll, M. C. Lux-Steiner, T. P. Niesen, S. Visbeck, F. Karg, *Journal of Chemical Physics* **2006**, *124*, DOI 10.1063/1.2168443.

[129] R. Scheer, H. -J. Lewerenz, *Journal of Vacuum Science & Technology A: Vacuum, Surfaces, and Films* **1995**, *13*, 1924.

[130] C. Wang, Z. Hu, Y. Liu, S. Cheng, Y. Yao, Y. Zhang, X. Yang, Z. Zhou, F. Liu, Y. Zhang, Y. Sun, W. Liu, *Journal of Materials Science: Materials in Electronics* **2022**, *33*, 11055.

[131] Joseph A. Curcio, Charles C. Petty, *J. Opt. Soc. Am.* **1951**, *41*, 302.

[132] Y. H. Chang, R. Carron, M. Ochoa, C. Bozal-Ginesta, A. N. Tiwari, J. R. Durrant, L. Steier, *Adv Energy Mater* **2021**, *11*, DOI 10.1002/aenm.202003446.

[133] P. W. Yu, *J Appl Phys* **1977**, *48*, 5043.

[134] S. A. Schumacher, J. R. Botha, V. Alberts, *J Appl Phys* **2006**, *99*, DOI 10.1063/1.2180429.

[135] M. H. Wolter, Optical Investigation of Voltage Losses in High-Efficiency Cu(In,Ga)Se2 Thin Film Solar Cells, University du Luxembourg, **2019**.

[136] Sugai Shunji, *J Physical Soc Japan* **1977**, *43*, 592.

[137] F. Oliva, S. Kretzschmar, D. Colombara, S. Tombolato, C. M. Ruiz, A. Redinger, E. Saucedo, C. Broussillou, T. G. de Monsabert, T. Unold, P. J. Dale, V. Izquierdo-Roca, A. Pérez-Rodríguez, *Solar Energy Materials and Solar Cells* **2016**, *158*, 168.

[138] S. Y. Kim, M. S. Mina, J. Lee, J. H. Kim, *ACS Appl Mater Interfaces* **2019**, *11*, 45702.

[139] C. Insignares-Cuello, V. Izquierdo-Roca, J. López-García, L. Calvo-Barrio, E. Saucedo, S. Kretzschmar, T. Unold, C. Broussillou, T. Goislard de Monsabert, V. Bermudez, A. Pérez-Rodríguez, *Solar Energy* **2014**, *103*, 89.

[140] D. Nam, J. U. Lee, H. Cheong, *Sci Rep* **2015**, *5*, DOI 10.1038/srep17113.

[141] Y. Ando, I. Khatri, H. Matsumori, M. Sugiyama, T. Nakada, *Physica Status Solidi (A) Applications and Materials Science* **2019**, *216*, DOI 10.1002/pssa.201900164.

[142] T. Klinkert, B. Theys, G. Patriarche, M. Jubault, F. Donsanti, J. F. Guillemoles, D. Lincot, *Journal of Chemical Physics* **2016**, *145*, DOI 10.1063/1.4964677.

[143] T. Terasako, Y. Uno, T. Kariya, S. Shirakata, *Solar Energy Materials and Solar Cells* **2006**, *90*, 262.

[144] C. Insignares-Cuello, C. Broussillou, V. Bermúdez, E. Saucedo, A. Pérez-Rodríguez, V. Izquierdo-Roca, *Appl Phys Lett* **2014**, *105*, DOI 10.1063/1.4890970.

[145] K. Wakita, T. Miyazaki, Y. Kikuno, S. Takata, N. Yamamoto, *Jpn J Appl Phys* **1999**, *38*, 664.

[146] "Instituto Italiano di Tecnologia (IIT)," can be found under https://www.iit.it/, **2024**.

[147] S. Niki, R. Suzuki, S. Ishibashi, T. Ohdaira, P. J. Fons, A. Yamada, H. Oyanagi, T. Wada, R. Kimura, T. Nakada, *Thin Solid Films* **2001**, *387*, 129134.

[148] L. M. Mansfield, D. Kuciauskas, P. Dippo, J. V. Li, K. Bowers, B. To, C. Dehart, K. Ramanathan, *IEEE J Photovolt* **2015**, *5*, 1769.

[149] S. Siebentritt, A. Lomuscio, D. Adeleye, M. Sood, A. Dwivedi, *Physica Status Solidi - Rapid Research Letters* **2022**, *16*, DOI 10.1002/pssr.202200126.

[150] C. Spindler, D. Regesch, S. Siebentritt, *Appl Phys Lett* **2016**, *109*, DOI 10.1063/1.4959557.

[151] Peter T. Erslev, Gregory M. Hanket, William N. Shafarman, J. David Cohen, in *MRS Online Proceedings Library* , **2009**.

[152] J. Keller, K. V. Sopiha, O. Stolt, L. Stolt, C. Persson, J. J. S. Scragg, T. Törndahl, M. Edoff, *Progress in Photovoltaics: Research and Applications* **2020**, *28*, 237.

[153] S. Chen, X. G. Gong, S. H. Wei, *Phys Rev B Condens Matter Mater Phys* **2007**, *75*, DOI 10.1103/PhysRevB.75.205209.

[154] J. H. Boyle, B. E. McCandless, W. N. Shafarman, R. W. Birkmire, *J Appl Phys* **2014**, *115*, DOI 10.1063/1.4880243.

[155] T. Nakada, K. Yamada, R. Arai, H. Ishizaki, N. Yamada, *Materials Research Society Symposium Proceedings* **2005**, *865*.

[156] P. T. Erslev, J. Lee, G. M. Hanket, W. N. Shafarman, J. D. Cohen, in *Thin Solid Films*, **2011**, pp. 7296–7299.

[157] K. Kim, J. W. Park, J. S. Yoo, J. S. Cho, H. D. Lee, J. H. Yun, *Solar Energy Materials and Solar Cells* **2016**, *146*, 114.

[158] G. M. Hanket, C. P. Thompson, J. K. Larsen, E. Eser, W. N. Shafarman, in *38th IEEE Photovoltaic Specialists Conference, Austin, TX, USA*, **2012**.

[159] L. Chen, J. Lee, W. N. Shafarman, *IEEE J Photovolt* **2014**, *4*, 447.

[160] M. Edoff, T. Jarmar, N. S. Nilsson, E. Wallin, D. Hogstrom, O. Stolt, O. Lundberg, W. Shafarman, L. Stolt, *IEEE J Photovolt* **2017**, *7*, 1789.

[161] Nicholas Valdes, JinWoo Lee, William Shafarman, *IEEE 7th World Conference on Photovoltaic Energy Conversion (WCPEC)* **2018**.

[162] N. Valdes, J. W. Lee, W. Shafarman, *Solar Energy Materials and Solar Cells* **2019**, *195*, 155.

[163] A. Kanevce, S. Essig, S. Paetel, W. Hempel, D. Hariskos, T. Magorian Friedlmeier, *EPJ Photovoltaics* **2022**, *13*, DOI 10.1051/epjpv/2022026.

[164] Y. Zhang, L. Shi, Z. Wang, H. Dai, Z. Hu, S. Zhou, H. Chen, X. Feng, J. Zhu, Y. Sun, W. Liu, Q. Zhang, *Solar Energy* **2021**, *227*, 334.

[165] Y. Zhao, S. Yuan, D. Kou, Z. Zhou, X. Wang, H. Xiao, Y. Deng, C. Cui, Q. Chang, S. Wu, *ACS Appl Mater Interfaces* **2020**, *12*, 12717.

[166] H. Mori, J. Chantana, Y. Kawano, T. Negami, T. Minemoto, *Materials Science and Engineering: B* **2023**, *297*, DOI 10.1016/j.mseb.2023.116758.

[167] K. Cheng, X. Shen, J. Liu, X. Liu, Z. Du, *Solar Energy* **2021**, *217*, 70.

[168] M. Krause, S. C. Yang, S. Moser, S. Nishiwaki, A. N. Tiwari, R. Carron, *Solar RRL* **2023**, *7*, DOI 10.1002/solr.202201122.

[169] S. Essig, S. Paetel, T. M. Friedlmeier, M. Powalla, *JPhys Materials* **2021**, *4*, DOI 10.1088/2515-7639/abd73d.

[170] G. Kim, W. M. Kim, J. K. Park, D. Kim, H. Yu, J. H. Jeong, *ACS Appl Mater Interfaces* **2019**, *11*, 31923.

[171] H. Rodriguez-Alvarez, R. Mainz, R. Caballero, D. Abou-Ras, M. Klaus, S. Gledhill, A. Weber, C. A. Kaufmann, H. W. Schock, *Solar Energy Materials and Solar Cells* **2013**, *116*, 102.

[172] D. J. Schroeder, G. D. Berry, A. A. Rockett, *Appl Phys Lett* **1996**, *69*, 4068.

[173] D. Colombara, *Phys Rev Mater* **2019**, *3*, DOI 10.1103/PhysRevMaterials.3.054602.

[174] J. Keller, L. Stolt, K. V. Sopiha, J. K. Larsen, L. Riekehr, M. Edoff, *Solar RRL* **2020**, *4*, DOI 10.1002/solr.202000508.

[175] S. De Wolf, J. Holovsky, S. J. Moon, P. Löper, B. Niesen, M. Ledinsky, F. J. Haug, J. H. Yum, C. Ballif, *Journal of Physical Chemistry Letters* **2014**, *5*, 1035.

[176] A. Czudek, A. Urbaniak, A. Eslam, R. Wuerz, M. Igalson, *Phys. Status Solidi RRL* **2022**, *16*.

[177] M. Igalson, M. Maciaszek, K. Macielak, A. Czudek, M. Edoff, N. Barreau, *Thin Solid Films* **2019**, *669*, 600.

[178] D. Rudmann, D. Brémaud, A. F. Da Cunha, G. Bilger, A. Strohm, M. Kaelin, H. Zogg, A. N. Tiwari, in *Thin Solid Films*, **2005**, pp. 55–60.

[179] D. Colombara, F. Werner, T. Schwarz, I. Cañero Infante, Y. Fleming, N. Valle, C. Spindler, E. Vacchieri, G. Rey, M. Guennou, M. Bouttemy, A. G. Manjón, I. Peral Alonso, M. Melchiorre, B. El Adib, B. Gault, D. Raabe, P. J. Dale, S. Siebentritt, *Nat Commun* **2018**, *9*, DOI 10.1038/s41467-018-03115-0.

[180] D. Macdonald, A. Cuevas, J. Wong-Leung, *J Appl Phys* **2001**, *89*, 7932.

[181] B. J. Baliga, *Fundamentals of Power Semiconductor Devices*, Springer, **2019**.

[182] J. Linnros, *J Appl Phys* **1998**, *84*, 275.

[183] J. Schmidt, D. MacDonald, *J Appl Phys* **2005**, *97*, DOI 10.1063/1.1929096.

[184] J. Schmidt, *Appl Phys Lett* **2003**, *82*, 2178.

[185] H. Bleichner, P. Jonsson, N. Keskitalo, E. Nordlander, *J Appl Phys* **1996**, *79*, 9142.

[186] K. Bothe, J. Schmidt, R. Hezel, in *Conference Record of the Twenty-Ninth IEEE Photovoltaic Specialists Conference*, **2002**, pp. 194–197.

[187] J. A. Giesecke, T. Niewelt, M. Rüdiger, M. Rauer, M. C. Schubert, W. Warta, *Solar Energy Materials and Solar Cells* **2012**, *102*, 220.

[188] D. Macdonald, L. J. Geerligs, *Appl Phys Lett* **2004**, *85*, 4061.

[189] Z. Cheng, A. E. Delahoy, K. K. Chin, in *IEEE 40th Photovoltaic Specialist Conference (PVSC)*, **2014**, pp. 1596–1600.

[190] J. Moseley, D. Krasikov, C. Lee, D. Kuciauskas, *J Appl Phys* **2021**, *130*, DOI 10.1063/5.0063028.

[191] S. Shirakata, T. Nakada, in *Physica Status Solidi (C) Current Topics in Solid State Physics*, **2009**, pp. 1059–1062.

[192] M. Maiberg, T. Hölscher, S. Zahedi-Azad, W. Fränzel, R. Scheer, *Appl Phys Lett* **2015**, *107*, DOI 10.1063/1.4931632.

[193] M. Maiberg, T. Hölscher, E. Jarzembowski, S. Hartnauer, S. Zahedi-Azad, W. Fränzel, R. Scheer, *Thin Solid Films* **2017**, *633*, 208.

[194] D. K. Schroder, *Semiconductor Material and Device Characterization*, Wiley, **2005**.

[195] S. Levcenko, V. E. Tezlevan, E. Arushanov, S. Schorr, T. Unold, *Phys Rev B Condens Matter Mater Phys* **2012**, *86*, DOI 10.1103/PhysRevB.86.045206.

[196] M. S. Tyagi, R. Van Overstraeten, **1983**, *26*, 577.

[197] B. C. Connelly, G. D. Metcalfe, H. Shen, M. Wraback, C. L. Canedy, I. Vurgaftman, J. S. Melinger, C. A. Affouda, E. M. Jackson, J. A. Nolde, J. R. Meyer, E. H. Aifer, *J Electron Mater* **2013**, *42*, 3203.

[198] B. Das, I. Aguilera, U. Rau, T. Kirchartz, *Phys Rev Mater* **2020**, *4*, DOI 10.1103/PhysRevMaterials.4.024602.

[199] T. Kirchartz, T. Markvart, U. Rau, D. A. Egger, *Journal of Physical Chemistry Letters* **2018**, *9*, 939.

[200] T. Markvart, in *In Recombination in Semiconductors* (Ed.: P. T. Landsberg), Cambridge University Press, Cambridge, **2003**, p. 467.

[201] C. H. Henry, D. V. Lang, *Phys Rev B* **1977**, *15*, 989.

[202] A. Schenk, *Solid State Electron* **1992**, *35*, 1585.

[203] M. J. Trimpl, A. D. Wright, K. Schutt, L. R. V. Buizza, Z. Wang, M. B. Johnston, H. J. Snaith, P. Müller-Buschbaum, L. M. Herz, *Adv Funct Mater* **2020**, *30*, DOI 10.1002/adfm.202004312.

[204] L. G. Kudriashova, D. Kiermasch, P. Rieder, M. Campbell, K. Tvingstedt, A. Baumann, G. V. Astakhov, V. Dyakonov, *Journal of Physical Chemistry Letters* **2017**, *8*, 4697.

[205] C. Rincón, R. Márquez, *Journal of physics and chemistry of solids* **1999**, *60*, 1865.

[206] S. A. Jensen, A. Kanevce, L. M. Mansfield, S. Glynn, S. Lany, D. Kuciauskas, *Sci Rep* **2017**, *7*, DOI 10.1038/s41598-017-14344-6.

[207] J. F. L. Salas, S. J. Heise, M. Richter, V. Gerliz, M. S. Hammer, J. Ohland, I. Hammer-Riedel, *Thin Solid Films* **2017**, *633*, 40.

[208] S. Gharabeiki, M. U. Farooq, T. Wang, M. Sood, M. Melchiorre, C. A. Kaufmann, A. Redinger, S. Siebentritt, *Journal of Physics: Energy* **2024**, DOI 10.1088/2515-7655/ad6104.

[209] F. Pianezzi, P. Reinhard, A. Chirilă, B. Bissig, S. Nishiwaki, S. Buecheler, A. N. Tiwari, *Physical Chemistry Chemical Physics* **2014**, *16*, 8843.

[210] S. H. Wei, S. B. Zhang, A. Zunger, *J Appl Phys* **1999**, *85*, 7214.

[211] A. Rockett, in *Thin Solid Films*, **2005**, pp. 2–7.

[212] M. Sugiyama, H. Sakakura, S. W. Chang, M. Itagaki, *Electrochim Acta* **2014**, *131*, 236.